PHYSICS DEPARTMENT

PhD Thesis

Neutron Star Mergers at the Dawn of Multimessenger Astrophysics

MASSIVE BINARIES, ACCRETION DISKS AND PHASE TRANSITIONS

Advisor:
Prof. Albino Perego

Candidate:
Camilletti Alessandro

Academic Year 2023/2024

Contents

Chapter 1

Introduction

Multimessenger astrophysics represents a new approach to understanding the nature of astrophysical phenomena. By combining data from various cosmic messengers, including electromagnetic radiation, cosmic rays, gravitational waves, and neutrinos, we have gained a multifaceted view of astrophysical events. This approach has facilitated the identification and characterization of high-energy astrophysical events that were previously beyond the capability of traditional astronomical observations.

The advent of the network of terrestrial gravitational wave (GW) detectors formed by Advanced LIGO [Aasi et al., 2015] and Advanced Virgo [Acernese et al., 2015], recently joined also by KAGRA [Aso et al., 2013, Akutsu et al., 2019] has opened the era of GW astronomy. At the end of the third observing run, the GW emission resulting from the late inspiral or from the merger of two black holes (BHs), one BH and a neutron star (NS), or two NSs were all observed [Abbott et al., 2019b, 2021a,b]. These groundbreaking observations have provided novel insights into the behavior of spacetime and have validated several key predictions of Einstein's theory of general relativity. Complementing these gravitational wave observatories, ground-based telescopes as the Very Large Telescope (VLT) and space-based telescopes like the The Fermi Gamma-ray Space Telescope and the Chandra X-ray Observatory have enabled the precise localization and characterization of electromagnetic counterparts associated with gravitational wave events, unraveling the intricate dynamics of these cosmic phenomena.

So far, two GW signals compatible with the inspiral of a binary neutron star (BNS) system were reported: GW170817 [Abbott et al., 2017b] and GW190425 [Abbott et al., 2020]. In the following we outline the properties of the first one, while the second is discussed at length in Chapter 4. GW170817 was observed in 2017 through the joint detection of the GW signal GW170817 by the Ligo-Virgo telescopes [Abbott et al., 2017b], of the gamma-ray by the *Fermi* Gamma-ray Burst Monitor [Goldstein et al., 2017] and of the electromagnetic transient AT2017gfo [Coulter et al., 2017, Arcavi et al., 2017, Lipunov et al., 2017, Soares-

Santos et al., 2017, Tanvir et al., 2017, Valenti et al., 2017]. It was interpreted as the merger of a BNS system with a chirp mass $\mathcal{M}_{\rm chirp} = (1.186 \pm 0.001)\ \mathrm{M}_\odot$ (see Sec. 2.2.2 for the definition of the chirp mass). The masses of the individual stars were $M_A = (1.46^{+0.12}_{-0.10})\ \mathrm{M}_\odot$ and $M_B = (1.27^{+0.09}_{-0.09})\ \mathrm{M}_\odot$, at 90 per cent credible level, resulting in a total mass in the range $2.72 - 2.76\ \mathrm{M}_\odot$ [Abbott et al., 2017b, 2019a]. The total mass of such a system is thus well within the expected range of Galactic BNS systems, as resulting from electromagnetic (EM) observations of pulsars in BNS systems [see e.g. Özel and Freire, 2016]. The NS nature of the colliding objects was further supported by the detection of several EM counterparts originated from a galaxy located at 40Mpc from us, including a short gamma-ray burst and its afterglow, a kilonova, and possibly the non-thermal emission produced by the high speed tail of the dynamical ejecta expelled in the merger [see e.g. Radice, 2020, Margutti and Chornock, 2021, and references therein]. The identification of a short gamma-ray burst, followed by a kilonova, provided compelling evidence for the production of heavy elements through the so-called rapid neutron capture nucleosynthesis (r-process), confirming the long standing prediction that BNS mergers have a cardinal role in the chemical evolution of the galaxies. The possibility of detecting GW170817 counterparts crucially depended on the availability of three detectors, which drastically reduced the sky localization area to 16 deg^2 [Abbott et al., 2017b,a, 2021a].

The field of multimessenger astrophysics continues to evolve, with ongoing advancements in detector technologies and data analysis techniques driving further exploration of the cosmos. The deployment of next-generation observatories, including the proposed Einstein Telescope [Maggiore et al., 2020], the Cosmic Explorer [Hofmann and Zanin, 2023] and the Cherenkov Telescope Array Evans et al. [2021], promises to extend the frontiers of multimessenger astrophysics, enabling more precise measurements and a deeper understanding of the underlying astrophysical phenomena. By leveraging the capabilities of advanced facilities, researchers aim to address a number of relevant questions in physics and astrophysics: the nature of dark matter, the attributes of BHs, and intricate properties of NSs, just to quote a few relevant examples.

In this landscape of opportunities, theoretical modeling has a key role and represents one of the major challenges in the field. On the one hand, detailed and sophisticated theoretical models are necessary to provide reliable predictions that can guide and help designing detection strategies. On the other hand, they are necessary to interpret the observation in terms of fundamental physics and astrophysics of the sources. In this context, numerical simulations of BNS mergers are the main tool to connect observations to underlying theoretical models. The merger and post-merger dynamics in BNS is highly non-linear and complex, involving many areas of physics. The intense gravitational field reached in this astrophysical events require a general relativistic description of the space-time. Theoretical models of nuclear

matter are needed to describe the NS composition and the thermodynamical properties of matter in the high-density and temperatures reached during the merger. The composition of matter is moreover determined by weak current reactions carried by neutrinos, which also transport a large fraction of the remnant energy to the outer region, influencing the composition and even the fate of the remnant [Perego et al., 2014].

In this complex scenario, it is thus clear that numerical modeling of BNS mergers is a necessary step to properly interpret results, address open questions, and extract the largest amount of information from available data, even from the potential lack of detections. The effects of different physical inputs can be simulated and then tested on the observations [see e.g. Baiotti and Rezzolla, 2017, Shibata and Hotokezaka, 2019, Radice et al., 2020, Bernuzzi, 2020, for recent reviews]. Many model of equation of state (EOS) have been already disfavored with the observation of the BNS merger GW170817 [Raaijmakers et al., 2020], and more precise constraints are expected with future detections.

In this thesis, we study the evolution of BNS systems through 3+1 numerical relativity simulations encompassing the latest orbits, the merger and the early post-merger phase, with the aim of answering some of the open, urgent questions in the field.

(a) In Chapter 4 we analyze a set of numerical simulations targeted to the BNS merger GW190425. GW190425 represented a significantly different event with respect to GW170817 in many aspects. While the latter was extensively studied, very few detailed studies of the former are available in the literature. In particular, no previous study tackled the modeling of GW190425 through simulations including a high degree of fidelity in the microphysics. It is then interesting to study this event including detailed microphysics to understand what we can expect from future detections of this kind in terms of remnant properties, dynamical ejecta, nucleosynthesis signature and kilonova light curves. Moreover, the lack of electromagnetic counterparts associated to GW190425 has left open many questions. For example, can the lack of an EM counterpart give constraints on the EOS and/or on the binary parameters? All these questions are at the very heart of our analysis.

(b) The matter expelled during the merger and post-merger concentrates around the central massive neutron star in a torus-shaped cloud of matter evolving as an accretion disk. Accretion disks formed in BNS mergers are the engine responsible for many relevant processes related to compact binary mergers and to multimessenger astrophysics. For example, the matter ejected from the accretion disk contributes for the nucleosynthesis of heavy elements which subsequently powers the kilonova transient. Morover, the interaction between the central remnant and the magnetic field in the disk is thought to be responsible for the production of the relativistic jet that eventually

produces a gamma-ray burst and its afterglow emission. In Chapter 5 we investigates the properties of the accretion disk formed in a BNS merger by analyzing a large sample of simulations, in their first $\sim$ 100 ms of their evolution, which are of major importance to understand their initial properties.

(c) The high densities reached during the merger open different concerns regarding the presence of a new state of matter, composed of deconfined quarks and gluons, called quark-gluon plasma (QGP). The properties of the QGP in the regime of high densities and moderate temperatures are unreachable in terrestrial laboratories. Multimessenger astrophisics give us the possibility to use BNS mergers as laboratories for fundamental physics. In Chapter 6 we investigate the possibility of forming QGP inside the newly formed massive neutron star remnant and the effects of different construction of the phase transition on some of the observables produced by BNS mergers.

Before entering into the details of our analysis, we will provide the minimal background in Chapter 2. The numerical methods employed to analyze the simulated data, such as the GW signal, the properties of the remnant and of the ejected material, the r-process yields and the kilonova light curves, are all presented in Chapter 3. Additionally, in Appendix C., we briefly discuss on the disk and ejected mass from BNS mergers with a total mass around the critical mass for a prompt collapse.

As we venture into this era of unprecedented discovery, multimessenger astrophysics stands as a testament to the remarkable potential of integrating multiple observational approaches to unlock the secrets of the cosmos.

The results, tables and figures in Chapter 4 and Chapter 5, as well as some parts of Chapter 2 are taken or adapted from Camilletti et al. [2022] and Camilletti et al. [2024]. The rest of the material, in particular Chapter 6 and Appendix C., is presented for the first time in this manuscript.

Chapter 2

Background

2.1 Isolated neutron stars

NSs were first theorized by Baade and Zwiky in 1933 [Baade and Zwicky, 1934] to explain supernova explosions. They realized that the collapse of an ordinary star to a very compact object, mainly composed of neutrons, would release large enough gravitational binding energy to produce a supernova. We must wait until 1967 for the first observation of a highly-magnetized, fast-spinning NS, i.e. a pulsar. In that year, Hewish and Bell, detected a strictly periodic signal, firstly thought as of artificial origin and referred as "little green man" [Hewish et al., 1968].

NSs originate from the gravitational collapse of massive stellar cores during a supernova explosion. The gravitational pressure exerted on the matter composing ordinary stars is counterbalanced by the gradient of pressure of the plasma. The latter is sustained against the energy loss due to photons and neutrinos by the thermonuclear reactions happening inside the star. Thermonuclear reactions, for a massive enough star, can synthetize all the elements up to iron group nuclei, starting from hydrogen and helium. The iron core produced at the end of hydrostatic burning collapses when its mass exceeds the Chandrasekhar limit of approximately $1.44(Y_e/0.5)^2$ $M_\odot$ (the maximum mass which can be supported by the pressure of a degenerate electron gas). The gravitational energy released by the contraction of the iron core is mainly converted into neutrinos, whose flux causes the expulsion of the external layers of the star [Burrows and Vartanyan, 2021]. The NS is the central remnant left by the core-collapse supernova (CCSN) just described[1].

During the collapse and the accretion phase, protons are converted to neutrons by the capture of electrons, with the consequent emission of electron neutrinos. Additionally, thermal processes and charged current reactions involving positrons produce neutrinos of all

[1]Other formation scenario are possible in stellar binary systems Kutschera [1998], Cerdá-Durán and Elias-Rosa [2018].

flavors. During this phase, there is an initial rise in the proto-neutron star (PNS) temperature as the energy from neutrino degeneracy is transferred to the matter and the PNS contracts. Subsequently, a deleptonization process cools the PNS to below approximately 5 MeV (5.8×10^{10} K), and the mean free path of neutrinos becomes greater than the stellar radius. At this point, the PNS becomes transparent to neutrinos and the nuclear reactions reach an equilibrium, i.e. neutron captures on protons are balanced by the beta decay of neutrons. Moreover, for times much larger than the cooling timescales, the isolated NS can be considered having $T = 0$ as it cools down to temperatures below 10^6 K. Indeed, NSs are composed by highly degenerate matter with a degeneration energy much higher than the thermal energy. The stable NS in this final stage is properly known as cold, β-equilibrated NS.

The least massive NS identified to date was detected in the Arecibo 327 MHz Drift Pulsar Survey [Deneva et al., 2013] in 2015, with a mass of 1.17 $M_\odot$ [Martinez et al., 2015]. In contrast, recent observations by the North American Nanohertz Observatory for Gravitational Waves (NANOGrav) [McLaughlin, 2013] and the Green Bank Telescope [DuPlain et al., 2008] established an upper limit of approximately 2.1 $M_\odot$ [Cromartie et al. [2019], see also Demorest et al. [2010], Antoniadis et al. [2013]]. NSs are compact objects characterized by their incredible density, packing up to two solar masses into a sphere with a radius of the order of 10 kilometers. This results in a typical average density of $\sim 10^{14} - 10^{15}$ g cm^{-3} and an astonishing gravitational field, with surface gravitational acceleration 10^{13} times the one on the Earth.

The structure and composition of the isolated, β-equilibrated NS varies with the density of the environment. The outer crust of a NS is composed by electrons, e^-, and ions, probably organized in a crystalline structure [Chamel and Haensel, 2008]. Increasing the density, the ions start to dissociate into neutrons n and protons p. Between half and twice nuclear saturation density, ρ_0, i.e. in the typical density range of the outer core of a NS, matter is composed of neutrons with a mixture of protons, electrons and even muons μ, in charge neutrality and beta equilibrium [Haensel et al., 2007]. The composition of the inner core, at even higher density, is mostly unknown. The density can reach up to $4 - 5\rho_0$ with the possible appearance of hyperons [Bombaci, 2017], pions, kaons [Ramos et al., 2001] and even quark matter. We will discuss more about deconfined quark matter in NSs and in BNSs [Most et al., 2019, Prakash et al., 2021] in Chapter 6.

The process of NS formation outlined above may occur within binary systems of ordinary massive stars, resulting in the emergence of two gravitationally bound NSs.

2.2 The evolution of binary neutron star systems

2.2.1 Gravitational wave emission from binary compact objects

When two compact objects orbit around each other, a portion of their gravitational energy is released in the form of GWs. Until the orbital speed of the two compact objects is small with respect to the speed of light, i.e. $v/c \ll 1$, the weak field approximation can be used: $g_{\mu\nu} = \eta_{\mu\nu} + h_{\mu\nu}$, where $h_{\mu\nu}$ is a small perturbation of the Minkowski metric $\eta_{\mu\nu}$. In this approximation, by expanding in powers of v/c the wave equation in vacuum $\Box\left(h_{\mu\nu} + 1/2\ \eta_{\mu\nu} h_{\sigma}^{\ \sigma}\right) = 0$, one can analytically describe the inspiral phase of the merger. The time evolution of the GW frequency, $f_{\rm GW}$, is governed by,

$$\dot{f}_{\rm GW} = \frac{12\sqrt[3]{2}}{5}\left(\frac{GM_{\rm chirp}}{c^3}\right) f_{\rm GW}^{11/3}\ , \tag{2.1}$$

where $M_{\rm chirp}$ is the chirp mass of the system,

$$M_{\rm chirp} = \sqrt[5]{\frac{\left(M_A M_B\right)^3}{M_A + M_B}}\ , \tag{2.2}$$

and M_A and M_B are the gravitational masses of the two compact objects, as measured by an observer at infinity. The solution of Eq. (2.1) is a monotonic increase of the frequency. The amplitude of the GW signal, proportional to $f_{\rm GW}^{2/3}$, also increase with time. The growth of amplitude and frequency are characteristic of the GW signal emitted during the inspiral phase, also referred as chirp signal.

This expansion in powers of v/c used to approximate the solutions of the Einstein equations is referred as post-Newtonian (PN) expansion. The PN approximations [see Blanchet, 2014, for a review] are a framework in which approximate solutions to the Einstein equations are found by expanding in powers of a small parameter (e.g. in power of v/c). Corrections to the chirp signal are found at higher order in the PN expansion. In particular, tidal interactions, encoded in the 5PN order (i.e. order $(v/c)^{10}$), play a crucial role in the merger, increasing the GW emission and reducing the time to merge.

To extract the value of the BNS parameters from an observed GW signal, a large number of wave templates are compared to the actual signal, after a complex noise-removing procedure. In order to have high quality templates, it is crucial to adopt advanced methods for modeling the GWs emitted by compact binary systems. The results obtained in the PN approximation can be resumed to incorporate some of the expected non-perturbative features of the exact result. This is one of the key ideas around the effecive one body (EOB) formalism [Damour and Nagar, 2009]. The EOB methods are capable of producing high

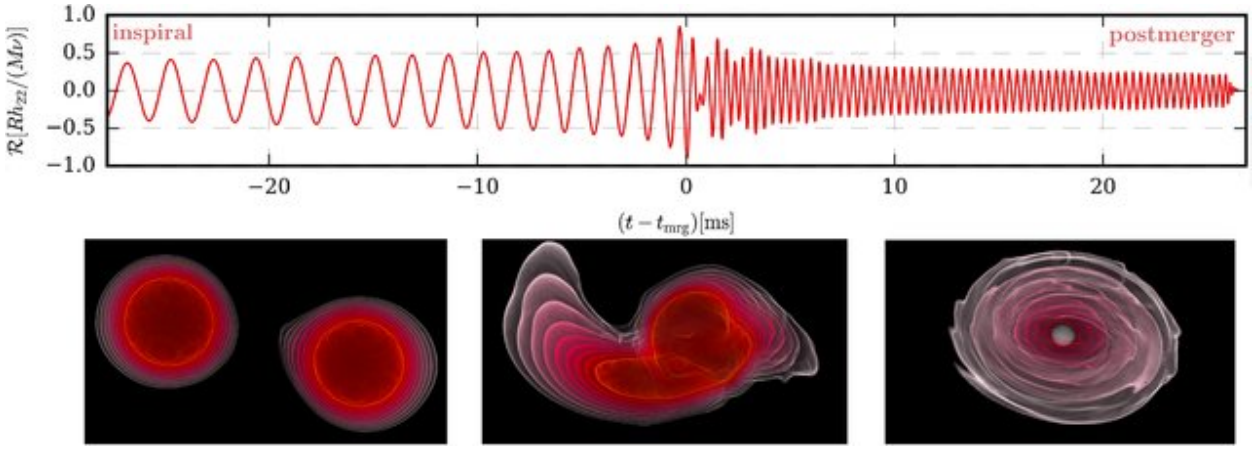

Figure 2.1: Top: real part of the strain h for the $l = m = 2$ mode of the GW emitted by a BNS system, from the late inspiral phase up to ~ 25 ms post-merger. Bottom: density contour in the orbital plane for the inspiral, merger and post-merger. Taken from Dietrich et al. [2021] Note that the remnant does not collapse to a BH in the simulated time.

quality templates for the waveform produced by the merger of compact objects. The actual GW signal detected by the GW interferometers is then matched against this collection of templates in order to determine the binary parameters such as the chirp mass, the mass ratio of the binary, $q = M_A/M_B$, and the single masses M_A, M_B of the compact binary system [Barack and Cutler, 2004, Biwer et al., 2019, Dudi et al., 2018] as well as their uncertainties. The chirp mass, being a parameter found at the first PN order, is associated with small uncertainties, while the errors on the parameters obtained from higher PN orders usually increase with the order of the expansion. PN expansion can address precisely only the GW signal corresponding to the inspiral phase of the merger. The merger and post-merger GW signal can be addressed only by means of numerical simulations (see Sec. 2.3).

Generally, we are interested in studying the GW emission from binary systems composed by BHs, NSs and a combination of both. The GW emission from binary black hole (BBH) differs from that of BH-NS and BNS systems. In the latter two scenarios, the properties of matter comprising the NSs play a crucial role in shaping the dynamics during the late inspiral, merger and post-merger phases. For the ensuing discussion, we will specifically address the GW signal and the dynamics associated with BNS systems.

Fig. 2.1 shows the real part of the GW strain h for the $l = m = 2$ mode, obtained from a numerical simulation of a BNS merger. The first part of the signal correspond to the inspiral, where the two NSs of the binary system orbits around each other. The distance between the two NSs decreases and the frequency and the amplitude of the signal increase, as described previously, until the two NSs merge. The merger, also depicted in the bottom central panel, is defined as the moment at which the GW strain of the gravitational wave reaches its maximum and it indicates, approximately, the moment in which the two compact objects

coalesce. GWs continue to be emitted during the post-merger and few milliseconds after the possible collapse of the central object. If the system collapses to a BH, the subsequent GW signal encodes details about the relaxation phase of the BH, referred as ring down. Indeed, during this phase, the BH oscillates in a series of characteristic damped frequencies called quasi-normal modes (QNMs), dissipating energy via GW emission until a Kerr metric is reached [Chandrasekhar and Detweiler, 1975, Kokkotas and Schmidt, 1999, Dhani et al., 2023].

2.2.2 The merger dynamics

Tight systems consisting of two orbiting compact objects eventually merge after a prolonged inspiral phase, during which they lose energy and angular momentum via gravitational radiation [Peters and Mathews, 1963, Peters, 1964]. At the end of the inspiral phase, tidal interactions cause the orbiting NSs to deform, forming spiral arms at the edges of the merging system. In the case of a significantly unequal mass binary, the lighter NS is tidally destroyed by the more massive one, and a significant fraction of its mass is spread around the more massive one, see e.g. [Rezzolla et al., 2010, Hotokezaka et al., 2013b, Bernuzzi et al., 2015, Hotokezaka et al., 2015, Bernuzzi et al., 2020]. During the subsequent merger, shocked matter is ejected from the collision interface of the two NSs. If the total mass of the system is large enough, a prompt-collapse to a BH occurs [Hotokezaka et al., 2011, Bauswein et al., 2013a, Köppel et al., 2019, Bauswein et al., 2021, Kashyap et al., 2022, Perego et al., 2022a, Kölsch et al., 2022, Tootle et al., 2021], halting matter ejection. Otherwise, core bounces of the newly-formed massive NS remnant expel hot matter in the first few milliseconds that follow the merger, see e.g. [Radice et al., 2018b, Perego et al., 2019]. An accretion disk is formed by the gravitationally bound matter expelled during this intricate dynamic. The subsequent disk evolution is governed by different physical processes, shaping its properties and determining its behavior. The absorption and emission of neutrinos influence the thermodynamic properties and composition of the disk [Ruffert et al., 1997, Rosswog and Liebendoerfer, 2003, Chen and Beloborodov, 2007, Perego et al., 2014, Siegel and Metzger, 2018, Fujibayashi et al., 2017, Nedora et al., 2021a]. Spiral waves [Nedora et al., 2019] and strong magnetic fields [Balbus and Hawley, 1991, Giacomazzo et al., 2011, Ciolfi et al., 2019] can efficiently transport angular momentum during the very first hundreds of milliseconds, while on longer, secular timescale the evolution is driven by viscous effects of turbulent magnetic origin [Zurek and Benz, 1986, Metzger et al., 2008, Fernández and Metzger, 2013, Just et al., 2015, Fujibayashi et al., 2020]. Additionally, the nature of the remnant heavily influences the disk properties. For example, spiral-waves or efficient neutrino irradiation are expected to occur as long as a massive NS remnant is present, while the formation of a BH

remnant causes the innermost and denser part of the disk to be swallowed inside the BH horizon, leading to the formation of a lighter torus, see e.g. [Bernuzzi et al., 2020, Nedora et al., 2021a].

2.2.3 Electromagnetic emissions

Differently from BBH mergers, detectable via GW observations only, NS-BH and BNS mergers also have multiple electromagnetic counterparts of different nature. In the aftermath of both NS-BH mergers and BNS mergers, when the remnant in the latter case collapse to a BH, the matter in the disk accretes into the central BH. It is commonly retained that, in the BH-engine scenario, the rapid accretion of a magnetized disk onto the BH can trigger the formation of a relativistic jet, possibly powering a gamma-ray bursts (GRBs), see e.g. [Blandford and Znajek, 1977, Blandford and Payne, 1982, Lee et al., 2000, Beloborodov, 2008, Giacomazzo et al., 2013, Berger, 2014, Siegel et al., 2014]. GRBs are extremely energetic bursts of gamma-ray radiation, lasting from a fraction of a second to several minutes.

The ejection of matter induces additional electromagnetic emissions. Fast ejecta with Lorentz factor $W \gtrsim 1.3$ can interact with the surrounding medium and magnetic fields. This interaction leads to acceleration, inducing non-thermal electromagnetic emissions [Nedora et al., 2021b, Hotokezaka et al., 2018, Most et al., 2021a]. Furthermore, the ejected material expands and progressively cools down. As far as the matter is approximately in nuclear statistical equilibrium (NSE), due to the equilibrium between photo-dissociation and proton/neutron captures, the nuclear composition is determined solely by the thermodynamical conditions of the matter, i.e. density, temperature, proton and neutron abundances. Typically, the ejected matter in this phase is composed by highly bound nuclei, such as alpha particles and iron group nuclei, forming the initial *seeds* that will contribute to the subsequent nucleosynthesis. As the temperature drops below $8 - 6$ GK, the temporal scale of nuclear reactions becomes comparable to the dynamical timescale of the expelled material. Consequently, the system exits the NSE (NSE *freeze-out*) phase. Following this transition, the dominant reactions include neutron capture, photo-dissociation and β^--decay[2]. Until the abundance of seeds significantly exceeds that of free neutrons, the fastest reaction is the neutron capture. This rapid capture of neutrons characterizes the r-process, leading to the production of neutron-rich elements from the initial seed nuclei [Symbalisty and Schramm, 1982, Argast et al., 2004, Wu et al., 2016, Siegel, 2022]. At slower pace, the β^--decay converts the neutrons inside the newly formed nuclei into protons. See, e.g. Perego et al. [2021], for a comprehensive review.

The radioactive decay of the nuclei releases a large amount of energy in the surrounding

[2] β^--decay is favored over β^+-decay in neutron rich nuclei. Numerous additional reactions must be considered to accurately model the ultimate abundances resulting from the r-process.

medium, powering the thermal transient emission commonly referred as kilonova [Smartt et al., 2017, Siegel, 2019, Curtis et al., 2022]. The kilonova AT2017gfo has been observed in two components: the blue and red components. The blue component of a kilonova is related to the shorter wavelengths of the electromagnetic spectrum, typically in the optical and shorter wavelength bands. The blue emission is associated with the early phase of the kilonova, occurring shortly after the merger event. On the contrary, the red component is associated with the later phases of the kilonova and it is characterized by longer wavelengths of the electromagnetic spectrum, typically in the infrared and longer wavelength bands. It is characterized by a more gradual and prolonged evolution compared to the blue component and it can persist for a longer duration as the kilonova evolves over time.

With the exception of very loud mergers, the GW signal alone is not sufficient to distinguish between BNS, BH-NS and BBH mergers. Since kilonovae are produced in neutron rich environments, the detection of a kilonova associated to a GW signal compatible with a compact object merger, is a smoking gun of a BNS or NS-BH merger event. We finally remark that the detection and analysis of kilonovae provide insights into the astrophysical processes associated with compact binary mergers, as well as contribute to our understanding of nucleosynthesis and the origin of heavy elements in the universe [Rosswog et al., 2018, Siegel, 2019, Schönrich and Weinberg, 2019].

2.3 Simulating binary neutron stars in general relativity

The merger of two neutrons stars is a complex scenario involving may areas of physics and requires state-of-the-art numerical simulations to be correctly described. In this thesis, we evolve BNS systems in full general relativity (GR) through 3+1 numerical relativity simulations encompassing the latest orbits, the merger and the early post-merger phase.

The Einstein equations are rewritten in the Arnowitt-Deser-Misner (ADM) formalism to split the space-time in a three dimensional space component and a one dimensional time direction. Let M be a hyperbolic pseudo Riemmanian 4-manifold and $\Sigma_t \otimes \mathbb{R}$ its *foliation*, i.e. a family of hypersurfaces defined by a timelike vector field. A schematic picture of the 3+1 splitting of the space-time is given in Fig. 2.2. The *deformation vector* describe the space-time evolution of a point P in P'. Its orthogonal and parallel components to the hypersurface Σ_t are the lapse function, α, and the shift vector, β^i, respectively. The foliation, as a sub-manifold, has a natural induced metric γ, related to the space-time metric g by,

$$g_{\mu\nu} = \begin{pmatrix} \gamma_{ij}\beta^i\beta^j - \alpha^2 & \gamma_{ij}\beta^j \\ \gamma_{ij}\beta^j & \gamma_{ij} \end{pmatrix} \qquad i = 1, 2, 3 \ . \tag{2.3}$$

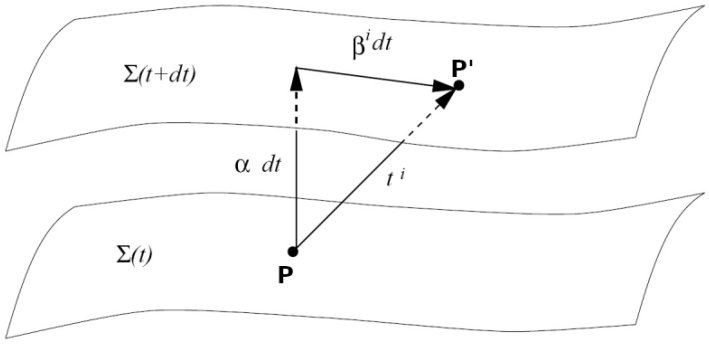

Figure 2.2: Hypersurface foliation of the space-time. P moves in P' following the deformation vector, whose normal component (parallel component) to Σ_t is the lapse function α (shift vector β^i).

In the simulation described in this thesis, matter is modeled as a perfect fluid with stress energy tensor

$$T_{\mu\nu} = \rho h u_\mu u_\nu + p g_{\mu\nu} \ , \tag{2.4}$$

where ρ is the rest-mass density of the fluid, u^μ is its four-velocity, p the pressure and h is the specific enthalpy

$$h = \epsilon + \frac{p}{\rho} \ , \tag{2.5}$$

with ϵ being the specific energy (rest mass energy included). Instead of the *primitive* quantities, i.e. the density ρ, the eluerian fluid velocity v_i and the specific energy ϵ, it is preferable to evolve the *conserved* quantities

$$D = \rho W \qquad \text{Conserved rest-mass density} \ , \tag{2.6}$$

$$S_i = \rho h W^2 v_i \qquad \text{Conserved momentum density} \ , \tag{2.7}$$

$$\mathcal{E} = \rho h W^2 - p - D \qquad \text{Conserved energy density} \ , \tag{2.8}$$

where W is the Lorentz factor. With this choice of variables the equations can be written in a conservative form. Expressing the relativistic hydrodynamic equations as a set of conservation laws ensures the preservation of the correct Rankine-Hugoniot conditions and facilitates the extension of advanced high-resolution shock-capturing schemes from classical fluid dynamics to the domain of relativity. These are the foundational ideas of the Valencia formulation adopted in our numerical simulations.

In all these stages of the evolution, the system emits GW, that we extract at a coordinate radius of ≈ 591 km from the BNS center of mass and extrapolate at null infinity. Because of the different mechanisms discussed before, a relevant fraction of matter is ejected from the late inspiral on. We are interested in study the properties of this ejected matter far from

the central object. The properties of the ejecta are established as it traverses a spherical detector with a coordinate radius of $r_{\rm E} \approx 294$ km. The detector is divided into a grid with $N_\theta = 51$ polar bins and $N_\phi = 93$ azimuthal bins, ensuring uniform angular discretization. The information derived from the simulations can be employed as input for kilonova models and nuclear network solvers like SkyNet [Lippuner and Roberts, 2017]. This provides the opportunity to explore r-process yields and the corresponding characteristic light curves.

2.3.1 Short summary of the employed codes

All the BNS simulations used in this work share the same numerical setup and microphysics treatment, making their outcome comparable The spacetime metric is evolved with the Z4c formulation of Einstein's equations [Bernuzzi and Hilditch, 2010, Hilditch et al., 2013] using the `CTGamma` code [Pollney et al., 2011, Reisswig et al., 2013b], developed within the `EinsteinToolkit` framework [Löffler et al., 2012, Brandt et al., 2021]. We use the `WhiskyTHC` code [Radice and Rezzolla, 2012, Radice et al., 2014], implemented within the `Cactus` [Goodale et al., 2003, Schnetter et al., 2007] framework to solve the GR hydrodynamic equations. `WhiskyTHC` evolves the proton and neutron number density equations, in addition to the relativistic version of the momentum and energy conservation equations, written in conservative form. To properly resolve the NS structure and merger dynamics, and at the same time track the evolution of the ejecta on a large enough domain, we employ a mesh refinement [Schnetter et al., 2004, Reisswig et al., 2013a] consisting in seven nested grids characterized by a 1:2 linear scaling between consecutive grids, with the most refined level covering the two NSs during the inspiral and the central remnant after merger. We characterize each simulation by the resolution of the innermost grid, h, and in particular $h \approx 246$ m for low resolution (LR), $h \approx 185$ m for standard resolution (SR) and $h \approx 123$ m for high resolution (HR) runs. Once the symmetry along the $z = 0$ plane is taken into account, the simulated space is a cube of side 3024 km. For further details on the numerical setup we refer to [Radice et al., 2018b]. Thanks to the use of a puncture gauge, the spacetime evolution can handle the formation of a singularity within the computational domain [Thierfelder et al., 2011, Dietrich and Bernuzzi, 2015]. The apparent horizon (AH) can possibly be detected by the `AHFinderDirect` thorn [Thornburg, 2004] of the `EinsteinToolkit`, from which the BH properties can be extracted.

In all simulations we include compositional and energy changes due to the emission and absorption of neutrinos of all flavours. In particular, a grey leakage scheme [Ruffert et al., 1996, Neilsen et al., 2014, Galeazzi et al., 2013] is used to model the net neutrino emission rates both from optically thick regions, where neutrinos are expected to form a diffusing gas in thermal and weak equilibrium with matter, and optically thin regions. Neutrinos are then

transported by an M0 scheme [Radice et al., 2018b] through optically thin regions, where the reabsorption of streaming electron flavours (anti)neutrinos can happen in addition to local emission.

Initial data for our simulations are constructed using the pseudo spectral elliptic solver Lorene [Gourgoulhon et al., 2001], using the EOS slice at the lowest available temperature and assuming neutrino-less beta-equilibrium. All simulations are initialized as irrotational binaries on quasicirular orbits of coordinate radius $45 - 50$ km. The residual initial eccentricity, estimated following [Kyutoku et al., 2014], is between 0.02 and 0.06 for all models.

2.4 Matter at extreme densities and finite temperature

The matter composition of a NS and its thermodynamical properties are referred as the EOS of neutron star matter. While isolated NS are described by the EOS of cold and β-equilibrated matter, the description of the final stages of evolution of a BNS system requires the extension of such EOS to finite temperature and arbitrary composition. We refer to the finite temperature, composition dependent EOS as the set of thermodynamic equations that fully specifies the state of the matter under a given set of physical conditions (state variables). In the context of interest here, the matter is modeled as a perfect fluid in local thermodynamic equilibrium, such that quantities like temperature, pressure and chemical potentials of the relevant species are well defined. In particular, chemical equilibrium between all reactions can be assumed if the timescale of the such reactions is shorter than the dynamical timescale of the system. When this condition is satisfied the system is said to be in NSE [Iliadis]. In this work, NSE is always assumed to hold in every phase of the evolution[3], with the exception of the r-process nucleosynthesis, where out of equilibrium condition, modeled by a complete nuclear reaction network, is considered instead (see Sec. 2.2.3).

Differently from nuclear reactions, the weak reactions that take part in the astrophysical environments discussed in the following chapters can be out-of-equilibrium, since their typical timescale can overcome the dynamical timescale of the astrophysical systems. For this reason it is important to include all the relevant weak reactions, like the processes involving neutrinos, to correctly describe changes in matter composition. Since neutrinos in astrophysical environments can be out-of-equilibrium, they are not directly included in the EOS relations, which assume local thermodynamical equilibrium, but their effects on the thermodynamic state of matter are handled via radiation hydrodynamics (see Sec. 2.3.1).

As mention in the previous section, the density inside the NS can reach values well above ρ_0. The EOS at supra-nuclear density cannot be reproduced in laboratory and cannot be computed exactly because first-principle computations of strong interacting many body

[3]For the topics discussed in this thesis, NSE is verified when the temperature $T \gtrsim 0.5$ MeV

particles are currently not possible. This translates in great uncertainties on the matter composition and the interactions above nuclear saturation density. The great effort of the nuclear physicist's community has produced a plethora of nuclear matter models, depending on the choice of the degrees of freedom (i.e. the particles included), the choice of the interactions and the selection of the many-body method. This models are able to correctly describe nuclear matter below and around nuclear saturation density, but the uncertainties increase with the density. In general, the models can be divided in *ab-initio*, which start from interactions inspired by first principle theories (e.g. quantum chromodynamics (QCD)) and phenomenological, whose description of the nuclear interactions depend on a number of parameters fitted on different experiments and experimental properties of nuclei. As examples in the first category, we find the chiral effective field theory (χEFT) [Weinberg, 1990, Machleidt and Entem, 2011, Scherer, 2003] and the pionless field theory ($\not\pi$EFT) [Bedaque and van Kolck, 2002, Barnea et al., 2015]. Commonly used phenomenological models are the one based on Skyrme interactions for non-relativistic calculations [Skyrme, 1959, Stone and Reinhard, 2007] and the models based on meson-exchange forces for relativistic interactions (see e.g. Oertel et al. [2017] for a complete review).

2.4.1 Equation of state models used in this work

In this work, to describe matter at arbitrary temperature and composition, we use a set of finite-temperature, composition-dependent EOSs broadly compatible with current astrophysical [Cromartie et al., 2019, Miller et al., 2019b, Riley et al., 2019] and nuclear [Capano et al., 2020, Jiang et al., 2020] constraints: BLh [Bombaci and Logoteta, 2018, Logoteta et al., 2021], HS(DD2) [Typel et al., 2010, Hempel and Schaffner-Bielich, 2010], SFHo [Steiner et al., 2013], SRO(SLy4) [Douchin and Haensel, 2001, Schneider et al., 2017] and LS220 Lattimer and Swesty [1991]. In the following, we will refer to the second and fourth ones simply as DD2 and SLy4. All these EOSs include neutrons, protons, nuclei, electrons, positrons, and photons as relevant thermodynamics degrees of freedom, and assume baryon matter in NSE.

The BLh EOS [Logoteta et al., 2021] is an extension of the zero-temperature BL EOS [Bombaci and Logoteta, 2018] that includes finite-temperature effects and arbitrary particle composition. It was obtained within the finite-temperature version of the BruecknerBetheGoldstone quantum many-body theory in the BruecknerHartreeFock approximation. The underlying two-body and three-body interactions were derived in chiral perturbation theory taking into account the effect of nucleon-nucleon and nucleon-nucleon-nucleon interactions. DD2 and SFHo were computed in the framework of relativistic mean field theories. The two EOSs differ because of the different parameterizations and coupling constants for modelling the mean-field nuclear interactions. The transition to inhomogeneous nuclear

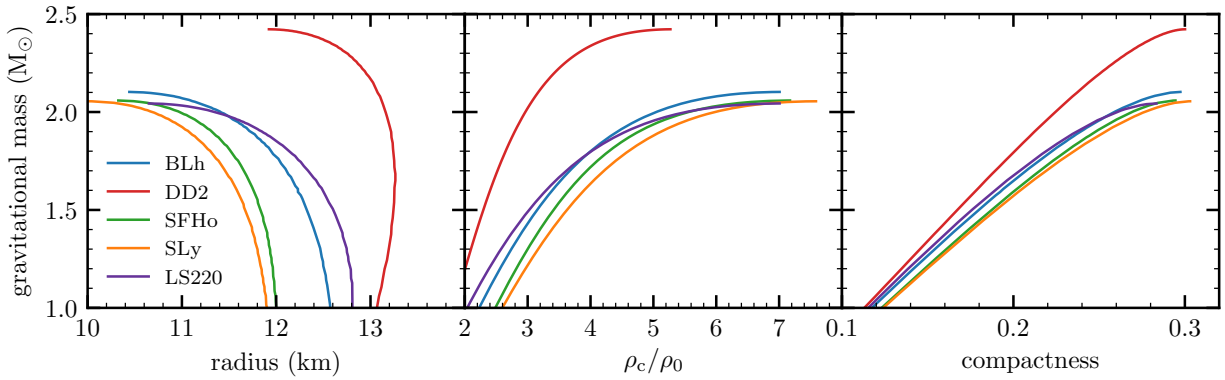

Figure 2.3: Mass-radius diagrams (left panel), mass as a function of the central density ρ_c in units of the saturation density ρ_0 (central panel) and as a function of the compactness (right panel) for a non-spinning, cold and β-equilibrated NS computed with the EOSs employed in the following chapters.

matter was done using an excluded volume approach. The LS220, as described in Lattimer and Swesty [1991], utilizes a liquid droplet model of the Skyrme interaction. This EOS incorporates surface effects and represents α-particles as an ideal, classical, non-relativistic gas. Single-nucleus approximation (SNA) is used to handle the heavy nuclei. The SLy4 used in the present work is the finite temperature extension of the Skyrme effective nuclear interactions introduced in Douchin and Haensel [2001]. The SLy4 EOS reproduces well empirical saturation properties of nuclear matter as well as several observables deduced from the masses of finite nuclei. Some EOSs could be disfavored by observational data or theoretical arguments, see e.g. Tews et al. [2018], Hempel et al. [2017] for LS220 or Abbott et al. [2019a] for DD2. However, the use of several EOSs allows us to better span present uncertainties.

Different EOSs are associated with distinct models of NSs. As an example, in Fig. 2.3 we show the mass-radius diagrams (left panel), the mass as a function of the central density, ρ_c (central panel), and as a function of the compactness, $C = GM/Rc^2$ (right panel), for a non-spinning, cold and β-equilibrated NS for the EOSs discussed above. The maximum mass of the NSs obtained from the EOS models is always above 2 $M_\odot$, as expected. Among the different EOSs, DD2 is the stiffest, i.e. it is able to provide more pressure at any given density, resulting in the NSs with highest maximum mass and smaller compactness at any given NS mass. On the contrary, the SLy EOS, being the softest EOS in the group, have the highest central density and compactness for any given NS mass.

Chapter 3

Method of analysis

In this chapter, we outline the procedures employed to analyze simulation data for the computation of various relevant quantities. We commence with the analysis methods for the GW signal in Sec. 3.1. The definitions of the characteristics of the disk and the remnant, as discussed in Chapter 5 and Chapter 4, are summarized in Sec. 3.2 and Sec. 3.3, respectively. Utilizing the ejecta properties as input parameters, the procedures for computing r-process yields and kilonova light-curves are elucidated in Sec. 3.4 and Sec. 3.5.

3.1 Gravitational waves analysis

We analyze the GW signal of a BNS merger as extracted at a coordinate radius of ≈ 591 km from the BNS center of mass for all the simulations in the present work. In particular, we extract the spherical harmonics expansion of the ψ^4 Weyl scalar, related to the polarization amplitudes h_+ and $h_\times$ by $\psi^4 = \partial_t^2(h_+ + ih_\times)$. Then, the GW strain h_{lm} for each spherical harmonics (l, m) is obtained by integrating in time ψ^4_{lm} using the fixed frequency integration with a low-frequency cut-off presented in Reisswig and Pollney [2011]. The energy and angular momentum radiated in gravitational waves are computed as

$$E^{\rm rad}_{\rm GW}(t) = \frac{1}{16\pi}\sum_{l=2}^{4}\sum_{m=-l}^{l}\int ||\dot{h}_{lm}(t)||^2\ dt'\ , \tag{3.1a}$$

$$J^{\rm rad}_{\rm GW}(t) = \frac{1}{16\pi}\sum_{l=2}^{4}\sum_{m=-l}^{l} m\int h_{lm}(t')\dot{h}^*_{lm}(t')\ dt'\ , \tag{3.1b}$$

where h^*_{lm} is the complex conjugate of h_{lm} and $\dot{}$ denotes the derivative with respect to the coordinate time. It is important to stress that the GWs are properly defined only at null infinity and in an appropriate coordinate system, while they are extracted from the simulations in a finite domain. The accurate estimation of the emitted gravitational waves

represents a non-trivial problem in numerical relativity [Teukolsky, 1972, 1973, Bishop and Rezzolla, 2016, Iozzo et al., 2021].

In Chapter 4, we focus on the characterization of the GW emission during the inspiral, merger and post-merger phases through integrated and peak quantities. In particular, we define the rescaled total energy radiated in GWs, $e^{\rm tot}_{\rm GW}$, and the rescaled angular momentum of the remnant, $j_{\rm rem}$, as:

$$e^{\rm tot}_{\rm GW} = \frac{(M - M_{\rm ADM})c^2 + E^{\rm rad}_{\rm GW}}{\nu M c^2} \ , \tag{3.2}$$

and

$$j_{\rm rem} = \frac{J_{\rm ADM} - J^{\rm rad}_{\rm GW}}{\nu G M^2/c} \ , \tag{3.3}$$

where $E^{\rm rad}_{\rm GW}$ and $J^{\rm rad}_{\rm GW}$ are the energy and angular momentum radiated in GWs during the whole simulation, $M_{\rm ADM}$ and $J_{\rm ADM}$ are the initial ADM mass and angular momentum of the system, and ν is the symmetric mass-ratio, $\nu = M_A M_B/M^2$.

3.2 Disk analysis

The analysis of the disk properties plays a central role both in Chapter 5 and Chapter 4. However, in the former the characterization of the disk emerging from the simulations is more relevant and structured. Thus, in the two chapters we use slightly different definitions for the accretion disk surrounding the central object. In Chapter 4 the disk is simply defined as the portion of the remnant outside the apparent horizon whose rest mass density is smaller than 10^{13} g cm^{-3}, [see e.g. Shibata et al., 2017]. The definition of the disks discussed in Chapter 5 involves 4 steps:

1. in addition to the limit of 10^{13} g cm^{-3} on the maximum rest mass density, we also impose a minimum rest mass density $\rho \geq \rho_{\rm min}$, where $\rho_{\rm min}$ is such that the disk mass is 95% of the total baryon mass enclosed in the grid with $\rho \leq 10^{13}$ g cm^{-3}. This method allows us to circumvent the need for defining a cut-off that depends on a minimum rest mass density. Such a definition could overly rely on this arbitrary choice, potentially influencing the total mass of the disk. At the same time, it prevents the inclusion of regions with extremely low densities in the disk, which might be susceptible to numerical artifacts;

2. if the BNS collapse to a BH, we remove matter in the space-time region whose lapse function is less than 0.3;

3. the ejecta is removed from the disk according to the geodesic criterion, i.e. we consider

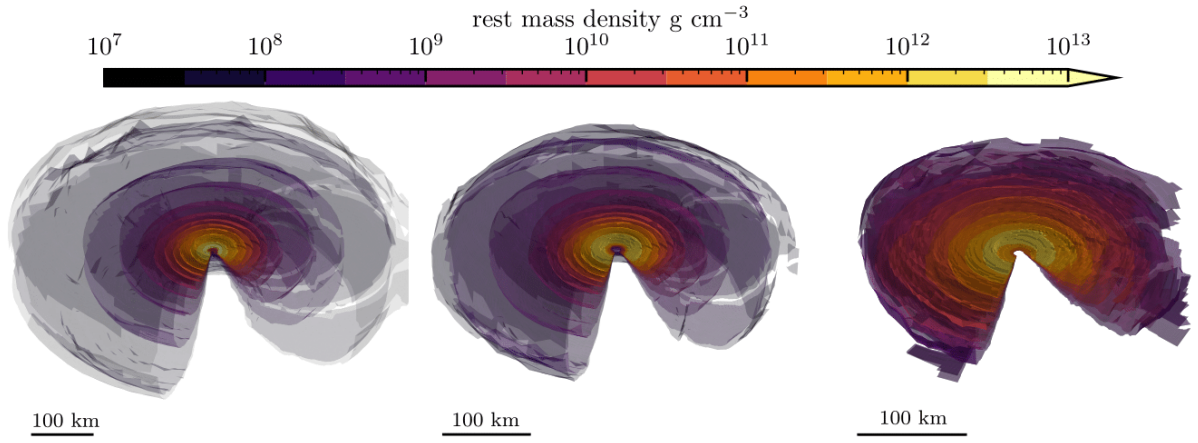

Figure 3.1: Isodensity surfaces for three representative simulations taken at the last available simulation timestep. Left: disk from a long-lived BNS merger, as obtained from the equal mass, HR simulation with the BLh EOS (without turbulent viscosity). Center: disk from a short-lived BNS merger, as obtained from the equal mass, SR simulation with the LS220 EOS (without turbulent viscosity). Right: disk from a prompt-collapsed BNS merger, as obtained from the SR simulation with SFHo EOS (with turbulent viscosity). Taken from Camilletti et al. [2024]

as ejecta fluid elements with $|u_t| \geq c$, where u_t is the time-component of the four-velocity;

4. the regions that satisfy the previous requirements but are disconnected from the main disk body are finally removed. Despite these regions are usually small, they can artificially affect the geometrical properties of the disk and must be removed. The isodensity surfaces of the disk obtained from the latter procedure are showed in Fig. 3.1 for three representative simulations.

Once the disk has been identified inside the computational domain, the disk mass is computed as the general-relativistic volume integral of the conserved baryon mass density inside the volume of the torus:

$$M_{\rm disk} = \int_{\rm disk} \sqrt{\gamma}\rho W \; r dr d\phi dz \; , \tag{3.4}$$

where ρ is the baryon rest mass density, W is the Lorentz factor of the fluid and $\sqrt{\gamma}$ is the determinant of the 3-metric. Analogously, assuming symmetry with respect to the rotational axis, we define the disk angular momentum as the general-relativistic volume integral of the baryon angular momentum density along the azimuthal direction $j = \rho h W^2 \tilde{v}_\phi$, i.e.

$$J_{\rm disk} = \int_{\rm disk} \sqrt{\gamma}\rho h W^2 \tilde{v}_\phi \; r dr d\phi dz \; , \tag{3.5}$$

where h is the fluid specific enthalpy and $\tilde{v}_\phi$ is the advective angular velocity in the azimuthal direction. We recall that, in cylindrical coordinates, the advective azimuthal velocity is related to the Cartesian components of the fluid Eulerian velocity v_i as $\tilde{v}_\phi = \alpha\,(x v_y - y v_x) - \beta_\phi$, where α is the lapse function and β_ϕ is the low index ϕ-component of the shift vector. Note that the assumption of an axial symmetric space-time is approximately satisfied after a relaxation phase occurring just after merger. The specific angular momentum, i.e. the angular momentum per unit of mass, is the ratio between the baryon angular momentum density and rest mass density, i.e. j/ρ.

We define the aspect ratio at every azimuthal angle ϕ_0 of the cylindrical grid as the ratio between the maximal radial and vertical extensions of the disk in the $\phi = \phi_0$ plane. An average over ϕ is then performed to obtain the global aspect ratio of the disk. Analogously, on each $\phi = \phi_0$ plane, the half opening angle is defined as the arcotangent of the ratio between the maximum vertical extension and the radial distance at which this maximum is found. An average over ϕ is then performed to obtain the half opening angle of the disk.

The flux of baryon mass is computed as $\mathbf{f} = \rho W \tilde{\mathbf{v}}$ (note that here and in the following we define the advective velocity $\tilde{\mathbf{v}} = \alpha \mathbf{v} - \boldsymbol{\beta}$). We derive the accretion/ejection rate $\dot{M}$ across a spherical surface as the flux integral:

$$\dot{M} = 2 \int_0^{\pi/2} \int_0^{2\phi} \sqrt{\gamma_S(\theta,\phi)} f^r(\theta,\phi)\; d\theta d\phi \tag{3.6}$$

where θ, ϕ are the polar and azimuthal coordinates on the spherical surface, γ_S is the pull-back of the spatial metric on it, and f^r is the radial component of the baryon mass flux (see Appendix A.). Note that, when computing the flux, we interpolate the latter quantities on a spherical grid.

3.3 Black hole analysis

When the central object collapse to a BH, we express its mass as

$$M_{\rm BH}^2 = M_{\rm irr}^2 + \left(\frac{c J_{\rm BH}}{2 G M_{\rm irr}} \right)^2 \,, \tag{3.7}$$

where $M_{\rm BH}$ and $J_{\rm BH}$ are the gravitational mass and spin of the BH, respectively, while $M_{\rm irr}$ is the irreducible BH mass:

$$M_{\rm irr} = \frac{c^2}{G} \sqrt{\frac{A_{\rm H}}{16\pi}} \,, \tag{3.8}$$

with $A_{\rm H}$ the AH area. For a Kerr-BH, the irreducible mass is a non-decreasing quantity, while it coincides with the gravitational mass for non rotating BHs. In analogy with the

Kerr solution, we define the dimensionless spin parameter as $a_{\rm BH} \equiv (cJ_{\rm BH})/(GM_{\rm BH}^2)$. The AH finder is able to give an estimate of such quantities by locating the AH of the singularity, albeit it is not guaranteed that it does locate the AH with sufficient accuracy. This issue can clearly have an impact on the estimated BH properties. We compare the gravitational mass provided by the AH finder with the expected BH mass

$$M_{\rm BH}^{\rm exp} = M_{\rm ADM} - M_{\rm disk} - E_{\rm GW}^{\rm rad}/c^2 \ , \tag{3.9}$$

where $E_{\rm GW}^{\rm rad}$ is the total energy radiated in GWs. In the above expression, we have neglected the ejecta mass and for the disk we have considered only the rest-mass energy. Similarly, for the spin parameter we compute the expected value as:

$$a_{\rm BH}^{\rm exp} = \frac{cJ_{\rm BH}^{\rm exp}}{G\left(M_{\rm BH}^{\rm exp}\right)^2} = \frac{c(J_{\rm ADM} - J_{\rm GW}^{\rm rad} - J_{\rm disk})}{G\left(M_{\rm BH}^{\rm exp}\right)^2} \ , \tag{3.10}$$

where $J_{\rm GW}^{\rm rad}$ is the angular momentum radiated in GWs and $J_{\rm disk}$ is the angular momentum of the surrounding disk.

3.4 Ejecta and nucleosynthesis calculations

From each simulation we consider the dynamical ejecta as the matter that becomes unbound within the end of the simulation on the basis of the geodesic criterion. The properties of the ejecta are determined as matter crosses a spherical detector of coordinate radius $r_{\rm E} = 200G\ {\rm M}_\odot/c^2 \approx 294$ km, discretized in $N_\theta = 51$ polar and $N_\phi = 93$ azimuthal uniform angular bins. For the unbound matter, the speed reached at infinity is computed as $v_\infty = c\sqrt{1-(c/u_t)^2}$.

The distribution of nuclei within the expanding ejecta is computed using the same approach and the same input data as the ones reported in [Perego et al., 2022b], that we briefly summarize in the following. We note that a similar approach was already used in [Radice et al., 2016, 2018b, Nedora et al., 2021a], but with different input data. To obtain time-dependent yield abundances we employ `SkyNet` [Lippuner and Roberts, 2017], a publicly available nuclear network which computes the nucleosynthesis depending on the evolution of a given Lagrangian fluid element. We evolve several trajectories with different initial parameters, with the aim of modeling the long-term expansion of the unbound matter measured in the simulations at the detector. All the trajectories start in NSE from an initial temperature of $T_0 = 6.0$ GK. The corresponding initial density, $\rho_0 \equiv \rho(s, Y_e, T = 6\,{\rm GK})$, is determined by the NSE solver implemented in `SkyNet` depending on the initial values of the electron fraction Y_e and of the specific entropy s. The subsequent evolution of the density

is set by the expansion time-scale τ, first as an exponentially decaying phase and then as a homologous expansion:

$$\rho(t) = \begin{cases} \rho_0 \, e^{-t/\tau} & \text{if } t \leq 3\tau \,, \\ \rho_0 \left(\dfrac{3\tau}{et} \right)^3 & \text{if } t > 3\tau \,. \end{cases} \tag{3.11}$$

Parametric nucleosynthesis calculations are repeated for a set of fluid elements characterized by different values of s, τ and Y_e, ranging on a $26 \times 18 \times 25$ regular grid that spans the typical conditions characterizing the ejecta in compact binary mergers, i.e., $1.5 \leq s \; [k_B \text{ baryon}^{-1}] \leq 300$, $0.5 \leq \tau \; [\text{ms}] \leq 200$ and $0.01 \leq Y_e \leq 0.48$, approximately logarithmic in the two former parameters while linear in the latter. To compute the nucleosynthesis yields in the ejecta we take the convolution of the output given by `SkyNet` with the distribution of the ejecta properties obtained from the numerical simulation at the extraction radius, $r_{\rm E}$. While s and Y_e are directly extracted from the numerical simulation, τ is computed assuming homologous expansion at the extraction surface, $\rho(t) = \rho_E (v_{\rm E} t / r_{\rm E})^{-3}$, where $\rho_{\rm E}$ and $v_{\rm E}$ are the density and velocity of the ejecta at the extraction radius, respectively. As done in Radice et al. [2016, 2018b], the expansion time-scale τ is then retrieved by matching the latter profile with the homologous expansion given in Eq. (3.11):

$$\tau = \left(\frac{\rho_0}{\rho_{\rm E}} \right)^3 \frac{e r_{\rm E}}{3 v_{\rm E}} \,. \tag{3.12}$$

3.5 Kilonova light curves calculations

In order to compute kilonova light curves from the outcome of our simulations, we employ the multi-component anisotropic framework presented in [Perego et al., 2017]. In this framework, axial symmetry and symmetry with respect to the BNS orbital plane are assumed, while the polar angle θ is discretized in $N_\theta = 30$ angular bins equally spaced in $\cos\theta$. The kilonova emission is then computed in a ray-by-ray fashion by summing up the photon fluxes coming from each angular slice, properly projected along the line of sight of an observer located at a polar angle $\theta_{\rm view}$. Inside each slice, a 1D kilonova model is used. The latter depends on the mass and (root mean square) speed of the ejecta, as well as on an effective gray opacity κ. Inside each ray, several ejecta components are considered, resulting from the expulsion of matter operated by different mechanisms, acting on different time-scales and providing distinct ejecta properties. The total luminosity is found by summing over the contributions of the different ejecta components, assuming that the energy emitted by the innermost ones is quickly reprocessed and emitted by the outermost component[1].

[1] The location of the components is determined by the location of the photospheres.

Differently from the model originally implemented in [Perego et al., 2017] and later employed, for example, in [Radice et al., 2018b,a, Breschi et al., 2021, Barbieri et al., 2020, 2019, 2021], here we adopt a new semi-analytical 1D kilonova model for each angular slice that we present in the following. The model assumes a spherically symmetric and optically thick outflow with a constant average gray opacity. The outflow expands with an homologous expansion law, i.e., the density of each fluid element decreases as t^{-3} while its expansion speed stays constant, starting from a few hours after merger. The kilonova emission is calculated as the combination of two contributions, one emitted at the photosphere and one coming from the optically thin layers above it. The contribution coming from the photosphere is computed starting from the semi-analytic formula for the luminosity originally proposed by [Wollaeger et al., 2018] and derived from a solution of the radiative transfer equation in the diffusion approximation [Pinto and Eastman, 2000]. This formula was further validated in [Wu et al., 2022], where it showed a very reasonable agreement with results provided by the radiation hydrodynamics code `SNEC`. While the original model assumes that the whole ejecta are in optically thick conditions, an increasing fraction of it resides outside of the photosphere, becoming optically thin to thermal radiation. For this reason, the outcome of this computation is rescaled by a factor $M_{\rm thick}/M_{\rm ej}$, where $M_{\rm thick}$ is the mass of the optically thick part of the ejecta, defined as the region enclosed by the photosphere. The photospheric radius $R_{\rm ph}(t)$ is found analytically by imposing the condition $\tau_\gamma(R_{\rm ph}) = 2/3$, where τ_γ is the optical depth of the material, and by using the homologous density profile as in [Wollaeger et al., 2018]:

$$\rho(t,x) = \rho_0 \left(\frac{t_0}{t}\right)^3 \left(1-x^2\right)^3, \tag{3.13}$$

where ρ_0 is the density at the initial time t_0 and $x = v/v_{\rm max}$ is the dimensionless radial variable. The photospheric temperature $T_{\rm ph}(t)$ is computed from the photospheric luminosity and radius using the Stefan-Boltzmann law. A temperature floor of 2000 K for $T_{\rm ph}(t)$ is applied in order to account for electron-ion recombination in the expanding ejecta. When $T_{\rm ph}(t)$ reaches the temperature floor, $R_{\rm ph}(t)$ is redefined using again the Stefan-Boltzmann law. Furthermore a Planckian black body spectrum is assumed at the photosphere.

The contribution to the luminosity from the thin part of the ejecta is computed by partitioning the latter into equal mass shells and by assuming that each shell with temperature T emits its radioactive decay energy assuming local thermodynamics equilibrium. To characterize the temperature of the thin part of the ejecta, we adopt a temperature profile similar to the one derived in [Wollaeger et al., 2018] under the assumption of radiation dominated, homologous expansion: $T(t,x) = T_0(x)\,(t_{\rm tr}(x)/t)$, where $T_0(x)$ is the temperature of the photosphere as it transits through the shell centered in x at the time $t_{\rm tr}(x)$. The bolometric luminosity contribution from the thin region is computed by multiplying the mass of each

shell by the specific heating rate.

For the nuclear heating rates powering the kilonova emission, we employ the analytic fitting formula first presented in [Wu et al., 2022] and based on the results from the nucleosynthesis calculations reported in [Perego et al., 2022b]: $\dot{\epsilon}_{\rm r}(t) = At^{-\alpha}$, where A and α are fit parameters. The latter are interpolated from tabulated values on the same (Y_e, s, τ) grid used for the nucleosynthesis calculations (see Sec. 3.4). A constant thermalization efficiency $\epsilon_{\rm th} = 0.5$ is employed for the thick region of the ejecta, while we construct a thermalization efficiency profile for the thin part starting from the analytic fitting formula proposed in [Barnes et al., 2016]. The expression for the thermalization efficiency profile reads:

$$\epsilon_{\rm th}(t, x) = 0.36 \left[\exp(-aX) + \frac{\ln(1 + 2bX^d)}{2bX^d} \right] , \tag{3.14}$$

where a, b and d are the fitting parameters reported in [Barnes et al., 2016] and interpolated from tabulated values on a grid spanning the intervals $1 \times 10^{-3} M_\odot < M_{\rm ej} < 5 \times 10^{-2} M_\odot$ and $0.1c < v_{\rm ej} < 0.3c$. In the original formulation of [Barnes et al., 2016], obtained assuming $\rho(t) = \rho_0 (t/t_0)^3$, $X(t, x) = t$. Due to the use in our model of the density profile Eq. (3.13), we adopt $X(t, x) = t/(1 - x^2)$, instead. In this work, we consider two ejecta components: a dynamical ejecta and a disk ejecta component, both symmetric with respect to the equatorial plane and to the polar axis. Following the same procedure described in Sec. 3.4, we directly extract from the simulations the profiles of the properties of the dynamical component, namely the distributions of the ejecta mass, of the root mean square velocity at infinity, of the average electron fraction, average entropy and average density at the extraction radius, as a function of the polar angle θ, averaged over the azimuthal angle ϕ. The opacity κ is computed by interpolating the results of the atomic calculations performed in [Tanaka et al., 2020] for a wide range of the electron fraction $0.01 \leq Y_e \leq 0.50$. In our simulations, we do not evolve the remnant and the disk long enough to take into accout all relevant kinds of ejecta, and in particular the emergence of disk winds. Nevertheless, inspired by disk simulations of [Wu et al., 2016], [Lippuner et al., 2017], [Siegel and Metzger, 2017], [Fernández et al., 2019], [Fahlman and Fernández, 2022], we assume that a fraction between ~ 20 and ~ 40 per cent of the disk mass inferred from our simulations (see Sec. 4.2.3) is ejected in the form of a viscosity-driven wind. We model the mass of this disk wind as uniformly distributed in θ, as we do not expect preferential latitudes for the ejection. Moreover, for the disk ejecta we assume a root mean square velocity of $0.06c$, a uniform opacity of 5 cm^2 g^{-1}, an average entropy of 20 $k_{\rm B}$ baryon^{-1} and an expansion time-scale of 30 ms. We stress that our kilonova model relies on a large number of assumptions and simplifications which limit its accuracy. However, for the parameters that are not directly fixed by our simulations, we chose representative values in broad agreement with what obtained by fitting AT2017gfo

data with the original kilonova model [Perego et al., 2017].

Chapter 4

Numerical simulations and analysis of the BNS merger GW190425

The results, tables and figures presented in this chapter are taken from Camilletti et al. [2022].

GW190425 represented a significantly different event with respect to GW170817 in many aspects [Abbott et al., 2020, 2021b]. The rest-frame chirp mass was (1.44 ± 0.02) $M_\odot$, while the NS mass ranges were $M_A = (2.0^{+0.6}_{-0.3})$ $M_\odot$ and $M_B = (1.4^{+0.3}_{-0.3})$ $M_\odot$, at 90 per cent credible level, resulting in a total mass in the range $3.3 - 3.7$ $M_\odot$. Such a high total mass qualifies GW190425 as a possible outlier in the Galactic BNS system distribution [Abbott et al., 2020, 2021c]. During the passage of the GW signal, the Livingston LIGO detector was offline and Virgo was unable to contribute to the measure because of the small signal-to-noise ratio (2.5) resulting from the large inferred distance ($D \approx 70 - 250$ Mpc). The effective presence of only one GW detector did not allow a good sky localization ($\sim 10^4$ deg^2). Despite an intense followup campaign within the first days after the GW detection, no firm identification of EM counterparts was possible so far [Coughlin et al., 2019, Steeghs et al., 2019]. In particular, the GROWTH and GRANDMA collaborations performed dedicated follow-up campaigns. GROWTH made use of the Zwicky Transient Facility (ZTF) and the Palomar Gattini-IR telescopes. The ZTF system covered 21 per cent of the probability integrated skymap and achieved a depth of 21 AB magnitudes in the g- and r-bands, while Palomar Gattini-IR covered 19 per cent of the probability integrated skymap in J-band to a depth of 15.5 mag [Coughlin et al., 2019]. With 9 of its 21 heterogeneous telescopes, the GRANDMA network imaged 70 galaxies covering $\lesssim 2$ per cent of the probability integrated skymap, attaining a depth of 17-23 AB magnitudes depending on the telescope [Antier et al., 2020]. In absence of an optical or infrared counterpart, Apertif-WSRT searched for afterglow radio emission in a 9.5 deg^2 region of the high probability skymap [Boersma et al., 2021]. Despite the reduced

fraction of the covered skymap, the apparent lack of EM counterparts and the unusually high total mass of the binary leave open questions both on the origin of the system and on the remnant properties.

GW170817 was the privileged target of several simulation campaigns in numerical relativity [Nedora et al., 2021a]. Recently, an independent study on GW190425 in numerical relativity has been proposed in [Dudi et al., 2021] (hereafter Dudi *et. al.*). The authors set up 36 BNS simulations targeted to GW190425 considering four mass ratios and three nuclear EOSs at different resolutions. They used cold EOSs with a density dependent composition fixed by neutrino-less beta-equilibrium conditions, and with thermal effects included by an effective Γ-law. Dudi *et. al.* compute kilonova light curves employing a wavelength-dependent radiative transfer code [Kawaguchi et al., 2020], for which the post-merger ejecta composition is fixed for all components. They concluded that, assuming an effective coverage of the event localization region in the GROWTH follow-up campaign, the lack of kilonova detection suggests that GW190425 is incompatible with a face-on, unequal BNS merger with more than 20 per cent of mass difference between the two NSs. In all other cases (soft EOSs, edge-on and more distant mergers, or more symmetric binaries) the lack of detection is still compatible with a fainter kilonova signal.

Several other works focused on GW190425 have recently appeared. For example [Han et al., 2020] and [Kyutoku et al., 2020] investigated the possibility that GW190425 originated from a BH-NS merger by studying the corresponding GW and kilonova signal, respectively. In [Raaijmakers et al., 2021] and [Barbieri et al., 2021] kilonova light curves for GW190425 were computed under the assumption that the originating event was a BH-NS or a BNS merger[1]. In both cases, the properties of the ejecta powering the kilonova signal were computed using fitting formulae derived from broad simulation samples, while the kilonova signals were computed using models with different levels of sophistication. In [Barbieri et al., 2021], the BNS fitting formulae were taken from [Radice et al., 2018b] and from the appendix of [Barbieri et al., 2021]. The NS masses were chosen to be compatible with the GW190425 chirp mass, while the two employed NS EOSs were compatible with present nuclear and astrophysical constraints. Additionally, using the same model, they also computed light curves directly using GW190425 posteriors [Abbott et al., 2020]. They concluded that a light BH in GW190425 would have produced a brighter kilonova emission compared to BNS case, allowing to distinguish the nature of the binary. However also in the BNS case, the merger could have produced kilonovae bright enough to have been possibly detected by ZTF, especially for stiff EOSs and for more asymmetric systems. In [Raaijmakers et al., 2021], only the posteriors from GW190425 [Abbott et al., 2020] and the EOS obtained from

[1]In both works, the focus was broader than GW190425 kilonova characterization, but this event was extensively studied as realistic test case.

GW170817 analysis [Abbott et al., 2018] were used as input for the BNS fitting formulae from [Krüger and Foucart, 2020] and [Foucart et al., 2017]. Based on the obtained ejecta and disk properties, kilonova light curves were computed using the semi-analytic model from [Hotokezaka and Nakar, 2019]. The latter adopts the radioactive heating rate fit from [Korobkin et al., 2012] and assumes a spherical symmetry for the ejecta geometry. Additionally, tests using the same kilonova model but fitting formulae from [Radice et al., 2018b, Barbieri et al., 2021, Dietrich et al., 2021] were also performed. Despite these works, several open questions regarding GW190425 still remain. For example, how robust are the results obtained in numerical relativity for GW190425-like events? And, in particular, what is the impact of input physics that was so far neglected in GW190425-targeted simulations, including finite temperature, composition dependent EOS, and neutrino radiation? What are the detailed properties of the dynamical ejecta expelled in these events and how do they depend on the binary properties and on the NS EOS? Is there a characteristic nucleosynthesis signature in these ejecta? Based on these results, what can we infer from the missing detection of electromagnetic counterparts for GW190425?

To answer these questions, we setup 28 simulations in numerical relativity targeted to GW190425 with finite temperature, composition dependent NS EOSs, and with neutrino radiation. We investigate the binary evolution up to the first ≈ 10 ms after merger. We extract both remnant and dynamical ejecta properties, to give credible answers to some of the above questions. In particular, we use the detailed outcome of our simulations to compute nucleosynthesis yields and to set up kilonova models. We found that, for a distance compatible with GW190425, only in the case of a very stiff EOS and a very asymmetric binary the resulting kilonova could have been bright enough to be observed by the ZTF facility. This suggests that the possible lack of kilonova counterpart for GW190425 provides much weaker constraints than previously thought.

The chapter is structured as follows: after a brief recap of the simulations properties in Sec. 4.1, we resume the qualitative behavior of the merger dynamics in Sec. 4.2.1 and analyze the GW energetics in Sec. 4.2.2. The quantitative description of the remnant is reported in Sec. 4.2.3, while we discuss the main properties of the dynamical ejecta in Sec. 4.2.4. In Sec. 4.3.1 and Sec. 4.3.2 we describe the output from the nucleosynthesis process and its related kilonova signal. We compare our results with the one discussed in the literature in Sec. 4.4. We summarize our results in the conclusions in Sec. 7.1.

I acknowledge the relevant contributions of Leonardo Chiesa in Sec. 4.3.1 and of Giacomo Ricigliano in Sec. 4.3.2. Additionally, Leonardo Chiesa also contributes to the analysis and writing of Sec. 4.4.

Table 4.1: NS initial properties grouped by EOS. From left to right: EOS, maximum TolmanOppenheimerVolkoff (TOV) mass $M_{\rm TOV}^{\rm max}$, maximum TOV compactness $C_{\rm TOV}^{\rm max}$, NS gravitational masses $M_{\rm A}, M_{\rm B}$, at infinite separation, ratio between the total baryonic mass M and $M_{\rm TOV}^{\rm max}$, BNS mass ratio $q \equiv M_{\rm A}/M_{\rm B}$, compactness of the two NSs $C_{\rm A}$, $C_{\rm B}$, tidal deformability of the BNS $\tilde{\Lambda}$ defined in Eq. (4.1), the coefficient $k_2^{\rm L}$ defined in equation 4 of [Zappa et al., 2018], Eq. (4.2), the initial GW frequency $f_{\rm GW}(0)$, the total ADM mass of the system $M_{\rm ADM}$ and the initial ADM angular momentum $J_{\rm ADM}$. Taken from Camilletti et al. [2022]

EOS	$M_{\rm TOV}^{\rm max}$ [$M_\odot$]	$C_{\rm TOV}^{\rm max}$	$M_{\rm A}$ [$M_\odot$]	$M_{\rm B}$ [$M_\odot$]	$M/M_{\rm TOV}^{\rm max}$ [$M_\odot$]	q	$C_{\rm A}$	$C_{\rm B}$	$\tilde{\Lambda}$	$\kappa_2^{\rm L}$	$f_{\rm GW}(0)$ [Hz]	$M_{\rm ADM}$ [$M_\odot$]	$J_{\rm ADM}$ [$M_\odot{}^2$]
BLh	2.103	0.299	1.654	1.654	1.765	1.0	0.201	0.201	129.525	194.3	608	3.272	10.23
BLh	2.103	0.299	1.750	1.557	1.721	1.12	0.215	0.187	133.008	198.6	603	3.271	10.19
BLh	2.103	0.299	1.795	1.527	1.775	1.18	0.222	0.183	131.172	195.0	609	3.284	10.23
BLh	2.103	0.299	1.914	1.437	1.799	1.33	0.242	0.172	134.612	196.8	611	3.313	10.24
DD2	2.420	0.300	1.654	1.654	1.522	1.0	0.184	0.184	257.963	386.9	608	3.270	10.23
DD2	2.420	0.300	1.795	1.527	1.532	1.18	0.200	0.170	256.534	382.8	609	3.285	10.24
DD2	2.420	0.300	1.914	1.437	1.550	1.33	0.214	0.160	254.057	375.1	611	3.312	10.24
DD2	2.420	0.300	2.149	1.289	1.609	1.67	0.244	0.144	247.763	354.8	616	3.400	10.25
SFHo	2.059	0.294	1.654	1.654	1.816	1.0	0.209	0.209	101.708	152.6	608	3.275	10.25
SFHo	2.059	0.294	1.795	1.527	1.829	1.18	0.230	0.191	102.689	152.7	609	3.290	10.26
SFHo	2.059	0.294	1.914	1.437	1.854	1.33	0.251	0.179	104.653	153.0	611	3.320	10.28
SLy4	2.055	0.303	1.654	1.654	1.820	1.0	0.212	0.212	89.251	133.9	608	3.271	10.23
SLy4	2.055	0.303	1.795	1.527	1.832	1.18	0.234	0.194	90.538	134.6	609	3.285	10.24
SLy4	2.055	0.303	1.914	1.437	1.858	1.33	0.256	0.181	93.140	136.0	611	3.314	10.25

4.1 Binary neutron star models

We set up and analyze a total of 28 simulations, 14 at SR and 14 at LR. In Table 4.1 we report a summary of all initial parameters characterizing our simulations, in particular: the values of the individual stellar masses $M_{A,B}$ with $M_A > M_B$, the total gravitational mass M, the mass ratio $q \equiv M_A/M_B > 1$, the total ADM mass and angular momentum of the system $M_{\rm ADM}$ and $J_{\rm ADM}$, the stellar compactness C_i for $i = A, B$, the the tidal deformability of the binary, $\tilde{\Lambda}$, defined as:

$$\tilde{\Lambda} = \frac{16}{13}\frac{(M_A + 12M_B)M_A^4}{M^5}\Lambda_A + A \leftrightarrow B\,, \tag{4.1}$$

and the coefficients $k_2^{\rm L}$ as defined in equation 4 of [Zappa et al., 2018], namely:

$$\kappa_2^L = 6\left[\frac{(3M_B + M_A)M_A^4}{M^5}\Lambda_A + A \leftrightarrow B\right]\,, \tag{4.2}$$

where the notation $(A \leftrightarrow B)$ indicates a second term identical to the first except that the indices A and B are exchanged. We also report the GW initial frequency $f_{\rm GW}(0)$ measured in Hertz. All BNS parameters are compatible with the ones inferred from the GW signal GW190425 [Abbott et al., 2020] using both the low- and high-spin priors, except for the ones

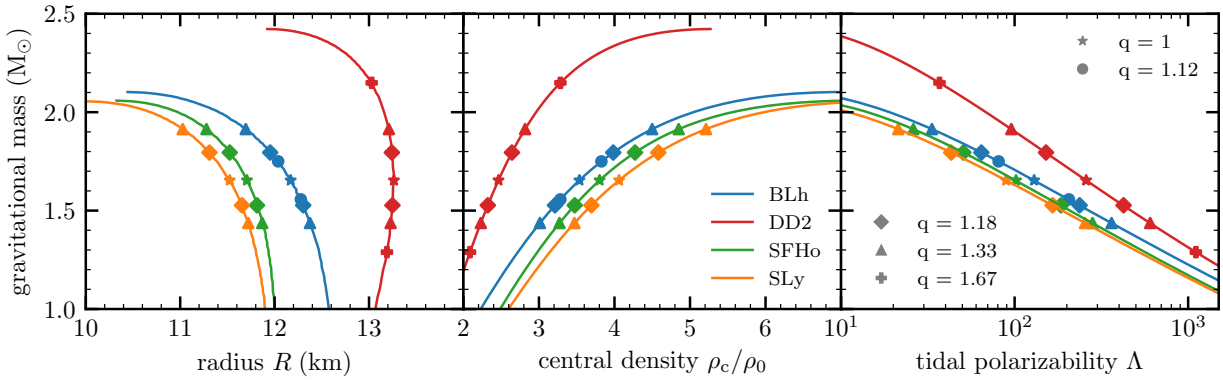

Figure 4.1: TOV sequences for the NS EOSs used in this work. Left panel: gravitational mass versus radius. Central panel: gravitational mass versus central density normalized to the nuclear saturation density, $\rho_0 = 2.67 \times 10^{14}$ g cm^{-3}. Right panel: gravitational mass versus tidal polarizability Λ. The different markers refer to the different mass ratios of the binaries evolved in the simulations. Taken from Camilletti et al. [2022]

characterized by $q = 1.33$ and $q = 1.67$, which are compatible only with high-spin prior.

To better characterize the binaries used in this work and their properties in relation to the different EOSs, in Fig. 4.1 we also highlight the properties of the NSs initially forming the binaries evolved by our simulations. Note that the initial conditions span a broad range of central densities, from $2.2\rho_0$ to $6.0\rho_0$ (in terms of the nuclear saturation density $\rho_0 = 2.67 \times 10^{14}$ g cm^{-3}) depending on the EOS and mass ratio. For the more asymmetric binaries, the central density of the heaviest NS is roughly 1.5 times larger than the one of the lightest NS, while in the equal mass case the two identical NSs have a central density ~ 1.2 times larger than the one of the lightest NS in our sample. The single star tidal polarizability varies between two orders of magnitudes and, again, to asymmetric BNS corresponds two NSs with rather different tidal polarizability: a more compact and less deformable NS along with a larger and more deformable one. Interestingly, $\tilde{\Lambda}$ varies only by a few percents within the same EOS, while it changes by almost a factor of three between the SLy4 and the DD2 EOS.

4.2 Results

4.2.1 Merger dynamics

All simulations in our sample follow a qualitative common evolution pattern with quantitative differences, mainly due to the different tidal deformability provided by the EOSs and BNS mass ratios. All simulations result in the prompt collapse of the central part of the remnant into a BH. In this context, we say that a BNS simulation has resulted in a

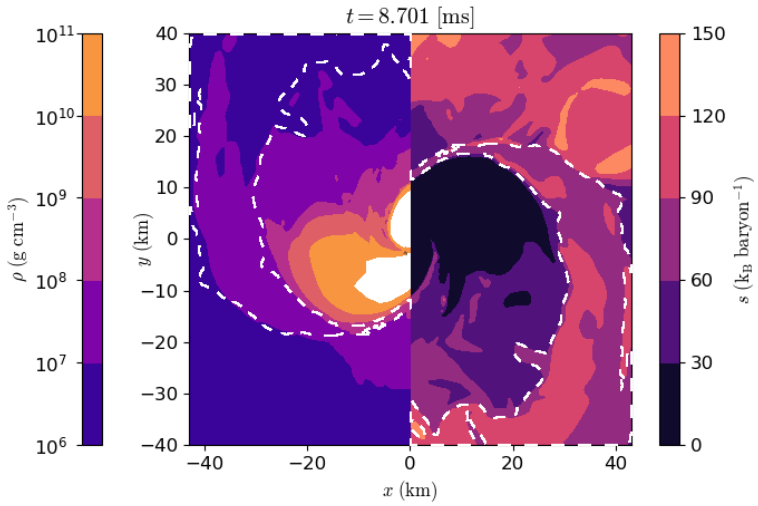

Figure 4.2: Snapshot of the rest mass density (left) and the entropy per baryon (right) taken at $\sim$ 0.3 ms after BH formation across the orbital plane for the equal mass BNS merger SR simulation with the SFHo EOS. Matter inside the dashed contour with entropy $90-120$ k_B baryon^{-1} and densities $< 10^8$ g cm^{-3} comes from the rotationally non-symmetric central object, expelled from the contact surface of the two stars. Since equal mass binaries eject few 10^{-5} $M_\odot$, this shocked matter have a prominent role in the median properties of the ejecta. Taken from Camilletti et al. [2022]

prompt collapse if the minimum of the lapse function inside the computational domain decreases monotonically immediately after merger without showing core bounces. We define the moment of formation of the BH as the time at which the lapse function drops below 0.2. In all simulations presented here the BH forms within a fraction of a ms after the merger ($t_{BH} < 0.47$ ms, see Table 4.2).

Tidal forces deform the NSs during the inspiral, especially the lighter and less compact one. This effect is more pronounced for BNS with stiffer EOSs, providing, for the same gravitational mass, a less compact NS. The subsequent merger dynamics is able to unbind matter from the tidal tails on a few dynamical time-scales. The neutron-rich matter ballistically expelled during this phase from the tidal tails has low entropy and can have large enough velocity to escape the potential barrier, contributing to the dynamical ejecta. The otherwise gravitationally bound matter forms a disk with toroidal shape around the forming BH. BNS models characterized by a stiffer EOS expel more matter, such that more dynamical ejecta and larger disks are found, as discussed in detail below.

During the few fractions of ms that precede BH formation, a small amount of very high-entropy matter coming from the NS contact interface is expelled, see Fig. 4.2. This extremely shocked matter is characterized by higher entropy and electron fraction than the ones that characterize matter expelled by tidal forces. This small component with entropy of $90-120$ k_B baryon^{-1} is responsible of the bimodal distribution of the entropy shown in

Table 4.2: For each simulation the table reports the rescaled angular momentum of the remnant, $j_{\rm rem}$; the rescaled total energy radiated in GWs, $e^{\rm tot}_{\rm GW}$; the BH expected mass (spin), $M^{\rm exp}_{\rm BH}$ ($a^{\rm exp}_{\rm BH}$) as defined in Eq. (3.9) (Eq. (3.10)); the BH mass (spin) as detected from the AH finder, $M_{\rm BH}$ ($a_{\rm BH}$), together with the related average on a sample time, $\langle M_{\rm HB}\rangle$ ($\langle a_{\rm BH}\rangle$). We report values from the SR simulations and the error inside brackets estimated as the absolute semi-difference between the SR and LR values. Uncertainties refers to the least significant digit(s). Taken from Camilletti et al. [2022]

EOS	q	AH finder	$t_{\rm BH}-t_{\rm mrg}$ (ms)	$j_{\rm rem}$	$e^{\rm tot}_{\rm GW}$	$L_{\rm peak}$ 10^{55}erg s^{-1}	$M^{\rm exp}_{\rm BH}$ $[M_\odot]$	$M_{\rm BH}$ $[M_\odot]$	$\langle M_{\rm BH}\rangle$ $[M_\odot]$	$a^{\rm exp}_{\rm BH}$	$a_{\rm BH}$	$\langle a_{\rm BH}\rangle$
BLh	1.0	✓	0.185 (2)	2.994 (8)	0.099 (1)	8.23 (13)	3.2259 (2)	3.2349 (2)	3.245 (2)	0.788 (2)	0.7860 (1)	0.801 (2)
BLh	1.12	✓	0.209 (2)	3.012 (8)	0.097 (1)	7.75 (22)	3.2250 (5)	3.2330 ($<10^{-1}$)	3.245 (2)	0.789 (2)	0.7865 (3)	0.802 (2)
BLh	1.18	✓	0.209 (30)	3.020 (6)	0.098 (1)	7.19 (9)	3.2411 (18)	3.2458 (4)	3.259 (2)	0.789 (2)	0.7866 (1)	0.803 (3)
BLh	1.33	✓	0.221 (8)	3.067 (6)	0.090 (1)	5.53 (8)	3.2559 (2)	3.2573 (6)	3.273 (1)	0.780 (5)	0.7779 ($<10^{-1}$)	0.796 (3)
DD2	1.0	✗	0.422 (10)	3.122 (9)	0.092 (2)	5.46 (18)	3.2210	-	-	0.826	-	-
DD2	1.18	✗	0.445 (6)	3.117 (6)	0.091 (1)	4.96 (12)	3.2298	-	-	0.820	-	-
DD2	1.33	✗	0.469 (41)	3.149 (2)	0.0877 (2)	4.06 (3)	3.2315	-	-	0.780	-	-
DD2	1.67	✗	0.374 (2)	3.204 (3)	0.077 (3)	2.89 (4)	-	-	-	-	-	-
SFHo	1.0	✓	0.138 (2)	2.953 (14)	0.102 (1)	9.98 (22)	3.223 (1)	3.25	3.26	0.778 (1)	0.774	0.79
SFHo	1.18	✓	0.138 (18)	2.976 (8)	0.097 (1)	8.86 (17)	3.240 (1)	3.27	3.28	0.776 (2)	0.775	0.79
SFHo	1.33	✓	0.126 (8)	3.066 (17)	0.0872 (4)	7.32 (16)	3.268	3.29	3.29	0.783	0.770	0.79
SLy4	1.0	✗	0.138 (18)	3.031 (6)	0.105 (1)	10.90 (32)	3.2167 (1)	-	-	0.801 (2)	-	-
SLy4	1.18	✗	0.114 (14)	3.010 (12)	0.103 (1)	9.67 (23)	3.2323 (6)	-	-	0.791 (3)	-	-
SLy4	1.33	✗	0.114 (2)	3.043 (9)	0.097 (1)	7.97 (7)	-	-	-	-	-	-

Fig. 4.7. Its unbound component contributes to the dynamical ejecta, while the bound mass contributes to the disk formation, spanning in both cases a broader polar angle than the bound and unbound matter of tidal origin. The resulting disk, ejecta and the central BH will be the focus of Sec. 4.2.3 and Sec. 4.2.4.

4.2.2 Gravitational-wave luminosity

In the left columns of Table 4.2, we report GW data (i.e., $j_{\rm rem}$, $e^{\rm tot}_{\rm GW}$, and $L_{\rm peak}$) as extracted from our GW190425-like BNS simulations. We first test the quasi-universal relation between $e^{\rm tot}_{\rm GW}$ and $j_{\rm rem}$ given in [Zappa et al., 2018]: $e^{\rm tot}_{\rm fit}(j_{\rm rem}) = c_2 j^2_{\rm rem} + c_1 j_{\rm rem} + c_0$, with $c_0 = 0.95$,

$c_1 = -0.44$ and $c_2 = 0.053$ [2]. These coefficients were fitted over a dataset containing more than 200 BNS merger simulations performed with the `BAM` [Brügmann et al., 2008] and `THC` codes. The BNS simulations were grouped in four categories according to the fate of the remnant: prompt collapse to a BH, short-lived hypermassive NS, supramassive NS and stable NS. This simple quadratic polynomial in $j_{\rm rem}$ was very effective in relating the angular momentum of the remnant with the total radiated energy in the whole dataset, despite the different fates of the remnants, nuclear EOSs, and intrinsic BNS parameters. Moreover, the ranges $j_{\rm rem} \in [2.944, 3.204]$ and $e^{\rm tot}_{\rm GW} \in [0.077, 0.105]$ are compatible with the respective ranges presented in [Zappa et al., 2018] for the case of BNS resulting in a prompt collapse. We notice that the absolute value of the relative error $|e^{\rm tot}_{\rm fit} - e^{\rm tot}_{\rm GW}|\,/e^{\rm tot}_{\rm GW} \lesssim \mathcal{O}(0.1)$ is in accordance with the residuals plotted in figure 4 of [Zappa et al., 2018]. Additionally, we remark that $e^{\rm tot}_{\rm GW} < e^{\rm fit}_{\rm GW}$, also in accordance with the behavior of the prompt-collapse simulations in [Zappa et al., 2018]. To further test the quality of the fit results with respect to the uncertainties of numerical origin we compute the ratio between the residuals and the estimated total error due to resolution uncertainties, $\sqrt{{\delta e^{\rm tot}_{\rm GW}}^2 + \delta e^{\rm tot 2}_{\rm fit}}$, where $\delta e^{\rm tot}_{\rm fit} = \sqrt{4c_2^2 j_{\rm rem}^2 + c_1^2}\ \delta j_{\rm rem}$. The uncertainties of numerical origin, $\delta j_{\rm rem}$ and $\delta e^{\rm tot}_{\rm GW}$, are computed as the absolute value of the semi-difference between SR and LR results. The typical values are $\lesssim 1$, indicating that the numerical error accounts for a significant fraction of the observed discrepancy. Finally we emphasize that the rescaled GW peak luminosity, $(q/\nu)^2\, L_{\rm peak}$, and κ_2^L coefficient span the same range of the prompt collapse BNSs reported in figure 2 of [Zappa et al., 2018], i.e., $[1.11, 2.36] \times 10^{58}$ erg s^{-1} and $[134, 387]$, respectively. We recall that κ_2^L is the coefficient that parametrizes the leading effect of tides on the GW emission from a BNS merger in the post-Newtonian expansion, Eq. (4.2).

4.2.3 Remnant properties

Remnants in our simulations are characterized by a light accretion disk surrounding a spinning BH formed $\lesssim 0.5$ ms after the merger. In the following we present the properties of both as extracted from our simulations.

Accretion disk

During the last few orbits, the disk starts to form because of the tidal interaction between the two stars. In high-mass binaries resulting in prompt BH formation, the tidal interaction that occurs before and at merger is the major source of the disk. A few ms after merger the disk mass and angular momentum reach a quasi-steady phase, and slowly decrease until the

[2] We notice that, despite referring to the same fit, the fitting values reported in this work have one more figure than the ones originally reported by [Zappa et al., 2018].

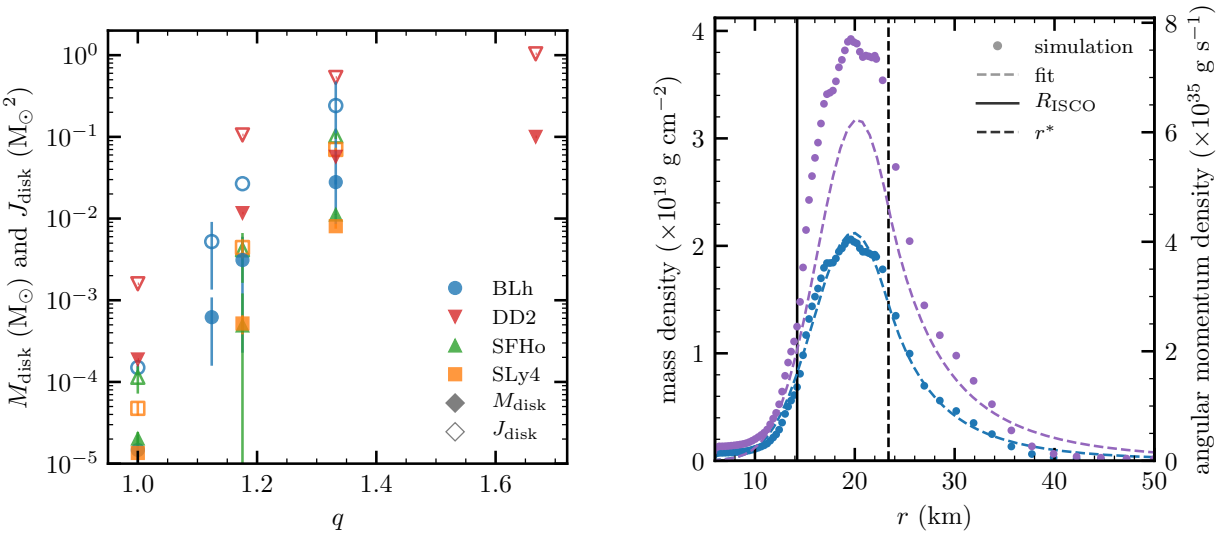

(a) (b)

Figure 4.3: (a). Disk mass (filled markers) and angular momentum (empty markers) at $4-7$ ms after merger for SR simulations. Mass and angular momentum increase with the mass ratio. The trends suggest a link between mass and angular momentum since $cJ_{\rm disk}/G \sim (8-10) M_\odot\, M_{\rm disk}$. Errors are estimated as $|{\rm SR}-{\rm LR}|$ when the LR is available. (b). Disk's radial density (blue points, left y-axis) and radial angular momentum density (purple points, right y-axis) for the BNS with BLh EOS and $q=1.33$. The blue dashed line is $\sigma(r)$ fitted on the numerical data, while the purple dashed line is the corresponding Keplerian angular momentum density. The vertical dashed line is the boundary between the Gaussian and the power-law r^* in Eq. (4.3). The vertical solid line is $R_{\rm ISCO}$. Adapted from Camilletti et al. [2022]

end of the simulation.

In Fig. 4.3a, we report the mass (filled markers) and angular momentum (unfilled markers) of the disks once they have reached their quasi-steady phase (i.e. $\sim 5-7$ ms after merger), computed as the integral of mass and angular momentum densities[3] extracted from our simulations. The masses (angular momenta) span a broad range from $\sim 10^{-5}$ $M_\odot$ to 0.1 $M_\odot$ (10^{-4} $-$ 1 $M_\odot^2$) depending on the BNS parameters. Both the disk mass and angular momentum increase as a function of the mass ratio q. We find that the increase is more pronounced for stiffer EOSs, where the tidal interaction is more efficient due to the larger $\tilde{\Lambda}$. For example, considering the trend for fixed $q=1.33$, the DD2 simulation ($\tilde{\Lambda}=254$) leads to the formation of a disk twice more massive than the one formed in the BLh simulation ($\tilde{\Lambda}=135$) and roughly six times more massive than those in the SFHo ($\tilde{\Lambda}=105$) and SLy4 ($\tilde{\Lambda}=93$) simulations. The errors on the disk mass, estimated when both resolutions are available as the absolute semi-difference between the SR and LR are in the range 25-40 per

[3]This approach assumes that the metric is axisymmetric.

cent for very light disks and get smaller ($\sim$ 3 per cent) as the disk mass increases above 10^{-3} $M_\odot$. Resolution effects are higher for the BLh simulation with $q = 1.18$, for which the disk mass of the LR simulation is ~ 14 times larger than the SR one. Despite efforts, we did not find the origin of such difference. Fig. 4.3a suggests a correlation between the mass and the angular momentum of the disk, i.e., $J_{\rm disk} \sim (8-10) M_\odot\, G M_{\rm disk}/c$, possibly independent from the EOS and mass ratio. Stated differently, the mean specific angular momentum of the disk is (roughly) constant: $J_{\rm disk}/M_{\rm disk} \sim (8-10) M_\odot\, G/c$.

In the following, we try to describe the accretion disks emerging from the simulations as Keplerian disks. As we will see in Sec. 5, this assumption is not fully correct, however it was often considered in the literature and we are going to explore it with the goal of better characterizing the relation between the total mass and angular momentum of the disks. We consider the radial density distributions, $\sigma(r) = \int d\phi dz\ \rho(r, \phi, z)$, as obtained from our numerical simulations, and we approximate it with a Gaussian peak smoothly connected to a radial power-law:

$$\sigma(r) = \begin{cases} b \exp\left(-\dfrac{(r - r_{\rm peak})^2}{2s^2}\right) & 0 \le r \le r^* \\ \sigma_0 \left(\dfrac{r}{r^*}\right)^{-\alpha} & r > r^* \end{cases} \tag{4.3}$$

where b, $r_{\rm peak}$, s and α are fitted against the actual radial density distribution in our simulations, while σ_0 and r^* are fixed requiring $\sigma(r)$ to be differentiable in r^*. In Fig. 4.3b, we show the result of the fit for $\sigma(r)$ (blue dashed line) on the numerical one (blue dots) for the simulation with the BLh EOS and $q = 1.33$. The values for relevant parameters for the radial distributions of simulations at SR are summarized in Fig. 4.4. The radius of the ISCO $R_{\rm ISCO}$ (crosses), of the density peak $r_{\rm peak}$ (up-triangles), of the junction between the Gaussian and the power decay r^* (stars) and of the half density peak $r_{\sigma_{\rm max}/2}$ span a small range, indicating similar radial density distributions despite the mass spans almost 3 order of magnitude. $R_{\rm ISCO}$ is found at $13-16$ km from the center, while the density peak is around $17-29$ km. In the right panel of Fig. 4.4, we show the power-law exponent α, obtained by fitting Eq. (4.4) over the numerical data as a function of $M_{\rm disk}$. Unfilled markers represent disks for which the mass of the Keplerian disk differs from the actual one by more than 20%. The exponent α changes considerably within our sample, from 4 up to 14, and more massive disks ($M_{\rm disk} > 10^{-2}$ $M_\odot$) have a shallower decline, characterized by $4.0 \lesssim \alpha \lesssim 5.4$.

To compute the angular momentum of the disk from the density distribution, we assume a Keplerian angular velocity profile, $\omega_{\rm kep}(r) = \sqrt{G M_{\rm BH}/r^3}$, inside the disk. The mass and

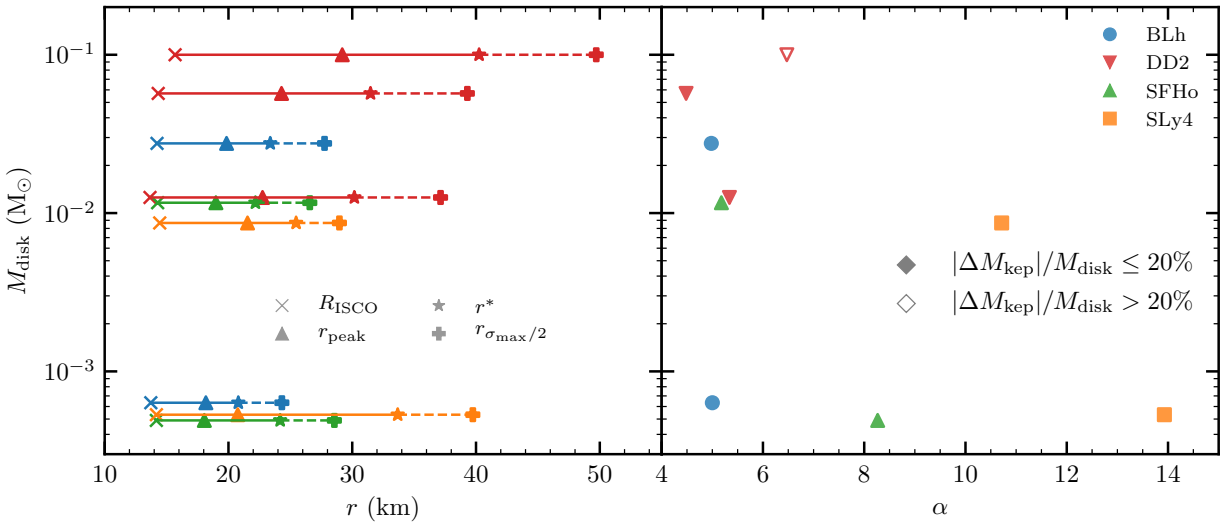

Figure 4.4: Left: fitted values of $R_{\rm ISCO}$, $r_{\rm peak}$ and r^* as defined in Eq. (4.3). Solid lines represent the radius spanned by the Gaussian, while dashed lines represent the power decay branch of $\sigma(r)$ up to the radius $r_{\sigma_{\rm max}/2}$ at which the value of the density is half of its maximum. Right: Power-law exponent, α, for each disk in our numerical simulation sample, as a function of the disk mass, $M_{\rm disk}$. Unfilled markers represent disks for which the mass inside the Keplerian disk differs from the numerical one by more than 0.2. Massive disks have a shallower decline corresponding to smaller values of $\alpha's$. Adapted from Camilletti et al. [2022]

angular momentum of the resulting Keplerian disk are:

$$M_{\rm disk}^{\rm kep} = \int_0^\infty r\sigma(r){\rm d}r, \qquad\qquad J_{\rm disk}^{\rm kep} = \int_0^\infty r^3\sigma(r)\,\omega_{\rm kep}(r){\rm d}r. \tag{4.4}$$

To integrate Eq. (4.4), we define

$$M_{\rm disk}^{\rm kep} \equiv M_{\rm disk}^{\rm G} + M_{\rm disk}^{\alpha}\ , \qquad\qquad J_{\rm disk}^{\rm kep} \equiv J_{\rm disk}^{\rm G} + J_{\rm disk}^{\alpha}\ , \tag{4.5}$$

where the superscript G and α indicate the Gaussian and power-law parts of the Keplerian disk in Eq. (4.3) and Eq. (4.4):

$$M_{\rm disk}^{\rm G} \equiv \int_{R_{\rm ISCO}}^{r^*} r\sigma(r){\rm d}r\ , \qquad\qquad M_{\rm disk}^{\alpha} \equiv \int_{r^*}^{r_{\rm max}} r\sigma(r){\rm d}r\ , \tag{4.6}$$

and similar for the angular momentum. We can solve the integration:

$$M^{\rm G}_{\rm disk} = bs^2 \left[\sqrt{\frac{\pi}{2}} \frac{r_{\rm peak}}{s} {\rm erf}\left(\frac{r - r_{\rm peak}}{\sqrt{2} s} \right) - \exp\left(- \frac{(r - r_{\rm peak})^2}{2 s^2} \right) \right]^{r*}_{R_{\rm ISCO}} , \tag{4.7}$$

$$M^{\alpha}_{\rm disk} = \frac{\sigma_0}{\alpha - 2} \left(1 - \frac{(r^*)^{\alpha-2}}{r^{\alpha-2}_{\rm max}} \right) (r^*)^2 , \tag{4.8}$$

$$J^{\rm G}_{\rm disk} = \sqrt{\frac{1}{2} G M_{\rm BH} r^3_{\rm peak} (bs)^2} \sum_{k=0}^{\infty} \binom{3/2}{k} \left(\frac{\sqrt{2} s}{r_{\rm peak}} \right)^k \Gamma\left(\frac{k+1}{2}, \frac{(r - r_{\rm peak})^2}{2 s^2} \right) \Big|^{r^*}_{R_{\rm ISCO}} , \tag{4.9}$$

$$J^{\alpha}_{\rm disk} = \frac{\sigma_0 \sqrt{G M_{\rm BH}}}{\alpha - 5/2} \left(1 - \frac{(r^*)^{\alpha-5/2}}{r^{\alpha-5/2}_{\rm max}} \right) (r^*)^{5/2} , \tag{4.10}$$

where ${\rm erf}(x) \equiv (2/\sqrt{\pi}) \int_0^x e^{-t}\ {\rm d}t$ is the error function and $\Gamma(a,x) \equiv \int_x^\infty t^{a-1} e^{-t} dt$ the incomplete gamma function. One can write:

$$\frac{J^{\rm kep}_{\rm disk}}{M^{\rm kep}_{\rm disk}} = \eta \frac{J^{\alpha}_{\rm disk}}{M^{\alpha}_{\rm disk}} , \tag{4.11}$$

where

$$\eta = \frac{1 + J^{\rm G}_{\rm disk}/J^{\alpha}_{\rm disk}}{1 + M^{\rm G}_{\rm disk}/M^{\alpha}_{\rm disk}} . \tag{4.12}$$

Assuming $r^* \ll r^{\rm max}$ (with an error $\lesssim 1$ per cent) we arrive at

$$\frac{J^{\rm kep}_{\rm disk}}{M^{\rm kep}_{\rm disk}} = \left(\eta \frac{\alpha - 2}{\alpha - 5/2} \sqrt{\frac{M_{\rm BH}}{{\rm M}_\odot} \frac{2 r^*}{R^{\rm Sch}_\odot}} \right) \frac{G\ {\rm M}_\odot}{c} , \tag{4.13}$$

where $R^{\rm Sch}_\odot$ is the Schwarzschild radius of the Sun. In 4.3b, we also show the radial angular momentum density from the numerical simulation (purple points) and the corresponding Keplerian analogue computed from Eq. (4.4) with the fitted $\sigma(r)$ (purple dashed line). We excluded the disks of equal mass BNS from this analysis since they are very light and $40-100$ per cent of their mass is inside the innermost stable circular orbit (ISCO) predicted according to the BH properties. Such disks will be accreted by the BH on the dynamical timescale.

In conclusion, we note that η varies between 0.78 and 0.90 with average 0.83 in our numerical simulations, r^* is such that $21{\rm km} \lesssim r^* \lesssim 40{\rm km}$, while $M_{\rm BH} \approx 3.21 - 3.26\ {\rm M}_\odot$ (see Sec. 4.2.3). The parameter which is subject to more significant variation is $\alpha \in [4.0, 13.9]$ whose average is 7.5. Inserting these ranges of values in Eq. (4.13), one obtains $J^{\rm kep}_{\rm disk}/M^{\rm kep}_{\rm disk} \sim 6 - 9\ {\rm M}_\odot$ with average of $7.3\ {\rm M}_\odot$, which is not too far from the average $\langle J_{\rm disk}/M_{\rm disk} \rangle = 8.8\ {\rm M}_\odot$ obtained by our numerical simulations. To better quantify this difference, in Fig. 4.5 we compare the angular momentum of the disks from our simulations

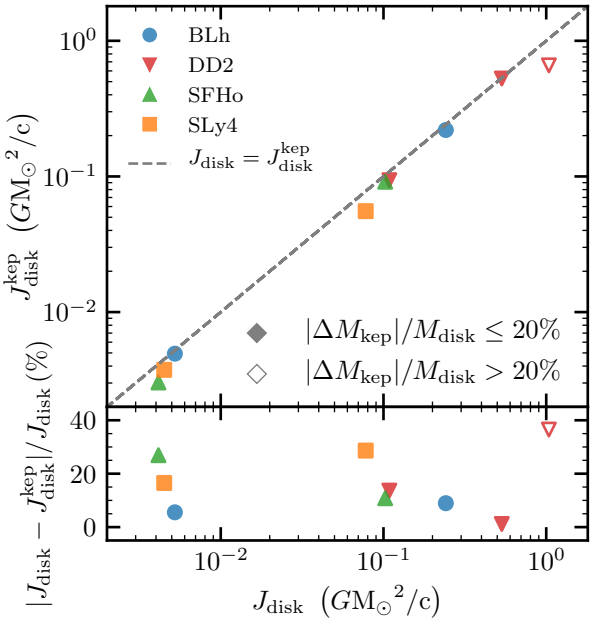

Figure 4.5: Top: Comparison between the disk angular momentum outside the ISCO from numerical simulations, $J_{\rm disk}$, and the one obtained by constructing a Keplerian disk whose radial density profile was fitted over the numerical results using Eq. (4.3), $J^{\rm kep}_{\rm disk}$. Bottom: Relative difference between the two values. Unfilled markers represent disks for which the Keplerian mass differs from the numerical one by more than 20 per cent. Taken from Camilletti et al. [2022]

at SR with the corresponding Keplerian analogue, given by Eq. (4.4). With the exception of DD2 EOS with $q = 1.67$, we found that $J^{\rm kep}_{\rm disk} \lesssim J_{\rm disk}$, is within 30 per cent over more than two orders of magnitudes in $J_{\rm disk}$. In Chapter 5 we will give a more accurate description of the accretion disk, demonstrating that the accretion disks resulting from non spinning BNS mergers exhibit non Keplerian behavior, at least in their first ~ 100 ms post-merger.

Black hole

In Fig. 4.6a we report the BH irreducible and gravitational masses, and the dimensionless spin as a function of time after the BH formation for the BLh simulation at SR with $q = 1.33$. We see that all the three quantities increase abruptly as the AH finder detects the apparent horizon. The horizontal dashed lines indicate the expected values $M^{\rm exp}_{\rm BH}$ and $a^{\rm exp}_{\rm BH}$, while the vertical dashed line indicates the time at which the irreducible mass reaches its maximum value (a few ms after the BH formation). Although $M_{\rm irr}$ is expected to remain constant or to increase, we find that after having reached the maximum it starts to slowly decrease. We attribute this behavior to numerical and discretization errors in tracing the AH location. While the AH shrinks, $M_{\rm BH}$ and $a_{\rm BH}$ continue to increase without reaching saturation. Matter accretion from the disk is not sufficient to explain this growth. The rise of $M_{\rm BH}$ after

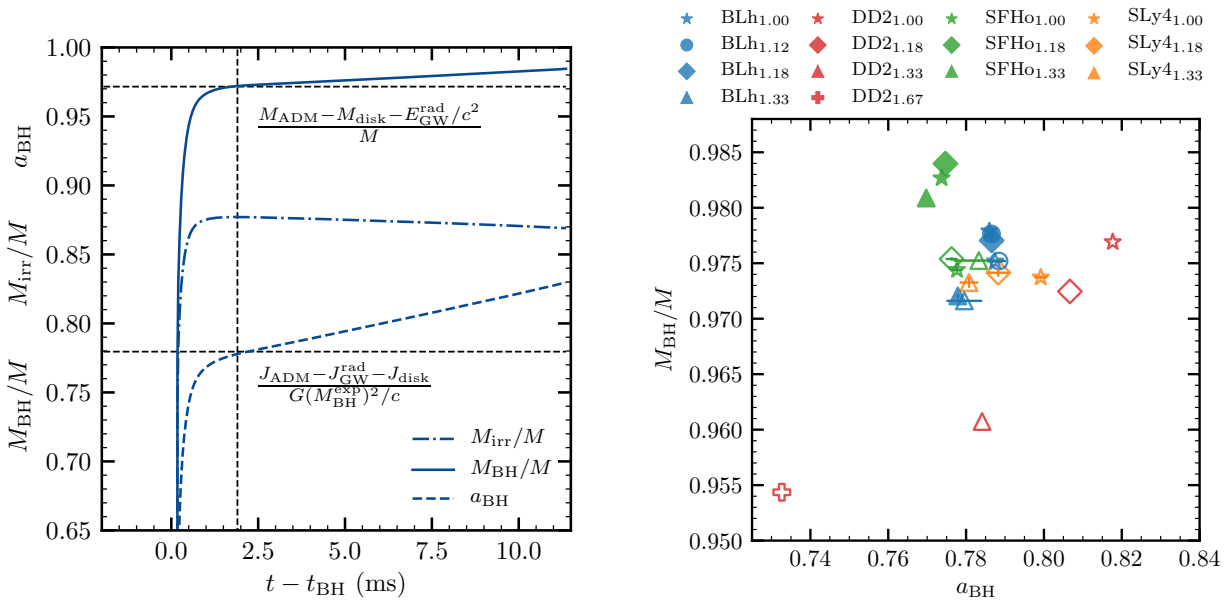

(a) (b)

Figure 4.6: (a). Evolution of the normalized BH irreducible mass $M_{\rm irr}/M$, gravitational mass $M_{\rm BH}/M$ and dimensionless spin parameter $a_{\rm BH}$ for a SR simulation based on the BLh EOS with $q = 1.33$. Horizontal dashed lines represent the expected values for the gravitational mass $(M_{\rm ADM} - E^{\rm rad}_{\rm GW} - M_{\rm disk})/M$ and the spin parameter $(J_{\rm ADM} - J^{\rm rad}_{\rm GW} - J_{\rm disk})/(M^{\rm exp}_{\rm BH})^2$. Vertical dashed lines indicate the time at which the irreducible mass starts to decrease and the corresponding value on the plotted line. (b). $M_{\rm BH}/M$ and dimensionless spin parameter $a_{\rm BH}$ distribution for the SR simulations of this work. Filled markers represent the values computed by the AH finder, while empty markers represent the expected ones. Errors are computed as the absolute semi-difference between SR and LR when available. For the filled markers errors are smaller than the symbol size. Adapted from Camilletti et al. [2022]

the maximum of $M_{\rm irr}$ is due to the continuous increase of the BH spin, which is an artifact of our simulations. Due to these uncertainties, we decide to focus on the gravitational mass and spin parameter of the BH at the moment when the irreducible mass is maximum.

In Table 4.2 we report the gravitational mass $M_{\rm BH}$ and the spin parameter $a_{\rm BH}$ of the BH computed on the basis of the latter definition. To give more conservative values of the BH properties, we report also the time averages of the BH mass, $\langle M_{\rm BH}\rangle$, and spin parameter, $\langle a_{\rm BH}\rangle$, over the first 7 ms after the time at which $M_{\rm irr}$ is maximum. We report the available data obtained by SR simulations and we estimate the uncertainties (when available) as the semi-difference with respect to the data from the corresponding LR simulations when available. In the case of simulations employing the BLh or SFHo EOS, the AH is resolved by the AH finder and the BH properties can be analyzed with appropriate accuracy. More quantitatively, $M_{\rm BH}$ and $a_{\rm BH}$ differ from the respective expected values less than 1 per cent. On the other hand, the AH finder was unable to detect the AH for the simulations employing

the DD2 or SLy4 EOS. In these cases we decided not to report the corresponding values in Table 4.2.

Regarding the dependence of the BH properties on the initial binary parameters, the final outcome depends mostly on two effects. On one hand, energy and angular momentum are extracted from the central object via the ejection of matter and the formation of a remnant disk. On the other hand, GWs carry energy and angular momentum away. Both these effects reduce at the same time $M_{\rm BH}$ and $J_{\rm BH}$. Since $J_{\rm disk} \approx 10\ \ {\rm M}_\odot\ G/c\ M_{\rm disk}$, the formation of a massive disk is particularly efficient in reducing the BH angular momentum, and ultimately also the spin parameter since the variation of $a_{\rm BH}^{\rm exp}$ due to the disk formation only becomes $\delta a_{\rm BH}^{\rm exp}|_{\rm disk} \approx (2a_{\rm BH}^{\rm exp} - 10\ {\rm M}_\odot/M_{\rm BH}^{\rm exp})\delta M_{\rm disk}/M_{\rm BH}^{\rm exp} \sim -0.468\ \delta M_{\rm disk}/(\ {\rm M}_\odot)$. As visible in Fig. 4.6b, (quasi) equal mass binary simulations employing the DD2 EOS have the largest spin parameters, since their symmetric character produces a smaller disk mass, while their larger $\kappa_2^{\rm L}$ implies a lower GW emission. However, very asymmetric binaries employing the same EOS produce massive disks reducing efficiently both $M_{\rm BH}$ and $a_{\rm BH}$. A similar, but less significant effect, is also observed for simulations employing the BLh and SFHo EOSs. For simulations employing the SLy EOS (whose disks are usually the lightest), $a_{\rm BH}$ decreases with q, while $M_{\rm BH}/M$ stays roughly constant. Focusing on the (quasi-)equal mass simulations using the BLh, SFHo or SLy4 EOS, the removal of mass and angular momentum through the disk formation becomes subdominant, while the dominant process is the GW emission. More symmetric binaries modeled with the SLy4 EOS (corresponding to lower values of $\kappa_2^{\rm L}$), have indeed the smallest BH masses.

4.2.4 Dynamical ejecta

In Table 4.3, we present the properties of the dynamical ejecta as extracted from our simulations, namely the mass of the ejecta, $M_{\rm ej}$; the standard deviation (SD) of the polar ($\theta \in [0°, 180°]$) and azimuthal ($\phi \in [0°, 360°]$, see Appendix B. for more details on its calculation) angular distributions, $\theta_{\rm ej}^{\rm SD}$ and $\phi_{\rm ej}^{\rm SD}$, respectively; the median of the distribution of the velocity at infinity, $v_\infty^{\rm med}$, of the electron fraction, $Y_e^{\rm med}$, and of the entropy per baryon, $s_{\rm ej}^{\rm med}$. The last column refers to the fraction of shocked ejecta X_s, defined as the fraction of the ejecta whose entropy is larger than $10\,k_{\rm B}$ baryon^{-1}. We report the values for both SR and LR simulations accompanied by the 15-75 percentile range around the median computed from the respective mass-weighted histogram. We do not report the ejecta properties when $M_{\rm ej} < 10^{-5}\ {\rm M}_\odot$, since the properties of such a small amount of ejected matter cannot be trusted due to numerical uncertainties. Additionally, in Fig. 4.7, we present mass histograms of the v_∞, Y_e, $s_{\rm ej}$ and $\theta_{\rm ej}$ distributions for simulations at SR for which $M_{\rm ej} \geq 10^{-5}\ {\rm M}_\odot$. The vertical solid (dashed) lines represent the medians (average) of the ejecta properties for the

Table 4.3: Dynamical ejecta properties for each simulation. $M_{\rm ej}$ is the total mass of the ejecta; $\theta_{\rm ej}^{\rm SD}$ and $\phi_{\rm ej}^{\rm SD}$ are the mass-weighted standard deviation of the polar and azimuthal angle, respectively; $v_\infty^{\rm med}$, $Y_e^{\rm med}$ and $s_{\rm ej}^{\rm med}$ are the median values of the electron fraction, speed and entropy distributions. The last column is the ratio $X_s \equiv M_{\rm ej}^{\rm shocked}/M_{\rm ej}$, where the shocked and tidal ejecta are defined as the components with entropy respectively above and below the threshold of 10 $k_{\rm B}$ baryon^{-1}. The subscript and superscript numbers indicate the 15 and 75 percentile around the median of the respective quantity. Taken from Camilletti et al. [2022]

EOS	q	Resolution	$M_{\rm ej}$ [10^{-4} M$_\odot$]	$\theta_{\rm ej}^{\rm SD}$	$\phi_{\rm ej}^{\rm SD}$	$v_\infty^{\rm med}$ [c]	$Y_e^{\rm med}$	$s_{\rm ej}^{\rm med}$ [$k_{\rm B}$ baryon^{-1}]	X_s
BLh	1.0	SR	0.002	-	-	-	-	-	-
		LR	0.023	-	-	-	-	-	-
BLh	1.12	SR	0.039	-	-	-	-	-	-
		LR	0.090	-	-	-	-	-	-
BLh	1.18	SR	0.164	21.3	82.0	$0.24^{+0.08}_{-0.12}$	$0.21^{+0.07}_{-0.08}$	$18.1^{+39.4}_{-11.6}$	0.78
		LR	0.182	23.3	89.8	$0.21^{+0.07}_{-0.10}$	$0.25^{+0.04}_{-0.07}$	$41.2^{+55.4}_{-31.5}$	0.94
BLh	1.33	SR	0.508	18.2	74.0	$0.27^{+0.10}_{-0.14}$	$0.17^{+0.9}_{-0.5}$	$9.71^{+17.4}_{-4.21}$	0.61
		LR	0.959	20.7	78.6	$0.29^{+0.10}_{-0.15}$	$0.16^{+0.14}_{-0.5}$	$12.3^{+22.0}_{-6.87}$	0.63
DD2	1.0	SR	0.586	26.3	95.1	$0.28^{+0.09}_{-0.12}$	$0.27^{+0.04}_{-0.06}$	$33.2^{+38.8}_{-18.3}$	1.00
		LR	0.416	23.8	92.1	$0.32^{+0.06}_{-0.08}$	$0.29^{+0.03}_{-0.05}$	$47.1^{+42.4}_{-31.4}$	1.00
DD2	1.18	SR	7.16	21.4	122	$0.27^{+0.10}_{-0.14}$	$0.17^{+0.05}_{-0.06}$	$10.28^{+7.18}_{-4.12}$	0.57
		LR	9.67	18.1	87.3	$0.27^{+0.11}_{-0.15}$	$0.19^{+0.06}_{-0.08}$	$9.36^{+5.42}_{-3.80}$	0.63
DD2	1.33	SR	4.00	17.3	76.6	$0.23^{+0.08}_{-0.11}$	$0.15^{+0.05}_{-0.05}$	$9.38^{+3.64}_{-3.66}$	0.65
		LR	3.94	21.7	80.7	$0.19^{+0.10}_{-0.11}$	$0.13^{+0.8}_{-0.05}$	$9.34^{+5.15}_{-3.29}$	0.52
DD2	1.67	SR	4.05	11.1	103	$0.20^{+0.14}_{-0.14}$	$0.10^{+0.03}_{-0.07}$	$5.66^{+4.27}_{-1.87}$	0.29
		LR	6.20	13.0	95.8	$0.13^{+0.13}_{-0.8}$	$0.06^{+0.08}_{-0.03}$	$6.15^{+3.70}_{-3.33}$	0.37
SFHo	1.0	SR	0.023	-	-	-	-	-	-
		LR	0.033	-	-	-	-	-	-
SFHo	1.18	SR	0.071	-	-	-	-	-	-
		LR	0.151	24.5	90.6	$0.22^{+0.07}_{-0.10}$	$0.26^{+0.03}_{-0.04}$	$72.3^{+51.3}_{-53.1}$	0.97
SFHo	1.33	SR	0.603	12.7	68.8	$0.26^{+0.10}_{-0.13}$	$0.13^{+0.04}_{-0.06}$	$7.55^{+4.97}_{-3.30}$	0.37
		LR	1.87	13.1	85.0	$0.32^{+0.10}_{-0.16}$	$0.13^{+0.05}_{-0.05}$	$6.45^{+5.08}_{-2.50}$	0.32
SLy4	1.0	SR	0.030	-	-	-	-	-	-
		LR	0.024	-	-	-	-	-	-
SLy4	1.18	SR	0.055	-	-	-	-	-	-
		LR	0.114	21.4	79.5	$0.22^{+0.10}_{-0.10}$	$0.24^{+0.05}_{-0.06}$	$38.1^{+97.5}_{-31.4}$	0.79
SLy4	1.33	SR	2.29	9.0	71.5	$0.40^{+0.12}_{-0.20}$	$0.10^{+0.03}_{-0.02}$	$5.48^{+1.82}_{-3.15}$	0.22
		LR	1.12	14.6	70.8	$0.30^{+0.10}_{-0.14}$	$0.12^{+0.09}_{-0.5}$	$7.40^{+8.42}_{-4.44}$	0.49

$q = 1.33$ cases, taken as representative case. While the difference between mean and median is small or even negligible for the velocity and the electron fraction, a significant difference is clear in the entropy distribution.

The ejecta mass ranges from values smaller than 10^{-5} M$_\odot$ up to $\sim 6\times10^{-4}$ M$_\odot$, increasing with the mass ratio q and the stiffness of the EOS, as visible in Fig. 4.8. For asymmetric systems ($q \neq 1$) and stiffer EOSs, the tidal interaction is more efficient in deforming the

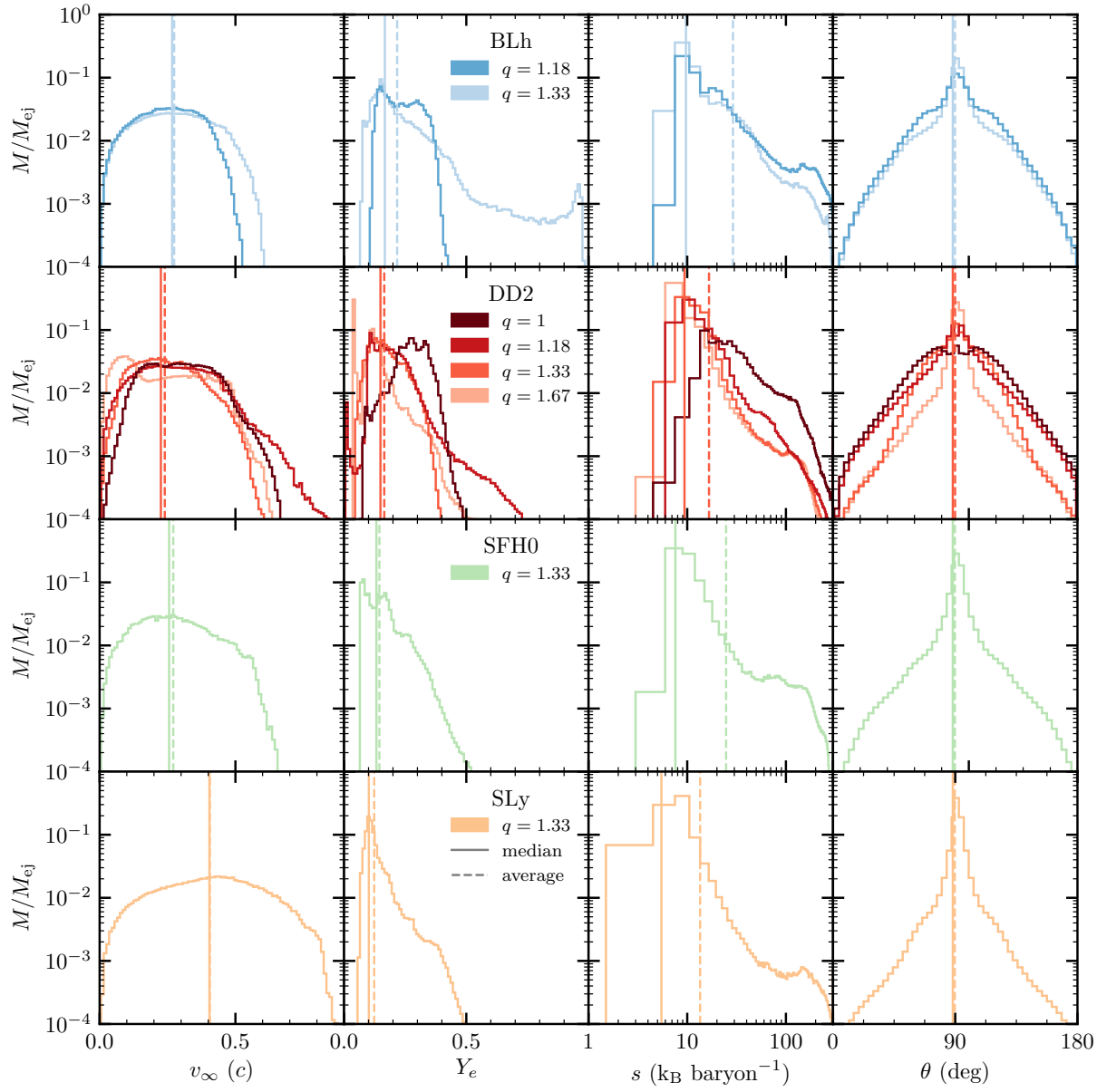

Figure 4.7: Histograms of the dynamical ejecta. From the first to the last column: velocity at infinity v_∞, electron fraction Y_e, entropy per baryon s and polar angle $\theta_{\rm ej}$. Each row represents a different EOS. From the first to the last line: BLh, DD2, SFHo, SLy4. As a representative case, we represent the median and the average values of all quantities for the $q = 1.33$ cases as vertical solid and dashed lines, respectively. The high Y_e tail in the BLh, $q = 1.33$ case is not robust due to the finite size of the EOS tables not extending above $Y_e = 0.6$. Taken from Camilletti et al. [2022]

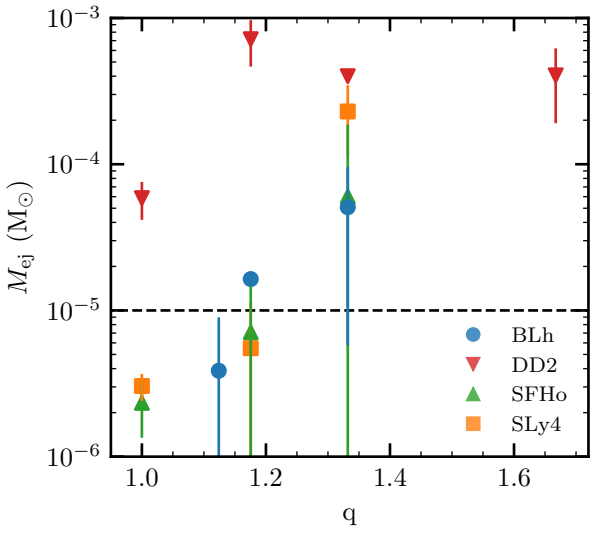

Figure 4.8: Dynamical ejecta mass as a function of the mass ratio q of the binary. Different symbols denote numerical simulations with different EOS. Simulations with $M_{\rm ej} < 10^{-6}$ $M_\odot$ have been excluded, while only ejecta with $M_{\rm ej} > 10^{-5}$ $M_\odot$ is trusted due to numerical uncertainties. Errors are computed as the absolute difference between SR and LR values. Taken from Camilletti et al. [2022]

secondary NS and the resulting merger dynamics is more effective in expelling matter from its tidal tails [see e.g. Hotokezaka et al., 2013a, Bauswein et al., 2013b, Sekiguchi et al., 2015, Rosswog, 2015, Lehner et al., 2016, Dietrich et al., 2017, Bernuzzi et al., 2020]. Simulations employing the DD2 EOS exhibit a deviation from this trend at higher mass ratios ($q = 1.33, 1.67$), for which the value of the ejecta mass saturates or even tends to decrease, similarly to what found in [Dudi et al., 2021] (see Sec. 4.4). We speculate that the ejection process at high q's is more sensitive to usually subdominant effects, including the detailed behavior of the NS radius and of $\tilde{\Lambda}$, see Fig. 4.1 and Table 4.1. For the latter quantity, for high-q BNSs, models employing the DD2 show a decreasing $\tilde{\Lambda}$ (see Table 4.1). It suggest that for asymmetric enough BNS ($q \gtrsim 1.2$ in our case), if an additional increase of the asymmetry is not accompanied by and increase of $\tilde{\Lambda}$, the ejecta mass can saturate or even decrease. More simulations at higher resolutions are needed to confirm the robustness of this trend.

The SD of the geometrical angles gives an indication of the spatial distribution of the ejected matter. We find that the ejecta spread over the whole space, but it is mostly concentrated close to the equator, with an opening angle $2\theta_{\rm ej}^{\rm SD}$ that varies across the range $18^\circ - 54^\circ$, depending on the binary properties and where higher values correspond to more symmetric binaries. This can be understood since the tidal interaction tends to distribute matter along the orbital plane. The SD of the azimuthal angle $\phi_{\rm ej}^{\rm SD}$ is related to the rotational

symmetry of the dynamical ejecta around the orbital axis. For a mass distribution uniform in ϕ and centered in 180° with symmetric support on $2\alpha \in [0, 360°]$, we expect a SD of $\phi_{\rm ej}^{\rm SD} = (\sqrt{3}/3)\ \alpha \approx 52°(\alpha/90°)$. The values of $\phi_{\rm ej}^{\rm SD}$ obtained in our simulations range within $65° - 96°$ and are compatible with a uniform distribution centered in 180° with support on $\sim 225° - 360°$ respectively, where higher values correspond to equal-mass systems. This indicates that the dynamical ejecta expelled by symmetric binaries is distributed over the whole azimuthal angle, while the anisotropy increases with q [see e.g. Bovard et al., 2017, Radice et al., 2018b, Bernuzzi et al., 2020].

The distribution of the radial velocity at infinity has $v_\infty^{\rm med}$ ranging from $\sim 0.2\,c$ to $\sim 0.4\,c$, with fast tails reaching $\sim 0.6 - 0.9\,c$ for the highest mass ratios. The median of the electron fraction distribution is always smaller than 0.3 and is lower for higher mass ratios: tidal interaction ejects cold neutron rich material only marginally subject to composition reprocessing from positron and neutrino captures [e.g. Wanajo et al., 2014, Sekiguchi et al., 2015, Perego et al., 2017, Martin et al., 2018]. Finally, the entropy per baryon has a distribution with a marked peak at relatively low entropy, between $\sim 5\ k_{\rm B}$ baryon^{-1} and $\sim 20\ k_{\rm B}$ baryon^{-1}, and a slow decrease towards higher entropy, with medians that in the SR cases range between $\sim 5\ k_{\rm B}$ baryon^{-1} and $\sim 18\ k_{\rm B}$ baryon^{-1} (with the only exception of the $q = 1$ simulation employing the DD2 EOS, and more often $\lesssim 10\ k_{\rm B}$ baryon^{-1}). All the entropy distributions show a second peak around $s_{\rm ej} \sim 120\ k_{\rm B}$ baryon^{-1} whose relative importance decreasing with q and with the stiffness of the EOS, ranging approximately between 10^{-2} and 10^{-3}. This high-entropy component reflects the presence of a shocked fraction of the ejecta coming from the collisional interface of the two NSs (see Sec. 4.2.1 and Fig. 4.2). We expect this component to be present also in BNS mergers characterized by lower total masses (and often not resulting in a prompt collapse), in which the total amount of ejected matter is typically larger than what found in our simulations. The compositional properties of the dynamical ejecta show distributions comparable to what studied in [Most et al., 2021a] for the case of an irrotational binary, with similar fast-tail, high ye and high entropy components.

In the analysis outlined above, we have found that many properties of the ejected matter correlate with q and with the EOS stiffness. We now explicitly explore correlations among the different ejecta properties. In Fig. 4.9, we show $M_{\rm ej}$, $Y_e^{\rm med}$ and $\theta_{\rm ej}^{\rm SD}$ as a function of $s_{\rm ej}^{\rm med}$ for each BNS simulation producing more than 10^{-5} $\rm M_\odot$ of dynamical ejecta. We recall that lower $s_{\rm ej}^{\rm med}$ correspond to higher values of q. In the left panel we observe that $M_{\rm ej}$ is larger for lower values of $s_{\rm ej}^{\rm med}$ and it is usually greater for stiffer EOSs. In the two middle panels, we observe that both $\theta_{\rm ej}^{\rm SD}$ and $Y_e^{\rm med}$ increase almost linearly with the logarithm of the median of the entropy distribution. This confirms that the tidal interaction tends to distribute cold, low-entropy ejecta along the orbital plane. Only for simulations in which the shock-heated component is relevant (i.e., symmetric or nearly symmetric BNSs), the angular distribution

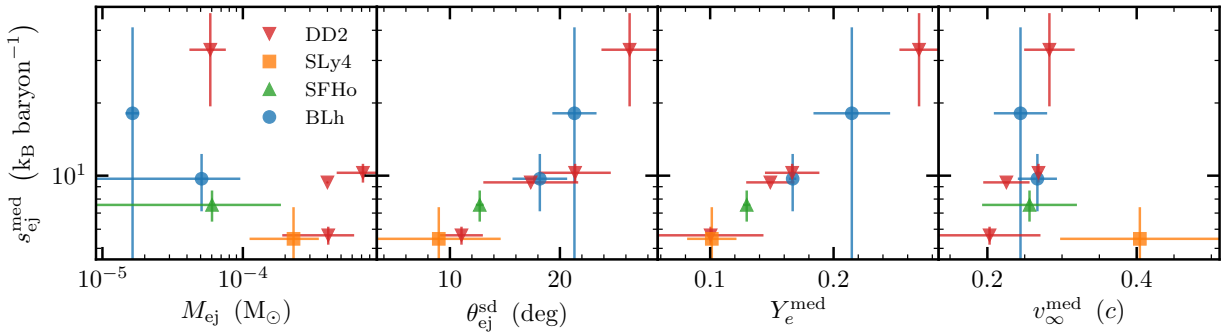

Figure 4.9: Correlation of the ejecta mass M_{ej}, standard deviation of the polar angle $\theta_{\rm ej}^{\rm SD}$, median of the electron fraction $Y_e^{\rm med}$ and median of the velocity at infinity $v_\infty^{\rm med}$ with the median of the entropy $s_{\rm ej}^{\rm med}$. Uncertainties are estimated as the absolute difference between SR and LR simulations, while SR values are used to represent the points. The simulations with higher mass ratios have higher values of the ejected mass. Taken from Camilletti et al. [2022]

of the ejecta departs significantly from the orbital plane, indicating that shocked matter spreads more over the solid angle. Similar results were found also for unequal-mass binaries that do not collapse promptly into a black hole. [see e.g. Bauswein et al., 2013b, Lehner et al., 2016, Dietrich et al., 2017, Radice et al., 2018b, Bernuzzi et al., 2020, Nedora et al., 2021b]. In the right panel, we study the correlations between the median of the entropy and the median of the velocity at infinity. In our simulations $v_\infty^{\rm med}$ decrease with $s_{\rm ej}^{\rm med}$, indicating that higher mass ratios result in faster ejecta, contrary to what usually found in relation to systems characterized by smaller total masses. This could be indeed a peculiar property of very massive BNSs.

4.3 Nucleosynthesis and kilonova

4.3.1 Nucleosynthesis

Using the procedure outlined in Sec. 3.4, we compute nucleosynthesis yields for the dynamical ejecta of all our GW190425 targeted simulations. In Fig. 4.10, we present nucleosynthesis yields for a subset of representative simulations at $t = 30$ years after merger, superimposed to the Solar residual r-process abundances taken from Prantzos et al. [2020] as a useful point of reference. To guide the comparison between the different models, the Solar residuals are scaled in order to reproduce the abundance of the simulation with $q = 1.33$ and the DD2 EOS at $A = 130$.

Unequal-mass merger simulations employing the DD2 EOS (left panel) robustly produce elements between the second and the third r-process peak, without showing any substantial

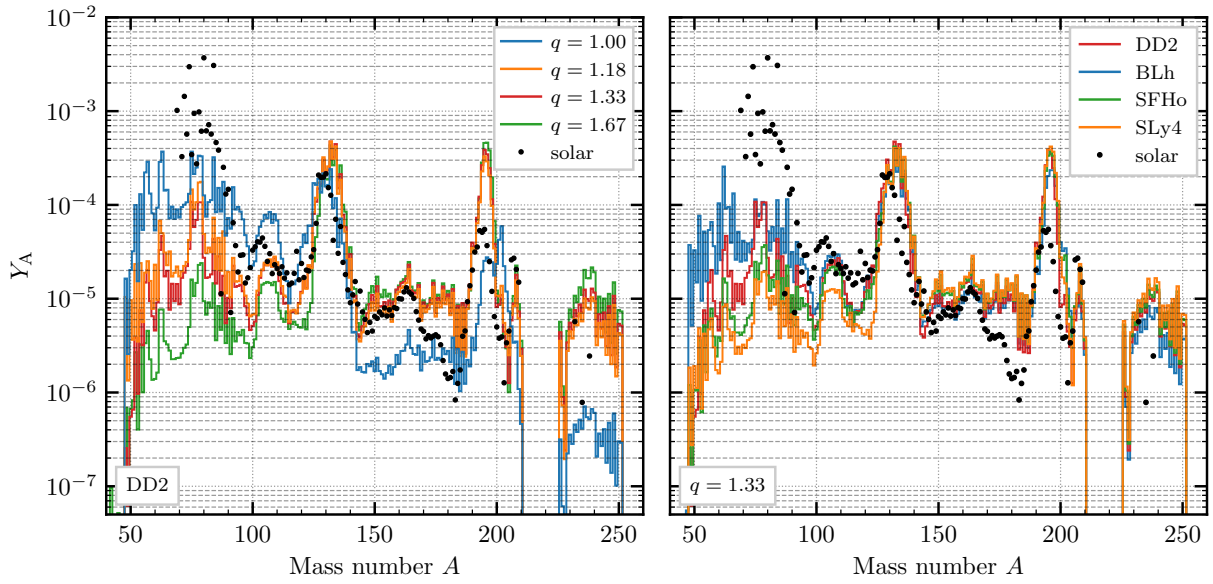

Figure 4.10: Nucleosynthesis pattern at $t = 30$ years after the merger as a function of the mass number A. Left: comparison between relative abundances from simulations employing the DD2 EOS. Right: comparison between relative abundances from numerical relativity (NR) simulations with mass ratio $q = 1.33$. Black dots represent the Solar r-process abundances, taken from Prantzos et al. [2020]. To guide the comparison, the Solar residuals are scaled in order to reproduce at $A = 130$ the abundance of the simulation with $q = 1.33$ and the DD2 EOS. Taken from Camilletti et al. [2022]

difference between the various mass ratios. Relative abundances are comparable to the Solar residuals with a significant excess in the third peak height with respect to the height of the second peak, and a significant production of translead nuclei. On the other hand, $A \lesssim 120$ nuclei are systematically underproduced. A weak dependence on the value of the mass ratio is visible, with more asymmetric mergers producing on average a larger amount of heavy nuclei. These behaviors are expected given the prompt collapse of the central remnant into a BH, the tidal character of the ejection mechanism and the consequent absence of a significant high-Y_e tail in the dynamical ejecta above a critical value $Y_e \gtrsim 0.22$ [e.g. Lippuner and Roberts, 2015, Radice et al., 2016], that is associated with the production of less than 10 per cent of the mass fraction of heavy nuclei above the second peak through an incomplete r-process.

The situation changes significantly when considering the DD2 equal-mass case (blue line). In fact, the relative abundances of heavy r-process nuclei ($A \gtrsim 130$ and even more for $A \gtrsim 140$) are less significant with respect to the unequal mass cases, while around the first peak the $q = 1$ pattern is the largest and the closest one to the Solar abundances. This is consistent with the fact that, despite having a small total mass, the bulk of the ejecta Y_e distribution for the equal-mass case lies within the interval $0.20 - 0.40$ (see Fig. 4.7).

The right panel of Fig. 4.10 shows, instead, the comparison between simulations characterized by the same mass ratio, namely $q = 1.33$, but different EOSs. Since the mass ratio differs significantly from 1, the nucleosynthesis outcome is in all cases similar to what described for unequal-mass merger simulations in the comparison between the DD2 simulations. All the curves are quite close to each other except around the first peak, where the spread between the various distributions becomes more evident and sensitive to the nuclear EOS, with the largest (smallest) relative values for the abundances obtained for the BLh (SLy4) EOS. Usually (and especially for equal or nearly equal mergers that do not promptly collapse to a BH), the synthesis of light r-process elements within BNS ejecta should be favored by soft EOSs, since the higher temperatures achieved in the shock-heated ejecta component leptonise matter in a more efficient way. However, we notice that for $A \lesssim 120$ the relative production of light r-process elements does not follow exactly this trend. This is because, for such asymmetric binaries promptly collapsing to BHs, the dynamical ejection of matter is usually dominated by the cold, neutron-rich tidal component. However a small, but non-negligible fraction of the dynamical ejecta comes from the contact surface of the colliding NSs and is characterized by relatively high entropies (see the $X_{\rm s}$ column in Table 4.3). The corresponding larger peak temperatures produce a tail in the Y_e distribution above ≈ 0.22. These ejecta are likely present in all BNS mergers, but their relatively low amount make them more relevant only in the case of mergers characterized by a very small dynamical ejecta mass. Moreover, these ejecta can more likely escape in the case of stiffer EOSs, characterized by larger radii and less deep gravitational well. We conclude that the nucleosynthesis patterns show a mild variability, depending on the mass ratios and EOSs. However, they are comparable with the ones obtained by BNS merger simulations of lighter binary systems and do not show peculiar behaviors [see e.g. Wanajo et al., 2014, Just et al., 2015, Radice et al., 2018b, Bovard et al., 2017, Nedora et al., 2021a]. Nevertheless, we point out that the nucleosynthesis yields obtained exhibit different features with respect to the Solar residuals, for example in the position and shape of the second and third r-process peaks. The fine structure of the abundance pattern in this region is indeed affected by the particular choice of the nuclear input data made for the nucleosynthesis calculations, like for example the nuclear mass model, the different fission channels considered (spontaneous, neutron-induced, β-delayed etc.) or the fission fragment distribution employed [see e.g. Eichler et al., 2015, de Jesús Mendoza-Temis et al., 2015, Goriely, 2015]. However, since we do not expect dynamical ejecta from high-mass BNS mergers to represent the dominant contribution to the r-process enrichment in the Universe, possible discrepancies with the solar pattern are not an issue. In addition, one should also remember that, even for high mass BNS mergers, the nucleosynthesis from the disk ejecta is expected to dominate the dynamical ejecta one.

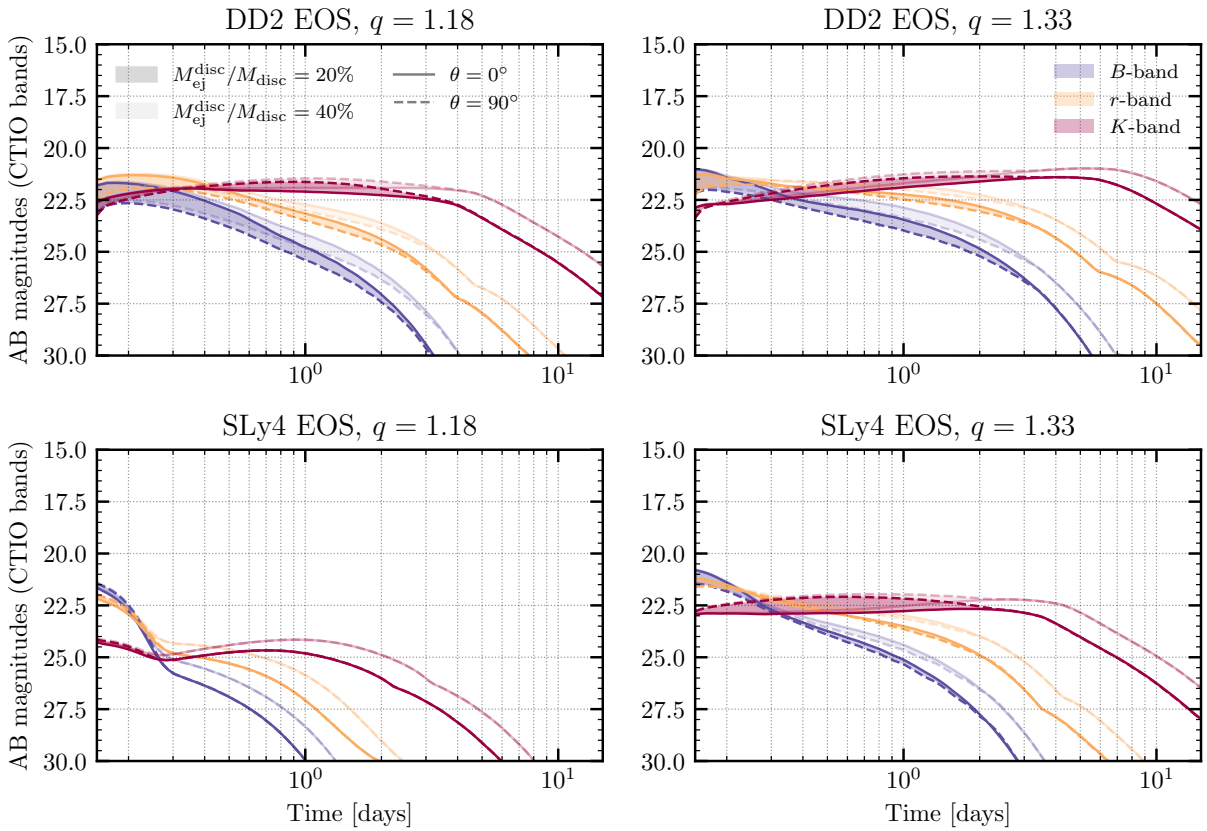

Figure 4.11: AB magnitudes in the blue, red and IR bands of CTIO telescope as a function of time. We report the results for the DD2 and SLy4 EOSs and for a binary mass ratio of $q = 1.18$ and $q = 1.33$ at standard resolution. The uncertainty in the source inclination angle (varying between $0° - 90°$) is represented using solid lines for $\theta = 0°$ and dotted lines for $\theta = 90°$, with intermediate values enclosed by the above lines. The source distance is set to 130 Mpc.In each panel, the darker and lighter areas refer to two different scenarios in which 20% and 40% of the disk mass is expelled, respectively. Taken from Camilletti et al. [2022]

4.3.2 Kilonovae

Using the model described in Sec. 3.5, we compute synthetic kilonova light curves for each of the SR models presented in this work for which the mass of the dynamical ejecta is larger than 10^{-5} $M_\odot$. In Fig. 4.11, we present the evolution of the AB magnitudes in three representative bands (B-, r-, and K-band), for two EOSs (the stiff DD2 and the soft SLy4) and two mass ratios ($q = 1.18$ and $q = 1.33$). In general, kilonova magnitudes depend both on the distance and on the viewing angle. Regarding the former, the wide range of distances compatible with GW190425 ($D = 70 - 250$ Mpc) implies a possible uncertainty of ~ 3 magnitudes, with lower magnitudes corresponding to shorter distances. On the other hand, the inclination angle is almost unconstrained by the GW190425 signal. Due to the degeneracy between

viewing angle and distance, viewing angles close to the polar axis ($\theta_{\rm view} \sim 0°$) are more compatible with larger distances, while shorter distances would imply edge-on configurations ($\theta_{\rm view} \sim 90°$). In Fig. 4.11, we set $D = 130$ Mpc while we explore all possible viewing angles, $\theta_{\rm view} \in [0°, 90°]$. The amount of ejecta and their composition are the most relevant parameters in shaping kilonova light curves. In general, since GW190425-like events are expected to eject a relatively small amount of mass, the resulting kilonovae are predicted to be relatively dim and fast-evolving, compared for example with GW170817-like events. More specifically, in Fig. 4.11 we observe that the kilonova associated to the simulation employing the DD2 EOS and with $q = 1.33$ is brighter and lasts longer with respect to both the simulation employing the same EOS but with $q = 1.18$, and the simulation with the same mass ratio but employing the SLy4 EOS, for all bands. This mostly reflects the difference in the amount of ejecta between the different models, see Sec. 4.2.3 and Sec. 4.2.4, with greater mass ejection resulting in brighter peak luminosities due to the stronger availability of nuclear fuel required for the kilonova emission.

Differences in the viewing angle affect the light curves at times shorter than a couple of days, while our results are insensitive to the specific viewing angle at later times. This can be explained by considering that the slower and significantly more massive disk wind component, eventually powering the kilonova at late times ($t \gtrsim 1$ day), is assumed to be isotropic in our model. Conversely, within the first days after merger, the dynamical ejecta component plays a relevant role. The angular distribution of its mass and composition are thus reflected in the band magnitude evolution. In particular, we obtain brighter light curves in the visual bands at angles closer to the pole ($\theta \sim 0°$), where matter with a higher initial Y_e (and thus lower opacity) can be found. Conversely, the emission in the IR band is typically brighter close to the equatorial plane ($\theta \sim 90°$), where the most neutron-rich (and thus more opaque) matter is concentrated, with respect to higher latitudes. Since for each of our SR models the disk wind ejecta component is determinant in generating the kilonova emission, we test our results sensitivity with respect to its mass. In particular, we notice that the increase in the fraction of ejected disk mass from a plausible 20% to an optimistic 40% results in an overall gain in brightness of ~ 1 magnitude for all bands at late times, when the disk ejecta component becomes dominant. We also test the sensitivity of light curves on the disk ejecta mass and composition angular distributions. We consider a density distribution $\rho_{\rm wind}(\theta) \propto \sin\theta$ as alternative to the isotropic case and an opacity distribution shaped as a step function with $k = 1$ cm^2 g^{-1} for $\theta < 45°$ and $k = 10$ cm^2 g^{-1} for $\theta > 45°$. While such modifications on the opacity can vary the final bolometric light curves up to a factor of a few, the different mass distribution results in a model dependence on the viewing angle also at late times. More specifically, since the wind density gradually increases towards the equator, the magnitudes decrease accordingly for all bands, and we obtain the brightest

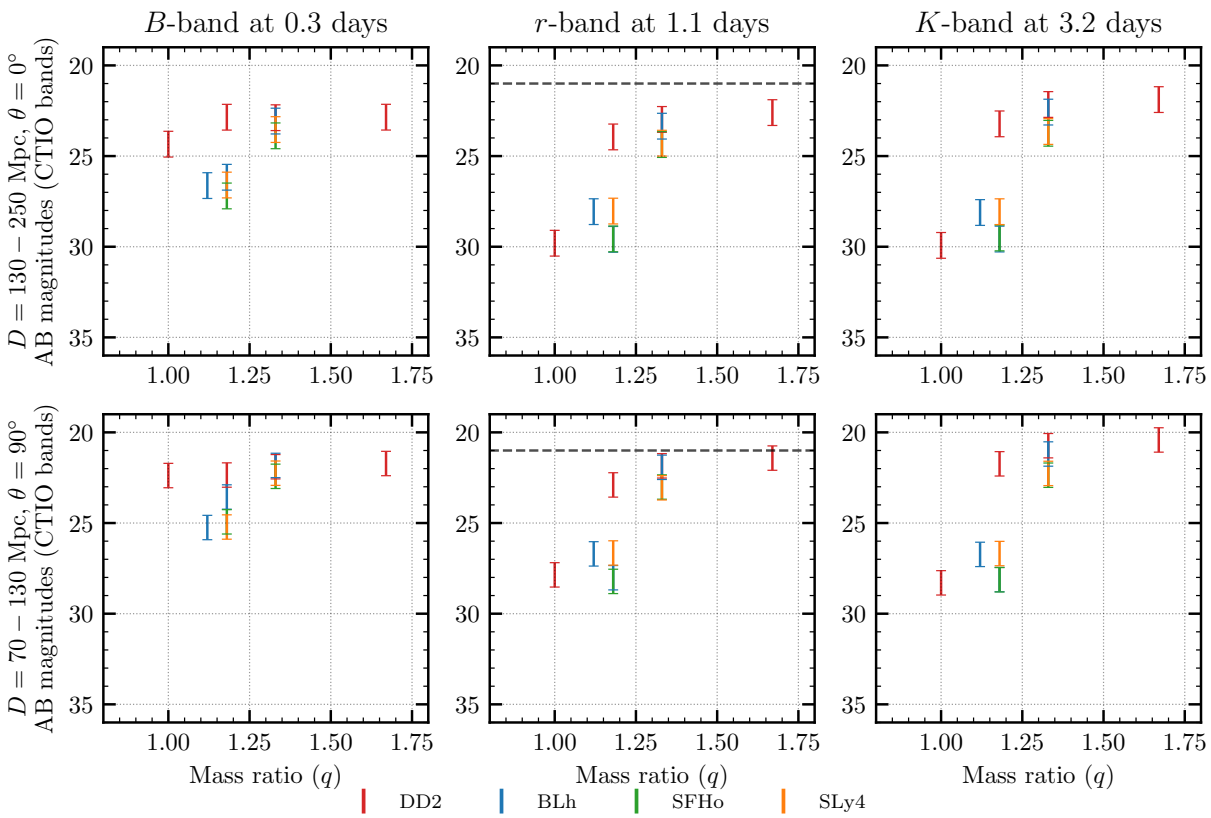

Figure 4.12: AB magnitudes in the blue, red and IR bands of CTIO telescope at fixed characteristic times as a function of the binary mass ratio q. The kilonova is obtained assuming an ejection of 20% of the disk mass. Results are colour-coded to indicate different EOSs. Only standard resolution simulations are shown. Two cases for the source distance and inclination angle are reported, with the error bars representing the uncertainty in the source distance. The dashed horizontal line represents the upper limit for GW190425 obtained with the ZTF by the GROWTH collaboration for the r and g-band [Coughlin et al., 2019]. Taken from Camilletti et al. [2022]

emission for $\theta_{\rm view} \sim 90°$, ~ 1 magnitude below the polar one. Despite the non-negligible dependences, these tests place our uncertainty in the luminosity due to the disk parameters well below the one due to the source distance and viewing angle.

For simulations with $q = 1.33$, providing a prominent tidal low-Y_e ejecta component, the infrared K-band lasts several days and nearly always dominates over bluer bands, due to the prevailing presence of lanthanides-rich material synthesized through a strong r-process both in the dynamical and in the disk wind ejecta. On the other hand, in the case of the simulation with $q = 1.18$ and the SLy4 EOS, the considerably lower ejecta mass with a broader Y_e distribution results in lower material opacities and slightly brighter blue band light curves at early times.

Due to the evolution of the photospheric temperature, the B-band magnitude is the first to peak, within the very first few hours, promptly followed by the r-band magnitude,

dominating within the first half-day after merger, while the infrared band peaks much later in time, possibly on a time-scale of days. While the precise peak times and magnitudes vary depending on the specific simulation, the presence of common trends in the light curve behavior allow us to identify characteristic time-scales for each band in which the latter typically dominates over or is comparable to the others. In Fig. 4.12, we present the values of the AB magnitudes in the same three bands as in Fig. 4.11 at three corresponding characteristic times for each available simulation, namely at 0.3 days, 1.1 days and 3.2 days for the B, r and K band, respectively. Since we want now to address the possible detectability of GW190425, two possible ranges for the source distance and inclination angle are considered in order to account for the large degeneracy in the estimation of these parameters for GW190425 [see also Dudi et al., 2021, for a similar choice]. Regardless of the specific band, magnitudes tend to decrease with the increase of the mass ratio, leading to emissions up to ~ 8 magnitudes brighter, moving from equal-mass to strongly asymmetric mergers. Likewise, the stiffest EOS corresponds to luminosities which can be as bright as ~ 6 magnitudes below the same results obtained using softer EOSs. Exceptions to these trends can be directly traced back to already emerged distinctive mass ejections. For example, the simulation employing the BLh EOS and a mass ratio of $q = 1.12$ returns brighter red and infrared luminosities with respect to the simulation employing the same EOS but with $q = 1.18$: this is due to the fact that in the first instance the computed disk mass is greater, leading to a more massive disk wind (which dominates over the dynamical component). Based on our analysis, from Fig. 4.12 it is clear that almost none of our models can be fully ruled out by the ZTF upper limits to the kilonova of GW190425 (shown as a dashed horizontal line), meaning that current data cannot help further constraining the model parameters. This leaves open the question as to whether the detection of events like GW190425 can shed light on the source properties, and hints to the necessity of determining the sky localization with high accuracy for these events, to employ deeper observations in order to resolve such EM counterparts.

4.4 Comparison with previous simulations and analyses of GW190425

In this section, we compare the results of our work with recent publications about the modeling of GW190425 and of its EM counterparts, in particular with results reported in Dudi et al. [2021], Raaijmakers et al. [2021], Barbieri et al. [2021].

During the preparation of this work, Dudi *et. al.* published an independent study on GW190425 in NR. They used the `BAM` code, a NR code which was shown to produce results consistent with `WhiskyTHC` [see e.g. Dietrich et al., 2018]. They considered four

mass ratios, ranging from 1 to 1.43, and for each of them they employed three cold, beta-equilibrated EOSs: the piecewise-polytropic EOS MPA1 [Read et al., 2009], a piecewise-polytropic representation of the tabulated DD2 EOS at the lowest available temperature, and the softer APR4 EOS [Akmal et al., 1998]. Each model was run at three different resolutions, with our SR being intermediate between their worst and middle resolution. Similarly to what we found in our simulations, all the BNS models presented by Dudi *et. al.* result in a prompt collapse. Regarding the properties of the remnant, the two works predict a comparable range for $M_{\rm BH}/M$, while we notice that the dimensionless spin parameter obtained by Dudi *et. al.* is systematically lower than the one obtained by our simulations by several percents, corresponding to $\Delta a_{\rm BH} \sim 0.05$, when comparing simulations characterized by similar mass ratios and EOSs. Both analyses agree in predicting more massive disks when considering more asymmetric binaries and stiffer EOSs. In particular, the disk results for the DD2 EOS share the same trend with respect to q, both on a qualitative and quantitative level. Moving to the comparison of the dynamical ejecta, we first notice that the amount of matter obtained for the MPA1 and APR4 EOSs by Dudi *et. al.* increases as the binary becomes more asymmetric, similarly to what observed in our BLh, SFHo and SLy4 simulations. Similarly, the amount of ejecta from the DD2 simulations first increases then decreases with q in both analyses. However, while in the former cases the amount of ejecta are comparable among them, the values obtained for the DD2 EOS differ significantly, with the ejecta reported in Dudi *et. al.* larger by $\sim$ one order of magnitude. According to the reported values, uncertainties due to different resolutions seem to account only for a fraction of this discrepancy and higher resolution seems to result in smaller ejecta masses. A potentially relevant source of discrepancy could be the different microphysical input. In addition to a more accurate temperature treatment, the presence of neutrino radiation can influence the dynamical ejecta, since simulations accounting for neutrino emission show systematically smaller dynamical ejecta masses [see e.g. Nedora et al., 2022], due to the emission of neutrinos occurring during the ejection process.

The different amount of ejecta obtained employing the DD2 EOS is directly reflected in the kilonova light curves, where for a similar mass ratio the r-band magnitudes reported in Dudi *et. al.* are systematically brighter. In particular, while for edge-on views the results are in good agreement, for a viewing angle close to the polar axis we find up to ~ 5 magnitudes of difference between light curves corresponding to the same binary configurations. On the one hand, this may reflect the substantially different mass and composition distributions resulting from the NR models. On the other hand, we also stress that the models employed for the light curves computation are significantly different: as opposed to our semi-analytic model described in Sec. 3.5, Dudi *et. al.* employ a more advanced wavelength-dependent radiative transfer approach [Kawaguchi et al., 2020], for which the post-merger ejecta composition

is fixed for all components. Additionally, our kilonova model decomposes the solid angle in radial slices. While this approach is reasonable for ejecta expelled over the entire solid angle, it could be inadequate for ejecta expelled only close to the equator for which it tends to underestimate magnitudes up to a few since it neglects possible lateral effects [Kawaguchi et al., 2016, 2018, Barbieri et al., 2019, Bernuzzi et al., 2020]. Keeping in mind the above differences for the GW190425 event and working under the assumption that the location of the source was covered by ZTF, Dudi *et. al.* disfavored a higher number of models with respect to this work, i.e., the ones employing DD2 or MPA1 EOSs with a high mass ratio and a source configuration similar to that used in the top panels of Fig. 4.12. On the contrary, our results imply that only the model employing the DD2 EOS with the highest mass ratio and a source distance close to $D \sim 70$ Mpc (corresponding to a edge-on view) would be disfavored (as visible in the bottom panels of Fig. 4.12).

Raaijmakers et al. [2021] studied the expected photometric light curves of BNS mergers with masses in the range compatible with the posteriors of GW190425. We recall that, due to the spherical symmetry of the employed kilonova model, it was not possible to investigate the light curve dependence on the viewing angle, even if selected tests with the multidimensional `POSSIS` code were performed [Bulla, 2019]. By fixing the source distance to 130 Mpc, we find that the spread in the magnitudes generated by the different NR models considered in this work is comparable to the comprehensive results displayed in Raaijmakers et al. [2021], which span ~ 4 magnitudes at times shorter than ~ 1 day. In the same time period, our light curves are generally dimmer with respect to those computed in Raaijmakers et al. [2021], with an average difference of ~ 3 magnitudes. A plausible source of this systematic discrepancy lies in the different ways in which the ejecta and disk masses were computed. In our case, they are the outcome of BNS merger simulations, while in Raaijmakers et al. [2021] they are estimated on the basis of the fitting formulae for the mass of the dynamical ejecta and of the disk proposed in Krüger and Foucart [2020, equations 4 and 6], and for the average dynamical ejecta speed proposed in Foucart et al. [2017]. These formulae take as input parameters the compactness and the masses of the binary components.

We test the fitting formulae for the ejecta and disk properties used in Raaijmakers et al. [2021] and Barbieri et al. [2021] in the parameter range of GW190425 to predict the associated kilonova light curves. Some of these formulae were originally proposed in Foucart et al. [2017], Krüger and Foucart [2020], Radice et al. [2018b] (see also Dietrich and Ujevic [2017]). Additionally, we include in the comparison fitting formulae from Nedora et al. [2022] in the form of their equation 6, i.e., a second-order polynomial in the mass ratio and tidal deformability. In particular, we use coefficients fitted on the dataset `RefM0Set & M0/M1Set`, i.e., on a set of simulations including neutrino emission and absorption, and microphysical EOSs. We stress that we examine the different formulae in an unexplored parameter region

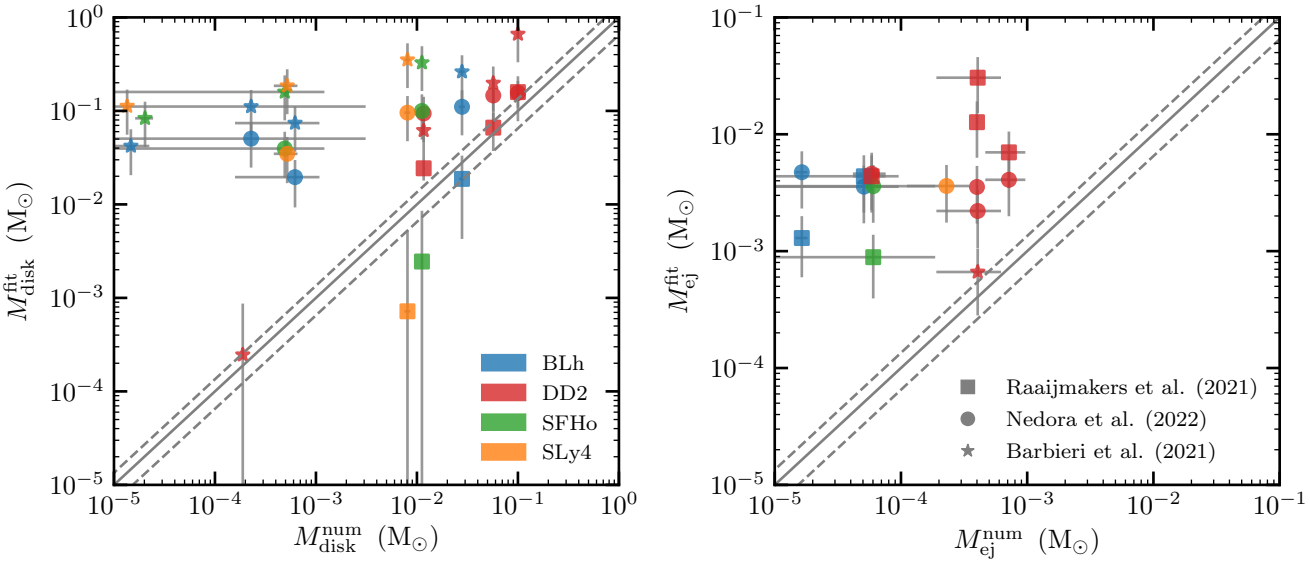

Figure 4.13: Left: Comparison of the disk masses obtained from our numerical simulations and from the fitting formulae used in Raaijmakers et al. [2021] (originally, from Krüger and Foucart [2020]) and in Barbieri et al. [2021]. Right: Comparison of the dynamical ejecta masses obtained from our numerical simulations and from the fitting formulae used in Raaijmakers et al. [2021] (originally, from Krüger and Foucart [2020]) and in Barbieri et al. [2021] (originally from Radice et al. [2018b]). Fitting formulae from Nedora et al. [2022] are also reported. The error bars on the vertical (horizontal) axis are estimated as the 50 per cent of the predicted value (absolute difference between the SR and LR values). For the BNS in our sample with $M_{\rm disk}^{\rm num} \lesssim 10^{-3}$ $M_\odot$ ($M_{\rm disk}^{\rm num} \lesssim 10^{-4}$ $M_\odot$), the formulae from Krüger and Foucart [2020] [Nedora et al., 2022] result in nonphysical values for the disk mass. Adapted from Camilletti et al. [2022]

since the binary systems within the calibration dataset are overall lighter and involve more deformable objects than those in our simulations.

In Fig. 4.13, we compare the disk (left) and ejecta (right) masses predicted by the various fitting formulae with the ones obtained by our simulations. The uncertainties in the fitted values are 50 per cent of the estimated value, summed to a floor value of 5×10^{-4} $M_\odot$ for the disk mass and 5×10^{-5} $M_\odot$ for the ejecta mass. The bisector is the "agreement line", while the dashed lines represent the 35 per cent deviation from the exact prediction. For the mass of the dynamical ejecta only simulations with $M_{\rm ej} > 10^{-5}$ $M_\odot$ have been taken into account.

In most of the cases, the fitting formulae significantly overestimate both the mass of the disk and the mass of the dynamical ejecta, and sometimes even predict opposite trends with respect to the binary parameters. Only in the case of the disk masses predicted by Krüger and Foucart [2020] [used in Raaijmakers et al., 2021] and of the ejecta masses by Radice et al. [2018b] [used in Barbieri et al., 2021] there is a partial agreement, at least within the estimated uncertainties. The estimates of Nedora et al. [2022] is rather insensitive to the

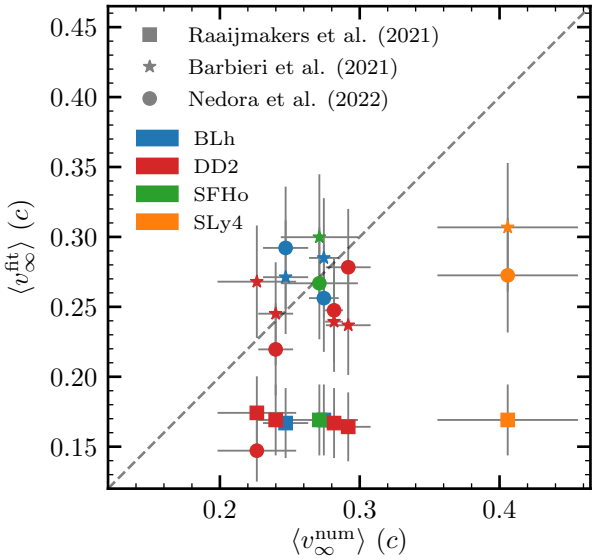

Figure 4.14: Comparison of the mass-weighted average velocity of the dynamical ejecta as obtained in our simulations and from the fitting formulae employed in the kilonova calculations of Raaijmakers et al. [2021] and Barbieri et al. [2021], taken from Foucart et al. [2017] and Radice et al. [2018b], respectively. Results from the fitting formulae from Nedora et al. [2022] are also reported. The (symmetric) uncertainties on the vertical axis are conservatively estimated as the 30 per cent of the values obtained from the fitting formulae. Error bars on the horizontal axis are estimated as the difference between the values inferred from the SR and LR simulations. Taken from Camilletti et al. [2022]

detailed binary parameters, giving rather similar ejecta mass and disk mass for each binary configuration.

Another physical input needed in kilonova light curves calculations is the velocity at which ejected matter is expelled from the binary system. In Fig. 4.14, we show the mass-weighted average asymptotic velocity of the dynamical ejecta obtained from our numerical simulations and from the fitting formulae presented in Radice et al. [2018b], Foucart et al. [2017], Nedora et al. [2022]. Only simulations with $M_{\rm ej} > 10^{-5}$ M$_\odot$ have been taken into account. We assume a conservative uncertainty of the 30 per cent on the values obtained from the fitting formulae. We observe that the formulae from Radice et al. [2018b] and Nedora et al. [2022] work reasonably well for outflow speed with $\langle v_\infty^{\rm num} \rangle$ in the range $0.24-0.30\,c$, while they underestimate the average velocity in the simulation with the fastest ejecta. The fitting formula from Foucart et al. [2017] used in Raaijmakers et al. [2021] to make predictions on the kilonova from the GW190425 event, but originally tailored for the dynamical ejecta of BHNS systems, predicts a very similar average velocity for all the binaries, that is systematically smaller than the outcome of the simulations. This is because the expression assumes that the average velocity of the ejecta is given by a constant value of ~ 0.15 plus a linear correction in the mass ratio, which is tiny in the case of BNS systems ($q \sim 1-2$).

In general, we find differences in the ejected mass and in the expansion speed, and less severe disagreement for the disk mass, which is consistent with the numerical data when errors are taken in consideration. In particular, the mass of the ejecta predicted by the fitting formulae is $\sim 10 - 100$ higher than in our simulations. Our comparison reveals how NR fitting formulae can become inaccurate when used far from their calibration regime.

Finally, we compare the light curves computed in this work with those obtained in Barbieri et al. [2021] for BNS systems, and, as in the case of Raaijmakers et al. [2021], we find typically lower peak luminosities. Since also Barbieri et al. [2021] used fitting formulae to predict the ejecta properties, we argue that disk and ejecta masses larger by one or even two orders of magnitudes can account for the observed differences. In addition, our results employing the DD2 EOS are significantly more sensitive to the binary configuration, as peak luminosities in the r-band and at IR frequencies vary by $\lesssim 7$ magnitudes for a mass ratio varying between $1 \leq q \lesssim 1.7$, while in Barbieri et al. [2021] the same bands exhibit a variation of ~ 3.5 magnitudes for a mass ratio between $1 \lesssim q \lesssim 2$. Also in this case, at least a part of these differences is possibly due to disk later irradiation, which is expected to occur in very asymmetric system, which was taken into account by Barbieri et al. [2021].

Both in Raaijmakers et al. [2021] and Barbieri et al. [2021], the overall brighter kilonovae allow the identification of some binary configurations potentially detectable by the ZTF within the first few days from merger, in addition to a major portion of the BHNS configurations considered in those works. In particular, in Barbieri et al. [2021] several configurations employing the DD2 EOS and the APR4 EOS can be ruled out by the GW190425 EM follow-up. Conversely, here almost all the our BNS simulations employing the DD2 EOS and the totality of those employing softer EOSs produce kilonovae which are not detectable by ZTF in a GW190425-like event at a comparable distance.

Chapter 5

Accretion disks in binary neutron star mergers

The results, tables and figures presented in this chapter are taken from Camilletti et al. [2024].

Accretion disks formed in BNS mergers are the engine responsible for many relevant processes related to compact binary mergers and to multimessenger astrophysics. It is commonly retained that, in the BH-engine scenario, gamma-ray bursts are triggered by the rapid accretion of a magnetized disk into the BH, see e.g. [Blandford and Znajek, 1977, Blandford and Payne, 1982, Lee et al., 2000, Beloborodov, 2008, Berger, 2014]. Moreover, a relevant portion of the accretion disk, up to $30 - 50\%$ of the initial torus mass [Fahlman and Fernández, 2022], is instead ejected by multiple mechanisms: redistribution of the angular momentum, thermal effects [Metzger et al., 2010], neutrino-driven winds [Perego et al., 2014], magnetic stresses [De Villiers et al., 2005]. This ejected matter is responsible for the nucleosynthesis of heavy elements by means of the so-called rapid neutron capture process (see [Cowan et al., 2021, Perego et al., 2021] and references therein). The radioactive decay of the freshly synthesized, unstable isotopes powers the kilonova transient [Li and Paczynski, 1998]. Therefore, the dynamic and thermodynamic properties of the matter inside the disk, together with the mechanisms accountable for the matter accretion and ejection, influence the final abundances of the expelled elements as well as the production of the electromagnetic counterparts associated to BNS mergers.

Due to their complexity and high computational costs, only a few previous works have so far simulated BNS mergers long enough to account for the evolution of the accretion disks on timescales comparable with the viscous timescale in a fully consistent way [Fujibayashi et al., 2020, Shibata et al., 2021, Radice and Bernuzzi, 2023, Kiuchi et al., 2022]. In many more cases, numerical simulations focusing on the evolution of the accretion disks around a BH or

a massive NS were used to investigate the effects of different mechanisms and the resulting properties of the ejected matter in such a complex scenario [Hawley, 2000, Fernández and Metzger, 2013, Just et al., 2015, Fernández et al., 2015, Metzger and Fernández, 2014, Siegel and Metzger, 2018, Fernández et al., 2019, Miller et al., 2019a, De and Siegel, 2021, Just et al., 2021, Fahlman and Fernández, 2022, Sprouse et al., 2023]. In these cases, the disks were initialized according to analytical prescriptions that were meant to provide a meaningful description of the disks produced in BNS mergers, but that did not directly emerged from merger simulations. However, the dynamic and thermodynamic properties of the matter inside these disk lack of an unique analytical description. As a consequence, the initial conditions in numerical simulations of accretion disks have some degree of arbitrariness. For example, in several cases the disks were initialized using a constant entropy and electron fraction profiles, whose specific values were considered as free parameters, together with the total mass of the disk.

Despite their relevance, a systematic and comprehensive characterization of the properties of accretion disks emerging from BNS mergers is still missing. While the properties of the accretion disks resulting from BH-NS mergers were investigated in Most et al. [2021b], analysis of the properties of disks emerging from BNS merger simulations were so far carried out for limited sets of merger simulations Nedora et al. [2021a], Combi and Siegel [2023a], Zenati et al. [2024]. In this work, we analyze in detail the geometrical, dynamical and thermodynamic properties of accretion disks from 38 BNS merger simulations, with the double objective of furnishing a comprehensive characterization of their properties and reliable initial conditions for disk simulations. In the case of a massive NS remnant, the latter and the disk form a continuous structure. However, we separate them by defining a threshold density. In the case of a BNS merger collapsing to a BH, we consider the disk as the gravitationally bound matter outside the BH apparent horizon. It is important to stress that the disk is an evolving system, so its properties depends also on the time at which they are analyzed. In this work, we focus on timescales larger than the formation timescale (a few milliseconds post-merger), but shorter than the secular evolution timescale ($\sim$ 100ms). We observe that some of the prescriptions commonly used to initialize disk simulations do not provide an accurate description of the disk properties as emerging from BNS mergers. In particular, we find that the disks are usually thick, with an aspect ratio decreasing with the mass ratio of the binary, and with the exception of disks from prompt-collapsed BNS mergers, which have a smaller aspect ratio. Despite the disk sample spans a broad range in mass and angular momentum, their ratio is independent on the EOS and on the mass ratio of the binary. This can be traced back to the rotational profile of the disks, characterized by a constant specific angular momentum. We provide fits for the radial and vertical distribution of the rest mass density and of the entropy per baryon and electron fraction distributions with the density.

Our observations might not only be interesting in their own right, but provide a useful and practical way to prescribe initial data for accretion disk simulations with a higher degree of realism.

The chapter is structured as follows. In Sec. 5.1 the simulation sample is described and the analysis procedure used to define the disk and its properties is illustrated in Sec. 5.2. The geometrical structure of the disks, i.e. the radial and vertical extensions, the aspect ratio and the half opening angle, are discussed in Sec. 5.3.1. The mass and angular momentum of the disks, as well as their specific angular momentum and accretion/ejection rates, are the arguments of Sec. 5.3.2. Finally, we investigates the thermodynamic properties, i.e. the electron fraction and the entropy per baryon in Sec. 5.3.3. We compare our results with previous numerical simulations of accretion disk in Sec. 5.4. In this section we also test the rotational model presented in Galeazzi et al. [2012]. The last Sec. 7.2 conclude the work summarizing the main results.

I specifically acknowledge Albino Perego for his work in Sec. 5.4.5 on the comparison with core-collapse simulations and for his significant contribution to Sec. 5.3.3.

5.1 Simulation sample

All the BNS simulations used in this work share the same numerical setup and microphysics treatment, making their outcome comparable. In particular, we use a subset of the simulations described in Perego et al. [2019], Endrizzi et al. [2020], Nedora et al. [2019], Bernuzzi et al. [2020], Nedora et al. [2021a], Cusinato et al. [2021], Perego et al. [2022a], Camilletti et al. [2022], part of the CoRe collaboration database Dietrich et al. [2018], Gonzalez et al. [2023]. The interested reader can find a detailed description of the employed codes in the aforementioned works.

A total of 12 simulations employed the general-relativistic large eddy simulations method (GRLES) for turbulent viscosity to mimic the effects of large-scale magnetic fields Radice [2017]. Since we observed no significant differences between disks from simulations with or without GRLES, we refrain from discussing these twelve cases separately.

We classify our simulations in three categories: long-lived, where the remnant does not collapse up to the end of the simulation; short-lived, where the remnant collapses within the end of the simulation; prompt-collapse, where the remnant collapse to a BH immediately after merger. We identify a prompt collapse when the minimum of the lapse function decreases monotonically after merger without any core bounce.

The time indicated as the end of simulation, $t_{\rm end}$, corresponds to the last iteration at which we can retrieve all the data needed for this study (see Sec. 5.2). Note that we always express the time with respect to merger. Among the simulations presented in the previous

works, we select the ones that last at least 10 ms post-merger for BNS merger with long-lived and short-lived remnant and at least 5 ms post-merger for simulations resulting in a prompt-collapse of the remnant. With respect to the time of merger, the shorter long-lived simulation in the sample lasts 10 ms, while the longer lasts 103 ms. Short-lived simulations last between 16 ms and 36 ms. In the prompt-collapse category, the simulations are as short as 5 ms and as long as 25 ms. Note that long-lived simulations are not necessary the longer in our sample and we cannot exclude that a prolonged evolution would not end up in a BH formation. Nevertheless, since the evolution of the system in the post-merger changes dramatically when the remnant includes a NS, this classification enable us to stress some important differences as well as genuine similarities between the categories.

The final sample consists of 20 long-lived, 9 short-lived and 9 prompt-collapsing BNS mergers for a total of 38 simulations, varying in numerical resolution, EOS, chirp mass $M_{\rm chirp}$, mass ratio q and total gravitational mass $M_{\rm tot}$. The mass ratio of the binaries in the sample spans the range $q \in [1, 1.67]$ and their total mass is within 2.6 and 3.3 $\mathrm{M}_\odot$. Most of the simulations in our sample are targeted to the BNS merger GW170817, with a chirp mass $M_{\rm chirp} = 1.18$ $\mathrm{M}_\odot$ [Abbott et al., 2017b]. A set of 6 simulations are targeted to the BNS merger GW190425 with $M_{\rm chirp} = 1.44$ $\mathrm{M}_\odot$ [Abbott et al., 2020].

Table 5.1 lists the main properties of the simulated binaries categorized according to the fate of remnant.

5.2 Data analysis procedure

To exploit the intrinsic symmetries of the system, we adopt cylindrical coordinates with the axial direction aligned to the rotational axis of the binary. The radial and axial extensions of the cylinder are ≈ 1181 km, characterized by a constant spacing of ≈ 148 m up to a distance of 295 km and a logarithmic spacing for the successive 200 grid points along both coordinates. The azimuthal angle ϕ is divided in 62 sections of $\approx 5.71°$. The cylindrical coordinates r, z and ϕ refer to the cell centers of the resulting grid. The hydrodynamic variables are linearly interpolated from the seven Cartesian refinement levels into the cylindrical grid, using values in the most refined level available around each cell center of the cylindrical grid.

In many occasions, we perform a non-linear least-square fit between two hydrodynamic variables x and y. For example, in Sec. 5.3.3 we fit the distribution of the entropy and of the electron fraction with respect to the rest mass density. If $\{\mu\}$ is a set of parameters of the fitting relation $y(x, \{\mu\})$, the determination of $\{\mu\}$ is performed by minimizing the residuals weighted by the mass fraction, i.e. $m_f|y - y(x, \{\mu\})|$, where $m_f = dm/\sum dm$ is the mass fraction and $dm = \rho r \Delta r \Delta z \Delta \phi$ is the baryon rest mass in each grid cell. In most cases we found similarities between the fit performed on simulations belonging to the same category,

Table 5.1: Simulation sample and the main properties of the disk computed at the end of the simulation. From left to the right: category according to the fate of remnant (see Sec. 5.2), EOS, total initial gravitational mass of the isolated neutron stars $M_{\rm tot}$, mass ratio q, inclusion of turbulent viscosity, resolution of the finest grid, time of BH formation, end time of the simulation at which the disk properties are extracted, disk mass $M_{\rm disk}^{\rm end}$, angular momentum $J_{\rm disk}^{\rm end}$, specific angular momentum $j_{\rm spec}^{\rm end}$, mass-fraction averaged entropy $\langle s^{\rm end}\rangle$ and electron fraction $\langle Y_{\rm e}^{\rm end}\rangle$. The times are given from the time of merger. The end time $t_{\rm end}$ indicates the time at which the last disk can be extracted. The rightmost column collects the references to the original works where the simulations have been presented. Taken from Camilletti et al. [2024]

Category	EOS	$M_{\rm tot}$ $M_\odot$	q	GRLES	res	$t_{\rm BH}$ ms	$t_{\rm end}$ ms	$H_{\rm max}$ km	aspect ratio	opening angle	$M_{\rm disk}^{\rm end}$ $M_\odot$	$J_{\rm disk}^{\rm end}$ $M_\odot{}^2$	$\langle j_{\rm spec}^{\rm end}\rangle$ $\times 10^{16}$ cm^2 s^{-1}	$\langle s^{\rm end}\rangle$ $k_{\rm B}$ baryon^{-1}	$\langle Y_{\rm e}^{\rm end}\rangle$	ref
long lived	BLh	2.728	1	✓	SR	✗	91	95	0.64	51°	0.1328	1.0831	3.70	7.09	0.12	Bernuzzi et al. [2020]
long lived	BLh	2.728	1	✓	HR	✗	23	74	0.65	49°	0.2081	1.5398	3.33	7.26	0.15	Nedora et al. [2021a]
long lived	BLh	2.728	1	✗	HR	✗	52	171	0.70	55°	0.1139	0.8875	3.53	8.11	0.16	Perego et al. [2022b]
long lived	BLh	2.730	1	✗	LR	✗	21	82	0.63	51°	0.1253	0.9321	3.37	8.11	0.18	Nedora et al. [2021a]
long lived	BLh	2.730	1	✗	SR	✗	103	113	0.67	53°	0.0955	0.7402	3.51	6.13	0.09	Nedora et al. [2021a]
long lived	BLh	2.765	1.34	✗	LR	✗	41	134	0.62	52°	0.2268	1.8612	3.74	7.80	0.16	Nedora et al. [2021a]
long lived	BLh	2.765	1.34	✗	SR	✗	44	113	0.57	51°	0.1664	1.3716	3.77	7.39	0.14	Nedora et al. [2021a]
long lived	BLh	2.765	1.34	✗	HR	✗	12	56	0.48	42°	0.2024	1.5797	3.57	7.17	0.14	this work
long lived	BLh	2.803	1.54	✗	LR	✗	40	74	0.54	45°	0.2594	2.2244	3.92	6.98	0.13	Nedora et al. [2021a]
long lived	BLh	2.803	1.54	✗	HR	✗	10	63	0.43	44°	0.2454	2.0294	3.80	6.29	0.11	Nedora et al. [2021a]
long lived	BLh	2.837	1.66	✓	LR	✗	64	91	0.52	45°	0.2439	2.2047	4.18	6.77	0.11	Bernuzzi et al. [2020]
long lived	BLh	2.837	1.66	✓	SR	✗	19	78	0.43	43°	0.2650	2.2929	3.99	6.86	0.12	Bernuzzi et al. [2020]
long lived	BLh	2.837	1.66	✓	HR	✗	15	65	0.40	43°	0.2538	2.1919	3.99	6.25	0.10	Bernuzzi et al. [2020]
long lived	DD2	2.728	1	✗	LR	✗	38	70	0.57	45°	0.2117	1.7140	3.67	6.79	0.13	Nedora et al. [2019]
long lived	DD2	2.728	1	✗	SR	✗	92	96	0.60	48°	0.1811	1.4914	3.73	6.00	0.10	Perego et al. [2019]
long lived	DD2	2.732	1.10	✗	LR	✗	41	49	0.51	45°	0.2349	1.9157	3.68	6.26	0.12	Cusinato et al. [2021]
long lived	DD2	2.733	1.11	✗	LR	✗	26	57	0.55	44°	0.2582	2.0782	3.63	6.72	0.14	Cusinato et al. [2021]
long lived	DD2	2.740	1.19	✗	LR	✗	28	76	0.57	44°	0.2557	2.0764	3.68	7.12	0.14	Cusinato et al. [2021]
long lived	DD2	2.742	1.20	✗	LR	✗	36	69	0.57	44°	0.2530	2.0934	3.74	6.75	0.14	Nedora et al. [2021a]
long lived	DD2	2.880	1.67	✓	SR	✗	30	117	0.50	48°	0.2753	2.5445	4.26	7.24	0.14	this work
short lived	LS220	2.728	1	✓	LR	18	27	111	0.58	49°	0.1605	1.2549	3.48	7.74	0.14	Nedora et al. [2019]
short lived	LS220	2.728	1	✓	SR	13	20	122	0.64	51°	0.0502	0.3901	3.45	8.60	0.19	Nedora et al. [2019]
short lived	LS220	2.728	1	✗	LR	17	32	130	0.68	55°	0.0697	0.5450	3.47	7.68	0.15	Nedora et al. [2019]
short lived	LS220	2.728	1	✗	SR	15	36	97	0.65	52°	0.0631	0.4951	3.49	7.21	0.13	Nedora et al. [2019]
short lived	LS220	2.737	1.16	✓	SR	20	26	151	0.66	55°	0.1238	0.9947	3.57	8.39	0.18	Nedora et al. [2021a]
short lived	LS220	2.781	1.43	✓	LR	15	19	103	0.58	51°	0.1855	1.6314	3.93	7.77	0.15	Nedora et al. [2021a]
short lived	SFHo	2.735	1.13	✗	SR	11	16	185	0.73	54°	0.0775	0.5902	3.38	9.74	0.23	Nedora et al. [2021a]
short lived	SLy4	2.728	1	✗	SR	13	21	264	0.66	56°	0.0417	0.3136	3.34	11.1	0.24	Endrizzi et al. [2020]
short lived	SLy4	2.735	1.13	✗	SR	12	19	229	0.61	55°	0.0687	0.5282	3.42	9.87	0.23	Nedora et al. [2021a]
prompt	BLh	3.307	1.12	✗	LR	0	10	15	0.33	27°	0.0010	0.0081	3.79	6.50	0.06	Camilletti et al. [2022]
prompt	BLh	3.307	1.12	✗	SR	0	12	11	0.26	23°	0.0005	0.0044	3.74	6.65	0.05	Camilletti et al. [2022]
prompt	BLh	3.322	1.18	✗	LR	0	7	5	0.17	15°	0.0030	0.0252	3.77	4.84	0.05	Camilletti et al. [2022]
prompt	LS220	2.837	1.66	✓	LR	1	14	58	0.30	28°	0.1185	1.2242	4.63	4.29	0.05	Bernuzzi et al. [2020]
prompt	LS220	2.837	1.66	✗	LR	1	14	58	0.30	30°	0.1155	1.1760	4.57	4.33	0.05	Bernuzzi et al. [2020]
prompt	SFHo	2.837	1.66	✓	SR	1	25	48	0.36	30°	0.0906	0.8925	4.40	5.72	0.07	Bernuzzi et al. [2020]
prompt	SFHo	3.322	1.18	✗	SR	0	7	13	0.27	20°	0.0005	0.0043	3.87	7.63	0.06	Camilletti et al. [2022]
prompt	SFHo	3.351	1.33	✗	SR	0	5	5	0.19	14°	0.0109	0.0957	3.89	3.61	0.04	Camilletti et al. [2022]
prompt	SLy4	3.322	1.18	✗	SR	0	6	6	0.18	18°	0.0005	0.0041	3.80	7.06	0.09	Camilletti et al. [2022]

i.e. prompt, short or long-lived. We characterize each category $\mathcal{C}$ with a representative set of parameters $\{\langle\mu_{\mathcal{C}}\rangle\}$ by computing a weighted average of the parameters μ_s obtained from the fit on each simulation $\mathcal{S}$ in the category $\mathcal{C}$:

$$\langle\mu_{\mathcal{C}}\rangle = \frac{\sum\limits_{s\in\mathcal{C}} \mu_s w_s}{\sum\limits_{s\in\mathcal{C}} w_s} \ , \tag{5.1}$$

where $w_s = 1/\sigma_s^2$, and $1/\sigma_s^2$ are the 1-σ standard deviations of the fitted parameter (as estimated by the least-squares method). The error $\sigma_{\langle\mu_{\mathcal{C}}\rangle}$ on each averaged parameter $\langle\mu_{\mathcal{C}}\rangle$ is computed as

$$\sigma_{\langle\mu_{\mathcal{C}}\rangle} = \sqrt{\frac{\sum\limits_{s\in\mathcal{C}} w_s(\langle\mu_{\mathcal{C}}\rangle - \mu_s)^2}{\sum\limits_{s\in\mathcal{C}} w_s}} \ . \tag{5.2}$$

If not stated differently, we discuss the disk properties at $t_{\rm end}$ defined in Sec. 5.1. Indeed, we are mostly interested in describing the disks properties once a steady configuration has been reached.

5.3 Results

5.3.1 Geometric properties

Spatial extension.

At the reference time $t_{\rm end}$, the radial extension of the disks in our sample spans the range $47 - 736$ km and the vertical extension can be as small as 7 km and as large as 390 km, where smaller values are found for lighter disks. In particular, the simulations targeted to the BNS merger GW190425 undergo prompt-collapse due to the high total mass of the system, resulting in lighter and smaller disks. These disks are characterized by radii between $47 - 85$ km and vertical extension between $7 - 22$ km.

Regarding the time evolution of the spatial extents (see Fig. 5.1), we note that after an initial expansion reflecting the disk formation, the accretion onto the central object and the ejection of matter contribute to reduce the disk volume, decreasing both the radial and vertical extensions. However, this change in volume essentially does not affect the shape of the disk and in particular its aspect ratio (see below).

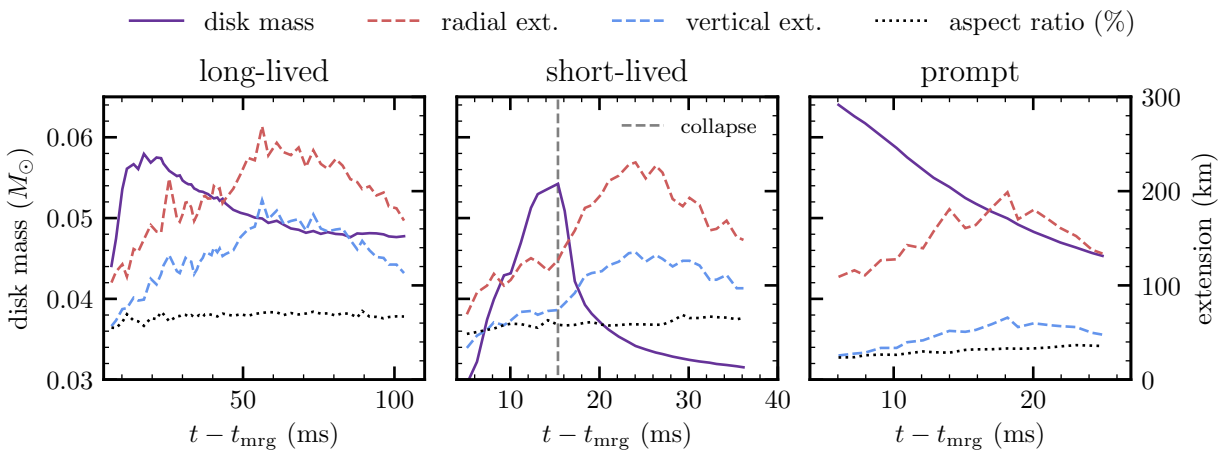

Figure 5.1: Disk mass (left axis), radial extension, vertical extension and aspect ratio in percentage (right axis) for a sample of SR simulations in each category. Left panel: long-lived BNS merger obtained from the $q = 1$, simulation with the BLh EOS (without turbulent viscosity). Central panel: short-lived BNS merger obtained from the $q = 1$ simulation with the LS220 EOS (without turbulent viscosity). Right panel: prompt-collapsed BNS merger obtained from the $q = 1.66$ simulation with the SFHo EOS and turbulent viscosity. Taken from Camilletti et al. [2024]

Aspect ratio and opening angle.

The left panel of Fig. 5.2 shows the relation between the aspect ratio of the disk and the mass ratio of the binary. All the disks in our simulation sample are considerably thick, with an aspect ratio between 0.2 and 0.7. This clearly indicate that, in addition to the rotational support, remnant disks are characterized by a significant thermal support. According to scaling relations related to the vertical structure of the disk, the aspect ratio can be estimated by the ratio between the sound and the rotational speed inside the disk. For a few representative simulations, we have verified that the ratio between these two speeds is $\sim 0.2 - 0.4$ across the orbital plane and within the innermost 100km, in good qualitative agreement with our aspect ratio results. The disks from prompt-collapsed BNS mergers are located in the lower region of the plot, below an aspect ratio ~ 0.4, while disks from long-lived and short-lived simulations span a broader range and are usually thicker. In general, the aspect ratio of the disks from long and short-lived simulations tends to decrease with q from a maximum of ~ 0.7 in the equal mass cases to a minimum of 0.4 for very asymmetric binaries, $q \gtrsim 1.6$. Moreover, for those simulations, the data suggest that the aspect ratio decreases faster for softer EOS, but more unequal BNS merger simulations are needed to clearly asses this trend. Both these trends are likely related to the effects of tidal interactions in the disk formation process, since they are more pronounced for stiffer EOSs and higher mass ratios. Indeed, tidal interactions expel matter from the central object predominantly

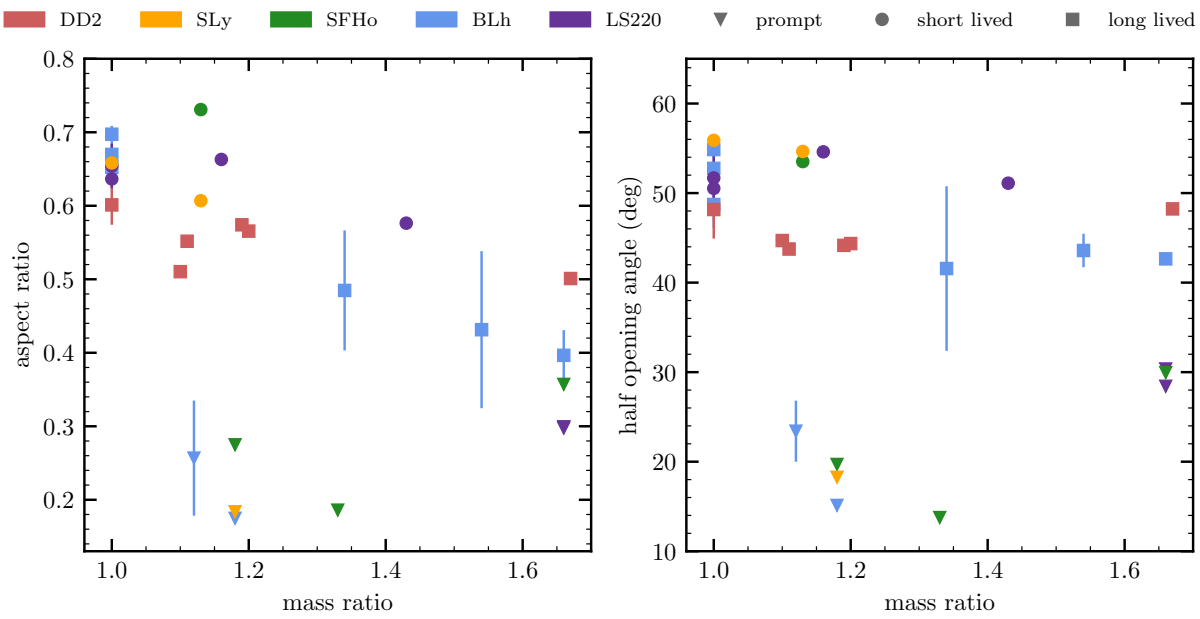

Figure 5.2: Relation between the aspect ratio (right panel) and the half opening angle (left panel) with the mass ratio of the binary. Colors represent the EOS while markers label the fate of remnant. Values are taken at the last timestep of the highest-resolution simulation available for each BNS model. Errors are estimated as the difference between the two higher resolutions available. Adapted from Camilletti et al. [2024]

towards the orbital plane, increasing the disk extend in this direction and therefore reducing the aspect ratio.

The right panel of Fig. 5.2 shows the opening angle as a function of the mass ratio. Again, disks from prompt-collapsed BNS mergers are in the low region of the plot, where the half opening angle is $\sim 10 - 30°$. Instead, the disks from simulations in the long and short-lived category are wider and have a higher half opening angle that goes from 42° to 56°. Differently from the aspect ratio, the trend of the half opening angle with q is less pronounced and is more ore less constant for $q \gtrapprox 1.3$. Indeed, while the matter at large latitude is expelled by shocks and remnant bounces during the merger, in the case of high mass ratio binaries, the disk tends to include a tail at large radii formed by the tidal disruption of the lighter NS, as shown in Fig. 5.3. Since the half opening angle is computed from the ratio between the maximum height and the radial distance at which the maximum height is found, it is not affected by the presence of a tail at larger radii, which instead affects the aspect ratio.

We note that our data do not allows us to infer the presence of any trends of aspect ratio or half opening angle vs. mass ratio regarding models that undergo prompt-collapse. Additional simulations covering a larger set of binary configurations would be needed to investigate this point.

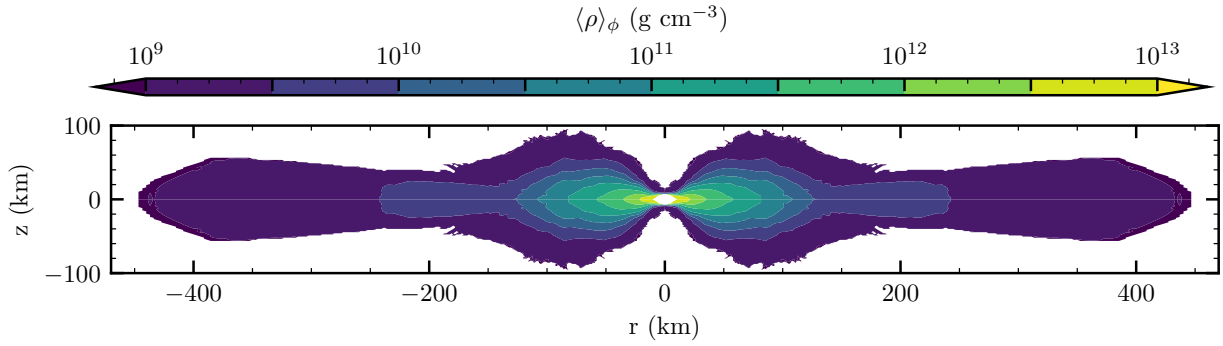

Figure 5.3: Mass fraction ϕ-averaged rest mass density distribution on the rz-plane for a $q = 1.66$ long-lived BNS merger HR simulation with BLh EOS (without turbulent viscosity). The distribution is taken at the last available timestep.

5.3.2 Dynamical properties

Minimum rest mass density.

The post-processing procedure described in Sec. 5.2 implies that every disk in our simulation sample has a different minimum rest mass density $\rho_{\rm min}$, which also changes in time. To give a reference, general values of $\rho_{\rm min}$ (taken at the last timestep of each simulation) are in the range $10^7 - 4 \times 10^{10}$ g cm^{-3} with a geometric mean of 2×10^8 g cm^{-3}.

Lower values of $\rho_{\rm min}$ are reached in light disks produced by prompt-collapsed BNS mergers: since their maximum density attains the typical value of $\sim 10^{12}$ g cm^{-3}, such disks extend towards lower densities to meet the requirement of containing 95% of the total baryon mass of the system.

Disk mass and angular momentum.

The mass and angular momentum of the disks span a broad range of values, going from 5×10^{-4} to 0.3 M$_\odot$ for the mass, and from 2×10^{13} to 10^{16} M$_\odot$ cm^2 s^{-1} for the angular momentum. Disk mass and angular momentum are summarized in the top panel of Fig. 5.4a and in Table 5.1. We underline that the values of $M_{\rm disk}$ and $J_{\rm disk}$ that we report are $\approx$ 5% smaller from those found in the papers in which the simulations considered here were presented first. This is due to slight differences in the definition of disk in those works with respect to the present one (see Sec. 5.2). From the figure it can be seen that $J_{\rm disk}$ and $M_{\rm disk}$ are distributed along a power law (i.e. a linear relation in log scale). Moreover, their ratio $J_{\rm disk}/M_{\rm disk}$ is almost constant over 3 orders of magnitude in $M_{\rm disk}$ spanning the tight range $3.3 - 4.6 \times 10^{16}$ cm^2 s^{-1}. This generalizes previous findings only related to disks produced in prompt-collapsing simulations targeted to GW190425 [Camilletti et al., 2022].

Similarly to the disk mass and angular momentum, also the respective integrands, i.e. the

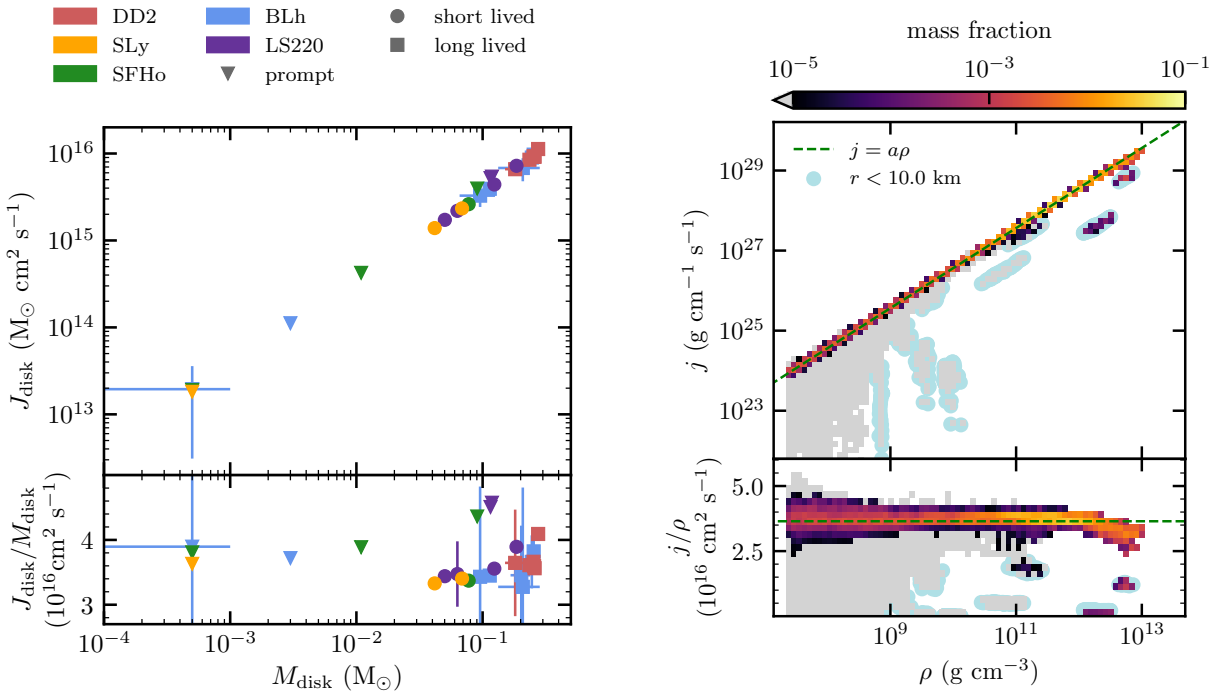

(a) (b)

Figure 5.4: (a). Disk mass $M_{\rm disk}$ and angular momentum $J_{\rm disk}$ as defined in Eq. (3.4) and Eq. (3.5) and their ratio for each BNS merger model at the highest resolution available in our sample. Values are taken at the end of the simulation. Errors are estimated as the difference between the two higher resolutions available. Colors (markers) represent the EOS (fate of the remnant). (b). Mass weighted histogram of the angular momentum density and the rest mass density of the disk (top) and of the specific angular momentum (bottom), obtained from the long-lived equal mass merger HR simulation with BLh EOS (without turbulent viscosity). The color scale represents the fraction of $M_{\rm disk}$ in every bin. When the mass fraction is smaller than 10^{-5} the bin is gray. Bins related to fluid elements at radii smaller than 10 km are highlighted in light blue. Adapted from Camilletti et al. [2024]

rest mass density and angular momentum density, exhibit a power law relation as depicted in Fig. 5.4b. Only the fluid elements near the remnant (highlighted in light blue) deviate from the trend, but their mass fraction is $\lessapprox 10^{-2} - 10^{-3}$ smaller than the mass fraction of the volume elements that follow the power law behavior. Fig. 5.4b suggest a power-law relation $j = a\rho^\gamma$ between the rest mass density and the angular momentum density. We have found that the power-law exponents γ are approximately 1 for all the simulations on which the fit has been performed. This implies that the specific angular momentum (i.e. the ratio between the angular momentum density j and the rest mass density ρ) is almost constant over the disk, as shown in the bottom panel of Fig. 5.4b. We characterize the proportionality

Table 5.2: Weighted averages and uncertainties, computing according to Eq. (5.1) and Eq. (5.2), respectively, for the parameters obtained from the least square fits of the $j = j(\rho)$ relation Eq. (5.3) (left) and of the $j_G = j_G(\Omega)$ relation Eq. (5.11) (right, see Sec. 5.4.1), separately for each simulation sub-sample (long-lived, short-lived, prompt). All the fits have been carried out at $t_{\rm end}$ for each simulation in the sample. Taken from Camilletti et al. [2024]

	$\langle a \rangle$ (10^{16} cm^2 s^{-1})	$\langle \Omega_c \rangle$ (kHz)	$\langle R_0 \rangle$ (km)	$\langle \alpha \rangle$
long-lived	3.9 ± 0.3	19 ± 4	13 ± 2	-1.03 ± 0.04
short-lived	3.5 ± 0.3	31 ± 11	8 ± 2	-1.02 ± 0.01
prompt	4.7 ± 0.3	45 ± 13	8 ± 1	-1.10 ± 0.01

between j and ρ by fitting a linear relation

$$j = a\rho \ , \tag{5.3}$$

minimizing the relative mean square error. Fig. 5.5 shows the specific angular momentum obtained by the linear fit for all the simulations in our sample, which is contained in the tight range $\sim 3 - 5 \times 10^{16}$ cm^2 s^{-1}. This is consistent with both the mass-weighted averages $\langle j^{\rm end}_{\rm spec} \rangle$ in Table 5.1 and the bottom panel of Fig. 5.4a, despite $J_{\rm disk}/M_{\rm disk}$ being the ratio of integrated quantities. Note that a mass-weighted average gives more relevance to the fluid elements with higher mass-fraction, i.e. in the disk regions at higher densities. The fit performed here is not weighted by the mass fraction and we believe it is a better estimator for the specific angular momentum of the whole disk. We find that the specific angular momentum increases with the disk mass and with the mass ratio of the binary. Furthermore, disks originating from prompt-collapsed BNS mergers possess specific angular momentum that falls within the higher bounds of the aforementioned range, with values between 4 and 5×10^{16} cm^2 s^{-1}. In these kinds of mergers, the disk is mostly composed of tidally ejected material, which is expelled with larger angular momentum during the late inspiral and from the merging NSs. In the long and short lived cases, and especially in the equal mass mergers, the disk is mostly formed by matter expelled after the merger through shocks and bounces originating from the remnant. Several mechanisms, including gravitational wave emission, are very effective in removing or redistributing angular momentum from the remnant. This has a quantitative impact on the specific angular momentum of the matter that forms the disk.

The values of the fitted parameter averaged among the simulations in each category are reported in Table 5.2. Note that Table 5.2 also contains the results of the fits for the parameters discussed in Sec. 5.4.1.

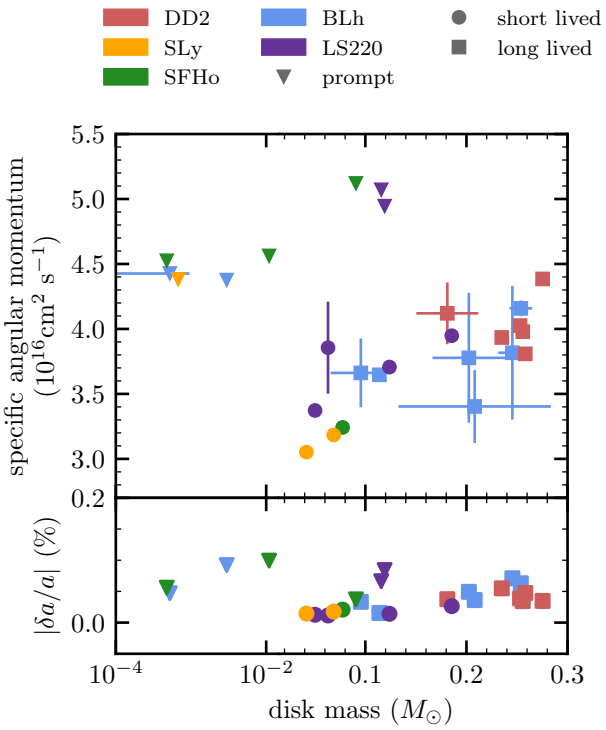

Figure 5.5: Specific angular momentum obtained from the linear fit of the angular momentum density as a function of the rest mass density (Eq. 5.3). Values are taken at $t_{\rm end}$ and for the simulation with highest resolution for each BNS merger model. Errors are estimated as the difference between the two highest resolutions available. The bottom panel shows the one standard deviation relative error on the fitted slope. Colors (markers) represent the EOS (the fate of the remnant). Taken from Camilletti et al. [2024]

Accretion rate

Fig. 5.6 show the ϕ-averaged flow lines of conserved rest mass density $\langle \rho W \tilde{\mathbf{v}} \rangle_\phi$ for a long-lived equal mass BNS merger at the last available timestep, where $\tilde{\mathbf{v}}$ is the advective velocity. At latitudes below 45° and within 1/3 of the total radial extension of the disk (e.g. 100 km in Fig. 5.6), the flux of matter is disordered, with alternating regions of inflow and outflow. However at larger radii the conserved mass density flux is mostly outgoing. The accretion/ejection rates of this matter flux are computed across spherical surfaces according to Eq. (3.6), without imposing a limit on the minimum and maximum rest mass density of the fluid elements considered. As summarized in Fig. 5.7, the absolute value of the accretion/ejection rates $|\dot{M}|$ can reach $\sim$ 10 $M_\odot$ s^{-1}. In the first ten milliseconds after merger, disks with a NS in the center have a persisting outflow of matter across every sphere of radius between 10 and 140 km, with peaks above 10 $M_\odot$ s^{-1}. The outflow decreases with time and can alternate with episodes of inflow in the inner region of the disk, where the flux of the conserved mass density is more disordered. Nevertheless, the total $\dot{M}$ remain positive

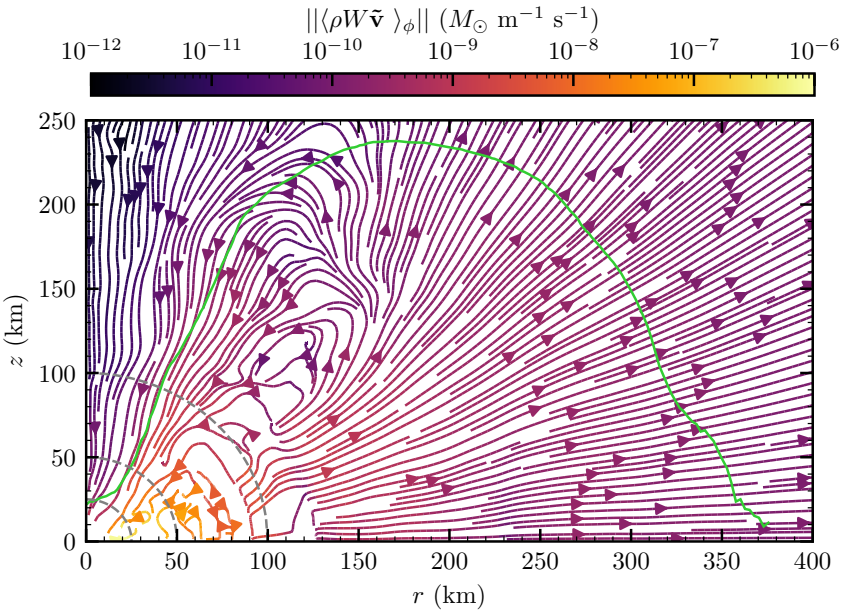

Figure 5.6: ϕ-averaged flow lines of matter for the long-lived equal mass merger HR simulation with BLh EOS (without turbulent viscosity), taken at $\sim$ 52ms post-merger. The green line is the disk border. The gray dashed circles represent spherical surfaces of 25, 50 and 100 km radius, on which the azimuthal distributions of $\dot{M}$ displayed in Fig. 5.8 are computed. Adapted from Camilletti et al. [2024]

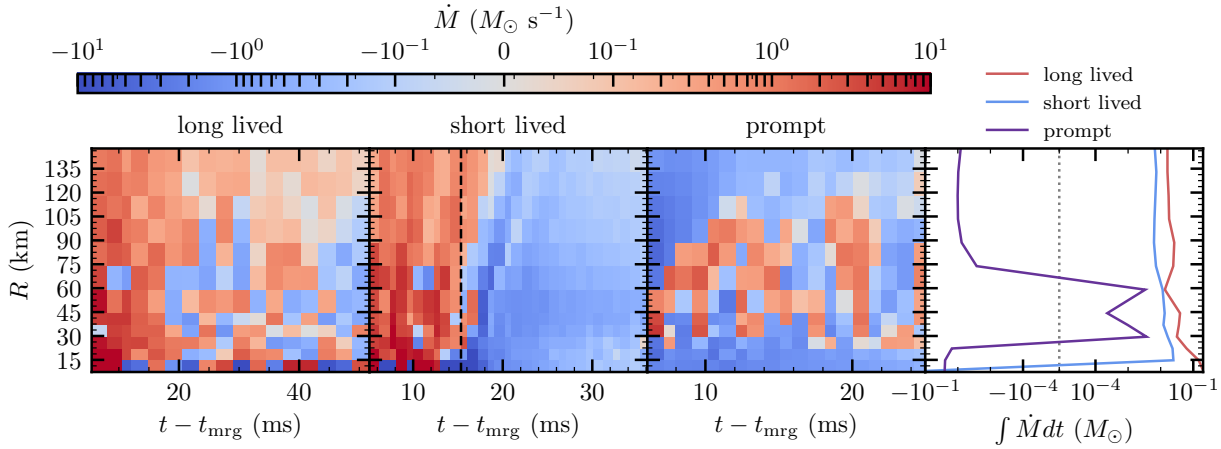

Figure 5.7: Time evolution of the total accretion / ejection rate across spherical surfaces of fixed coordinate radius R. From left to right: long-lived, short-lived and prompt-collapsed BNS mergers chosen from the simulations sample, i.e. the equal mass merger HR simulation with BLh EOS (without turbulent viscosity), the equal mass merger SR simulation with LS220 EOS (without turbulent viscosity) and the SR simulation with SFHo EOS and $q = 1.66$. The last plot on the right shows the total (i.e. time integrated) mass crossing each spherical surface for the three scenarios. The vertical dashed line in the short-lived plot indicates the BH formation time. Taken from Camilletti et al. [2024]

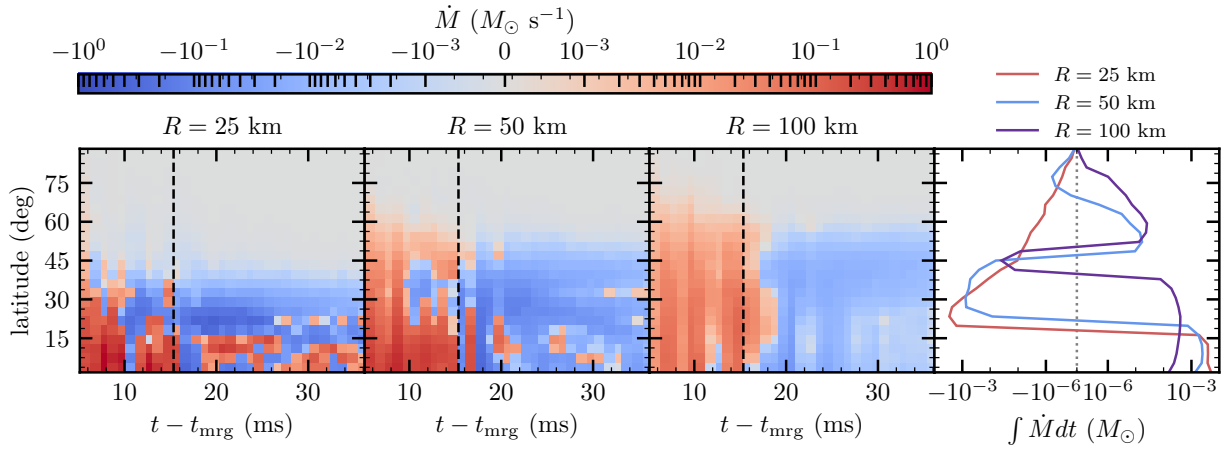

Figure 5.8: Time evolution of the angular distribution of the accretion/ejection rate across spherical surfaces of radii $R = 25,\ 50,\ 100$ km (from left to right) for the same short-lived simulation of Fig. 5.7. The last plot on the right shows the total mass crossing each spherical surface at the various angles. The vertical dashed lines indicate the BH formation time. Note that the color coded scale is different with respect to Fig. 5.7. Taken from Camilletti et al. [2024]

at every radius with values $\sim 10 - 100$ $\mathrm{M}_\odot$ s^{-1} (see rightmost top panel).

Before BH formation, the accretion/ejection rate in BNS mergers with short-lived remnant have a behavior similar to the long-lived ones, characterized by a net ejection of matter for sufficiently large radii. This persistent outflow is due to a combination of multiple mechanism. In the very first milliseconds after merger, the outflow is due to the tidal torques in the late inspiral and to the expanding shocks produced at merger and originating from the bouncing remnant in the center. On longer timescales, the absorption of neutrinos and the spiral waves from the central NS further contribute to the outflow. A significant accretion onto the central object only occurs after the BH formation (vertical dashed line). In the prompt-collapsed BNS mergers the total outflow strongly depends on the radius of the spherical surface in consideration. The central BH of prompt-collapsed BNS mergers always accretes matter at small radii but a net outflow is possible in the inner regions of the disk. At larger radii the trend inverts again with a net inflow of matter.

The polar distribution of the accretion/ejection rate across spherical surfaces of radius 25, 50 and 100 km, integrated along the azimuthal coordinate, is shown in Fig. 5.8 for the same short-lived simulation of Fig. 5.7. At very early times ($t - t_{\rm mrg} \sim 1$ms) the shock-heated matter expelled from the central NS spreads to all latitudes and, in the successive 10 ms, the matter forming the disk is expelled at latitudes $\lesssim 30°$. Near the central NS (left panel), after the first 10 ms accretion dominates at latitudes $\gtrsim 30°$, while episodes of inflow and outflow alternate closer to the orbital plane. Indeed, the ratio between the radial and azimuthal velocity in the equatorial plane is $\sim 10^{-2}$ and the orbital period is ~ 1.5 ms, suggesting

that the radial flux can change sign rapidly. Increasing the distance from the central NS (middle and right panels), neutrino absorption and nuclear recombination release energy in the regions at intermediate latitude $\sim 30-60°$, where the density and temperature are lower (see e.g. figure 16 of Perego et al. [2014]), increasing the outflow at such latitudes. At larger distances (center and right panels) and until BH formation, a significant ejection of matter characterizes a broad range of latitude, up to 60°. Afterwards, but with a delay increasing with the radial distance, the ejection turns into an accretion flow at all latitudes. At any spherical surface the higher values of outflow rate are reached at lower latitudes where most of the mass is concentrated (see the rightmost panel of Fig. 5.8). BNS mergers with different fate of the remnant display similar behavior in the polar distribution of $\dot{M}$, with ejection on broader angles at larger radii and a transition to an inflow after a BH is formed.

Spatial distribution of the rest mass density.

In the following, we discuss the results of an empirical fitting procedure applied to the mass-weighted ϕ-average of the rest mass density as a function of the radial and height coordinates, $\rho(r, z)$. Note that the coordinates in the simulations are gauge dependent and the results presented here are qualitative in nature. However, the disks extend into a region where the gravitational pull of the central object is rather weak, and the gauge conditions employed in our simulations tend towards geodesic coordinates in these conditions. We can therefore expect to be able to provide a useful description of the mass distribution despite its gauge dependence. Indeed, we show that our procedure produces satisfactory results even when applied to simulations with different EOS, mass ratio and fate.

We observe that the rest mass density distribution in the rz plane can be approximated by the product of three terms: the maximum of the rest mass density at $z = 0$, $\max \rho(r, z = 0)$, its rescaled radial distribution, $\rho_0(r) \equiv \rho(r, z = 0)/\max \rho(r, z = 0)$, and its rescaled rest mass density distribution along z, i.e. $\rho_{\bar{r}}(z) \equiv \rho(\bar{r}, z)/\max(\rho(\bar{r}, z))$. In the following, we describe the fitting procedure for $\rho_0(r)$ and $\rho_r(z)$ in detail.

We fit $\rho_0(r)$ with the same relation used in Sec. 4.2.3 (Eq. (4.3)) apart from a normalization, i.e. a Gaussian centered on a radius r_0 and of variance σ_0 smoothly joined to a power-law decay

$$\rho_0(r) = \begin{cases} \exp\left[-(r - r_0)^2/\sigma_0^2\right] & r \leq r_* \ , \\ \exp\left[-(r_* - r_0)^2/\sigma_0^2\right] (r/r_*)^{-\alpha} & r > r_* \ , \end{cases} \tag{5.4}$$

where $\alpha = 2r_*(r_* - r_0)/\sigma_0^2$ and the threshold r_* is a free parameter. We note that for long-lived remnants, r is always greater than r_* due to the 10^{13} g cm^{-3} threshold on the rest mass density. In this case we fit only the power law decay as $\rho_0(r) = \max\{(r/r_*)^{-\alpha}, 1\}$, with α being a free parameter in the fit.

Inspired by the analytic solution for an isothermal not-self-gravitating disk, the rescaled rest mass density distribution along z, i.e. $\rho_{\bar{r}}(z)$ at every fixed $\bar{r}$ in the grid, is fitted using a Gaussian continuously joined to a decaying exponential

$$\rho_{\bar{r}}(z) = \begin{cases} \exp\left[-z^2/H(\bar{r})^2\right] & z \leq z_*(\bar{r}) \ , \\ \exp\left[-z_*(\bar{r})^2/H(\bar{r})^2\right] e^{-\beta} & z > z_*(\bar{r}) \ , \end{cases} \tag{5.5}$$

where $\beta = (z - z_*(\bar{r}))/z_0(\bar{r})$. The scale-height of the disk, $H(\bar{r})$, and the $z_0(\bar{r})$ and $r_*(\bar{r})$ parameters are then fitted as functions of radius with the following relations:

$$H(r) = mr + p \ , \tag{5.6a}$$

$$z_0(r) = ar^2 + br + c \ , \tag{5.6b}$$

$$z_*(r) = A \log_{10}(r/B) \ . \tag{5.6c}$$

Eqs. (5.6a), (5.6b) and (5.6c) have no direct physical interpretation and are modeled ad-hoc on the data. In Table 5.3 we report the values of the various parameters obtained from the fitting procedure described above separately for each of our simulations. Simulations with short-lived and prompt-collapsed remnant have values of r_0, r_* ad σ_0 in the ranges $12 - 127$ km, $15 - 40$ km and $6 - 27$ km, respectively. In the case of long-lived simulations, r_* varies from 15 to 24 km and α from 3 to 5. Regarding the parameters in Eq. (5.6a), m (p) varies between 0.07 (-7 km) and 1 (10 km). Note that H given by Eq. (5.6a) is negative for $r < -p/m$ when $p < 0$. This imposes a minimum radius at which the fitting procedure can effectively approximate the rest mass density distribution of the disk. The minimum and maximum of the parameters a, b and c of Eq. (5.6b) are -0.003 and 0.015, -0.9 and 0.6, -5 and 18, respectively for each parameter. Finally, A and B of Eq. (5.6c) varies from 4 to 93 and from 0.01 to 8.5, respectively. It is apparent that some of the parameters may not be independent from each other. In Fig. 5.9 we show the parameters of Eq. (5.4) as functions of each other. Clearly r_* and $|\sigma_0|$ show some hint of correlation. A similar observation holds for Fig. 5.10. One can see that, e.g. parameter b appears to be a linear function of parameter a. The same could be said of p with respect to m and other couples of parameters. This suggests that the fit formulas proposed in Sec. 5.3.2 are to some extent redundant and could be simplified. However we leave the investigation of this possibility to future work.

The complete rest mass density as a function or r and z is finally obtained as $\rho(r, z) = \max \rho(r, z = 0)\rho_0(r)\rho_r(z)$ inserting Eqs. (5.6) into Eq. (5.5). Since this procedure only involves rescaled quantities, the maximum of the rest mass density on the xy plane, $\max \rho(r, z = 0)$, can be chosen to obtain the desired disk mass once the other parameters have been fixed. Fig. 5.11 shows the relative difference between the logarithms of the mass-fraction ϕ-averaged rest mass density and the results of the fitting procedure. The fit is able to capture the rest

Table 5.3: Parameters obtained from the fitting procedure described in Sec. 5.3.2. From left to the right: category according to the fate of remnant (see Sec. 5.2), EOS, total initial gravitational mass of the isolated neutron stars $M_{\rm tot}$, mass ratio q, inclusion of turbulent viscosity, resolution of the finest grid, disk mass $M_{\rm disk}^{\rm end}$, angular momentum $J_{\rm disk}^{\rm end}$, values of the parameters σ_0, r_0, r_*, α of Eq. (5.4) and m, p, a, b, c, A, B of Eq. (5.5). Note that α is computed as $\alpha = 2r_*(r_* - r_0)/\sigma_0^2$ for short-lived and prompt-collapse BNS mergers (values in parenthesis), while it is a free parameter of the fit for long-lived BNS mergers.

Category	EOS	$M_{\rm tot}$	q	GRLES	res	$M_{\rm disk}^{\rm end}$	$J_{\rm disk}^{\rm end}$	σ_0	r_0	r_*	α	m	p	a	b	c	A	B
						$M_\odot$	$M_\odot{}^2$n	km	km	km			km	10^{-3} km^{-1}		km	km	km
long lived	BLh	2.728	1	✓	HR	0.2081	1.5398	–	–	22.30	4.77	0.54	-3.19	4.70	-0.14	8.17	52.45	7.72
long lived	BLh	2.728	1	✓	SR	0.1328	1.0831	–	–	22.16	5.00	0.56	-7.10	2.80	0.04	3.45	55.35	10.31
long lived	BLh	2.728	1	✗	HR	0.1139	0.8875	–	–	16.40	4.27	0.57	-5.28	2.48	0.04	11.43	36.76	3.71
long lived	BLh	2.730	1	✗	SR	0.0955	0.7402	–	–	17.67	4.94	0.52	-6.25	0.73	0.42	-4.78	36.49	6.87
long lived	BLh	2.730	1	✗	LR	0.1253	0.9321	–	–	18.99	4.33	0.59	-4.81	5.91	-0.21	9.64	50.30	7.43
long lived	BLh	2.765	1.34	✗	HR	0.2024	1.5797	–	–	17.00	3.35	0.40	0.42	1.37	0.15	1.02	37.32	5.64
long lived	BLh	2.765	1.34	✗	SR	0.1664	1.3716	–	–	19.09	4.20	0.49	-4.06	1.52	0.15	4.53	42.54	7.06
long lived	BLh	2.765	1.34	✗	LR	0.2268	1.8612	–	–	20.80	4.14	0.51	-3.25	2.20	0.02	6.43	47.62	6.77
long lived	BLh	2.803	1.54	✗	HR	0.2454	2.0294	–	–	18.97	3.15	0.05	10.34	-1.11	0.20	8.21	10.02	0.62
long lived	BLh	2.803	1.54	✗	LR	0.2594	2.2244	–	–	22.95	4.17	0.43	-1.28	4.41	-0.33	15.51	46.75	7.23
long lived	BLh	2.837	1.66	✓	HR	0.2538	2.1919	–	–	15.52	2.89	0.20	4.28	0.59	-0.15	20.32	11.38	0.38
long lived	BLh	2.837	1.66	✓	SR	0.2650	2.2929	–	–	18.04	3.21	0.14	7.84	-0.20	0.14	11.32	8.27	0.02
long lived	BLh	2.837	1.66	✓	LR	0.2439	2.2047	–	–	26.97	4.55	0.37	0.68	1.29	0.05	8.91	36.86	4.19
long lived	DD2	2.728	1	✗	SR	0.1811	1.4914	–	–	23.39	5.01	0.47	-5.64	3.51	-0.08	7.16	45.90	8.82
long lived	DD2	2.728	1	✗	LR	0.2117	1.7140	–	–	23.33	4.63	0.50	-4.03	6.17	-0.48	17.69	51.63	8.60
long lived	DD2	2.732	1.10	✗	LR	0.2349	1.9157	–	–	24.13	4.85	0.44	-2.48	9.93	-0.90	26.59	24.55	2.78
long lived	DD2	2.733	1.11	✗	LR	0.2582	2.0782	–	–	24.18	4.56	0.50	-3.11	7.11	-0.49	14.28	43.49	6.56
long lived	DD2	2.740	1.19	✗	LR	0.2557	2.0764	–	–	23.48	4.36	0.53	-4.27	5.25	-0.41	16.82	48.61	8.08
long lived	DD2	2.742	1.20	✗	LR	0.2530	2.0934	–	–	23.89	4.51	0.47	-3.11	5.46	-0.28	11.20	46.21	7.91
long lived	DD2	2.880	1.67	✓	SR	0.2753	2.5445	–	–	16.72	3.17	0.12	10.00	-0.12	0.05	27.29	12.63	0.13
short lived	LS220	2.728	1	✓	SR	0.0502	0.3901	8.29	19.53	25.32	(4.26)	0.50	-3.43	4.56	-0.06	6.25	34.24	5.04
short lived	LS220	2.728	1	✓	LR	0.1605	1.2549	14.23	21.44	34.63	(4.52)	0.50	-2.71	7.25	-0.64	26.71	30.47	1.60
short lived	LS220	2.728	1	✗	SR	0.0631	0.4951	7.78	21.50	26.94	(4.83)	0.44	-4.32	2.64	0.18	-2.30	12.69	0.81
short lived	LS220	2.728	1	✗	LR	0.0697	0.5450	8.04	21.44	26.95	(4.60)	0.57	-7.81	3.33	-0.00	9.32	60.65	11.17
short lived	LS220	2.737	1.16	✓	SR	0.1238	0.9947	9.95	19.86	26.96	(3.87)	0.49	-2.88	1.52	0.41	-6.75	30.22	2.85
short lived	LS220	2.781	1.43	✓	LR	0.1855	1.6314	11.47	21.19	28.82	(3.34)	0.09	7.10	-1.94	0.62	-6.02	10.20	0.22
short lived	SFHo	2.735	1.13	✗	SR	0.0775	0.5902	9.61	16.22	23.48	(3.69)	0.64	-5.62	0.60	0.52	3.88	65.16	6.68
short lived	SLy4	2.728	1	✗	SR	0.0417	0.3136	5.24	12.46	15.39	(3.29)	0.71	1.29	3.73	0.06	23.56	137.87	12.48
short lived	SLy4	2.735	1.13	✗	SR	0.0687	0.5282	6.43	12.84	16.73	(3.15)	0.48	-1.90	0.19	0.57	-3.45	71.85	8.16
prompt	LS220	2.837	1.66	✓	LR	0.1185	1.2242	26.44	17.59	41.26	(2.79)	0.18	1.93	0.37	-0.09	12.82	28.54	8.48
prompt	LS220	2.837	1.66	✗	LR	0.1155	1.1760	21.76	21.55	38.53	(2.77)	0.16	3.23	0.28	-0.03	7.04	18.45	1.91
prompt	SFHo	2.837	1.66	✓	SR	0.0906	0.8925	15.04	27.00	39.44	(4.33)	0.21	2.68	2.11	-0.07	3.80	6.31	0.07

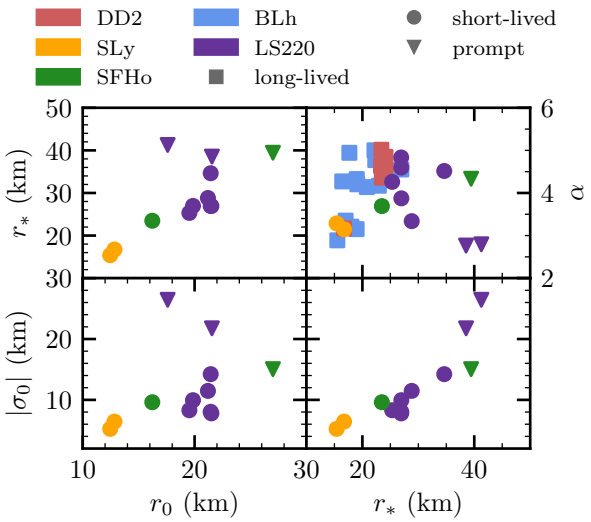

Figure 5.9: Parameters obtained from the fit described in Par. 5.4. Taken from Camilletti et al. [2024]

mass density distribution with average relative error of $\sim 10^{-2}$, excepting for a narrow region near the remnant where it can reach a factor of the order of 10. The geometric mean of the relative difference of the logarithms $\log(\rho/\rho^{\rm fit})/\log(\rho)$, averaged over the simulation sample is contained in the range $0.3 - 6 \times 10^{-2}$. Furthermore the accuracy of the fit is slightly poorer for high-q models than for low-q ones. Overall, this indicates that the fit is able to appropriately describe the rest mass density distribution of most of the disk over a variety of configurations.

5.3.3 Thermodynamic properties

Entropy

We find that the distribution of the entropy in the disk changes significantly depending on the mass ratio of the binary. In particular, $q \approx 1.3$ seems to be a threshold between two different regimes as also found in Perego et al. [2022a]. This motivate us to separate the discussion in small and high mass ratio cases.

Small mass ratio ($q \lessapprox 1.3$) Fig. 5.12 shows the typical distribution of the matter inside the disk in terms of the rest mass density and entropy per baryon. Most of the disk, in terms of mass, has entropy between 4 and 8 $k_{\rm B}$ baryon^{-1}, as also found in Combi and Siegel [2023a]. These values are found in the high density region with $\rho \sim 10^{10} - 10^{13}$ g cm^{-3}. This region may be only very roughly be regarded as isentropic. At lower density the entropy

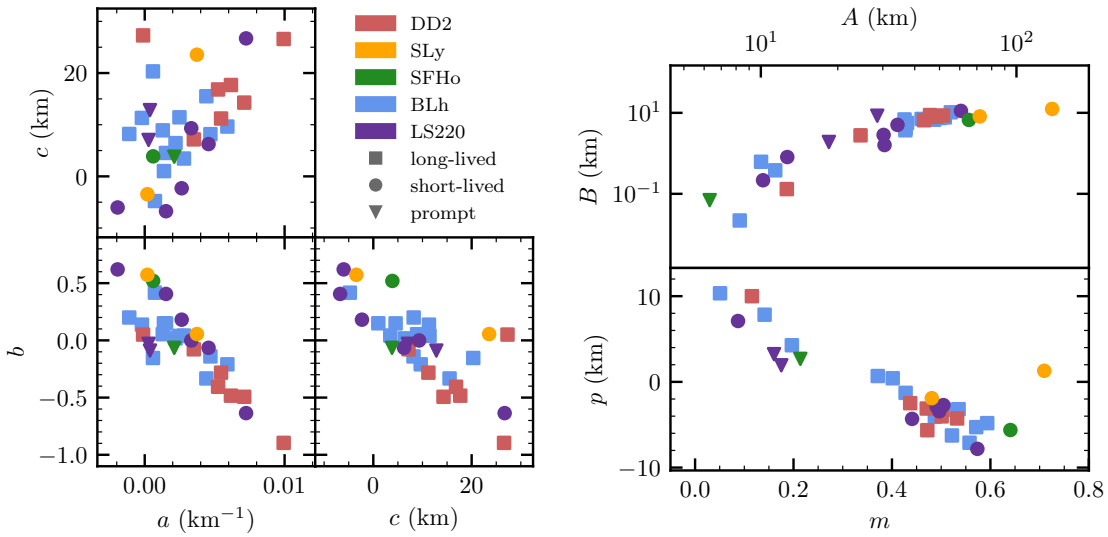

Figure 5.10: Parameters obtained from the fit described in Par. 5.3.2 (Eqs. 5.6). Taken from Camilletti et al. [2024]

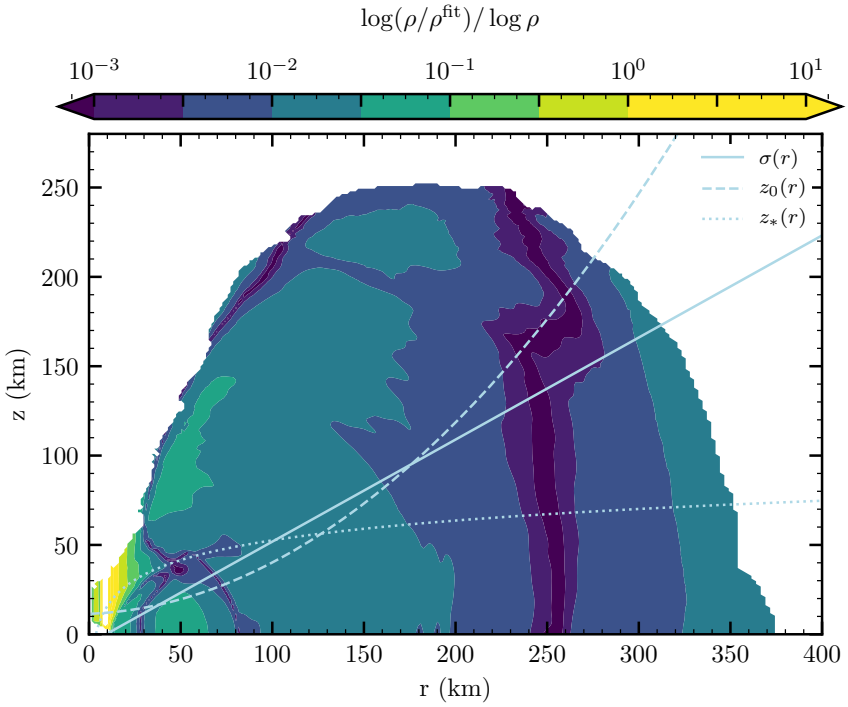

Figure 5.11: Relative difference between the logarithms of the mass-weighted ϕ-average rest mass density and the fit discussed in Sec. 5.3.2, for the equal mass long-lived BNS merger HR simulation with BLh EOS (without turbulent viscosity), at the end of the simulation. The computation of the relative difference has been limited to the region occupied by the disk. Solid, dashed and dotted lines represent, respectively, the quantities $H(r)$, $z_0(r)$ and $z_*(r)$ obtained by fitting the parameters of Eq. (5.5) using Eq. (5.6). Adapted from Camilletti et al. [2024]

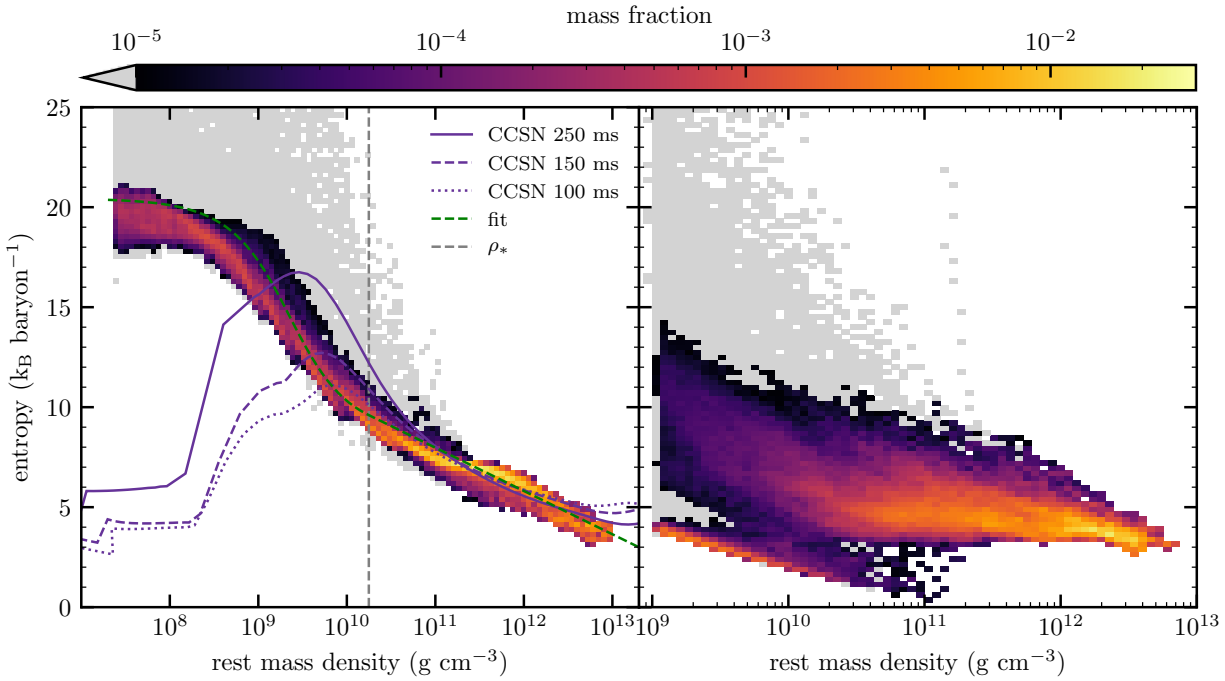

Figure 5.12: Left: histogram of the distribution of the baryon mass vs. rest mass density and entropy of the disk for the representative equal mass long-lived BNS merger HR simulation with BLh EOS (without turbulent viscosity), taken at the last available timestep. The fit with Eq. (5.8) is shown using a green dashed line. The purple lines are the density - entropy distributions from the CCSN simulation discussed in 5.4 at different post-bounce time. Right: rest mass density and entropy per baryon histogram for the prompt-collapsed BNS merger SR simulation with $q = 1.66$ and SFHo EOS, at 11 ms after merger. The fluid elements in the low density ($\sim 10^9 - 10^{11}$ g cm^{-3}) and low entropy ($\lesssim 5\ k_B$ baryon^{-1}) belong to the tidal component of the disk. Adapted from Camilletti et al. [2024]

per baryon increases and reaches a plateau around $15 - 20 k_B$ baryon^{-1} at $\rho \lesssim 10^9$ g cm^{-3}. The distribution produced by BNS mergers characterized by the prompt-collapse of the remnant shows a similar behavior, but the final plateau in entropy occurs at lower values of $\sim 10 - 15 k_B$ baryon^{-1}.

The entropy distribution in the disk is determined by the dynamics that follows the first milliseconds after merger and the initial disk formation. Matter inside the inspiraling NSs has very low entropy. The subsequent dynamics produces shocks that increase the entropy in many different ways [see also Bauswein et al., 2013b]. First, there is the production of a shock at merger, at the collisional interface between the two merging NSs. Despite the large speed of the collision, the resulting shock is weak due to the large sound speed of nuclear matter ($c_s \gtrsim 0.2c$ for matter around saturation density). Under these conditions, the jump

in entropy per baryon can be estimated as

$$\Delta s \sim \frac{\Gamma(\Gamma+1)}{12}\left(\frac{\Delta v}{c_s}\right)^3 , \tag{5.7}$$

where Γ is the adiabatic index ($\sim 5/3$ for non-relativistic nucleons, while $\sim 4/3$ if the equation of state is dominated by relativistic electrons or photons) and Δv the variation of the speed at the shock front. Considering that the speed variation cannot exceed the orbital speed at merger ($v_{\rm orb} \sim 0.4c$), $\Delta s \lesssim 3k_{\rm B}$ baryon^{-1}. Secondly, the bounces of the central object produce radial sound waves that become shock waves at the edges of the forming remnant, expelling shock-heated dynamical ejecta, with a typical entropy between 10 and 15 $k_{\rm B}$ baryon^{-1}. At the same time, they also expel shock-heated matter from the collisional interface, which collides with the faster and rotating spiral arms formed by the tidal tails of the two NSs. The latter are characterized by initially unshocked matter at lower entropy that gets shocked by the collision with the warmer and slower matter in the disk. The typical sound speed inside the disk decreases down to 0.02c for $\rho \sim 10^8$ g cm^{-3}, while Δv across the shock front is a decreasing fraction of $v \sim v_{\rm orb} \propto R^{-1}$ such that $\Delta v/c_s$ is of the order of a few and $\Delta s \sim 10k_{\rm B}$ baryon^{-1}. The overall effect is a monotonic increase of the specific entropy. After a few orbits, the action of the shocks ceases. Until gravitational collapse to a BH, the aftermath of the merger is marked by the propagation of spiral waves originating from the central NS Nedora et al. [2019]. The propagation of these waves is adiabatic and any change in the entropy distribution occurs solely due to expansion, which brings matter with $s \sim 20 - 25k_{\rm B}$ baryon^{-1} to densities below $\sim 10^9$ g cm^{-3}. Note that in this discussion we are not considering fluid elements in the disk with mass fraction below 10^{-5}, where the entropy can be much higher.

Based on the data found in our sample, we propose a functional relation between the entropy per baryon s and the rest mass density ρ, consisting in an arcotangent smoothly joined to a logarithm:

$$s(\rho) = \begin{cases} s_0 - \bar{s}\arctan(\rho/\rho_0) & \rho \leq \rho_* \ , \\ \\ s_0 - \bar{s}\arctan(\rho_*/\rho_0) - \frac{\ln 10}{\rho_0/\rho_* + \rho_*/\rho_0} s_0 \log(\rho/\rho_*) & \rho > \rho_* \ . \end{cases} \tag{5.8}$$

The parameters s_0, $\bar{s}$, ρ_0 and ρ_* are obtained by a non-linear least-squares fit with residuals weighted by the mass fraction m_f of the fluid elements. In Table 5.4 we report the averaged values of the parameters appearing in Eq. 5.8 for each simulation category. The parameters s_0 and $\bar{s}$, i.e. the entropy of the plateau at low density and the magnitude of the jump in the transition region, are comparable among simulations in the long-lived and short-lived

Table 5.4: Same as in Table 5.2, but for the parameters obtained from the least square fits of the $s = s(\rho)$ relation Eq. (5.8). The column "No. of sims" indicates the number of simulations in each category over which the average is performed. Taken from Camilletti et al. [2024]

Category	No. of sims	s_0 (k_B baryon^{-1})	$\bar{s}$	ρ_0 ($\times 10^{10}$g cm^{-3})	ρ_*
long-lived	14	17 ± 2	6 ± 1	0.3 ± 0.1	3 ± 1
short-lived	8	17 ± 1	6 ± 1	1.1 ± 0.3	11 ± 3
prompt	4	10 ± 5	6 ± 2	0.2 ± 0.1	4.2 ± 0.1

categories. The central density ρ_0, around which the transition from low entropy to the entropy plateau occurs, differs by almost one order of magnitude instead.

High mass ratio ($q \gtrsim 1.3$). As the mass ratio increases, the lower-mass star in the system is more and more likely to be tidally disrupted at the time of merger. This disrupted matter is then flung outwards, mostly along the orbital plane. By this process, the proportion of the tidally-ejected mass forming the disk increases with respect to the portion ejected by shock heating. At mass ratios $q \gtrsim 1.3$, part of the tidally-ejected matter in the early post-merger forms a component separated from the bulk of the disk. This component is clearly visible in the low entropy, low density region of Fig. 5.12 (right panel). This component has entropy per baryon below $5k_B$ baryon^{-1} and density of $\rho \lesssim 10^{11}$ g cm^{-3}. Furthermore we have observed that, as the system evolves, $\lessapprox 10\%$ of this tidal tail migrates outwards reaching densities smaller than the minimum density of the disk (at which point we stop tracking it), while the rest is reabsorbed in the disk.

The remaining component, corresponding to the bulk of the disk, has nearly constant entropy of about $\simeq 4.5k_B$ baryon^{-1} (the entropy does reach values as high as $\simeq 12k_B$ baryon^{-1}, but only for fluid elements characterized by a small mass fraction of $\simeq 10^{-5}$ or lower). The constancy of the entropy in the more asymmetric models, as opposed to the trend described above for the near-symmetric ones, can be explained by noting that tidally ejected matter remains cold, and in time undergoes an isothermal expansion which increases its entropy of $\lesssim 3k_B$ baryon^{-1}. Since the contribution of the tidal component becomes more relevant for increasing mass ratio, the density dependence of the entropy also becomes less noticeable.

Taking into account these observations, for such high-mass ratio models we do not provide a functional form for the $s = s(\rho)$ relation, since it can reasonably be modeled by a constant value.

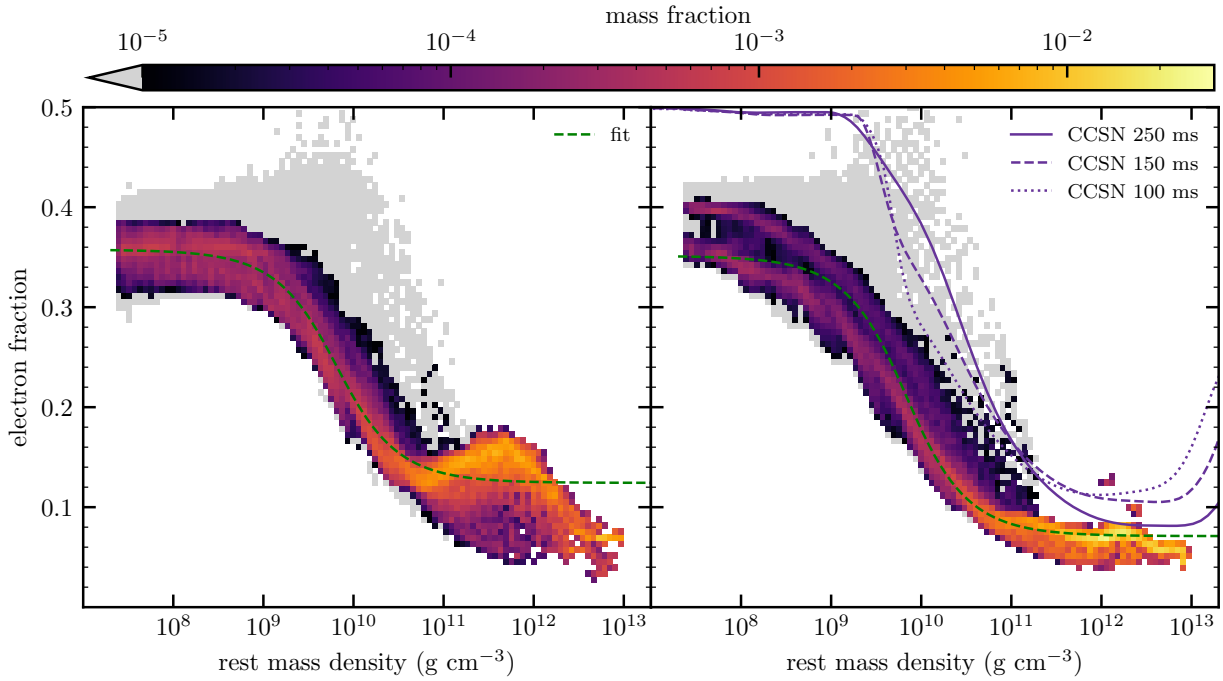

Figure 5.13: Left: mass weighted histograms of the rest mass density and electron fraction of the disk for the same representative simulation of the left panel in Fig. 5.12. Right: similar histogram for the equal mass long-lived BNS merger SR simulation with BLh EOS (without turbulent viscosity) taken at the end the simulated time. The fit with Eq. (5.10) is shown using a green dashed line. The purple lines are the density - Y_e distributions from the CCSN simulation discussed in 5.4 at different post-bounce time. Adapted from Camilletti et al. [2024]

Electron fraction.

Matter inside the two NSs is in neutrinoless, weak equilibrium. However, during the subsequent merger and post-merger phases, the electron fraction in the disk changes due to charged current reactions, both in equilibrium and out-of-equilibrium conditions. The most relevant reactions that we will consider in the following to analyze the electron fraction profiles are the electron capture on protons, the positron capture on neutrons and their inverse reactions:

$$
\begin{aligned}
e^- + p &\rightarrow n + \nu && \text{electron capture,} \\
e^+ + n &\rightarrow p + \bar{\nu} && \text{positron capture,} \\
\nu + n &\rightarrow p + e^- && \text{neutrino absorption,} \\
\bar{\nu} + p &\rightarrow n + e^+ && \text{antineutrino absorption.}
\end{aligned}
$$

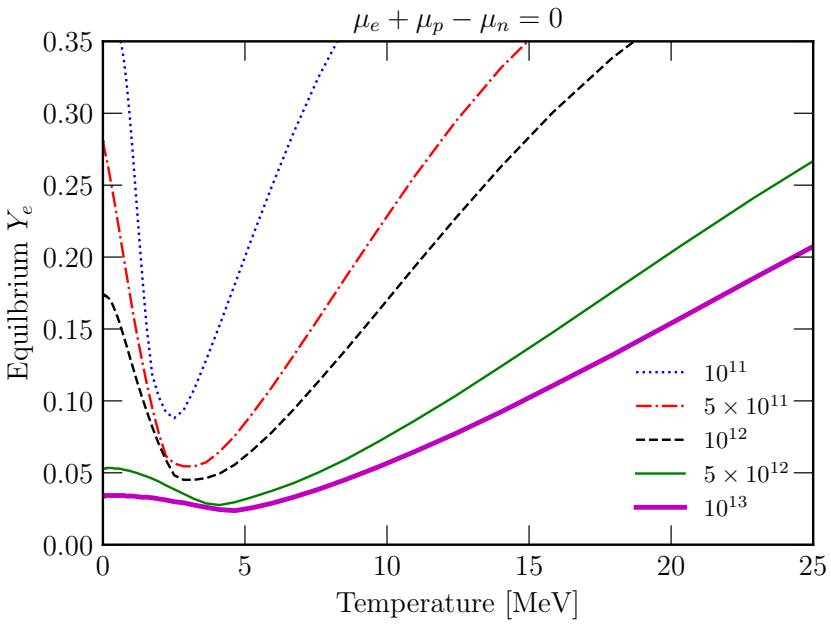

Figure 5.14: Equilibrium electron fraction for weak reaction in marginally optically thick conditions, i.e. for negligible neutrino fractions, as a function of the temperature and for different rest mass densities ranging between 10^{11} g cm^{-3} and 10^{13} g cm^{-3}. The equilibrium is found by solving $\mu_e + \mu_p - \mu_n = 0$ for the BLh EOS. Taken from Camilletti et al. [2024]

Small mass ratio ($q \lessapprox 1.3$). The mass weighted histogram of Fig. 5.13 shows the disk's electron fraction distribution with respect to the rest mass density. Most of the mass is characterized by a low electron fraction, with values in the interval $0.1 - 0.2$. At very high densities, $\rho \sim 10^{11} - 10^{13}$ g cm^{-3}, the matter reaches an even lower electron fraction ($Y_{\rm e} \lesssim 0.1$). This is a feature that characterizes all the simulations, regardless of the EOS or mass ratio. In particular, the value of the electron fraction can drop below its initial minimum value in the cold, neutrinoless beta-equilibrium NSs. At such high densities the initial post-merger temperature is $\approx 5 - 15$ MeV and decreases to $3 - 10$ MeV after the first ~ 30 ms due to the efficient neutrino cooling. These regions are, however, inside the neutrino decoupling regions for both electron neutrinos and antineutrinos. The composition is then set by the equilibrium between neutrino emission and absorption processes. In the limit where the presence of trapped neutrinos is negligible the equilibrium is set by the condition $\mu_{\rm p} - \mu_{\rm n} + \mu_{\rm e} \approx 0$, where $\mu_{\rm n}$, $\mu_{\rm p}$, $\mu_{\rm e}$ are the chemical potentials of neutrons, protons and electrons, respectively. In Fig. 5.14 we present the equilibrium Y_e for the BLh EOS. For matter in the rest mass interval $\rho \sim 10^{12} - 10^{13}$ g cm^{-3} and temperature interval $T \sim 5 - 10$ MeV, the equilibrium $Y_{\rm e}$ is always < 0.1 and it decreases if T decreases or if ρ increases. This result is not specific for one EOS, since it relies on generic features of the matter properties in the relevant temperature and density conditions. Indeed, modeling the

nucleons as a Maxwell-Boltzmann ideal gas of free protons and neutrons, and the electrons as an ultrarelativistic, strongly degenerate ideal gas (under these conditions positrons are suppressed by degeneracy and Y_e becomes a good proxy of the abundance of electrons), the equilibrium conditions can be approximately expressed by:

$$k_{\rm B}T \ln\left(\frac{1-Y_{\rm e}}{Y_{\rm e}}\right) - E_{\rm F}\left(1-\frac{\pi^2}{6}\left(\frac{k_{\rm B}T}{E_{\rm F}}\right)^2\right) = 0\,, \tag{5.9}$$

where for electrons we used $E_{\rm F} = p_{\rm F}c$ and $p_{\rm F} = \hbar(3\pi^2 Y_{\rm e}\rho/m_b)^{1/3}$ [see also Siegel and Metzger, 2018, for a discussion on Eq. (5.9)]. Furthermore we made use of the Sommerfeld lemma to compute the first order correction in T for the electron chemical potential. For 5 MeV $\lesssim T \lesssim$ 10 MeV and 10^{11} g cm^{-3} $\lesssim \rho \lesssim 10^{13}$ g cm^{-3} the results obtained by solving Eq. (5.9) are consistent with the ones presented in Fig. 5.14.

For early enough time, in the $\rho \sim 10^{11} - 10^{12}$ g cm^{-3} density region, the electron fraction as a function of density shows a local peak. The increase in $Y_{\rm e}$ immediately below 10^{12} g cm^{-3} is mostly due to positron captures happening in hot matter locally shocked or expanding from the innermost part of the disk in a region where electron antineutrinos start to decouple from matter [Endrizzi et al., 2020]. Below this density, electron antineutrinos are out of equilibrium and their capture on protons becomes more effective than positron capture, eventually decreasing $Y_{\rm e}$[1]. Nevertheless, this feature is a transient which disappear on a timescale of 100 ms, producing an almost monotonic increase between the high and the low density regimes (see bottom panel of Fig. 5.13). For large enough time, the conditions inside this part of the disk resemble the innermost conditions inside accretion disk around black holes. Since eventually matter becomes optically thin to neutrinos, the electron fraction reaches an equilibrium condition which is set by the balance between electron and positron captures [Beloborodov, 2003, Foucart et al., 2014]. We speculate that on longer timescale the disk will set to a self-regulating stage, in which the neutrino cooling is balanced by the local heat production, for example due to viscous processes [Beloborodov, 2003, Just et al., 2021, Siegel and Metzger, 2018].

Going from 10^{11} to 10^{9} g cm^{-3}, the temperature approximately decreases from 4 to 2 MeV. The drop in temperature and density is responsible for a progressive decrease of the relevance of electron and positron captures, while the decoupling of electron neutrinos from matter favors their absorption on neutron rich matter in free streaming and out-of-equilibrium conditions. The overall effect is a progressive increase of the electron fraction.

[1]Note that the assessment of the robustness of this feature would require a more realistic neutrino transport treatment, since the interplay between different neutrino species in the semi-transparent regime (when some species are coupled to matter and others are not) is delicate and it is not obvious that the combination of a leakage and an M0 scheme we employ is able to correctly model all the relevant processes.

Below $\rho \sim 10^9$ g cm^{-3} the temperature further drops below $\lesssim 2$ MeV. As a consequence, electron and positron captures become negligible. Over time, the electron fraction in the outer part of the disk approaches an equilibrium state around 0.4, determined by the electron (anti)neutrino luminosities and mean energies [Qian and Woosley, 1996, Martin et al., 2015].

In contrast to both long and short-lived BNS mergers, the disks in the prompt-collapse category are not irradiated by the neutrinos emitted by the central NS. Under these conditions the electron fraction is exclusively determined by the equilibrium between electron and positron captures. We observe that the electron fraction of the disks from prompt-collapse mergers with $q \lesssim 1.3$ increases from 0.04 to ~ 0.2 as the density (temperature) decrease from 10^{11} g cm^{-3} (4 MeV) to 10^7 g cm^{-3} (1 MeV). We emphasize however that these values do not represent the equilibrium values of Y_e. Indeed, the typical timescales of the electron and positron captures in this thermodynamic conditions range from ~ 10 ms to 10 s. Our simulations do not extend to such timescales (being shorter than 20 ms post-merger), therefore we cannot ascertain the ultimate equilibrium value of the electron fraction. This accounts for the consistently lower Y_e values observed in the considered disks, which are below the anticipated equilibrium value for neutrino-transparent matter at the same densities and temperatures Foucart et al. [2014].

Similarly to what is done in Sec. 5.3.3, for BNS mergers that do not undergo prompt-collapse, it is possible to fit the electron fraction as a function of the rest mass density using a sigmoidal function, e.g. an arcotangent:

$$Y_\mathrm{e}(\rho) = Y_{\mathrm{e},0} - \bar{Y}_\mathrm{e} \arctan(\rho/\rho_0) \ . \tag{5.10}$$

The result of the fit is shown in Fig. 5.13 for the same long-lived simulation of Fig. 5.12 (left panel). The fitting function does not take into account the presence of the local maximum around $\rho \sim 10^{13} - 10^{11}$ g cm^{-3}. This feature is indeed a transient as the neutrino and anti-neutrino diffusion spheres tend to coincide at longer simulation time. The local maximum is indeed disappearing in simulations lasting longer than 100 ms. However, the presence of this transient in most of the simulations on which we performed the fit shifts the arcotangent plateau at high density to higher electron fraction, decreasing $\bar{Y}_\mathrm{e}$. The values of the fitted parameters averaged over each category are summarized in Table 5.5. The parameters $Y_{\mathrm{e},0}$ and $\bar{Y}_\mathrm{e}$ are comparable between disks of BNS mergers with long-lived and short-lived remnants, indicating that neutrinos are efficient in reprocessing the matter even when the central object collapses in tens of milliseconds. Note that these values too have a qualitative nature, as commented above for the analogue case of the entropy distribution.

Table 5.5: Same as in Table 5.4, but for the parameters obtained from the least square fits of the $Y_{\rm e} = Y_{\rm e}(\rho)$ relation Eq. (5.10). Taken from Camilletti et al. [2024]

category	number of sim	$Y_{e,0}$	$\bar{Y_{\rm e}}$	ρ_0 ($\times 10^{10}$g cm^{-3})
long-lived	11	0.35 ± 0.02	0.15 ± 0.02	0.63 ± 0.05
short-lived	8	0.33 ± 0.03	0.14 ± 0.03	1.2 ± 0.3

High mass ratio ($q \gtrapprox 1.3$). Similarly to the entropy for very asymmetric binaries, the electron fraction differs among the tidal and shocked component.

The $Y_{\rm e}$ of the shocked component is determined by the decrease of the electron and positron captures with the temperature and the density, and by the flux of neutrinos, as discussed previously for the BNS with $q \lesssim 1.3$. For long and short-lived BNS mergers, the electron fraction of the shocked component goes from 0.05 up to 0.4. Only a very small fraction ($< 10^{-5} M_{\rm disk}$) of this component can reach values as high as 0.5. If, on the other hand, the remnant undergoes immediate collapse, the maximum $Y_{\rm e}$ is reduced by the lack of neutrino irradiation from the central NS.

In all the models, the tidal component is characterized by very neutron-rich matter with very low temperature and $\rho \lesssim 10^{11}$ g cm^{-3}. In this thermodynamic conditions, only electron captures can contribute to the change of the matter composition, reducing the $Y_{\rm e}$ to $0.02 - 0.08$. Further electron conversions are then prevented by the high neutron chemical potential.

Since for high mass ratio the tidal component accounts for most of the disk, disks from high mass ratio BNS can be approximately regarded as having constant low $Y_{\rm e} \sim 0.05$.

5.4 Discussion about the disk properties

5.4.1 Specific angular momentum

In Galeazzi et al. [2012] the authors proposed a parameterized rotation profile able to describe different classes of differentially rotating NSs. Even though rotating NSs are the intended use case of this model, we apply it here to accretion disks. We have found that this leads to some interesting insights regarding the disks' rotational profile. The profile presented in Galeazzi et al. [2012] is written as:

$$g(\Omega) = \frac{\frac{R_0^2}{\Omega_c^\alpha}\Omega(\Omega^\alpha - \Omega_c^\alpha)}{1 - \frac{R_0^2}{\Omega_c^\alpha}\Omega^2(\Omega^\alpha - \Omega_c^\alpha)},$$

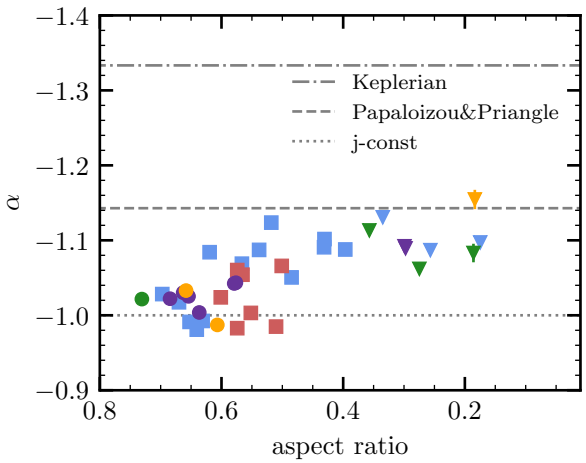

Figure 5.15: α vs the aspect ratio of the disks. Dotted, dashed and dash-dotted horizontal lines represent the j-const, Papaloizou and Pringle [1984] and Keplerian values of α. Taken from Camilletti et al. [2024]

where the quantity on the left-hand side is defined as $j/(1-j\Omega)$. Here Ω is the angular frequency measured by an asymptotic inertial observer, while α, R_0 and Ω_c are free parameters of the model. In particular, in the Newtonian limit, Ω_c is the angular frequency around the axis of rotation. The corresponding specific angular momentum of the model j_G is

$$j_G(\Omega) = \frac{R_0^2}{\Omega_c^\alpha}\Omega(\Omega^\alpha - \Omega_c^\alpha)\,. \tag{5.11}$$

Interestingly $\alpha = -1$ and $-4/3$ represent, respectively, the specific angular momentum of a j-const law [Eriguchi and Mueller, 1985] and of the Kepler law. Table 5.2 shows the one sigma weighted averages of the parameters obtained from a mass-weighted non-linear least square fit on the specific angular momentum of the disk as a function of the angular velocity, taken at the end of each simulation in the sample. It is worth noting that $\alpha \sim -1$ as expected from the results in Sec. 5.3.2. We also fit the Newtonian limit of the specific angular momentum $j_{\rm G}(R) = \Omega_{\rm G} R$ as a function of the radius, where Ω_G is the Newtonian limit of the angular velocity given by the model (equation (11) in Galeazzi et al. [2012]) finding similar results.

Previous works on BNS merger simulations [e.g. Ciolfi et al., 2019, Hanauske et al., 2017] suggested that the Newtonian limit of the angular velocity outside the remnant approach the Kepler law. In the previous Chapter 5 we tried to explain the relation between $J_{\rm disk}$ and $M_{\rm disk}$ using the Kepler law to approximate the radial distribution of the angular momentum integrated along ϕ and z. The results presented here suggest that the specific angular momentum is instead constant. Since the absolute difference of the angular velocity between the j-const and Kepler laws decreases with the distance from the rotational axis, we believe that the trend of the specific angular momentum is a better discriminant between the two

laws. Indeed, in this case the absolute difference between the two models increases with the radius as $r^{2/3}$ and a least-squares fit can easily differentiate between the two cases. In Fig. 5.15 we plot α vs. the aspect ratio of the disks. We find that the α parameter increases with the aspect ratio, indicating that thinner disks are closer to being Keplerian than thicker ones. In particular, disks characterized by a lower aspect ratio in our sample ($0.4-0.2$) have radial distribution of the specific angular momentum broadly compatible with what found by Papaloizou and Pringle [1984], Zurek and Benz [1986], Nealon et al. [2017]. These works study the redistribution of the angular momentum due to the Papaloizou-Pringle instability, and they find a decrease of the aspect ratio over time and a change in the exponent of the specific angular momentum radial distribution, which tend to a power law whose exponent is ≈ 0.25, i.e. $\alpha \approx 1.14$. This may suggest that BNS accretion disks evolve in time from a j-const rotational state to a Keplerian one. However this evolution is likely to take place over long timescales that we cannot investigate due to the limitations of our data sample.

To conclude, note that disks should satisfy the Rayleigh criterion for stability, which states that the specific angular momentum must not decrease outward, i.e. $\alpha \lesssim -1$ [Papaloizou and Pringle, 1984]. This condition is fulfilled by most of the disks we study, and in particular j-const disks are marginally stable under this criterion.

5.4.2 Comparison with disks from black hole - neutron star mergers

In Most et al. [2021b], hereafter Most et al., the authors study the properties of the disk formed in BH-NS mergers. Among their different binary setups, our results are more comparable with the BH-NS mergers with a non-spinning BH (see figure 6 of Most et al., $\tilde{\chi} = 0.00$ case). In this scenario, the entropy per baryon has a similar trend compared to what we have found, despite having lower values. This difference is expected since some of the shock's mechanisms described in Sec. 5.3.3 are possible only in the collision resulting in a BNS merger. The electron fraction of the disk in Most et al. is usually $Y_{\rm e} \leq 0.1$ as in the prompt cases discussed in Sec. 5.3.3. Despite this similarity, the simulations in Most et al. show a local peak in $Y_{\rm e}$ at $\rho \approx 10^9$ g cm^{-3} that we cannot recognize in our prompt-collapse simulations. Note that the local peak of the electron fraction discussed in Sec. 5.3.3 for long and short-lived BNS mergers is not compatible with what showed in Most et al.. Notably, only the BH-NS mergers with a non spinning BH result in a disk exhibiting nearly constant angular momentum within the range $4 - 7 \times 10^{16}$ cm^2 s^{-1}, consistent with our findings.

5.4.3 Accretion rate

Works that investigated the accretion of the disk onto the central object in the aftermath of a BNS merger include Fernández and Metzger [2013] (2D long-term simulations); Siegel and Metzger [2018] and De and Siegel [2021] (3D general-relativistic magnetohydrodynamic (GRMHD) simulations); and Fahlman and Fernández [2022] (pseudo-Newtonian, MHD long-term simulations). They all consider as initial conditions disks characterized by constant specific angular momentum, constant entropy and constant electron fraction around a BH of prescribed mass and spin. The typical accretion rates measured in these works span the range $10^{-3} - 1$ $M_\odot$ s^{-1}. We find instead higher values of the accretion rate during and after the merger at around 10 $M_\odot$ s^{-1}, also in agreement with the simulation in Kiuchi et al. [2022] (self-consistent one second long BNS merger simulation). However we observe that on a timescale of ~ 5 ms the accretion rates decreases below 1 $M_\odot$ s^{-1}. The smaller rates measured right from the start in the cited works likely are a consequence of the equilibrium configurations they employ. Indeed, when an initial relaxation phase is included, as in De and Siegel [2021], the measured accretion rate is consistent to the values found in our data

5.4.4 Aspect ratio

In this Section we compare the disk aspect ratio as measured in our analysis (see Sec. 5.3.1) to the values inferred from the disks presented in the literature. Note however that this quantity is not provided explicitly in most published material. Instead, we extract its value from published 2D plots of discs. To this end we consider a density isocontour in the xz plane around to the typical $\rho_{\rm min}$, e.g. $10^8 - 10^9$ g cm^{-3}. Given this difficulty, the values we obtain are rough estimates at best. Nonetheless they allow to reach some valuable conclusions. An exception applies to the work of Kiuchi et al. [2022], for which we directly compute the aspect ratio from the simulation data. In this instance, the disk's aspect ratio at 117 ms, derived from the isocontour at 10^8 g cm^{-3}, is 0.30, while it extends to 0.49 for the isocontour taken at 10^9 g cm^{-3}. Regarding the `S_def` model of Fernández and Metzger [2013] at 1.16 s, the aspect ratio is $\approx 1/4$, as estimated from their Fig. 5. For a density of $\sim 10^6$ g cm^{-3} the aspect ratio would instead increase to $\approx 1/3$. Fig. 7 of Perego et al. [2014] also returns an aspect ratio of $\approx 1/3$, while the 10^9 g cm^{-3} isocontour of Fig. 4 in Siegel and Metzger [2018] results in a value of ≈ 0.4. Finally from Fig. 1 of Fahlman and Fernández [2022] we recover an aspect ratio of ≈ 0.5 or 1, for the 10^8 g cm^{-3} or 10^9 g cm^{-3} isocontours, respectively. The disks in the referenced works are axisymmetric tori around a BH. Therefore it is appropriate to compare them to our data from near equal mass mergers with short-lived or prompt-collapsed central objects. We find the aspect ratio of the disks in this subset to be in the range $0.6 - 0.8$, i.e. significantly larger than the disks employed in the

literature (the work by Fahlman and Fernández [2022] being the only possible exception). While these works cannot be said to employ "thin" disks (typically this means $H \simeq 10^{-3}$ or lower), better realism might be achieved by setting up initial conditions with disks that are almost as thick as they are wide, similar to what we find in our data sample.

5.4.5 Comparison with core-collapse supernova profiles

The long term evolution of the specific entropy and electron fraction profiles as a function of the rest mass density inside the disk show that both these quantities reach a relatively tight relation, which is relatively insensitive to the properties of the initial binary and of the nuclear EOS. This suggests that the shape of these profiles depends on the properties of matter and on the effects of shocks on it in a way that is largely independent from the details of the way in which these profiles are reached. To further test this conclusion, in Fig. 5.12 and 5.13 we compare the specific entropy and the electron fraction profiles inside a representative BNS merger simulation with those obtained from spherically symmetric core-collapse supernova simulations of a zero-age main sequence 15 $M_\odot$ progenitor star from Woosley and Weaver [1995] at different times post-bounce, namely 100ms, 150ms and 250ms. In particular, we consider publicly available results obtained by the `AGILE-BOLTZTRAN` code [Liebendoerfer et al., 2002, 2004] and published in Liebendoerfer et al. [2005]. This simulation included detailed neutrino transport and employed the Lattimer-Swesty EOS [Lattimer and Swesty, 1991]. In the CCSN simulation, the shock wave is launched at bounce from an enclosed mass of 0.5 $M_\odot$, where the rest mass density is $\sim 10^{14}$ g cm^{-3}. Afterward, it moves outward shocking radially infalling, low-entropy matter of the stellar layers forming the iron core and the shells above it. As soon as the matter crosses the shock front, the entropy increases. As time passes, even if the radial expansion of the shock stops as it reaches the so-called shock stalling phase, the shock still moves outward in the enclosed mass coordinate due to the continuous mass accretion, reaching lower densities. Around 100ms (a time which is comparable to our BNS merger simulation) the shock is located at $\sim 2 \times 10^8$ g cm^{-3} and within a few km the matter density increases by one order of magnitude while increasing also its specific entropy. The latter further increases between $\sim 2 \times 10^8$ g cm^{-3} and $\sim 1 \times 10^9$ g cm^{-3} due to the effect of neutrino heating. The resulting entropy profile between a few 10^9 g cm^{-3} and 10^{13} g cm^{-3} follows very closely the one observed in the disk. At later times, and in particular at 250ms, a substantial deviation is observed between a few times 10^8 g cm^{-3} and 10^{11} g cm^{-3}. This is due to the prolonged neutrino heating and to the contraction of the shock front. Such a discrepancy is expected, since our BNS merger simulation was evolved only for 100ms and matter in the disk tend to expand rather than to contract.

In the case of the electron fraction, the profiles have a similar shape, but the ones of the CCSN simulation are systematically higher than the one of the disk. The reason is that in CCSNe matter with an initial $Y_e \lesssim 0.5$ and contained inside the stellar core is accreted by the shock and deleptonizes toward the cold β-equilibrated conditions that characterize a NS. This condition is achieved passing through the intermediate proto-neutron star phase in which matter is hot and neutrino trapping occurs for high enough matter densities. In BNS mergers, the opposite process occurs: cold β-equilibrated NS matter with $Y_e \lesssim 0.1$ is heated and decompressed inside the disk, and it tends to leptonize, at least for low enough densities. At late enough time, in the high density part of the profile ($\rho \gtrsim 10^{12}$ g cm^{-3}), the CCSN profile approaches the one inside the disk, as weak reaction equilibrium is achieved. For lower densities the visible discrepancy is due to the out-of-equilibrium character of the weak reactions, which prevents the profiles from reaching a state that has completely lost memory of its history. Moreover, such an equilibrium depends also on the neutrino irradiation, which has different features in CCSNe and BNS mergers.

Chapter 6

Effects of first order QCD phase transitions in BNS mergers

QCD is the theory describing the strong interaction of quarks and gluons. At low energies quarks and gluons are bound together forming hadrons and mesons. Increasing the energy scale, the interaction becomes asymptotically weaker carrying to a new state of matter made of a deconfined plasma of quark and gluons called QGP. The study of this phase transition (PT) from hadronic to deconfined matter, schematically depicted in Fig. 6.1, is a hard theoretical and experimental task. QGP has been observed experimentally for the first time in the late 1980s at the Conseil Européen pour la Recherche Nucléaire (CERN) and in Brookhaven National Laboratory (BNL) [Schmidt and Schukraft, 1993, Schukraft and Stock, 2015], probing the transition in the high temperature and low density (i.e zero baryon chemical potential) regime. In the same regime, lattice QCD (LQCD) calculations give reliable information on the PT, showing that the transition is a smooth crossover from the hadronic to the deconfined state [Aoki et al., 2006], with critical temperature $T_c = 154 \pm 9$ MeV [Bazavov et al., 2012]. Despite many efforts [Giordano et al., 2020, Nagata, 2022], the nature of the PT at non-zero baryon chemical potential cannot be investigated with LQCD, instead effective theoretical models can be used, suggesting a first order PT at finite densities [Ejiri, 2008, Bowman and Kapusta, 2009, Schaefer and Wagner, 2009]. The PT in this non zero density and moderate temperature regime can be probed experimentally with heavy ion collisions [Mohanty, 2011], but a deconfinement to quarks and gluons is expected to occur also at zero temperature and very high density, which are unreachable in current experiments.

This is the regime reached in NSs, where the central density can be few times the nuclear saturation density $\rho_0 \sim 2.8 \times 10^{14}$ g cm^{-3} [Haensel et al., 2007]. Isolated NSs cannot easily provide useful information on their core composition, where the higher densities are found and quark matter can be expected. Instead, BNS mergers are fruitful laboratory for high

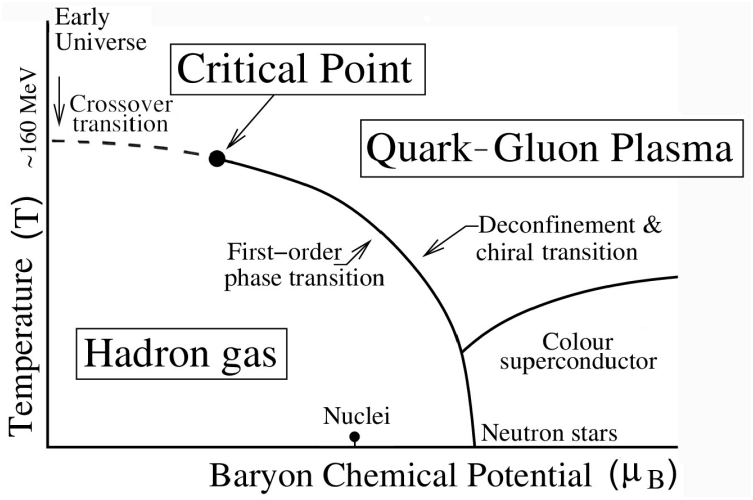

Figure 6.1: Phase diagram of QCD. Taken from Bhalerao [2014]

density physics. Indeed, the EOS of nuclear matter is linked to the properties of the GWs emitted during the inspiral, merger and post-merger phases.

Since the properties of the PT to quark matter are highly uncertain, different constructions have been used to simulate its apparence and its effects during the merger of binary neutron stars. To give few examples, in [Most et al., 2019] the authors used a Chiral Mean Field (CMF) model [Papazoglou et al., 1999] to describe a first-order PT between the hadronic and the quark phase. In Prakash et al. [2021], the authors use the BLh EOS for the hadronic matter and an extension of the MIT bag model [Weissenborn et al., 2011] for the quark matter, including a first-order phase transition between the two phases. In general, various studies indicate that the PT to quark matter can leave some imprints on the GW signal [see e.g. Bauswein et al., 2019, Prakash et al., 2021]. In particular, compared to scenarios with purely hadronic EOS, BNS merger simulations implementing an EOS with a PT to quark matter demonstrate an increase in the post-merger peak frequency, f_{22}, of the $l = 2,\ m = 2$ mode. The detectability of this effect is still uncertain, but promising, and can depend on the PT construction implemented. However, since the simulation setups between different authors differ by many aspects, it is not possible to isolate the differences on the BNS merger outcome solely due to the implemented PT construction. Then, the systematic of the QCD PT on the outcomes of a BNS merger has not been assessed yet. In this chapter we present an ongoing project aimed at comparing different first-order PT constructions within a consistent simulation setup. The purpose is to clearly asses the systematic behind the PT model.

In Sec. 6.1 we give an introduction on the EOS models, both for the hadronic and quark sector, and on the different PTs implemented in this work. After briefly discussing the simulation sample in Sec. 6.2, we present our results in Sec. 6.3, discussing the quark forma-

tion during the merger and post-merger, its imprint on the GW signal and the dependence of our findings with the numerical resolution of the simulations. Finally, we delineate our conclusions in Sec. 7.3.

I acknowledge Domenico Logoteta for the construction of the EOSs implemented in this chapter.

6.1 Description of the equation of states

To include a PT from nuclear matter to deconfined quarks in the description of the NS matter, we need to describe separately the hadronic state and the pure quark state. Moreover we need to consistently describe the PT between the two phases. In this work, we employ the DD2 equation of state (EOS), as detailed in Sec. 2.4.1, to model the hadronic matter. The quark matter is characterized using the Nambu-Jona-Lasinio (NJL) model, as discussed in Sec. 6.1.1 below. We incorporate two opposite first order phase transitions to connect the two models as described in Sec. 6.1.2.

6.1.1 Nambu-Jona-Lasinio model

The three flavor NJL model [Nambu and Jona-Lasinio, 1961a,b] has been widely used to study quark matter in relation with neutron stars [Benhar, O. and Cipollone, A., 2011, Buballa et al., 2004]. One of the redeeming features of the NJL model is the explicit presence of the dynamical chiral symmetry breaking, an important symmetry of QCD. Oppositely, its main drawback is the lack of quarks and gluons confinement at low energy.

Here we use the NJL model supplemented by the t Hooft interaction [Logoteta et al., 2012, Rehberg et al., 1996], with Lagrangian:

$$\begin{aligned}\mathcal{L} = \; & \bar{q}(i\gamma_\mu\partial^\mu - m_0)q + G\sum_{k=0}^{8}\left[(\bar{q}\lambda_k q)^2 + (\bar{q}i\gamma_5\lambda_k q)^2\right] \\ & - K\left[\det_f(\bar{q}(1+\gamma_5)q + \det_f(\bar{q}(1-\gamma_5)q)\right] \;,\end{aligned} \tag{6.1}$$

where $q = (u, d, s)$ is the quark field with the respective quark bare masses $m_0 = \mathrm{diag}(m_0^u, m_0^d, m_0^s)$, G is the coupling constants of the chiral condensate and K is the so called 't Hoff term. The NJL Lagrangian of Eq. (6.1) is not renormalizable and we incorporate of a sharp cut-off Λ to handle the divergent integrals. The model has 6 free parameters: K, G, the three quark masses and the sharp cut-off Λ. This parameters are fixed by low energy scattering data of mesons. More in detail, the coupling constants of the chiral condensate and of the 't Hoff term, the quarks bare masses and a renormalization cut-off, are fixed such that the model

can reproduce the masses of the eta (η), eta prime (η'), kaon (K) and pion (π) mesons and the pion decay constant. From the Lagrangian, the grand canonical potential can be computed as

$$\Omega = \sum_{i=\{u,d,s\}} \Omega_{m_i} + 2G\langle\bar{q}_i q_i\rangle^2 - 4k\langle\bar{u}u\rangle\langle\bar{d}d\rangle\langle\bar{s}s\rangle + B_0 \ , \tag{6.2}$$

where Ω_{m_i} is the grand canonical potential of a free Fermi gas composed by q_i quarks, $\langle\bar{q}_i q_i\rangle$ is the quark condensate and B_0 is a constant introduced to ensure zero pressure at zero density and temperature (for a thorough presentation of the equations the reader can refer to Buballa [2005] and Logoteta et al. [2012]). From Eq. (6.2) the pressure p, the entropy density s and the energy density ϵ of the fluid in the quark phase can be computed as

$$p = -\Omega \ , \tag{6.3a}$$

$$s = -\left(\frac{\partial\Omega}{\partial T}\right)_{\mu_i,V} \ , \tag{6.3b}$$

$$\epsilon = -P + \sum_{i=\{u,d,s\}} n_i\mu_i + sT \ , \tag{6.3c}$$

where n_i and μ_i are the number density and the chemical potential of the quark i, respectively.

6.1.2 First order phase transitions

In a first-order PT the three phases of matter (namely, pure hadronic, mixed and pure quark matter) coexist together in mechanical and chemical equilibrium. Because of the lack of experimental data and reliable theoretical models, many constructions of the mixed phase are possible. We aim to use two first order PT constructions from hadronic to quark matter: the Gibbs construction (GC) and the Maxwell construction (MC), which represent the two most extreme cases, meaning that a realistic first order PT will have intermediate properties between them [Bhattacharyya et al., 2010, Constantinou et al., 2023]. In the GC hadrons and quarks are mixed together in a globally neutral ensemble. On the other side, in the MC, hadrons and quark remain separated during the PT and the charge neutrality is only local. Indeed, the large surface tension between the two phases in a MC disfavors the formation of charged clusters of quark matter immersed in hadronic matter. For the sake of comparison, both the two PTs start at the same density $\rho^*(T, Y_e)$, i.e. for $\rho < \rho^*(T, Y_e)$ the NSs are composed by purely hadronic matter described by the DD2 EOS. For cold, beta-equilibrated NSs, $\rho^* \approx 2.3\rho_0$.

Gibbs construction. The GC requires global charge neutrality to be maintained during the whole transition. A significant implication of global charge neutrality is the coexistence of the hadronic and quark phases within a specific pressure range. The Gibbs conditions for phase equilibrium requires that the two phases have same temperature T, baryon chemical potential μ^b, charge chemical potential μ^c and pressure p:

$$T_Q = T_H \ , \tag{6.4}$$
$$\mu^b_Q = \mu^b_H \ , \tag{6.5}$$
$$\mu^c_Q = \mu^c_H \ , \tag{6.6}$$
$$p_Q(\mu^b_Q, \mu^c_Q, T_Q) = p_H(\mu^b_H, \mu^c_H, T_H) \ , \tag{6.7}$$

where the index H and Q indicate the hadron and quark phase, respectively. Note that the chemical potentials in the quark phase can be written as

$$\mu^u = \frac{1}{3}(\mu^b - 2\mu^c) \ , \tag{6.8}$$
$$\mu^d = \frac{1}{3}(\mu^b + \mu^c) \ , \tag{6.9}$$
$$\mu^s = \mu^d \ . \tag{6.10}$$

The last equation come from considering β-stable strange quark matter, i.e. the balance of the weak reactions $u+s \leftrightarrow d+s$ and $u+e^- \leftrightarrow s+\nu_e$. Indeed the timescale of this reactions is $10^{-5} - 10^{-7}$ shorter than the dynamical timescale of the simulations, so that we can assume them to be in equilibrium.

Maxwell construction. The MC is described by the same Eqs. 6.4 as the GC but the charge neutrality is imposed only locally. Since the charges are conserved only locally, the two phases of matter cannot mix together, then each phase is either made of hadrons or of quarks and no mixture is possible during the PT. The quark fraction Y_q is then not well defined during this kind of PT. The complete disconnection of the hadron and quark phases implies the formation of a separation surface between the two phases, characterized by an infinite surface tension σ. In this respect, the MC is opposed to the GC where the surface tension is zero and the two PT can be taken as two extremes of a first-order PT. Another important difference between the two constructions regards the behavior of the pressure with the baryon density. During the PT the pressure remain constant in the MC, while it varies smoothly in the GC (see also Fig. 6.3). The constancy of the pressure in the MC implies zero sound speed in the PT. The NR codes we employ are not able to evolve systems in which the sound speed is identically zero. As a workaround, we add a small slope (of the

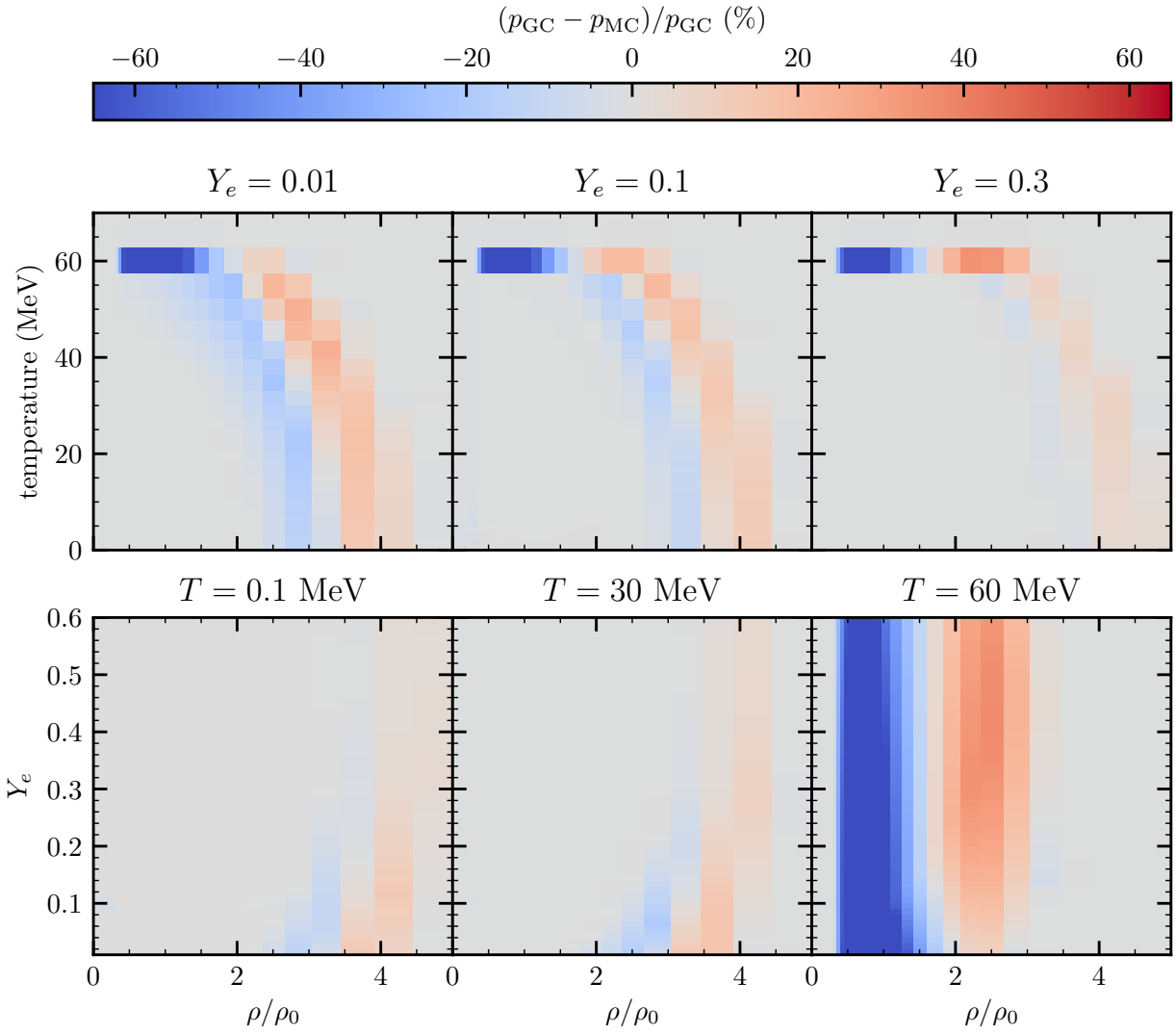

Figure 6.2: Relative difference of the pressure as a function of the density provided by the DD2njlG and DD2njlM EOSs, taken at different constant electron fractions (first row) and temperatures (second row).

order of few percent), to the pressure as a function of the density. The MC outlined in this study is a minor adaptation of the exact MC. Nevertheless, the adjustment is minimal and has only a slight impact on the results of our simulations.

The two EOSs obtained by combining the DD2 EOS for the pure hadronic part, the GC and the MC for the PT, and the NJL model for the pure quark phase are referred in the following as the DD2njlG and the DD2njlM EOSs, respectively. Below the PT the DD2njlG and DD2njlM EOSs are identical to the pure hadronic EOS. However, from the occurrence of the PT on, the tree EOS differentiate. In particular, the pure hadronic DD2 EOS exhibits greater pressure support at any given temperature and electron fraction, resulting in a stiffer EOS capable of sustaining more massive NSs compared to the two EOSs incorporating

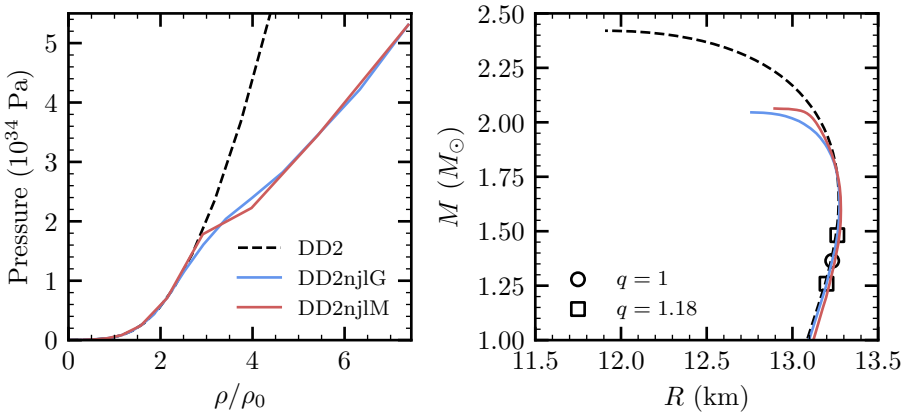

Figure 6.3: Pressure support (left) and mass-radius diagram (right) for isolated, cold, β-equilibrated, and spherically symmetric NSs modeled using the pure hadronic DD2 EOS (black dashed line), the DD2njlG EOS (blue solid line) and the DD2njlM EOS (red solid line). The different markers refer to the different mass ratios of the binaries presented in this work.

the PT (see also the left panel of Fig. 6.3 discussed below, for $T = 0$, β-equilibrated NS matter). Fig. 6.2 shows the relative difference between the pressure as a function of the density provided by the DD2njlG and the DD2njlM EOSs. The first (second) row shows the pressure's relative difference at some fixed electron fractions (temperatures). The colored regions in blue and red highlight the thermodynamic conditions where the two EOSs deviate. The DD2njlG and the DD2njlM EOSs are nearly identical, except for the small range of thermodynamic values where the PT occurs. The most significant differences emerge around the temperature $T \sim 60$ MeV and in the density range $0.5\rho_0 \lesssim \rho \lesssim 3\rho_0$. Generally, DD2njlM EOS is stiffer than the DD2jlG EOS in the lower density part of the PT, while the opposite occurs going towards higher densities. Notably, the difference depends only to a small extent on the electron fraction.

To different constructions of the PT correspond different NS models. In Fig. 6.3, we show the pressure as a function of the density and the mass-radius diagrams of three isolated, cold, β-equilibrated, and spherically symmetric NSs models: one with a pure hadronic DD2 EOS, and two with the EOSs incorporating the Gibbs and Maxwell constructions for the quark transition. As the DD2 EOS is capable of provide more pressure support, is also capable of sustaining the more massive NS among the EOSs implemented in this work. The DD2njlG and the DD2njlM EOSs have instead very similar mass-radius diagrams, with a slightly larger maximum TOV mass reached by the DD2njlM one.

Table 6.1: NS initial properties grouped by EOS. From left to right: EOS, maximum TOV mass $M_{\rm TOV}^{\rm max}$, maximum TOV compactness $C_{\rm TOV}^{\rm max}$, gravitational mass of the two isolated NS M_A, M_B, total gravitational mass $M_{\rm tot}$, mass ratio of the binary $q = M_A/M_B$, numerical resolution of the simulation, duration of the simulation $t_{\rm end}$ referenced to the time of merger, peak frequency of GW power spectral density (PSD) for the dominant $l = m = 2$ mode f_2 in the post-merger, shift of f_2 with respect to the corresponding simulation without PT (pure hadronic) Δf_2 and nominal uncertainty in the Fourier transform $\Delta{\rm FT} = {\rm t}_{\rm end}^{-1}$.

EOS	$M_{\rm TOV}^{\rm max}$ ($M_\odot$)	$C_{\rm TOV}^{\rm max}$	M_A ($M_\odot$)	M_B ($M_\odot$)	$M_{\rm tot}$ ($M_\odot$)	q	res	$t_{\rm end}$ (ms)	f_2 (kHz)	Δf_2 (Hz)	ΔFT (Hz)
DD2njlM	2.06	0.24	1.365	1.365	2.730	1.00	HR	10.86	2.51	-79	92
DD2njlM	2.06	0.24	1.365	1.365	2.730	1.00	SR	17.52	2.36	-174	57
DD2njlM	2.06	0.24	1.365	1.365	2.730	1.00	LR	21.99	2.50	-83	45
DD2njlM	2.06	0.24	1.259	1.482	2.741	1.18	HR	12.69	2.43	-54	79
DD2njlM	2.06	0.24	1.259	1.482	2.741	1.18	SR	17.41	2.41	-46	57
DD2njlM	2.06	0.24	1.259	1.482	2.741	1.18	LR	22.23	2.41	-41	45
DD2njlG	2.05	0.24	1.365	1.365	2.730	1.00	HR	13.38	2.50	-90	75
DD2njlG	2.05	0.24	1.365	1.365	2.730	1.00	SR	18.64	2.49	-44	54
DD2njlG	2.05	0.24	1.365	1.365	2.730	1.00	LR	20.49	2.50	-90	49
DD2njlG	2.05	0.24	1.259	1.482	2.741	1.18	HR	12.92	2.52	32	77
DD2njlG	2.05	0.24	1.259	1.482	2.741	1.18	SR	18.68	2.44	-16	54
DD2njlG	2.05	0.24	1.259	1.482	2.741	1.18	LR	20.03	2.48	23	50
DD2	2.42	0.30	1.364	1.364	2.728	1.00	HR	74.30	2.59	✗	13
DD2	2.42	0.30	1.364	1.364	2.728	1.00	SR	112.89	2.54	✗	9
DD2	2.42	0.30	1.364	1.364	2.728	1.00	LR	122.88	2.59	✗	8
DD2	2.42	0.30	1.497	1.245	2.742	1.20	HR	53.08	2.49	✗	19
DD2	2.42	0.30	1.497	1.245	2.742	1.20	SR	88.94	2.45	✗	11
DD2	2.42	0.30	1.497	1.245	2.742	1.20	LR	88.94	2.45	✗	11

6.2 Simulation sample

All the simulations discussed in this chapter have fixed chirp mass of $M_{\rm chirp} = 1.188$, corresponding to the one measured for GW170817 (see Chapter 1). We choose the initial masses of the two NSs in each simulated BNS system such that no quark are present, i.e. the densities reached are lower than the PT density of cold, β-equilibrated NS matter for both the DD2njlG and DD2njlM EOSs. Since the difference in the BNS merger dynamics due to differences in the PT construction are expected to be rather small, it is of great relevance to simulate each BNS model at high resolution (HR). To better asses the numerical errors we also make use of a low resolution (LR) and a standard resolution (SR) simulation for each BNS model (see Sec. 2.3.1 for a reference on the numerical resolutions). Finally, for each PT construction, we setup two different BNS systems: one equal mass and one unequal mass with mass ratio $q = 1.18$, for a total of 12 simulations employing a PT.

To this sample we add two BNS configurations with the same $M_{\rm chirp}$ and similar NS

masses and mass ratios as the BNS systems just presented, but employing the pure hadronic DD2 EOS. Each of this BNS merger is simulated at the usual three numerical resolutions: LR, SR and HR. The final sample, resumed in Table 6.1, consist in a total of 18 BNS merger simulations with three EOS (DD2, DD2njlG and DD2njlM), three mass ratios ($q = 1$, $q = 1.18$ and $q = 1.20$) and three resolutions. The pure hadronic simulations with $q = 1$ and $q = 1.20$ are considered as the analogue of the $q = 1$ and $q = 1.18$ simulations with a PT, respectively. Note that, despite having slightly different mass ratios, we compare the outcome from the $q = 1.20$ simulations employing the DD2 EOS, with the $q = 1.18$ simulations which make use of the DD2njlG and the DD2njlM EOSs.

It is important to observe that, in terms of their initial mass and radius, the neutron stars in the binary systems discussed in this study are identical, as showed in the right panel Fig. 6.3 by the different markers.

6.3 Results

6.3.1 Quark phase during the merger and post-merger

The fraction of quarks, Y_q, varies during the different stages of the merger and post-merger, following the changes of the temperature and density. In Fig. 6.4 the density, the temperature and the quark fraction are showed for three representative times taken from the HR simulations implementing the DD2njlG and DD2njlM EOSs. During the merger, hot matter is expelled at the collisional interface while the two NS cores remain cold. Despite the density of the shocked matter is approximately below $2\rho_0$, the high temperatures above 40 MeV ignite the transition to the quark phase, increasing Y_q up to 0.1 for the DD2njlG EOS. In the following millisecond the NSs heat up and fuse in a dense remnant. The quark fraction starts concentrating in the center of the remnant, where the density increase above $2\rho_0$. After ≈ 10 ms the quark phase is present only inside the remnant core, where $\rho \geq 3\rho_0$, reaching values of Y_q up to 0.3 for the DD2njlG EOS and 1 for the DD2njlM EOS. In this stage Y_q does not correlate with the temperature, since the hot matter with $T \sim 50$ MeV is found in the outer region of the remnant, where the density $\rho \lesssim 1.5\rho_0$ is too low to induce a PT to quark matter.

A quantitative comparison of the Y_q between the simulations employing the DD2njlG and the DD2njlM EOSs is not possible during the first millisecond of the merger, since the quark fraction is not well defined during the PT with a MC. After ≈ 10 ms the core of the remnant ($\rho \sim 2.5\rho_0$) with DD2njlM EOS is completely made of deconfined quark matter, i.e. achieves $Y_q = 1$. The DD2njlG EOS remnant exhibits lower value of the quark fraction, reaching $Y_q \gtrapprox 0.3$ only in the innermost region of the core, where $\rho \gtrsim 3\rho_0$. This occurs

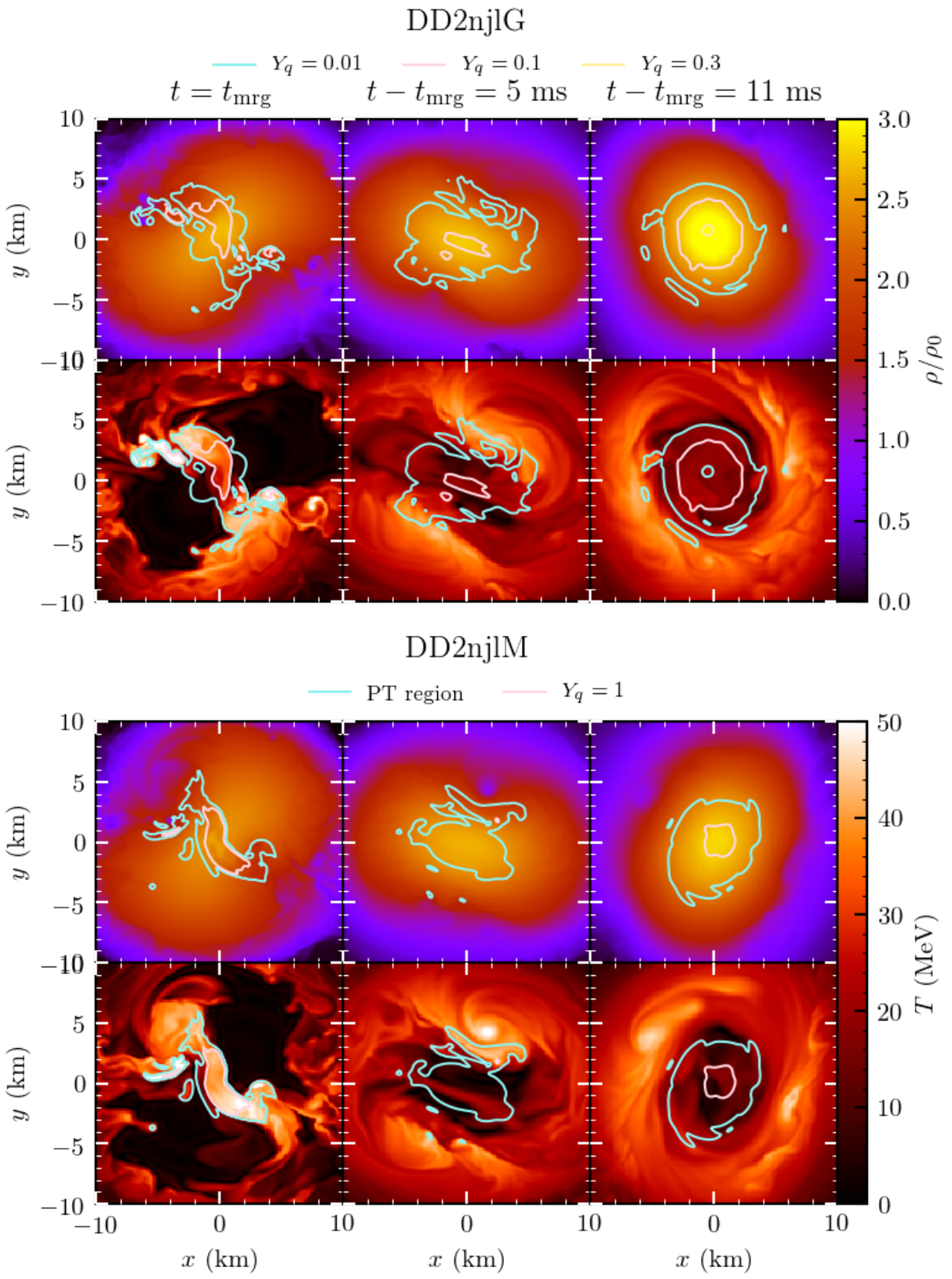

Figure 6.4: Remnant's density, temperature and quark fraction across the xy plane during the merger of the equal mass binaries with the DD2njlG EOS (top panel) and the DD2njlM EOS (bottom panel) at different times from merger. Note that, since Y_q is not defined during the PT with the MC, we cannot indicate the value of Y_q.

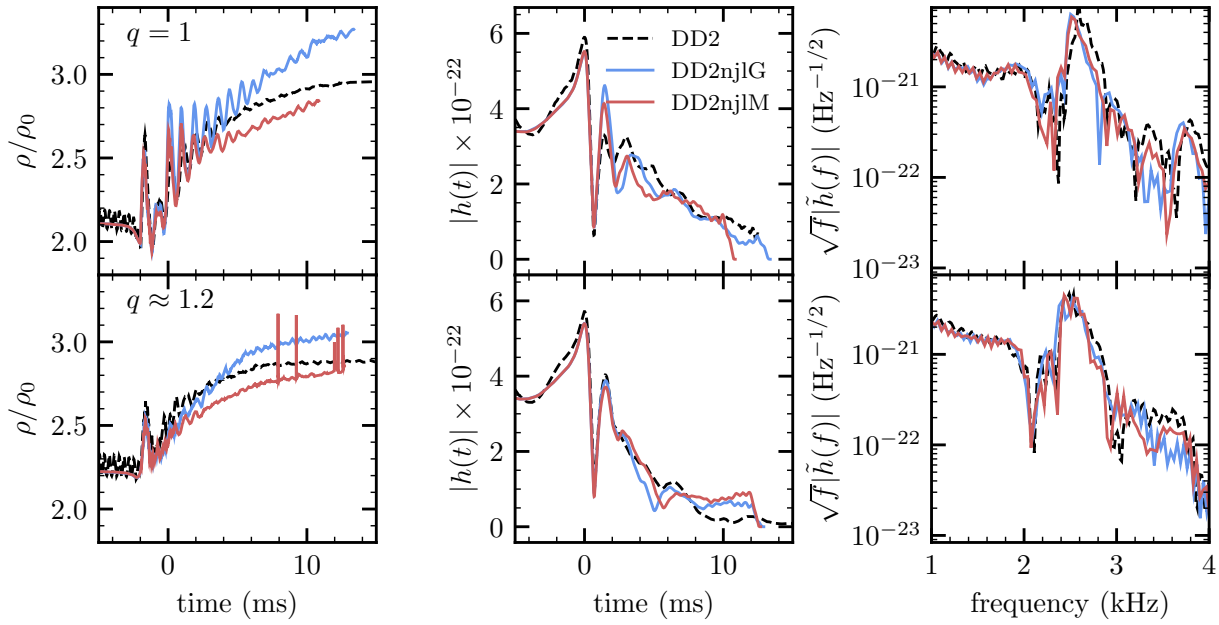

Figure 6.5: From left to right, central density, strain of the $l = 2,\ m = 2$ mode and PSD of the $l = 2,\ m = 2$ mode for the HR simulations with $q = 1$ (upper panels) and $q = 1.18$ and $q = 1.20$ (lower panels), employing the pure hadronic DD2 EOS (black dashed), the DD2njlG EOS (blue) and the DD2njlM EOS (red). We consider a GW source at a distance of 40 Mpc.

despite the higher density is reached in the merger employing the DD2njlG EOS, as also shown in the left panel of Fig. 6.5.

To conclude we remark that, since the electron fraction of the remnant remains low during the merger and post-merger, varying only by a little amount, we do not observe any dependence of Y_q by the electron fraction.

6.3.2 Effects of the phase transitions on the gravitational waves

As done in Chapter 4 we analyze the GW signal as extracted at a coordinate radius of ≈ 591 km from the BNS center of mass. The merger dynamics, as so as the GW signal, between the pure hadronic DD2, the DD2njlG and DD2njlM EOSs is indistinguishable during the inspiral phase, where no quarks are present. As the thermodynamics conditions of the PT are reached, i.e. from the merger on, the three EOSs describe different mergers.

In Fig. 6.5 the maximum rest mass density (left panel), the GW strain of the $l = m = 2$ mode (central panel) and the GW PSD of the $l = m = 2$ mode (right panel) as computed from the equal and unequal BNS mergers with the DD2, DD2njlG and the DD2njlM EOSs are compared. During the post-merger phase, the remnant's maximum rest mass density behaves differently across the three EOSs. Core bounces are smaller with the purely hadronic

DD2 EOS while they are larger with the DD2njlM and DD2njlG EOSs, with the latter showing greater fluctuations. Indeed, stiffer EOSs result in smaller density changes for the same external pressure variation (see Fig. 6.3 as a reference). Within the first 7 milliseconds post-merger, when the more relevant core bounces are found, the three BNS mergers exhibit maximum density and temperature ranging from $2-3\rho_0$ and $40-80$ MeV, respectively. In this density and temperature range, the purely hadronic DD2 EOS is the stiffest, followed by the DD2njlM EOS, while the DD2njlG EOS is the softest (see Fig. 6.2). The core bounce amplitudes follow this trend. Despite providing more pressure support, mergers utilizing the pure hadronic DD2 EOS reach higher central density than the mergers employing the DD2njlM EOS. Indeed, the core bounces tend to distribute the matter from the center of the remnant towards the exterior, thereby reducing the central density. While the remnants with DD2njlG and DD2njlM EOSs have similar radial density distributions beyond 5 km from the center, the remnant with the DD2 EOS is less dense in the regions around 5 and 15 km from the center in comparison with the other two, primarily due to less prominent core bounces. This explain why the remnant described by the purely hadronic DD2 EOS is $\approx 2-3\%$ denser than its counterpart with the DD2njlM EOS.

Despite the difference in the maximum density, the GW strain of the $l=m=2$ mode $|h(t)|$ is very similar in all the simulated BNS mergers, independently on the EOS. The same can be said for the post-merger PSD of the $l=m=2$ mode of the GWs $|\tilde{h}(f)|$. In particular we are interested in the post-merger peak frequency f_2 of the PSD computed from the simulations employing the DD2njlG and DD2njlM EOSs and its shift Δf_2 with respect to the pure hadronic case. Despite being very similar, most of the BNS mergers employing a PT to quark matter shows a negative Δf_2 from -16 to -174 Hz, as summarized in Table 6.1 (see the Δf_2 column). Only the $q=1.18$ HR and LR simulations employing the DD2njlM EOS show a positive shift of the f_2 peak with respect to the respective LR and SR simulations with $q=1.20$ and DD2 EOS. However, we must stress that the comparison of all the unequal mass BNS simulations is only indicative, since the mass ratio of the simulations employing the PTs is slightly different from the one implementing the pure hadronic EOS. This may affect the comparison of the Δf_2 computed from the unequal BNS merger simulations with different EOSs. Overall, we can conclude that our findings do not agree with recent studies in the literature, which indicate an increase in the post-merger frequency of few 100 Hz [Most et al., 2019, Prakash et al., 2021, Bauswein et al., 2019]. The cause of this inconsistency remains unclear. Our intention is to explore the source of this discrepancy in a future work.

In all the simulations with a PT to quark matter presented in this work, the differences in the peak frequency are broadly comparable to the uncertainties in the Fourier transform [1] $\Delta\mathrm{FT} = \mathrm{t}_{\mathrm{end}}^{-1}$ (see rightest column of Table 6.1) so they cannot be measured even in the

[1] Since the remnant in our simulation sample does not collapse before t_{end} we can take t_{end}^{-1} as the nominal

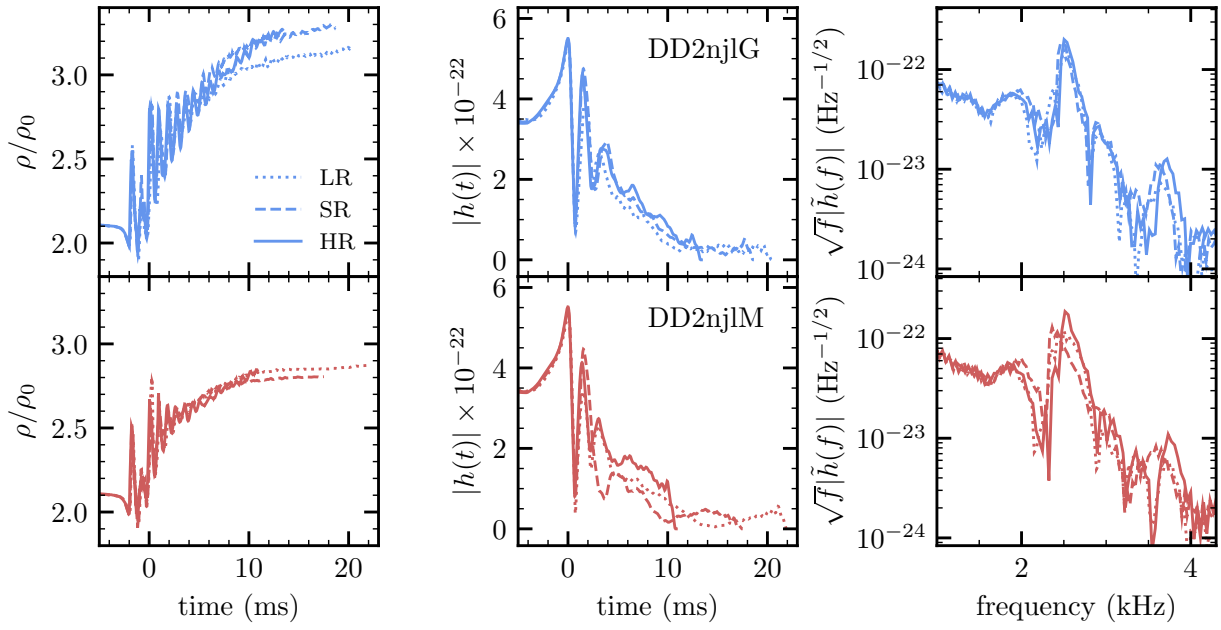

Figure 6.6: Maximum baryon rest mass density, GW strain and power spectrum of the LR (dotted lines), SR (dashed lines) and HR (solid lines) equal mass simulations employing the DD2njlG (upper row, blue) and the DD2njlM (lower row, red) EOSs. We consider a GW source at a distance of 40 Mpc.

scenario of signals with very high signal to noise ratio (SNR). At least from a formal point of view, this can change if the remnant does not collapse for long enough time, such that ΔFT decrease sufficiently enabling the measure of Δf_2.

6.3.3 Dependence of the results on the numerical resolution

As previously discussed, the numerical resolution of the simulation (see Sec. 2.3.1) can have an impact on the outcome. In Fig. 6.6 we compare the maximum baryon rest mass density, the GW strain and the power spectrum of the simulations with the DD2njlG and the DD2njlM EOSs at different resolutions. We note that, on each quantity, there is no clear systematic on the effect of the numerical resolution. For example, the maximum density reached by the LR simulation with the DD2njlG EOS is lower than the one reached by the SR and HR simulations, while the opposite occurs for the simulations with the DD2njlM EOS. Anyway, the asymptotic value of the rest mass density only vary of $\sim 3\%$ among the simulations with different resolutions. Similarly, also the differences between the strain and the power spectrum depend weakly on the numerical resolution. In particular, the difference in f_2 due to the numerical resolution is at most of 150 Hz. However, one must note that for the two simulations in question, i.e. the HR and SR equal mass simulations employing the

uncertainty on the Fourier transform.

DD2njlM EOS, the uncertainties on the f_2 are of 92 and 57 Hz, respectively and then the error on the f_2 difference is 149 Hz.

We can conclude that our findings are solid with respect to the numerical resolution of the simulations.

Chapter 7

Conclusions

In this thesis, we explored the evolution of BNS systems using 3+1 numerical relativity simulations that cover the latest orbits, the merger, and the early post-merger phase. The main goal was to address some of the unsolved questions in the field in terms of theoretical modeling, with a close connection with observables and observational aspects of compact binary mergers.

The thesis focused mostly on three research directions:

1. In Chapter 4, we analyze a series of numerical simulations targeted to the BNS merger event GW190425, also to anticipate the outcomes of future detections of similar events in terms of remnants properties, dynamical ejecta, nucleosynthesis signatures, and kilonova light curves. Moreover, the possible absence of an electromagnetic counterpart raises intriguing questions, such as whether the lack of an EM counterpart can impose constraints on the equation of state (EOS) and/or the binary parameters.

2. The material expelled during the merger and post-merger phase forms a torus-shaped cloud around the proto-neutron star, known as an accretion disk. Accretion disks resulting from BNS mergers play a crucial role in various processes related to compact binary mergers and multimessenger astrophysics. In Chapter 5, we have characterized the accretion disks resulting from BNS mergers starting from a large sample of simulations.

3. The extremely high densities reached during the merger phase raise concerns about the potential existence of a novel state of matter, comprising deconfined quarks and gluons, known as a quark-gluon plasma (QGP). Properties of the QGP under conditions of high densities and moderate temperatures remain unattainable in terrestrial laboratories. Multimessenger astrophysics provides an opportunity to use BNS mergers as natural laboratories for fundamental physics. In Chapter 6, we have studied

the effect of different PT construction in the EOS of nuclear matter on some potential observables, including GWs.

Below, we detail the major conclusions of each analysis and we critically discuss them.

7.1 Numerical simulations and analysis of the BNS merger GW19045

In Chapter 4, we investigated in detail the outcome of BNS merger simulations targeted to GW190425 with detailed microphysics. We set up 28 simulations with finite temperature, composition dependent NS EOSs, and neutrino radiation. For each simulation we extracted remnant and dynamical ejecta properties, and we computed in post-processing nucleosynthesis yields and kilonova light curves. Using 4 EOSs compatible with present constraints and considering a broad range of mass ratios, we aimed at giving an accurate description of GW190425-like BNS mergers and answering a number of questions, including: what can we expect from future detection of this kind of events in terms of remnant, dynamical ejecta, nucleosynthesis signature and kilonova light curves? Despite the wide sky localization of GW190425, can the lack of an EM counterpart give constraints on the EOS and/or the binary parameters?

We found that such BNS mergers, characterized by an unusual high total mass of 3.4 $M_\odot$ and a chirp mass of 1.44 $M_\odot$, prompt collapse to a light black hole of $\sim$ 3.2 $M_\odot$ with a dimensionless spin parameter that ranges from 0.73 to 0.83, surrounded by a light disk formed by tidal interactions. Asymmetric BNS mergers with stiffer EOS have more massive remnant disk, ranging from 10^{-5} $M_\odot$ for equal mass binaries with soft EOS, to 0.1 $M_\odot$ for the most asymmetric BNS in our sample.

During the late inspiral and merger, previous to the collapse, the simulated binaries expel a small amount of matter in the form of dynamical ejecta. The high compactness is responsible for less deformable NSs while the prompt collapse inhibits the production of shock-heated ejecta. This explains the lower values of ejected mass compared to what previously found for BNS whose chirp mass is closer to what is observed in the Galactic BNS population and in GW170817. Since tidal interactions are the main cause of dynamical ejection, we found that asymmetric BNS mergers with a stiff EOS are able to unbind up to $\sim 10^{-3}$ $M_\odot$ of ejecta, while equal mass BNS with a soft EOS only eject $\lesssim 5 \times 10^{-6}$ $M_\odot$ of matter. Also the properties mostly depend on the mass ratio and on the EOS of the BNS merger. Dynamical ejecta spread all over the space but it is mainly concentrated along the orbital plane in an opening angle which goes from 54° for symmetric BNS to 18° for the more asymmetric BNS in our sample. We also discuss the distributions of electron fraction,

velocity at infinity and entropy of the dynamical ejecta and their trends with the binary parameters.

In all the considered simulations, the resulting r-process nucleosynthesis pattern does not show peculiar behaviors and reflects directly the properties of the matter outflow. For ejecta dominated by cold, neutron-rich matter, we noticed a remarkably robust production of heavy elements between the second and the third r-process peaks, as opposed to the less significant one of lighter elements. The latter is however more sensitive to the binary parameters. In fact, around the first peak the nucleosynthesis pattern changes depending on the EOS considered (even if not with a clear trend) and increases with decreasing mass ratio, but always on a lower level with respect to the Solar residuals.

For the kilonova, we found that narrow-band light curves in the B- and r-bands peak within the first few hours after the merger with a rapid subsequent decline, while the emission at IR frequencies lasts several days. Assuming a distance of 70-130 Mpc or 130-250 Mpc, compatible with what was inferred for GW190425, and combined with a edge-on or face-on inclination, respectively, the peak magnitude in every band is not brighter than ~ 20 magnitudes, as opposed to the case of kilonovae resulting from BNS more compatible with the Galactic BNS population or with GW170817. As such, we conclude that it could be difficult to observe such a transient at the distances inferred for GW190425 with present wide-field surveys, unless a good sky localization allows for deeper and localized searches. This can be traced back to the low mass of the dynamical ejecta and of the disk remnant. Only a BNS with a particularly stiff EOS, a high mass ratio and a source distance around ~ 70 Mpc would have been detected by the ZTF facility according to our findings. This would favor a BH-NS merger in the case of a kilonova detection resulting from a compact binary merger similar to GW190425 by ZTF.

Future follow-up campaigns will be joined by Vera Rubin (LSST) observatory. In spite of the relatively small field of view (~ 10 deg^2) compared to ZTF, the short read-out time, the all-sky reference and a sensitivity of $24.7 - 27.5$ AB magnitudes in the r-band will permit Vera Rubin to be a powerful resource to detect faint kilonovae [Andreoni et al., 2021]. Vera Rubin is potentially able to detect kilonova signals from some of the simulated BNS mergers. For a kilonova at a distance of $130 - 250$ Mpc, a kilonova signal would be detectable for BNS mergers with $q > 1.33$ and, in the case of a very stiff EOS (as DD2) for the BNS with $q = 1.18$. In addition, for smaller distances, i.e. $70 - 130$Mpc, also kilonovae resulting from slightly asymmetric BNS mergers could be observable. Finally, for a distance comparable to the one of GW170817, all the simulated kilonovae could be potentially detected. However, despite the increased sensitivity, Vera Rubin's field of view will cover efficiently up to 200 deg^2, far less than the confidence region of GW190425. Thus, a better sky localization will be crucial.

We compared our results with recent works that aim to predict the remnant and ejecta

properties, as well as the kilonova light curves of GW190425. We find overall similar qualitative trends, but with some quantitative differences. In the case of Dudi *et. al.*, who explored a comparable set of simulations in numerical relativity, trends in the ejecta masses and disk masses are very similar, with a better quantitative agreement for the latter than for the former. We speculate that these differences could be due to the different microphysical setups (both polytropic EOSs and the lack of neutrino radiation tend to overestimate the dynamical ejecta) as well as resolution effects. All these uncertainties could be even amplified in this case due to the small amount of ejecta, that makes their identification and tracking inside the computational domain more challenging. Raaijmakers et al. [2021] and Barbieri et al. [2021] computed kilonova light curves for GW190425-like events and they found kilonova transients systematically brighter than ours. A plausible source of discrepancy could be the use of existing fitting formulae to predict the dynamical ejecta and the disk mass. Indeed the peculiarity of GW190425 slip to the predictions given by the formulae presented in previous works [Foucart et al., 2017, Nedora et al., 2022, Barbieri et al., 2019, Radice et al., 2018b] that we took into exam. Fitted on large sample of numerical simulations of BNS mergers with parameters however different from the ones of GW190425, they usually predict an enhancement of the dynamical ejecta and of the disk mass with respect to our simulations, with observable consequences on the kilonova. This result underlines the difficulty in providing fitting formulae for the ejecta properties valid over a broad range of binary parameters and even outside of the fitting range. This could indeed strongly affect their effectiveness. The detection of GW190425 demonstrated that, in addition to the sample of BNS mergers whose properties are close to the ones observed in the current population of Galactic BNS systems, there could be a population of GW-loud events characterized by larger chirp masses. Their modeling is less developed and their properties (including the smaller ejecta and disk masses) are possibly more challenging to study. Our work represents a step forward in the direction of better characterizing such systems. Considering the GW190425 follow-up campaign, we conclude that, even assuming that the sky coverage was enough and the binary was a BNS system, no strong constraints on the BNS parameters nor on the EOS can be inferred by the lack of EM signal. Only the corner case of very stiff EOS and extreme mass ratios could be possibly excluded. Future observations of EM counterparts by wide-field surveys, such as ZTF or Paolmar Gattini-IR telescope, for such a population outsider will be non trivial, unless the merger distance decreases to $\lesssim 40$ Mpc. However, large uncertainties still remain. We mostly quantified errors due to finite resolutions, but we expect possibly larger uncertainties due to systematics and modeling limitations. Further works in the modeling of both BNS mergers and their EM counterparts is required to properly assess these limitations.

7.2 Accretion disks in binary neutron star mergers

In Chapter 5, we have studied the geometrical, dynamical and thermodynamical properties of 38 disks from numerical relativity simulations of BNS mergers, classified by the fate of remnant: 20 long-lived, 9 short-lived and 9 prompt-collapsed. Most of our simulations are targeted to the BNS merger GW170817, with $M_{\rm chirp} = 1.18$ M$_\odot$. A subset of 6 simulations are targeted to GW190425, with $M_{\rm chirp} = 1.44$ M$_\odot$.

We found that BNS accretion disks are remarkably thick. In particular, the aspect ratio of the disks from mergers that do not undergo prompt-collapse decreases with the mass ratio, going from ≈ 0.8 to below 0.3, while disks from prompt-collapsed mergers span the range $0.4 - 0.15$. Such a large aspect ratio reflects the significant thermal support inside the disk during the first tens of milliseconds after merger.

The mass and angular momentum of the disks span a broad range of values, going from 5×10^{-4} to 0.3 M$_\odot$, for the mass and from 2×10^{13} to 10^{16} M$_\odot$ cm^2 s^{-1} for the angular momentum. We have found that the specific angular momentum is almost constant in any of the disk in our sample, taking values between 3 and 5 $\times 10^{16}$ cm^2 s^{-1}. This is also confirmed by the distribution of the specific angular momentum with the angular velocity, which is compatible with the so called j-const law.

In the first $10 - 15$ ms after merger, disks where a central massive NS is present show an outflow of matter at any radial distance from the remnant, which decrease with time and radius from a maximum of 10 M$_\odot$ s^{-1}. A persistent accretion only occurs when the central object collapse to a BH, with an initial accretion of 10 M$_\odot$ s^{-1}. After an initial transient phase which lasts ~ 5 ms, both ejection and accretion rates decrease to 1 M$_\odot$ s^{-1}, similar to the values found in many works of long-term disk evolution, where the initial disks are considered as equilibrium tori.

The specific entropy in the disk has different behaviors depending on the mass ratio of the binary. For small mass ratios ($\lessapprox 1.3$), most on the matter in the disk spans the rather limited entropy range, with entropy of $4 - 8 k_{\rm B}$ baryon^{-1} in the density range $10^{10} - 10^{13}$ g cm^{-3}. It must be stressed that, at lower densities, the entropy of a non-negligible fraction of the disk increases to $15 - 20 k_{\rm B}$ baryon^{-1}. We have found that the entropy is distributed around a sigmoidal function of the rest mass density, which can be satisfactorily modeled using a modified arcotangent. For higher mass ratios, the disks decompose in a tidal and a shocked components. In this case the bulk of the disk can be regarded as approximately isentropic.

Similar to the specific entropy, also the behavior of the electron fraction inside the disk changes according to the mass ratio. For $q \lesssim 1.3$, in the high density region ($10^{11} - 10^{13}$ g cm^{-3}) the matter is neutron rich ($Y_{\rm e} \approx 0.1 - 0.2$). At lower density the electron fraction increases to ≈ 0.4 and a negligible amount of matter, with respect to the total

disk mass, reaches even higher Y_e. The distribution of the electron fraction with the density follows a sigmoidal function, for which we provide a fit in terms of an arcotangent. At higher mass ratios the electron fraction, as the entropy, is nearly constant and very low.

We note that the simulations that constitute our sample and on which we base our analysis do not include some physical input that might affect our findings. In particular, they do not take into account the presence magnetic fields. Although the effects of magnetic fields might be less significant in the first few tens of milliseconds following a merger, they have been demonstrated to strongly influence the redistribution of mass and angular momentum on timescales exceeding 20-30 milliseconds after the merger [Combi and Siegel, 2023b]. In addition, the treatment of neutrino interactions and transport is somewhat simplistic, due to the use of the `Leakage + M0` (see Sec. 2.3.1). Having access to more realistic datasets that model these processes might have an impact on e.g. the spatial distribution of matter in the disks (affecting the aspect ratio and rotational profile) and/or their composition and thermodynamics. Despite we use GRLES as a source of turbulent viscosity in some of our simulations, a more realistic physical source of viscosity could affect the geometry and the dynamical evolution of the disk, possibly affecting also the specific angular momentum distribution.

In this thesis however, our objective is to provide a comprehensive qualitative description of BNS accretion disks, until now missing in the literature on the subject. The effects mentioned above are going to have only rather limited quantitative effects, such as varying our estimates for disks parameters to the level of a few percents. Therefore we are confident that the description we provide is qualitatively realistic and sound, and very unlikely to dramatically change by more realistic simulation setups.

In light of these considerations, we think that the characterization of BNS accretion disks that we provide can be useful to the scientific community. First of all, the structure of such disks is interesting in its own right and it has not yet systematically been studied in the literature. Furthermore, as mentioned in previous Sections, many works that perform simulations of BNS accretion disks employ initial conditions that lack in realism, particularly regarding the setup of the thermodynamic state and composition of the disks. Such simulations could achieve greater realism by employing disks models that are closer to the specifics we have provided.

Finally, we have uncovered some properties of the accretion disks that deserve further investigation in their own right, e.g. the mechanism by which their rotational profile achieves a configuration of constant specific angular momentum and whether they evolve towards a Keplerian profile on secular timescales. We however leave this investigation for future work.

7.3 Effects of first order QCD phase transitions in BNS mergers

In Chapter 6, we introduced 12 new BNS mergers simulations employing fully general relativistic neutrino-radiation hydrodynamics with two new finite-temperature EOSs with a PT to quark matter. All the simulations share the same hadronic DD2 EOS, the same treatment of pure quark matter within the NJL model and differs only by the PT construction and the mass ratio. We make use of the MC and the GC to investigate the effects of two extremes of a first order PT to quark matter on the BNS merger dynamics and its observable outcomes. The two new EOSs, DD2njlG and DD2njlM, obtained from the GC and the MC of the PT, respectively, only differ in the region of the PT.

We found that quark matter start to form at the collisional interface during the merger, where the temperatures are above 40 MeV. After the first ~ 10 ms post-merger the quarks are collected in the inner part of the remnant core. The higher values of the Y_q are reached by the DD2njlM EOS, where pure quark matter is found. On the contrary, the DD2njlG EOS, despite reaching higher densities than the DD2njlM EOS, only arrive at $Y_q \approx 0.3$ in the central denser part of the remnant.

The softening of the EOS prompted by a PT to quark matter slightly modifies the GW signal with respect to the one form pure hadronic BNS merger. In particular, the change in the moment of inertia is expected to shift the post-merger peak frequency f_2 of the GW PSD. Despite we found a systematic shift of f_2 to lower values (with the exception of two simulations, see Sec. 6.3.2), the magnitude of the shift is small and usually comparable to the nominal uncertainty on the Fourier transform even for a GW signal lasting ≈ 20 ms. This reveals the difficulty of detecting a PT to quark matter in a BNS merger event. Long-living remnants with sufficiently high SNRs are needed in order to detect such a frequency shifts. In general, we are not able to delineate particular signatures capable of differentiate between an EOS with a Maxwell or Gibbs transition to quark matter.

In order to systematically asses the differences in the BNS merger dynamics and outcomes, we only focus on one pure hadronic EOS, one single quark model (the NJL model) and two extreme end of a first order PT, namely the GC and the MC. Different hadronic sector of the EOS, as well as different quark model, as the MIT extended model implemented in Prakash et al. [2021], should be eventually implemented into a similar framework to asses the robustness of the result presented here.

Appendix

A. Flux on an embedded spherical surface

We want the fluxes of extensive variables along a spherical surface S^2 of radius R embedded in the 3D space of cactus. Given R we interpolate the hydrodynamic variables of the most refined level that contains S^2. Then we compute the fluxes of a generic extensive quantity P as $f_P = \rho v_r$, where $\rho(\theta, \phi)$ is the volume density of P interpolated along S^2 and v_r is the radial velocity along the radial direction.

In order to integrate quantities on S^2 we need the volume element, i.e. the square root of the determinant of the induced metric on S^2. Given an immersion $F : S^2 \to \mathcal{C}$, where $\mathcal{C}$ is the 3-dimensional manifold in which the spherical surface is embedded, the induced metric on S^2 is the pull-back induced by F of the metric on $\mathcal{C}$. An usual parametrization in local coordinates is

$$\begin{aligned} x &= R\sin\theta\cos\phi \quad \theta \in [0, \pi/2] \\ y &= R\sin\theta\sin\phi \quad \phi \in [0, 2\pi] \\ z &= R\cos\theta \end{aligned} \tag{1}$$

then, in local coordinates the pull-back $f^* \circ g$, where g is the metric on $\mathcal{C}$, is:

$$g_{ij}^{S^2} = g_{kl}\frac{\partial x^k}{\partial\theta^i}\frac{\partial x^l}{\partial\theta^j} \ , \tag{2}$$

where $\theta^1 = \theta$, $\theta^2 = \phi$. Then,

$$\mathrm{vol}_{\mathrm{S}^2} = \sqrt{\mathrm{g}^{\mathrm{S}^2}_{\theta\theta}\mathrm{g}^{\mathrm{S}^2}_{\phi\phi} - 2\mathrm{g}^{\mathrm{S}^2}_{\theta\phi}} \ . \tag{3}$$

Explicitly,

$$\begin{aligned} g_{\theta\theta} = &\left(g_{xx}\cos^2\phi + g_{yy}\sin^2\phi + 2g_{xy}\cos\phi\sin\phi\right)R^2\cos^2\theta \\ &- 2\left(g_{xz}\cos\phi + g_{yz}\sin\phi\right)R^2\cos\theta\sin\theta + g_{zz}R^2\sin^2\theta \ , \end{aligned} \tag{4a}$$

$$g_{\phi\phi} = \left(g_{xx}\sin^2\phi + g_{yy}\cos^2\phi - 2g_{xy}\cos\phi\sin\phi\right)R^2\sin^2\theta \ , \tag{4b}$$

$$g_{\theta\phi} = \left[(-g_{xx} + g_{yy})\cos\phi\sin\phi + g_{xy}(\cos^2\phi - \sin^2\phi)\right] R^2\cos\theta\sin\theta + (g_{xz}\sin\phi - g_{yz}\cos\phi)R^2\sin^2\theta \ . \tag{4c}$$

Note that we obtain the Euclidean metric of the spherical surface $ds^2 = R^2 d\theta + R^2\sin^2\theta d\phi$ in the limit of $R \to \infty$. For large R we can write $g_{ij} = \delta_{ij} + \epsilon_{ij}$ and, assuming $\epsilon_{11} = \epsilon_{22} = \epsilon$, $\epsilon_{12} \ll \epsilon$ for simplicity[1], the $\phi\phi$ component can be written as

$$g_{\phi\phi} = (1+\epsilon)R^2\sin^2\theta \ ,$$

then the relative deviation from the $\phi\phi-$component of the Euclidean metric on S^2 is

$$\frac{g_{\phi\phi}}{R^2\sin^2\theta} - 1 = \epsilon \sim 3\% \ , \tag{5}$$

Where the estimate come from the analysis of some BNS simulations with $R = 200$ $M_\odot$.

B. Standard deviation of the azimuthal angle

The azimuthal angle of the dynamical ejecta distribution $\phi_{\rm ej}$ has a 2π-rotational symmetry. So its mass weighted SD $\phi_{\rm ej}^{\rm SD}$ depends on an arbitrary chosen reference. For each angular bin ϕ_i of normalized weight w_i of the ejecta distribution we define the periodic shift $S_\delta(\phi_i)$ as:

$$S_\delta(\phi_i) := \begin{cases} \phi_i + \delta & \text{if } \phi_i < 2\pi - \delta \ , \\ \phi_i + \delta - 2\pi & \text{if } \phi_i \geq 2\pi - \delta \ . \end{cases} \tag{6}$$

Let's indicate with $S_\delta(\phi_{\rm ej})$ the distribution obtained after the shift of awl the ϕ_i.The average $\langle\phi_{\rm ej}\rangle_\delta \equiv \langle S_\delta(\phi_{\rm ej})\rangle$ is then

$$\langle\phi_{\rm ej}\rangle_\delta = \langle\phi_{\rm ej}\rangle_0 + \delta - 2\pi W_\delta \, , \tag{7}$$

where W_δ is the total weight of the bins $\phi_i \geq 2\pi - \delta$,

$$W_\delta = \sum_{\phi_i \geq 2\pi - \delta} w_i \leq 1 \, . \tag{8}$$

We choose $\delta = \delta^*$ such that $\langle\phi_{\rm ej}\rangle_\delta$ is centered in the half of the interval, i.e in π [2]:

$$\delta^* - 2\pi W_{\delta^*} = \pi - \langle\phi_{\rm ej}\rangle_0 \, . \tag{9}$$

[1] $\epsilon_{12} \sim 10^{-2}\epsilon$ from numerical computations at $R = 200$.

[2] Multiple δ^* that satisfy this condition can exist, so we also add the condition that the mode of the distribution lies in the interval $\pi - \pi/4 \leq \phi \leq \pi + \pi/4$.

The root mean square (RMS) of $\phi_{\rm ej}$ after the shift S_δ is

$$\mathrm{RMS}_\delta(\phi_{\rm ej}) = \left[\mathrm{RMS}_0(\phi_{\rm ej})^2 + 2\delta\langle\phi_{\rm ej}\rangle_0 + \delta^2 + 4\pi\left((\pi-\delta)W_\delta - \overline{\langle\phi_{\rm ej}\rangle}_\delta\right)\right]^{1/2}, \tag{10}$$

where $\mathrm{RMS}_0(\phi_{\rm ej})$ and $\langle\phi_{\rm ej}\rangle_0$ are the unshifted RMS and average of ϕ and $\overline{\langle\phi_{\rm ej}\rangle}_\delta$ is the average of the bins $\phi_i \geq 2\pi - \delta$,

$$\overline{\langle\phi_{\rm ej}\rangle}_\delta = \sum_{\phi_i \geq 2\pi-\delta} w_i\phi_i\,. \tag{11}$$

Finally, the SD with respect to the new average $\langle\phi_{\rm ej}\rangle_\delta$ is

$$\begin{aligned}\sigma_\delta(\phi_{\rm ej}) &= \sqrt{\sum_i w_i(S_\delta(\phi_i) - \langle\phi_{\rm ej}\rangle_\delta)^2} \\ &= \sqrt{\mathrm{RMS}_\delta(\phi_{\rm ej})^2 - \langle\phi_{\rm ej}\rangle_\delta^2}\,.\end{aligned} \tag{12}$$

C. Prompt and delayed collapse

In this section we summarize the analysis of 188 numerical simulations of irrotational BNS mergers, with total gravitational mass $M_{\rm tot} \in [2.7, 3.3]$, mass ratios from 1 to 1.67, 6 different EOSs and, usually, two resolutions: low resolution (LR) and standard resolution (SR). Roughly 100 BNS models undergoes to a prompt-collapse to a BH. Most of the remaining models show a delayed collapse within few milliseconds. A small fraction of 8 simulations collapse to a BH after 5 ms or more and 29 mergers does not collapse within the simulated time. This simulations has been already presented in Kashyap et al. [2022] and Perego et al. [2022a], where the focus of the study was to determine the threshold mass $M_{\rm thr}$ for the onset of a prompt-collapse to a BH.

The aim of the analysis presented here is to asses the possible difference between prompt-collapsed and delayed-collapsed BNS mergers in the post-merger evolution, especially in the first milliseconds after merger. The main targets of this study are the mass of the newly formed disk that surrounds the central object and the mass of the ejected mass. In the first milliseconds after merger, if the remnant does not promptly collapse to a BH, the subsequent core bounces eject mass to the exterior. The gravitationally bound fraction of this matter contributes to the disk mass, while the unbound matter constitute the dynamical ejecta. Naively, more are the number of remnant's core bounce, more expelled matter is expected. Therefore, an important distinction between prompt-collapsed and delayed-collapsed BNS mergers would be in the disk and ejected masses. In particular, for every given mass ratio q, the aforementioned quantities should increase with the number of core bounces, defined here as the peaks in the minimum of the lapse function. In Fig. 1 we plot the disk and

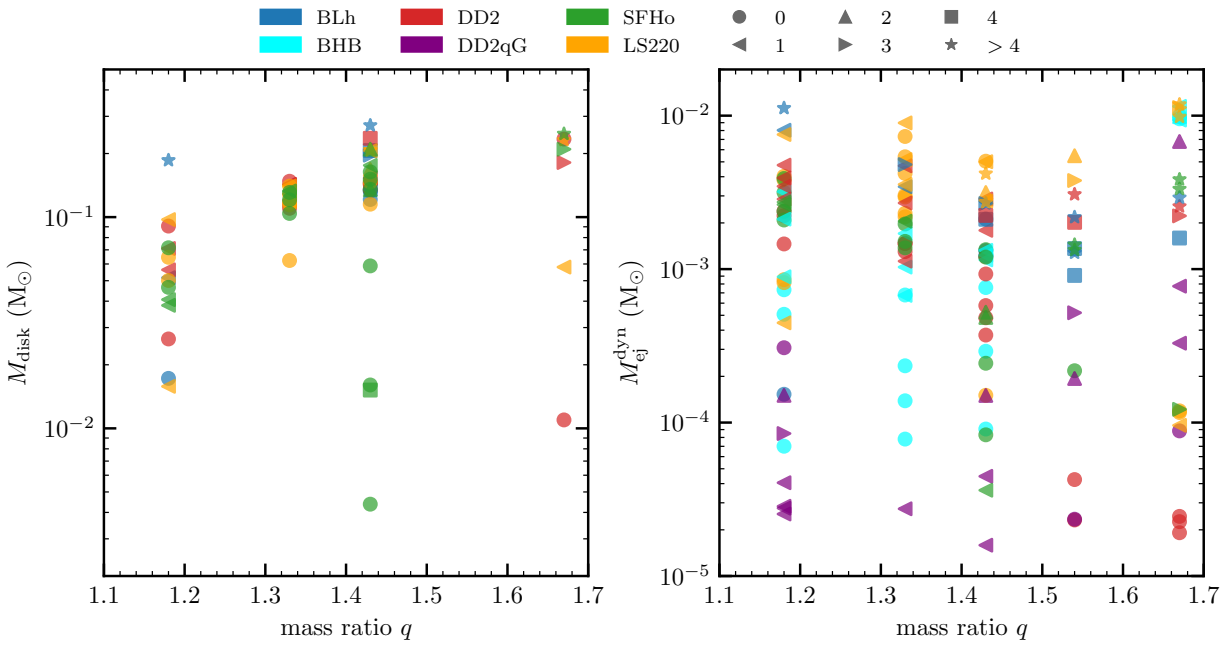

Figure 1: Disk and ejected mass as a function of the mass ratio. Colors indicates the different EOSs while the markers represent the number of bounces. Note that has been possible to compute the disk mass only for a subsample of simulations.

ejected mass as a function of the mass ratio q. The number of bounces, represented by the different markers, is only marginally responsible to the total ejected material. Indeed, some of the prompt-collapsed remnant (circles) have higher disk and ejected mass than some of the delayed-collapsed ones. Nevertheless, large number of bounces (e.g. larger than 4), is in general related to the higher values of both disk and ejected mass in the sample. This is supported by Fig. 2, where the dynamical ejecta and disk mass are plotted against the collapse time. Remnant that collapse in more than 5 ms show higher values of both ejecta and disk masses.

In Fig. 3 the histograms of the dynamical ejecta mass $M_{\rm ej}^{\rm dyn}$ is showed. BNS mergers categorized as prompt and delayed collapsed has slightly different distributions of $M_{\rm ej}^{\rm dyn}$. The former is characterized by a longer tail toward lower values of $M_{\rm ej}^{\rm dyn}$ with respect to the latter. Nevertheless, prompt-collapsed merger are able to expel the same amount of matter as the delayed-collapsed ones, as indicated by the peak around $M_{\rm ej}^{\rm dyn} \sim 10^{-3}$ $M_\odot$.

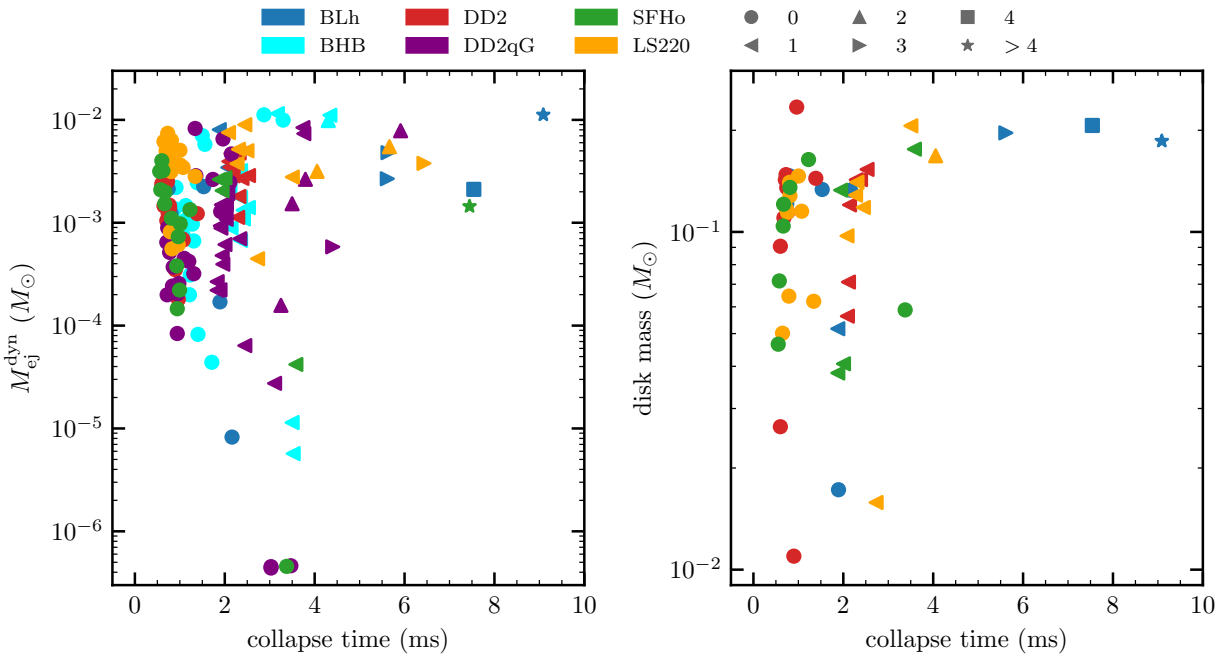

Figure 2

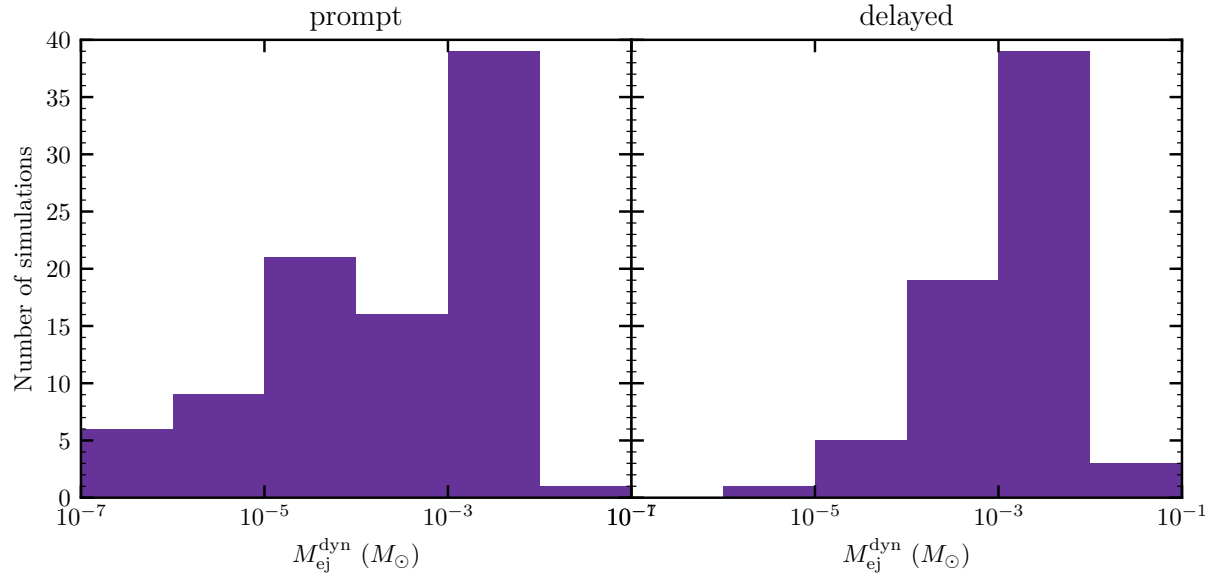

Figure 3: Histogram of the dynamical ejecta mass for the prompt-collapsed (left) and the delayed-collapsed simulations (right).

Bibliography

J. Aasi et al. Advanced LIGO. *Class. Quant. Grav.*, 32:074001, 2015. doi: 10.1088/0264-9381/32/7/074001.

B. P. Abbott et al. Multi-messenger Observations of a Binary Neutron Star Merger. *Astrophys. J.*, 848(2): L12, 2017a. doi: 10.3847/2041-8213/aa91c9.

B. P. Abbott et al. GW170817: Measurements of neutron star radii and equation of state. *Phys. Rev. Lett.*, 121(16):161101, 2018. doi: 10.1103/PhysRevLett.121.161101.

B. P. Abbott et al. Properties of the binary neutron star merger GW170817. *Phys. Rev.*, X9(1):011001, 2019a. doi: 10.1103/PhysRevX.9.011001.

B. P. Abbott et al. GWTC-1: A Gravitational-Wave Transient Catalog of Compact Binary Mergers Observed by LIGO and Virgo during the First and Second Observing Runs. *Phys. Rev.*, X9(3):031040, 2019b. doi: 10.1103/PhysRevX.9.031040.

Benjamin P. Abbott et al. GW170817: Observation of Gravitational Waves from a Binary Neutron Star Inspiral. *Phys. Rev. Lett.*, 119(16):161101, 2017b. doi: 10.1103/PhysRevLett.119.161101.

B.P. Abbott et al. GW190425: Observation of a Compact Binary Coalescence with Total Mass $\sim 3.4 M_{\odot}$. *Astrophys. J. Lett.*, 892:L3, 2020. doi: 10.3847/2041-8213/ab75f5.

R. Abbott et al. GWTC-2: Compact Binary Coalescences Observed by LIGO and Virgo During the First Half of the Third Observing Run. *Phys. Rev. X*, 11:021053, 2021a. doi: 10.1103/PhysRevX.11.021053.

R. Abbott et al. GWTC-3: Compact Binary Coalescences Observed by LIGO and Virgo During the Second Part of the Third Observing Run. 11 2021b.

R. Abbott et al. The population of merging compact binaries inferred using gravitational waves through GWTC-3. 11 2021c.

F. Acernese et al. Advanced Virgo: a second-generation interferometric gravitational wave detector. *Class. Quant. Grav.*, 32(2):024001, 2015. doi: 10.1088/0264-9381/32/2/024001.

A. Akmal, V. R. Pandharipande, and D. G. Ravenhall. The equation of state for nucleon matter and neutron star structure. *Phys. Rev.*, C58:1804–1828, 1998. doi: 10.1103/PhysRevC.58.1804.

T. Akutsu et al. KAGRA: 2.5 Generation Interferometric Gravitational Wave Detector. *Nature Astron.*, 3 (1):35–40, 2019. doi: 10.1038/s41550-018-0658-y.

Igor Andreoni et al. Target of Opportunity Observations of Gravitational Wave Events with Vera C. Rubin Observatory. 11 2021.

S. Antier et al. GRANDMA observations of advanced LIGO's and advanced Virgo's third observational campaign. *Mon. Not. Roy. Astron. Soc.*, 497(4):5518–5539, 2020. doi: 10.1093/mnras/staa1846.

John Antoniadis, Paulo C.C. Freire, Norbert Wex, Thomas M. Tauris, Ryan S. Lynch, et al. A Massive Pulsar in a Compact Relativistic Binary. *Science*, 340:6131, 2013. doi: 10.1126/science.1233232.

Y. Aoki, G. Endrodi, Z. Fodor, S. D. Katz, and K. K. Szabo. The Order of the quantum chromodynamics transition predicted by the standard model of particle physics. *Nature*, 443:675–678, 2006. doi: 10.1038/nature05120.

Iair Arcavi, Curtis McCully, Griffin Hosseinzadeh, D. Andrew Howell, Sergiy Vasylyev, Dovi Poznanski, Michael Zaltzman, Dan Maoz, Leo Singer, Stefano Valenti, Daniel Kasen, Jennifer Barnes, Tsvi Piran, and Wen fai Fong. Optical follow-up of gravitational-wave events with las cumbres observatory. *The Astrophysical Journal*, 848(2):L33, oct 2017. doi: 10.3847/2041-8213/aa910f. URL `https://doi.org/10.3847%2F2041-8213%2Faa910f`.

D. Argast, M. Samland, F.K. Thielemann, and Y.Z. Qian. Neutron star mergers versus core-collapse supernovae as dominant r-process sites in the early galaxy. *Astron. Astrophys.*, 416:997–1011, 2004. doi: 10.1051/0004-6361:20034265.

Yoichi Aso, Yuta Michimura, Kentaro Somiya, Masaki Ando, Osamu Miyakawa, Takanori Sekiguchi, Daisuke Tatsumi, and Hiroaki Yamamoto. Interferometer design of the KAGRA gravitational wave detector. *Phys. Rev. D*, 88(4):043007, 2013. doi: 10.1103/PhysRevD.88.043007.

W. Baade and F. Zwicky. Remarks on super-novae and cosmic rays. *Phys. Rev.*, 46:76–77, Jul 1934. doi: 10.1103/PhysRev.46.76.2. URL `https://link.aps.org/doi/10.1103/PhysRev.46.76.2`.

Luca Baiotti and Luciano Rezzolla. Binary neutron star mergers: a review of Einsteins richest laboratory. *Rept. Prog. Phys.*, 80(9):096901, 2017. doi: 10.1088/1361-6633/aa67bb.

Steven A. Balbus and John F. Hawley. A Powerful Local Shear Instability in Weakly Magnetized Disks. I. Linear Analysis. ApJ, 376:214, July 1991. doi: 10.1086/170270.

Leor Barack and Curt Cutler. LISA capture sources: Approximate waveforms, signal-to-noise ratios, and parameter estimation accuracy. *Phys. Rev. D*, 69:082005, 2004. doi: 10.1103/PhysRevD.69.082005.

C. Barbieri, O. S. Salafia, A. Perego, M. Colpi, and G. Ghirlanda. Light-curve models of black hole neutron star mergers: steps towards a multi-messenger parameter estimation. *Astron. Astrophys.*, 625:A152, 2019. doi: 10.1051/0004-6361/201935443.

C. Barbieri, O. S. Salafia, A. Perego, M. Colpi, and G. Ghirlanda. Electromagnetic counterparts of black hole-neutron star mergers: dependence on the neutron star properties. *Eur. Phys. J.*, A56(1):8, 2020. doi: 10.1140/epja/s10050-019-00013-x.

C. Barbieri, O. S. Salafia, M. Colpi, G. Ghirlanda, and A. Perego. Exploring the nature of ambiguous merging systems: GW190425 in low latency. *Astron. Astrophys.*, 654:A12, 2021. doi: 10.1051/0004-6361/202037778.

N. Barnea, L. Contessi, D. Gazit, F. Pederiva, and U. van Kolck. Effective Field Theory for Lattice Nuclei. *Phys. Rev. Lett.*, 114(5):052501, 2015. doi: 10.1103/PhysRevLett.114.052501.

Jennifer Barnes, Daniel Kasen, Meng-Ru Wu, and Gabriel Martinez-Pinedo. Radioactivity and thermalization in the ejecta of compact object mergers and their impact on kilonova light curves. *Astrophys. J.*, 829 (2):110, 2016. doi: 10.3847/0004-637X/829/2/110.

A. Bauswein, T.W. Baumgarte, and H. T. Janka. Prompt merger collapse and the maximum mass of neutron stars. *Phys.Rev.Lett.*, 111(13):131101, 2013a. doi: 10.1103/PhysRevLett.111.131101.

A. Bauswein, S. Goriely, and H.-T. Janka. Systematics of dynamical mass ejection, nucleosynthesis, and radioactively powered electromagnetic signals from neutron-star mergers. *Astrophys.J.*, 773:78, 2013b. doi: 10.1088/0004-637X/773/1/78.

Andreas Bauswein, Niels-Uwe F. Bastian, David B. Blaschke, Katerina Chatziioannou, James A. Clark, Tobias Fischer, and Micaela Oertel. Identifying a first-order phase transition in neutron star mergers through gravitational waves. *Phys. Rev. Lett.*, 122(6):061102, 2019. doi: 10.1103/PhysRevLett.122.061102.

Andreas Bauswein, Sebastian Blacker, Georgios Lioutas, Theodoros Soultanis, Vimal Vijayan, and Nikolaos Stergioulas. Systematics of prompt black-hole formation in neutron star mergers. *Phys. Rev. D*, 103(12):123004, 2021. doi: 10.1103/PhysRevD.103.123004.

A. Bazavov et al. The chiral and deconfinement aspects of the QCD transition. *Phys. Rev. D*, 85:054503, 2012. doi: 10.1103/PhysRevD.85.054503.

Paulo F. Bedaque and Ubirajara van Kolck. Effective field theory for few nucleon systems. *Ann. Rev. Nucl. Part. Sci.*, 52:339–396, 2002. doi: 10.1146/annurev.nucl.52.050102.090637.

Andrei M. Beloborodov. Nuclear composition of gamma-ray burst fireballs. *Astrophys. J.*, 588:931–944, 2003. doi: 10.1086/374217.

Andrei M. Beloborodov. Hyper-accreting black holes. *AIP Conf. Proc.*, 1054:51, 2008. doi: 10.1063/1.3002509.

Benhar, O. and Cipollone, A. Implementation of the nambu jona-lasinio model in hybrid stars. *A&A*, 525: L1, 2011. doi: 10.1051/0004-6361/201015686. URL `https://doi.org/10.1051/0004-6361/201015686`.

Edo Berger. Short-duration gamma-ray bursts. *Annual Review of Astronomy and Astrophysics*, 52 (1):43–105, 2014. doi: 10.1146/annurev-astro-081913-035926. URL `https://doi.org/10.1146/annurev-astro-081913-035926`.

Sebastiano Bernuzzi. Neutron Star Merger Remnants. *Gen. Rel. Grav.*, 52(11):108, 2020. doi: 10.1007/s10714-020-02752-5.

Sebastiano Bernuzzi and David Hilditch. Constraint violation in free evolution schemes: comparing BSSNOK with a conformal decomposition of Z4. *Phys. Rev.*, D81:084003, 2010. doi: 10.1103/PhysRevD.81.084003.

Sebastiano Bernuzzi, Alessandro Nagar, Tim Dietrich, and Thibault Damour. Modeling the Dynamics of Tidally Interacting Binary Neutron Stars up to the Merger. *Phys.Rev.Lett.*, 114(16):161103, 2015. doi: 10.1103/PhysRevLett.114.161103.

Sebastiano Bernuzzi et al. Accretion-induced prompt black hole formation in asymmetric neutron star mergers, dynamical ejecta and kilonova signals. *Mon. Not. Roy. Astron. Soc.*, June 2020. doi: 10.1093/mnras/staa1860.

Rajeev S. Bhalerao. Relativistic heavy-ion collisions. In *1st Asia-Europe-Pacific School of High-Energy Physics*, pages 219–239, 2014. doi: 10.5170/CERN-2014-001.219.

Abhijit Bhattacharyya, Igor N. Mishustin, and Walter Greiner. Deconfinement Phase Transition in Compact Stars : Maxwell vs. Gibbs Construction of the Mixed Phase. *J. Phys.*, G37:025201, 2010. doi: 10.1088/0954-3899/37/2/025201.

Nigel T. Bishop and Luciano Rezzolla. Extraction of Gravitational Waves in Numerical Relativity. *Living Rev. Rel.*, 19:2, 2016. doi: 10.1007/s41114-016-0001-9.

C.M. Biwer, Collin D. Capano, Soumi De, Miriam Cabero, Duncan A. Brown, Alexander H. Nitz, and V. Raymond. PyCBC Inference: A Python-based parameter estimation toolkit for compact binary coalescence signals. *Publ. Astron. Soc. Pac.*, 131(996):024503, 2019. doi: 10.1088/1538-3873/aaef0b.

Luc Blanchet. Gravitational Radiation from Post-Newtonian Sources and Inspiralling Compact Binaries. *Living Rev. Relativity*, 17:2, 2014. doi: 10.12942/lrr-2014-2.

R. D. Blandford and D. G. Payne. Hydromagnetic flows from accretion discs and the production of radio jets. *Mon. Not. Roy. Astron. Soc.*, 199:883, 1982.

R. D. Blandford and R. L. Znajek. Electromagnetic extractions of energy from Kerr black holes. *Mon. Not. Roy. Astron. Soc.*, 179:433–456, 1977. doi: 10.1093/mnras/179.3.433.

Olivér Boersma et al. A search for radio emission from double-neutron star merger GW190425 using Apertif. *Astron. Astrophys.*, 650:A131, 2021. doi: 10.1051/0004-6361/202140578.

Ignazio Bombaci. The Hyperon Puzzle in Neutron Stars. *JPS Conf. Proc.*, 17:101002, 2017. doi: 10.7566/JPSCP.17.101002.

Ignazio Bombaci and Domenico Logoteta. Equation of state of dense nuclear matter and neutron star structure from nuclear chiral interactions. *Astron. Astrophys.*, 609:A128, 2018. doi: 10.1051/0004-6361/201731604.

Luke Bovard, Dirk Martin, Federico Guercilena, Almudena Arcones, Luciano Rezzolla, and Oleg Korobkin. r-process nucleosynthesis from matter ejected in binary neutron star mergers. *Phys. Rev.*, D96(12):124005, 2017. doi: 10.1103/PhysRevD.96.124005.

E. S. Bowman and J. I. Kapusta. Critical points in the linear σ model with quarks. *Phys. Rev. C*, 79:015202, Jan 2009. doi: 10.1103/PhysRevC.79.015202. URL `https://link.aps.org/doi/10.1103/PhysRevC.79.015202`.

Steven R. Brandt, Gabriele Bozzola, Cheng-Hsin Cheng, Peter Diener, Alexandru Dima, William E. Gabella, Miguel Gracia-Linares, Roland Haas, Yosef Zlochower, Miguel Alcubierre, Daniela Alic, Gabrielle Allen, Marcus Ansorg, Maria Babiuc-Hamilton, Luca Baiotti, Werner Benger, Eloisa Bentivegna, Sebastiano Bernuzzi, Tanja Bode, Brockton Brendal, Bernd Bruegmann, Manuela Campanelli, Federico Cipolletta, Giovanni Corvino, Samuel Cupp, Roberto De Pietri, Harry Dimmelmeier, Rion Dooley, Nils Dorband, Matthew Elley, Yaakoub El Khamra, Zachariah Etienne, Joshua Faber, Toni Font, Joachim Frieben, Bruno Giacomazzo, Tom Goodale, Carsten Gundlach, Ian Hawke, Scott Hawley, Ian Hinder, E. A. Huerta, Sascha Husa, Sai Iyer, Daniel Johnson, Abhishek V. Joshi, Wolfgang Kastaun, Thorsten Kellermann, Andrew Knapp, Michael Koppitz, Pablo Laguna, Gerd Lanferman, Frank Löffler, Joan Masso, Lars Menger, Andre Merzky, Jonah Maxwell Miller, Mark Miller, Philipp Moesta, Pedro Montero, Bruno Mundim, Andrea Nerozzi, Scott C. Noble, Christian Ott, Ravi Paruchuri, Denis Pollney, David Radice, Thomas Radke, Christian Reisswig, Luciano Rezzolla, David Rideout, Matei Ripeanu, Lorenzo Sala, Jascha A Schewtschenko, Erik Schnetter, Bernard Schutz, Ed Seidel, Eric Seidel, John Shalf, Ken Sible, Ulrich Sperhake, Nikolaos Stergioulas, Wai-Mo Suen, Bela Szilagyi, Ryoji Takahashi, Michael Thomas, Jonathan Thornburg, Malcolm Tobias, Aaryn Tonita, Paul Walker, Mew-Bing Wan, Barry Wardell, Leonardo Werneck, Helvi Witek, Miguel Zilhão, and Burkhard Zink. The einstein toolkit, December 2021. URL `https://doi.org/10.5281/zenodo.5770803`. To find out more, visit http://einsteintoolkit.org.

Matteo Breschi, Albino Perego, Sebastiano Bernuzzi, Walter Del Pozzo, Vsevolod Nedora, David Radice, and Diego Vescovi. AT2017gfo: Bayesian inference and model selection of multicomponent kilonovae and constraints on the neutron star equation of state. *Mon. Not. Roy. Astron. Soc.*, 505(2):1661–1677, 2021. doi: 10.1093/mnras/stab1287.

Bernd Brügmann, Jose A. Gonzalez, Mark Hannam, Sascha Husa, Ulrich Sperhake, et al. Calibration of Moving Puncture Simulations. *Phys.Rev.*, D77:024027, 2008. doi: 10.1103/PhysRevD.77.024027.

M. Buballa, F. Neumann, M. Oertel, and I. Shovkovy. Quark mass effects on the stability of hybrid stars. *Phys. Lett. B*, 595:36–43, 2004. doi: 10.1016/j.physletb.2004.05.064.

Michael Buballa. NJL model analysis of quark matter at large density. *Phys. Rept.*, 407:205–376, 2005. doi: 10.1016/j.physrep.2004.11.004.

Mattia Bulla. POSSIS: predicting spectra, light curves and polarization for multi-dimensional models of supernovae and kilonovae. *Mon. Not. Roy. Astron. Soc.*, 489(4):5037–5045, 2019. doi: 10.1093/mnras/stz2495.

Adam Burrows and David Vartanyan. Core-Collapse Supernova Explosion Theory. *Nature*, 589(7840):29–39, 2021. doi: 10.1038/s41586-020-03059-w.

A. Camilletti, L. Chiesa, G. Ricigliano, A. Perego, L. C. Lippold, S. Padamata, S. Bernuzzi, D. Radice, D. Logoteta, and F. M. Guercilena. Numerical relativity simulations of the neutron star merger GW190425: microphysics and mass ratio effects. *Mon. Not. Roy. Astron. Soc.*, 516(4):4760–4781, 2022. doi: 10.1093/mnras/stac2333.

Alessandro Camilletti, Albino Perego, Federico Maria Guercilena, Sebastiano Bernuzzi, and David Radice. Geometric and thermodynamic characterization of binary neutron star accretion discs. *Phys. Rev. D*, 109 (6):063023, 2024. doi: 10.1103/PhysRevD.109.063023.

Collin D. Capano, Ingo Tews, Stephanie M. Brown, Ben Margalit, Soumi De, Sumit Kumar, Duncan A. Brown, Badri Krishnan, and Sanjay Reddy. Stringent constraints on neutron-star radii from multimessenger observations and nuclear theory. *Nature Astron.*, 4(6):625–632, 2020. doi: 10.1038/s41550-020-1014-6.

Pablo Cerdá-Durán and Nancy Elias-Rosa. Neutron stars formation and Core Collapse Supernovae. *Astrophys. Space Sci. Libr.*, 457:1–56, 2018. doi: 10.1007/978-3-319-97616-7_1.

N. Chamel and P. Haensel. Physics of Neutron Star Crusts. *Living Rev. Rel.*, 11:10, 2008. doi: 10.12942/lrr-2008-10.

S. Chandrasekhar and Steven L. Detweiler. The quasi-normal modes of the Schwarzschild black hole. *Proc. Roy. Soc. Lond.*, A344:441–452, 1975.

Wen-Xin Chen and Andrei M. Beloborodov. Neutrino-Cooled Accretion Disks around Spinning Black Hole. *Astrophys. J.*, 657:383–399, 2007. doi: 10.1086/508923.

Riccardo Ciolfi, Wolfgang Kastaun, Jay Vijay Kalinani, and Bruno Giacomazzo. First 100 ms of a long-lived magnetized neutron star formed in a binary neutron star merger. *Phys. Rev.*, D100(2):023005, 2019. doi: 10.1103/PhysRevD.100.023005.

Luciano Combi and Daniel M. Siegel. GRMHD Simulations of Neutron-star Mergers with Weak Interactions: r-process Nucleosynthesis and Electromagnetic Signatures of Dynamical Ejecta. *Astrophys. J.*, 944(1):28, 2023a. doi: 10.3847/1538-4357/acac29.

Luciano Combi and Daniel M. Siegel. Jets from neutron-star merger remnants and massive blue kilonovae. 3 2023b.

Constantinos Constantinou, Tianqi Zhao, Sophia Han, and Madappa Prakash. Framework for phase transitions between the Maxwell and Gibbs constructions. *Phys. Rev. D*, 107(7):074013, 2023. doi: 10.1103/PhysRevD.107.074013.

Michael W. Coughlin et al. GROWTH on S190425z: Searching thousands of square degrees to identify an optical or infrared counterpart to a binary neutron star merger with the Zwicky Transient Facility and Palomar Gattini IR. *Astrophys. J. Lett.*, 885(1):L19, 2019. doi: 10.3847/2041-8213/ab4ad8.

D. A. Coulter et al. Swope Supernova Survey 2017a (SSS17a), the Optical Counterpart to a Gravitational Wave Source. *Science*, 2017. doi: 10.1126/science.aap9811. [Science358,1556(2017)].

John J. Cowan, Christopher Sneden, James E. Lawler, Ani Aprahamian, Michael Wiescher, Karlheinz Langanke, Gabriel Martínez-Pinedo, and Friedrich-Karl Thielemann. Origin of the heaviest elements: The rapid neutron-capture process. *Rev. Mod. Phys.*, 93(1):15002, 2021. doi: 10.1103/RevModPhys.93.015002.

H. Thankful Cromartie et al. Relativistic Shapiro delay measurements of an extremely massive millisecond pulsar. *Nat. Astron.*, 4(1):72–76, 2019. doi: 10.1038/s41550-019-0880-2.

Sanjana Curtis, Philipp Mösta, Zhenyu Wu, David Radice, Luke Roberts, Giacomo Ricigliano, and Albino Perego. r-process nucleosynthesis and kilonovae from hypermassive neutron star post-merger remnants. *Mon. Not. Roy. Astron. Soc.*, 518(4):5313–5322, 2022. doi: 10.1093/mnras/stac3128.

Marco Cusinato, Federico Maria Guercilena, Albino Perego, Domenico Logoteta, David Radice, Sebastiano Bernuzzi, and Stefano Ansoldi. Neutrino emission from binary neutron star mergers: characterizing light curves and mean energies. *Eur.Phys.J.A*, 58(99):5, 11 2021. doi: 10.1140/epja/s10050-022-00743-5.

Thibault Damour and Alessandro Nagar. The Effective One Body description of the Two-Body problem. 2009.

Soumi De and Daniel M. Siegel. Igniting Weak Interactions in Neutron Star Postmerger Accretion Disks. *Astrophys. J.*, 921(1):94, 2021. doi: 10.3847/1538-4357/ac110b.

Joel de Jesús Mendoza-Temis, Meng-Ru Wu, Gabriel Martinez-Pinedo, Karlheinz Langanke, Andreas Bauswein, and Hans-Thomas Janka. Nuclear robustness of the r process in neutron-star mergers. *Phys. Rev.*, C92(5):055805, 2015. doi: 10.1103/PhysRevC.92.055805.

Jean-Pierre De Villiers, John F. Hawley, Julian H. Krolik, and Shigenobu Hirose. Magnetically driven accretion in the Kerr metric. 3. Unbound outflows. *Astrophys. J.*, 620:878–888, 2005. doi: 10.1086/427142.

Paul Demorest, Tim Pennucci, Scott Ransom, Mallory Roberts, and Jason Hessels. Shapiro Delay Measurement of A Two Solar Mass Neutron Star. *Nature*, 467:1081–1083, 2010. doi: 10.1038/nature09466.

J. S. Deneva, K. Stovall, M. A. McLaughlin, S. D. Bates, P. C. C. Freire, J. G. Martinez, F. Jenet, and M. Bagchi. Goals, Strategies and First Discoveries of AO327, the Arecibo All-sky 327 MHz Drift Pulsar Survey. *Astrophys. J.*, 775:51, 2013. doi: 10.1088/0004-637X/775/1/51.

Arnab Dhani, David Radice, Jan Schütte-Engel, Susan Gardner, Bangalore Sathyaprakash, Domenico Logoteta, Albino Perego, and Rahul Kashyap. Prospects for Direct Detection of Black Hole Formation in Neutron Star Mergers with Next-Generation Gravitational-Wave Detectors. 6 2023.

Tim Dietrich and Sebastiano Bernuzzi. Simulations of rotating neutron star collapse with the puncture gauge: end state and gravitational waveforms. *Phys.Rev.*, D91(4):044039, 2015. doi: 10.1103/PhysRevD.91.044039.

Tim Dietrich and Maximiliano Ujevic. Modeling dynamical ejecta from binary neutron star mergers and implications for electromagnetic counterparts. *Class. Quant. Grav.*, 34(10):105014, 2017. doi: 10.1088/1361-6382/aa6bb0.

Tim Dietrich, Maximiliano Ujevic, Wolfgang Tichy, Sebastiano Bernuzzi, and Bernd Brügmann. Gravitational waves and mass ejecta from binary neutron star mergers: Effect of the mass-ratio. *Phys. Rev.*, D95 (2):024029, 2017. doi: 10.1103/PhysRevD.95.024029.

Tim Dietrich, David Radice, Sebastiano Bernuzzi, Francesco Zappa, Albino Perego, Bernd Brügmann, Swami Vivekanandji Chaurasia, Reetika Dudi, Wolfgang Tichy, and Maximiliano Ujevic. CoRe database of binary neutron star merger waveforms. *Class. Quant. Grav.*, 35(24):24LT01, 2018. doi: 10.1088/1361-6382/aaebc0.

Tim Dietrich, Tanja Hinderer, and Anuradha Samajdar. Interpreting Binary Neutron Star Mergers: Describing the Binary Neutron Star Dynamics, Modelling Gravitational Waveforms, and Analyzing Detections. *Gen. Rel. Grav.*, 53(3):27, 2021. doi: 10.1007/s10714-020-02751-6.

F. Douchin and P. Haensel. A unified equation of state of dense matter and neutron star structure. *Astron. Astrophys.*, 380:151–167, 2001.

Reetika Dudi, Francesco Pannarale, Tim Dietrich, Mark Hannam, Sebastiano Bernuzzi, Frank Ohme, and Bernd Bruegmann. Relevance of tidal effects and post-merger dynamics for binary neutron star parameter estimation. 2018.

Reetika Dudi, Ananya Adhikari, Bernd Brügmann, Tim Dietrich, Kota Hayashi, Kyohei Kawaguchi, Kenta Kiuchi, Koutarou Kyutoku, Masaru Shibata, and Wolfgang Tichy. Investigating GW190425 with numerical-relativity simulations. 9 2021.

Ron DuPlain, Scott Ransom, Paul Demorest, Patrick Brandt, John Ford, and Amy L. Shelton. Launching GUPPI: the Green Bank Ultimate Pulsar Processing Instrument. In Alan Bridger and Nicole M. Radziwill, editors, *Advanced Software and Control for Astronomy II*, volume 7019 of *Society of Photo-Optical Instrumentation Engineers (SPIE) Conference Series*, page 70191D, August 2008. doi: 10.1117/12.790003.

M. Eichler et al. The Role of Fission in Neutron Star Mergers and its Impact on the r-Process Peaks. *Astrophys. J.*, 808(1):30, 2015. doi: 10.1088/0004-637X/808/1/30.

Shinji Ejiri. Canonical partition function and finite density phase transition in lattice QCD. *Phys. Rev. D*, 78:074507, 2008. doi: 10.1103/PhysRevD.78.074507.

Andrea Endrizzi, Albino Perego, Francesco M. Fabbri, Lorenzo Branca, David Radice, Sebastiano Bernuzzi, Bruno Giacomazzo, Francesco Pederiva, and Alessandro Lovato. Thermodynamics conditions of matter in the neutrino decoupling region during neutron star mergers. *Eur. Phys. J. A*, 56(1):15, 2020. doi: 10.1140/epja/s10050-019-00018-6.

Y. Eriguchi and E. Mueller. A general computational method for obtaining equilibria of self-gravitating and rotating gases. A&A, 146(2):260–268, May 1985.

Matthew Evans et al. A Horizon Study for Cosmic Explorer: Science, Observatories, and Community. 9 2021.

Steven Fahlman and Rodrigo Fernández. Long-term 3D MHD simulations of black hole accretion discs formed in neutron star mergers. *Mon. Not. Roy. Astron. Soc.*, 513(2):2689–2707, 2022. doi: 10.1093/mnras/stac948.

Rodrigo Fernández and Brian D. Metzger. Delayed outflows from black hole accretion tori following neutron star binary coalescence. *Mon. Not. Roy. Astron. Soc.*, 435:502, 2013. doi: 10.1093/mnras/stt1312.

Rodrigo Fernández, Eliot Quataert, Josiah Schwab, Daniel Kasen, and Stephan Rosswog. The interplay of disc wind and dynamical ejecta in the aftermath of neutron starblack hole mergers. *Mon. Not. Roy. Astron. Soc.*, 449(1):390–402, 2015. doi: 10.1093/mnras/stv238.

Rodrigo Fernández, Alexander Tchekhovskoy, Eliot Quataert, Francois Foucart, and Daniel Kasen. Long-term GRMHD simulations of neutron star merger accretion discs: implications for electromagnetic counterparts. *Mon. Not. Roy. Astron. Soc.*, 482(3):3373–3393, 2019. doi: 10.1093/mnras/sty2932.

Francois Foucart, M. Brett Deaton, Matthew D. Duez, Evan O'Connor, Christian D. Ott, Roland Haas, Lawrence E. Kidder, Harald P. Pfeiffer, Mark A. Scheel, and Bela Szilagyi. Neutron star-black hole mergers with a nuclear equation of state and neutrino cooling: Dependence in the binary parameters. *Phys. Rev.*, D90:024026, 2014. doi: 10.1103/PhysRevD.90.024026.

Francois Foucart, Dhruv Desai, Wyatt Brege, Matthew D. Duez, Daniel Kasen, Daniel A. Hemberger, Lawrence E. Kidder, Harald P. Pfeiffer, and Mark A. Scheel. Dynamical ejecta from precessing neutron star-black hole mergers with a hot, nuclear-theory based equation of state. *Class. Quant. Grav.*, 34(4): 044002, 2017. doi: 10.1088/1361-6382/aa573b.

Sho Fujibayashi, Yuichiro Sekiguchi, Kenta Kiuchi, and Masaru Shibata. Properties of Neutrino-driven Ejecta from the Remnant of a Binary Neutron Star Merger: Pure Radiation Hydrodynamics Case. *Astrophys. J.*, 846(2):114, 2017. doi: 10.3847/1538-4357/aa8039.

Sho Fujibayashi, Masaru Shibata, Shinya Wanajo, Kenta Kiuchi, Koutarou Kyutoku, and Yuichiro Sekiguchi. Mass ejection from disks surrounding a low-mass black hole: Viscous neutrino-radiation hydrodynamics simulation in full general relativity. *Phys. Rev. D*, 101(8):083029, 2020. doi: 10.1103/PhysRevD.101.083029.

Sho Fujibayashi, Shinya Wanajo, Kenta Kiuchi, Koutarou Kyutoku, Yuichiro Sekiguchi, and Masaru Shibata. Postmerger Mass Ejection of Low-mass Binary Neutron Stars. *Astrophys. J.*, 901(2):122, October 2020. doi: 10.3847/1538-4357/abafc2.

Filippo Galeazzi, Shin'ichirou Yoshida, and Yoshiharu Eriguchi. Differentially-rotating neutron star models with a parametrized rotation profile. *Astron. Astrophys.*, 541:A156, 2012. doi: 10.1051/0004-6361/201016316.

Filippo Galeazzi, Wolfgang Kastaun, Luciano Rezzolla, and José A. Font. Implementation of a simplified approach to radiative transfer in general relativity. *Phys.Rev.*, D88:064009, 2013. doi: 10.1103/PhysRevD.88.064009.

Bruno Giacomazzo, Luciano Rezzolla, and Luca Baiotti. Accurate evolutions of inspiralling and magnetized neutron-stars: equal-mass binaries. *Phys. Rev.*, D83:044014, 2011. doi: 10.1103/PhysRevD.83.044014.

Bruno Giacomazzo, Rosalba Perna, Luciano Rezzolla, Eleonora Troja, and Davide Lazzati. Compact Binary Progenitors of Short Gamma-Ray Bursts. *Astrophys. J.*, 762:L18, 2013. doi: 10.1088/2041-8205/762/2/L18.

Matteo Giordano, Kornel Kapas, Sandor D. Katz, Daniel Nogradi, and Attila Pasztor. New approach to lattice QCD at finite density; results for the critical end point on coarse lattices. *JHEP*, 05:088, 2020. doi: 10.1007/JHEP05(2020)088.

A. Goldstein et al. An Ordinary Short Gamma-Ray Burst with Extraordinary Implications: Fermi-GBM Detection of GRB 170817A. *Astrophys. J.*, 848(2):L14, 2017. doi: 10.3847/2041-8213/aa8f41.

Alejandra Gonzalez et al. Second release of the CoRe database of binary neutron star merger waveforms. *Class. Quant. Grav.*, 40(8):085011, 2023. doi: 10.1088/1361-6382/acc231.

Tom Goodale, Gabrielle Allen, Gerd Lanfermann, Joan Massó, Thomas Radke, Edward Seidel, and John Shalf. The Cactus framework and toolkit: Design and applications. In *Vector and Parallel Processing – VECPAR'2002, 5th International Conference, Lecture Notes in Computer Science*, Berlin, 2003. Springer.

S. Goriely. The fundamental role of fission during r-process nucleosynthesis in neutron star mergers. *Eur. Phys. J. A*, 51(2):22, 2015. doi: 10.1140/epja/i2015-15022-3.

Eric Gourgoulhon, Philippe Grandclement, Keisuke Taniguchi, Jean-Alain Marck, and Silvano Bonazzola. Quasiequilibrium sequences of synchronized and irrotational binary neutron stars in general relativity: 1. Method and tests. *Phys.Rev.*, D63:064029, 2001. doi: 10.1103/PhysRevD.63.064029.

P. Haensel, A. Y. Potekhin, and D. G. Yakovlev. *Neutron stars 1: Equation of state and structure*. Springer, New York, USA, 2007.

Ming-Zhe Han, Shao-Peng Tang, Yi-Ming Hu, Yin-Jie Li, Jin-Liang Jiang, Zhi-Ping Jin, Yi-Zhong Fan, and Da-Ming Wei. Is GW190425 consistent with being a neutron star−black hole merger? *Astrophys. J.*, 891 (1):L5, 2020. doi: 10.3847/2041-8213/ab745a.

Matthias Hanauske, Kentaro Takami, Luke Bovard, Luciano Rezzolla, José A. Font, Filippo Galeazzi, and Horst Stöcker. Rotational properties of hypermassive neutron stars from binary mergers. *Phys. Rev. D*, 96(4):043004, 2017. doi: 10.1103/PhysRevD.96.043004.

John F. Hawley. Global magnetohydrodynamical simulations of accretion tori. *The Astrophysical Journal*, 528(1):462, jan 2000. doi: 10.1086/308180. URL `https://dx.doi.org/10.1086/308180`.

Matthias Hempel and Jurgen Schaffner-Bielich. Statistical Model for a Complete Supernova Equation of State. *Nucl. Phys.*, A837:210–254, 2010. doi: 10.1016/j.nuclphysa.2010.02.010.

Matthias Hempel, Micaela Oertel, Stefan Typel, and Thomas Klähn. How Well Do We Know The Supernova Equation of State? *JPS Conf. Proc.*, 14:010802, 2017. doi: 10.7566/JPSCP.14.010802.

A. Hewish, S. J. Bell, J. D. H Pilkington, P. F. Scott, and R. A. Collins. Observation of a rapidly pulsating radio source. *Nature*, 217:709–713, 1968. doi: 10.1038/217709a0.

David Hilditch, Sebastiano Bernuzzi, Marcus Thierfelder, Zhoujian Cao, Wolfgang Tichy, and Bernd Brueg-mann. Compact binary evolutions with the Z4c formulation. *Phys. Rev.*, D88:084057, 2013. doi: 10.1103/PhysRevD.88.084057.

Werner Hofmann and Roberta Zanin. The Cherenkov Telescope Array. 5 2023.

Kenta Hotokezaka and Ehud Nakar. Radioactive heating rate of r-process elements and macronova light curve. 9 2019. doi: 10.3847/1538-4357/ab6a98.

Kenta Hotokezaka, Koutarou Kyutoku, Hirotada Okawa, Masaru Shibata, and Kenta Kiuchi. Binary Neutron Star Mergers: Dependence on the Nuclear Equation of State. *Phys.Rev.*, D83:124008, 2011. doi: 10.1103/PhysRevD.83.124008.

Kenta Hotokezaka, Kenta Kiuchi, Koutarou Kyutoku, Hirotada Okawa, Yu-ichiro Sekiguchi, et al. The mass ejection from the merger of binary neutron stars. *Phys.Rev.*, D87:024001, 2013a. doi: 10.1103/PhysRevD.87.024001.

Kenta Hotokezaka, Koutarou Kyutoku, and Masaru Shibata. Exploring tidal effects of coalescing binary neutron stars in numerical relativity. *Phys.Rev.*, D87(4):044001, 2013b. doi: 10.1103/PhysRevD.87.044001.

Kenta Hotokezaka, Koutarou Kyutoku, Hirotada Okawa, and Masaru Shibata. Exploring tidal effects of coalescing binary neutron stars in numerical relativity. II. Long-term simulations. *Phys. Rev.*, D91(6):064060, 2015. doi: 10.1103/PhysRevD.91.064060.

Kenta Hotokezaka, Kenta Kiuchi, Masaru Shibata, Ehud Nakar, and Tsvi Piran. Synchrotron radiation from the fast tail of dynamical ejecta of neutron star mergers. *Astrophys. J.*, 867(2):95, 2018. doi: 10.3847/1538-4357/aadf92.

Christian Iliadis.

Dante A. B. Iozzo, Michael Boyle, Nils Deppe, Jordan Moxon, Mark A. Scheel, Lawrence E. Kidder, Harald P. Pfeiffer, and Saul A. Teukolsky. Extending gravitational wave extraction using Weyl characteristic fields. *Phys. Rev. D*, 103(2):024039, 2021. doi: 10.1103/PhysRevD.103.024039.

Jin-Liang Jiang, Shao-Peng Tang, Yuan-Zhu Wang, Yi-Zhong Fan, and Da-Ming Wei. PSR J0030+0451, GW170817 and the nuclear data: joint constraints on equation of state and bulk properties of neutron stars. *Astrophys. J.*, 892:1, 2020. doi: 10.3847/1538-4357/ab77cf.

Oliver Just, Andreas Bauswein, Ricard Ardevol Pulpillo, Stephane Goriely, and H. Thomas Janka. Comprehensive nucleosynthesis analysis for ejecta of compact binary mergers. *Mon. Not. Roy. Astron. Soc.*, 448(1):541–567, 2015. doi: 10.1093/mnras/stv009.

Oliver Just, Stephane Goriely, Hans-Thomas Janka, Shigehiro Nagataki, and Andreas Bauswein. Neutrino absorption and other physics dependencies in neutrino-cooled black hole accretion discs. *Mon. Not. Roy. Astron. Soc.*, 509(1):1377–1412, 2021. doi: 10.1093/mnras/stab2861.

Rahul Kashyap et al. Numerical relativity simulations of prompt collapse mergers: Threshold mass and phenomenological constraints on neutron star properties after GW170817. *Phys. Rev. D*, 105(10):103022, 2022. doi: 10.1103/PhysRevD.105.103022.

Kyohei Kawaguchi, Kotarou Kyutoku, Masaru Shibata, and Masaomi Tanaka. Models of Kilonova/macronova Emission From Black Holeneutron Star Mergers. *Astrophys. J.*, 825(1):52, 2016. doi: 10.3847/0004-637X/825/1/52.

Kyohei Kawaguchi, Masaru Shibata, and Masaomi Tanaka. Radiative transfer simulation for the optical and near-infrared electromagnetic counterparts to GW170817. *Astrophys. J.*, 865(2):L21, 2018. doi: 10.3847/2041-8213/aade02.

Kyohei Kawaguchi, Masaru Shibata, and Masaomi Tanaka. Diversity of Kilonova Light Curves. *Astrophys. J.*, 889(2):171, February 2020. doi: 10.3847/1538-4357/ab61f6.

Kenta Kiuchi, Sho Fujibayashi, Kota Hayashi, Koutarou Kyutoku, Yuichiro Sekiguchi, and Masaru Shibata. Self-consistent picture of the mass ejection from a one second-long binary neutron star merger leaving a short-lived remnant in general-relativistic neutrino-radiation magnetohydrodynamic simulation. 11 2022.

Kostas D. Kokkotas and Bernd G. Schmidt. Quasi-normal modes of stars and black holes. *Living Rev. Rel.*, 2:2, 1999.

Maximilian Kölsch, Tim Dietrich, Maximiliano Ujevic, and Bernd Bruegmann. Investigating the mass-ratio dependence of the prompt-collapse threshold with numerical-relativity simulations. *Phys. Rev. D*, 106(4):044026, 2022. doi: 10.1103/PhysRevD.106.044026.

Sven Köppel, Luke Bovard, and Luciano Rezzolla. A General-relativistic Determination of the Threshold Mass to Prompt Collapse in Binary Neutron Star Mergers. *Astrophys. J.*, 872(1):L16, 2019. doi: 10.3847/2041-8213/ab0210.

O. Korobkin, S. Rosswog, A. Arcones, and C. Winteler. On the astrophysical robustness of neutron star merger r-process. *Mon. Not. Roy. Astron. Soc.*, 426:1940, 2012. doi: 10.1111/j.1365-2966.2012.21859.x.

Christian Jürgen Krüger and Francois Foucart. Estimates for Disk and Ejecta Masses Produced in Compact Binary Mergers. *Phys. Rev. D*, 101(10):103002, 2020. doi: 10.1103/PhysRevD.101.103002.

Marek Kutschera. Neutron stars: Formation and structure. *Acta Phys. Polon. B*, 29:25–46, 1998.

Koutarou Kyutoku, Masaru Shibata, and Keisuke Taniguchi. Reducing orbital eccentricity in initial data of binary neutron stars. *Phys. Rev.*, D90(6):064006, 2014. doi: 10.1103/PhysRevD.90.064006.

Koutarou Kyutoku, Sho Fujibayashi, Kota Hayashi, Kyohei Kawaguchi, Kenta Kiuchi, Masaru Shibata, and Masaomi Tanaka. On the possibility of GW190425 being a black hole–neutron star binary merger. *Astrophys. J.*, 890(1):L4, 2020. doi: 10.3847/2041-8213/ab6e70.

James M. Lattimer and F. Douglas Swesty. A Generalized equation of state for hot, dense matter. *Nucl. Phys.*, A535:331–376, 1991. doi: 10.1016/0375-9474(91)90452-C.

H. K. Lee, R. A. M. J. Wijers, and G. E. Brown. The Blandford-Znajek process as a central engine for a gamma-ray burst. *Phys. Rept.*, 325:83–114, 2000. doi: 10.1016/S0370-1573(99)00084-8.

Luis Lehner, Steven L. Liebling, Carlos Palenzuela, O. L. Caballero, Evan O'Connor, Matthew Anderson, and David Neilsen. Unequal mass binary neutron star mergers and multimessenger signals. *Class. Quant. Grav.*, 33(18):184002, 2016. doi: 10.1088/0264-9381/33/18/184002.

Li-Xin Li and Bohdan Paczynski. Transient events from neutron star mergers. *Astrophys.J.*, 507:L59, 1998. doi: 10.1086/311680.

M. Liebendoerfer, O. E. B. Messer, A. Mezzacappa, S. W. Bruenn, C. Y. Cardall, and F. K. Thielemann. A Finite difference representation of neutrino radiation hydrodynamics for spherically symmetric general relativistic supernova simulations. *Astrophys. J. Suppl.*, 150:263–316, 2004. doi: 10.1086/380191.

Matthias Liebendoerfer, Stephan Rosswog, and Friedrich-Karl Thielemann. An Adaptive grid, implicit code for spherically symmetric, general relativistic hydrodynamics in comoving coordinates. *Astrophys. J. Suppl.*, 141:229–246, 2002. doi: 10.1086/339872.

Matthias Liebendoerfer, M. Rampp, H. Th. Janka, and A. Mezzacappa. Supernova simulations with Boltzmann neutrino transport: A Comparison of methods. *Astrophys. J.*, 620:840–860, 2005. doi: 10.1086/427203.

Jonas Lippuner and Luke F. Roberts. r-Process Lanthanide Production and Heating Rates in Kilonovae. *Astrophys. J.*, 815(2):82, 2015. doi: 10.1088/0004-637X/815/2/82.

Jonas Lippuner and Luke F. Roberts. SkyNet: A modular nuclear reaction network library. *Astrophys. J. Suppl.*, 233(2):18, 2017. doi: 10.3847/1538-4365/aa94cb.

Jonas Lippuner, Rodrigo Fernández, Luke F. Roberts, Francois Foucart, Daniel Kasen, Brian D. Metzger, and Christian D. Ott. Signatures of hypermassive neutron star lifetimes on r-process nucleosynthesis in the disc ejecta from neutron star mergers. *Mon. Not. Roy. Astron. Soc.*, 472(1):904–918, 2017. doi: 10.1093/mnras/stx1987.

V. M. Lipunov, E. Gorbovskoy, V. G. Kornilov, N . Tyurina, P. Balanutsa, A. Kuznetsov, D. Vlasenko, D. Kuvshinov, I. Gorbunov, D. A. H. Buckley, A. V. Krylov, R. Podesta, C. Lopez, F. Podesta, H. Levato, C. Saffe, C. Mallamachi, S. Potter, N. M. Budnev, O. Gress, Yu. Ishmuhametova, V. Vladimirov, D. Zimnukhov, V. Yurkov, Yu. Sergienko, A. Gabovich, R. Rebolo, M. Serra-Ricart, G. Israelyan, V. Chazov, Xiaofeng Wang, A. Tlatov, and M. I. Panchenko. Master optical detection of the first ligo/virgo

neutron star binary merger gw170817. *The Astrophysical Journal Letters*, 850(1):L1, nov 2017. doi: 10.3847/2041-8213/aa92c0. URL `https://dx.doi.org/10.3847/2041-8213/aa92c0`.

Frank Löffler et al. The Einstein Toolkit: A Community Computational Infrastructure for Relativistic Astrophysics. *Class. Quant. Grav.*, 29:115001, 2012. doi: 10.1088/0264-9381/29/11/115001.

Domenico Logoteta, Ignazio Bombaci, Constanca Providencia, and Isaac Vidana. A Chiral model approach to quark matter nucleation in neutron stars. *Phys. Rev. D*, 85:023003, 2012. doi: 10.1103/PhysRevD.85.023003.

Domenico Logoteta, Albino Perego, and Ignazio Bombaci. Microscopic equation of state of hot nuclear matter for numerical relativity simulations. *Astron. Astrophys.*, 646:A55, 2021. doi: 10.1051/0004-6361/202039457.

R. Machleidt and D. R. Entem. Chiral effective field theory and nuclear forces. *Phys. Rept.*, 503:1–75, 2011. doi: 10.1016/j.physrep.2011.02.001.

Michele Maggiore et al. Science Case for the Einstein Telescope. *JCAP*, 03:050, 2020. doi: 10.1088/1475-7516/2020/03/050.

Raffaella Margutti and Ryan Chornock. First Multimessenger Observations of a Neutron Star Merger. *Ann. Rev. Astron. Astrophys.*, 59:155–202, 2021. doi: 10.1146/annurev-astro-112420-030742.

D. Martin, A. Perego, W. Kastaun, and A. Arcones. The role of weak interactions in dynamic ejecta from binary neutron star mergers. *Class. Quant. Grav.*, 35(3):034001, 2018. doi: 10.1088/1361-6382/aa9f5a.

Dirk Martin, Albino Perego, Almudena Arcones, Friedrich-Karl Thielemann, Oleg Korobkin, and Stephan Rosswog. Neutrino-driven winds in the aftermath of a neutron star merger: nucleosynthesis and electromagnetic transients. *Astrophys. J.*, 813(1):2, 2015. doi: 10.1088/0004-637X/813/1/2.

J. G. Martinez, K. Stovall, P. C. C. Freire, J. S. Deneva, F. A. Jenet, M. A. McLaughlin, M. Bagchi, S. D. Bates, and A. Ridolfi. Pulsar J0453+1559: A Double Neutron Star System with a Large Mass Asymmetry. *Astrophys. J.*, 812(2):143, 2015. doi: 10.1088/0004-637X/812/2/143.

Maura A. McLaughlin. The North American Nanohertz Observatory for Gravitational Waves. *Class. Quant. Grav.*, 30:224008, 2013. doi: 10.1088/0264-9381/30/22/224008.

B. D. Metzger, A. Arcones, E. Quataert, and G. Martinez-Pinedo. The effects of r-process heating on fall-back accretion in compact object mergers. *Mon. Not. Roy. Astron. Soc.*, 402:2771, 2010. doi: 10.1111/j.1365-2966.2009.16107.x.

B.D. Metzger, A.L. Piro, and E. Quataert. Time-Dependent Models of Accretion Disks Formed from Compact Object Mergers. *Mon.Not.Roy.Astron.Soc.*, 390:781, 2008. doi: 10.1111/j.1365-2966.2008.13789.x.

Brian D. Metzger and Rodrigo Fernández. Red or blue? A potential kilonova imprint of the delay until black hole formation following a neutron star merger. *Mon.Not.Roy.Astron.Soc.*, 441:3444, 2014. doi: 10.1093/mnras/stu802.

Jonah M. Miller, Benjamin R. Ryan, Joshua C. Dolence, Adam Burrows, Christopher J. Fontes, Christopher L. Fryer, Oleg Korobkin, Jonas Lippuner, Matthew R. Mumpower, and Ryan T. Wollaeger. Full Transport Model of GW170817-Like Disk Produces a Blue Kilonova. *Phys. Rev.*, D100(2):023008, 2019a. doi: 10.1103/PhysRevD.100.023008.

M. C. Miller et al. PSR J0030+0451 Mass and Radius from $NICER$ Data and Implications for the Properties of Neutron Star Matter. *Astrophys. J.*, 887(1):L24, 2019b. doi: 10.3847/2041-8213/ab50c5.

Bedangadas Mohanty. STAR experiment results from the beam energy scan program at RHIC. *J. Phys. G*, 38:124023, 2011. doi: 10.1088/0954-3899/38/12/124023.

Elias R. Most, L. Jens Papenfort, Veronica Dexheimer, Matthias Hanauske, Stefan Schramm, Horst Stöcker, and Luciano Rezzolla. Signatures of quark-hadron phase transitions in general-relativistic neutron-star mergers. *Phys. Rev. Lett.*, 122(6):061101, 2019. doi: 10.1103/PhysRevLett.122.061101.

Elias R. Most, L. Jens Papenfort, Samuel Tootle, and Luciano Rezzolla. Fast ejecta as a potential way to distinguish black holes from neutron stars in high-mass gravitational-wave events. *Astrophys. J.*, 912(1): 80, 2021a. doi: 10.3847/1538-4357/abf0a5.

Elias R. Most, L. Jens Papenfort, Samuel D. Tootle, and Luciano Rezzolla. On accretion discs formed in MHD simulations of black hole–neutron star mergers with accurate microphysics. *Mon. Not. Roy. Astron. Soc.*, 506(3):3511–3526, 2021b. doi: 10.1093/mnras/stab1824.

Keitaro Nagata. Finite-density lattice QCD and sign problem: Current status and open problems. *Prog. Part. Nucl. Phys.*, 127:103991, 2022. doi: 10.1016/j.ppnp.2022.103991.

Y. Nambu and G. Jona-Lasinio. Dynamical model of elementary particles based on an analogy with superconductivity. i. *Phys. Rev.*, 122:345–358, Apr 1961a. doi: 10.1103/PhysRev.122.345. URL `https://link.aps.org/doi/10.1103/PhysRev.122.345`.

Y. Nambu and G. Jona-Lasinio. Dynamical model of elementary particles based on an analogy with superconductivity. ii. *Phys. Rev.*, 124:246–254, Oct 1961b. doi: 10.1103/PhysRev.124.246. URL `https://link.aps.org/doi/10.1103/PhysRev.124.246`.

Rebecca Nealon, Daniel J. Price, Clément Bonnerot, and Giuseppe Lodato. On the PapaloizouPringle instability in tidal disruption events. *Monthly Notices of the Royal Astronomical Society*, 474(2):1737–1745, 11 2017. ISSN 0035-8711. doi: 10.1093/mnras/stx2871. URL `https://doi.org/10.1093/mnras/stx2871`.

Vsevolod Nedora, Sebastiano Bernuzzi, David Radice, Albino Perego, Andrea Endrizzi, and Néstor Ortiz. Spiral-wave wind for the blue kilonova. *Astrophys. J.*, 886(2):L30, 2019. doi: 10.3847/2041-8213/ab5794.

Vsevolod Nedora, Sebastiano Bernuzzi, David Radice, Boris Daszuta, Andrea Endrizzi, Albino Perego, Aviral Prakash, Mohammadtaher Safarzadeh, Federico Schianchi, and Domenico Logoteta. Numerical Relativity Simulations of the Neutron Star Merger GW170817: Long-Term Remnant Evolutions, Winds, Remnant Disks, and Nucleosynthesis. *Astrophys. J.*, 906(2):98, 2021a. doi: 10.3847/1538-4357/abc9be.

Vsevolod Nedora, David Radice, Sebastiano Bernuzzi, Albino Perego, Boris Daszuta, Andrea Endrizzi, Aviral Prakash, and Federico Schianchi. Dynamical ejecta synchrotron emission as possible contributor to the rebrightening of GRB170817A. *preprint (ArXiv:2104.04537)*, April 2021b.

Vsevolod Nedora, Federico Schianchi, Sebastiano Bernuzzi, David Radice, Boris Daszuta, Andrea Endrizzi, Albino Perego, Aviral Prakash, and Francesco Zappa. Mapping dynamical ejecta and disk masses from numerical relativity simulations of neutron star mergers. *Class. Quant. Grav.*, 39(1):015008, 2022. doi: 10.1088/1361-6382/ac35a8.

David Neilsen, Steven L. Liebling, Matthew Anderson, Luis Lehner, Evan OConnor, et al. Magnetized Neutron Stars With Realistic Equations of State and Neutrino Cooling. *Phys.Rev.*, D89(10):104029, 2014. doi: 10.1103/PhysRevD.89.104029.

M. Oertel, M. Hempel, T. Klähn, and S. Typel. Equations of state for supernovae and compact stars. *Rev. Mod. Phys.*, 89(1):015007, 2017. doi: 10.1103/RevModPhys.89.015007.

J. C. B. Papaloizou and J. E. Pringle. The dynamical stability of differentially rotating discs with constant specific angular momentum. *Monthly Notices of the Royal Astronomical Society*, 208(4):721–750, 06 1984. ISSN 0035-8711. doi: 10.1093/mnras/208.4.721. URL `https://doi.org/10.1093/mnras/208.4.721`.

P. Papazoglou, D. Zschiesche, S. Schramm, J. Schaffner-Bielich, Horst Stoecker, and W. Greiner. Nuclei in a chiral SU(3) model. *Phys. Rev.*, C59:411–427, 1999. doi: 10.1103/PhysRevC.59.411.

A. Perego, F. K. Thielemann, and G. Cescutti. r-Process Nucleosynthesis from Compact Binary Mergers. In *Handbook of Gravitational Wave Astronomy*, page 1. 2021. doi: 10.1007/978-981-15-4702-7_13-1.

Albino Perego, Stephan Rosswog, Ruben Cabezon, Oleg Korobkin, Roger Kaeppeli, et al. Neutrino-driven winds from neutron star merger remnants. *Mon.Not.Roy.Astron.Soc.*, 443:3134, 2014. doi: 10.1093/mnras/stu1352.

Albino Perego, David Radice, and Sebastiano Bernuzzi. AT2017gfo: An Anisotropic and Three-component Kilonova Counterpart of GW170817. *Astrophys. J.*, 850(2):L37, 2017. doi: 10.3847/2041-8213/aa9ab9.

Albino Perego, Sebastiano Bernuzzi, and David Radice. Thermodynamics conditions of matter in neutron star mergers. *Eur. Phys. J.*, A55(8):124, 2019. doi: 10.1140/epja/i2019-12810-7.

Albino Perego, Domenico Logoteta, David Radice, Sebastiano Bernuzzi, Rahul Kashyap, Abhishek Das, Surendra Padamata, and Aviral Prakash. Probing the Incompressibility of Nuclear Matter at Ultrahigh Density through the Prompt Collapse of Asymmetric Neutron Star Binaries. *Phys. Rev. Lett.*, 129(3): 032701, 2022a. doi: 10.1103/PhysRevLett.129.032701.

Albino Perego et al. Production of Very Light Elements and Strontium in the Early Ejecta of Neutron Star Mergers. *Astrophys. J.*, 925(1):22, 2022b. doi: 10.3847/1538-4357/ac3751.

P. C. Peters. Gravitational Radiation and the Motion of Two Point Masses. *Phys. Rev.*, 136:B1224–B1232, 1964. doi: 10.1103/PhysRev.136.B1224.

P. C. Peters and J. Mathews. Gravitational radiation from point masses in a Keplerian orbit. *Phys. Rev.*, 131:435–439, 1963. doi: 10.1103/PhysRev.131.435.

Philip A. Pinto and Ronald G. Eastman. The Physics of the type Ia supernova light curves. 1. Analytic results and time dependence. *Astrophys. J.*, 530:744–756, 2000. doi: 10.1086/308376.

Denis Pollney, Christian Reisswig, Erik Schnetter, Nils Dorband, and Peter Diener. High accuracy binary black hole simulations with an extended wave zone. *Phys. Rev.*, D83:044045, 2011. doi: 10.1103/PhysRevD.83.044045.

Aviral Prakash, David Radice, Domenico Logoteta, Albino Perego, Vsevolod Nedora, Ignazio Bombaci, Rahul Kashyap, Sebastiano Bernuzzi, and Andrea Endrizzi. Signatures of deconfined quark phases in binary neutron star mergers. *Phys. Rev. D*, 104(8):083029, 2021. doi: 10.1103/PhysRevD.104.083029.

N. Prantzos, C. Abia, S. Cristallo, M. Limongi, and A. Chieffi. Chemical evolution with rotating massive star yields ii. a new assessment of the solar s- and r-process components. *mnras*, 491(2):1832–1850, jan 2020. doi: 10.1093/mnras/stz3154.

Y.Z. Qian and S.E. Woosley. Nucleosynthesis in neutrino driven winds: 1. The Physical conditions. *Astrophys. J.*, 471:331–351, 1996. doi: 10.1086/177973.

G. Raaijmakers et al. Constraining the dense matter equation of state with joint analysis of NICER and LIGO/Virgo measurements. *Astrophys. J. Lett.*, 893(1):L21, 2020. doi: 10.3847/2041-8213/ab822f.

Geert Raaijmakers et al. The Challenges Ahead for Multimessenger Analyses of Gravitational Waves and Kilonova: A Case Study on GW190425. *Astrophys. J.*, 922(2):269, 2021. doi: 10.3847/1538-4357/ac222d.

David Radice. General-Relativistic Large-Eddy Simulations of Binary Neutron Star Mergers. *Astrophys. J.*, 838(1):L2, 2017. doi: 10.3847/2041-8213/aa6483.

David Radice. Binary Neutron Star Merger Simulations with a Calibrated Turbulence Model. *Symmetry*, 12(8):1249, 2020. doi: 10.3390/sym12081249.

David Radice and Sebastiano Bernuzzi. Ab-initio General-relativistic Neutrino-radiation Hydrodynamics Simulations of Long-lived Neutron Star Merger Remnants to Neutrino Cooling Timescales. *Astrophys. J.*, 959(1):46, 2023. doi: 10.3847/1538-4357/ad0235.

David Radice and Luciano Rezzolla. THC: a new high-order finite-difference high-resolution shock-capturing code for special-relativistic hydrodynamics. *Astron. Astrophys.*, 547:A26, 2012. doi: 10.1051/0004-6361/201219735.

David Radice, Luciano Rezzolla, and Filippo Galeazzi. Beyond second-order convergence in simulations of binary neutron stars in full general-relativity. *Mon.Not.Roy.Astron.Soc.*, 437:L46–L50, 2014. doi: 10.1093/mnrasl/slt137.

David Radice, Filippo Galeazzi, Jonas Lippuner, Luke F. Roberts, Christian D. Ott, and Luciano Rezzolla. Dynamical Mass Ejection from Binary Neutron Star Mergers. *Mon. Not. Roy. Astron. Soc.*, 460(3): 3255–3271, 2016. doi: 10.1093/mnras/stw1227.

David Radice, Albino Perego, Sebastiano Bernuzzi, and Bing Zhang. Long-lived Remnants from Binary Neutron Star Mergers. *Mon. Not. Roy. Astron. Soc.*, 481(3):3670–3682, 2018a. doi: 10.1093/mnras/sty2531.

David Radice, Albino Perego, Kenta Hotokezaka, Steven A. Fromm, Sebastiano Bernuzzi, and Luke F. Roberts. Binary Neutron Star Mergers: Mass Ejection, Electromagnetic Counterparts and Nucleosynthesis. *Astrophys. J.*, 869(2):130, 2018b. doi: 10.3847/1538-4357/aaf054.

David Radice, Sebastiano Bernuzzi, and Albino Perego. The Dynamics of Binary Neutron Star Mergers and of GW170817. *Ann. Rev. Nucl. Part. Sci.*, 70, 2020. doi: 10.1146/annurev-nucl-013120-114541.

Angels Ramos, Jurgen Schaffner-Bielich, and Jochen Wambach. Kaon condensation in neutron stars. *Lect. Notes Phys.*, 578:175–202, 2001.

Jocelyn S. Read, Benjamin D. Lackey, Benjamin J. Owen, and John L. Friedman. Constraints on a phenomenologically parameterized neutron- star equation of state. *Phys. Rev.*, D79:124032, 2009. doi: 10.1103/PhysRevD.79.124032.

P. Rehberg, S. P. Klevansky, and J. Hufner. Hadronization in the SU(3) Nambu-Jona-Lasinio model. *Phys. Rev. C*, 53:410–429, 1996. doi: 10.1103/PhysRevC.53.410.

C. Reisswig, R. Haas, C. D. Ott, E. Abdikamalov, P. Mösta, D. Pollney, and E. Schnetter. Three-Dimensional General-Relativistic Hydrodynamic Simulations of Binary Neutron Star Coalescence and Stellar Collapse with Multipatch Grids. *Phys. Rev.*, D87(6):064023, 2013a. doi: 10.1103/PhysRevD.87.064023.

C. Reisswig, C.D. Ott, E. Abdikamalov, R. Haas, P. Mösta, et al. Formation and Coalescence of Cosmological Supermassive Black Hole Binaries in Supermassive Star Collapse. *Phys.Rev.Lett.*, 111:151101, 2013b. doi: 10.1103/PhysRevLett.111.151101.

Christian Reisswig and Denis Pollney. Notes on the integration of numerical relativity waveforms. *Class.Quant.Grav.*, 28:195015, 2011. doi: 10.1088/0264-9381/28/19/195015.

Luciano Rezzolla, Luca Baiotti, Bruno Giacomazzo, David Link, and Jose A. Font. Accurate evolutions of unequal-mass neutron-star binaries: properties of the torus and short GRB engines. *Class. Quant. Grav.*, 27:114105, 2010. doi: 10.1088/0264-9381/27/11/114105.

Thomas E. Riley et al. A *NICER* View of PSR J0030+0451: Millisecond Pulsar Parameter Estimation. *Astrophys. J.*, 887(1):L21, 2019. doi: 10.3847/2041-8213/ab481c.

S. Rosswog, J. Sollerman, U. Feindt, A. Goobar, O. Korobkin, R. Wollaeger, C. Fremling, and M. M. Kasliwal. The first direct double neutron star merger detection: implications for cosmic nucleosynthesis. *Astron. Astrophys.*, 615:A132, 2018. doi: 10.1051/0004-6361/201732117.

Stephan Rosswog. The multi-messenger picture of compact binary mergers. *Int.J.Mod.Phys.*, D24(05): 1530012, 2015. doi: 10.1142/S0218271815300128.

Stephan Rosswog and M. Liebendoerfer. High resolution calculations of merging neutron stars. 2: Neutrino emission. *Mon.Not.Roy.Astron.Soc.*, 342:673, 2003. doi: 10.1046/j.1365-8711.2003.06579.x.

M. Ruffert, H.T. Janka, K. Takahashi, and Gerhard Schäfer. Coalescing neutron stars: A Step towards physical models. 2. Neutrino emission, neutron tori, and gamma-ray bursts. *Astron.Astrophys.*, 319: 122–153, 1997.

M. H. Ruffert, H. T. Janka, and Gerhard Schäfer. Coalescing neutron stars: A step towards physical models. I: Hydrodynamic evolution and gravitational- wave emission. *Astron. Astrophys.*, 311:532–566, 1996.

Bernd-Jochen Schaefer and Mathias Wagner. On the QCD phase structure from effective models. *Prog. Part. Nucl. Phys.*, 62:381, 2009. doi: 10.1016/j.ppnp.2008.12.009.

Stefan Scherer. Introduction to chiral perturbation theory. *Adv. Nucl. Phys.*, 27:277, 2003.

H R Schmidt and J Schukraft. The physics of ultra-relativistic heavy-ion collisions. *Journal of Physics G: Nuclear and Particle Physics*, 19(11):1705, nov 1993. doi: 10.1088/0954-3899/19/11/006. URL `https://dx.doi.org/10.1088/0954-3899/19/11/006`.

A. S. Schneider, Luke F. Roberts, and Christian D. Ott. Open-source nuclear equation of state framework based on the liquid-drop model with Skyrme interaction. *Phys. Rev.*, C96(6):065802, 2017. doi: 10.1103/PhysRevC.96.065802.

Erik Schnetter, Scott H. Hawley, and Ian Hawke. Evolutions in 3-D numerical relativity using fixed mesh refinement. *Class.Quant.Grav.*, 21:1465–1488, 2004. doi: 10.1088/0264-9381/21/6/014.

Erik Schnetter, Christian D. Ott, Gabrielle Allen, Peter Diener, Tom Goodale, Thomas Radke, Edward Seidel, and John Shalf. Cactus Framework: Black Holes to Gamma Ray Bursts. 2007.

Jurgen Schukraft and Reinhard Stock. Toward the Limits of Matter: Ultra-relativistic nuclear collisions at CERN. *Adv. Ser. Direct. High Energy Phys.*, 23:61–87, 2015. doi: 10.1142/9789814644150_0003.

Ralph Schönrich and David H. Weinberg. The chemical evolution of r-process elements from neutron star mergers: the role of a 2-phase interstellar medium. *Mon. Not. Roy. Astron. Soc.*, 487(1):580–594, 2019. doi: 10.1093/mnras/stz1126.

Yuichiro Sekiguchi, Kenta Kiuchi, Koutarou Kyutoku, and Masaru Shibata. Dynamical mass ejection from binary neutron star mergers: Radiation-hydrodynamics study in general relativity. *Phys.Rev.*, D91(6):064059, 2015. doi: 10.1103/PhysRevD.91.064059.

Masaru Shibata and Kenta Hotokezaka. Merger and Mass Ejection of Neutron-Star Binaries. *Ann. Rev. Nucl. Part. Sci.*, 69:41–64, 2019. doi: 10.1146/annurev-nucl-101918-023625.

Masaru Shibata, Sho Fujibayashi, Kenta Hotokezaka, Kenta Kiuchi, Koutarou Kyutoku, Yuichiro Sekiguchi, and Masaomi Tanaka. Modeling GW170817 based on numerical relativity and its implications. *Phys. Rev.*, D96(12):123012, 2017. doi: 10.1103/PhysRevD.96.123012.

Masaru Shibata, Sho Fujibayashi, and Yuichiro Sekiguchi. Long-term evolution of a merger-remnant neutron star in general relativistic magnetohydrodynamics: Effect of magnetic winding. *Phys. Rev. D*, 103(4):043022, 2021. doi: 10.1103/PhysRevD.103.043022.

Daniel M. Siegel. GW170817–the first observed neutron star merger and its kilonova: implications for the astrophysical site of the r-process. *Eur. Phys. J. A*, 55(11):203, 2019. doi: 10.1140/epja/i2019-12888-9.

Daniel M. Siegel. r-process nucleosynthesis in gravitational-wave and other explosive astrophysical events. *Nature Reviews Physics*, 4(5):306–318, May 2022. ISSN 2522-5820. doi: 10.1038/s42254-022-00439-1. URL `https://doi.org/10.1038/s42254-022-00439-1`.

Daniel M. Siegel and Brian D. Metzger. Three-Dimensional General-Relativistic Magnetohydrodynamic Simulations of Remnant Accretion Disks from Neutron Star Mergers: Outflows and r-Process Nucleosynthesis. *Phys. Rev. Lett.*, 119(23):231102, 2017. doi: 10.1103/PhysRevLett.119.231102.

Daniel M. Siegel and Brian D. Metzger. Three-dimensional GRMHD simulations of neutrino-cooled accretion disks from neutron star mergers. *Astrophys. J.*, 858(1):52, 2018. doi: 10.3847/1538-4357/aabaec.

Daniel M. Siegel, Riccardo Ciolfi, and Luciano Rezzolla. Magnetically driven winds from differentially rotating neutron stars and X-ray afterglows of short gamma-ray bursts. *Astrophys. J.*, 785:L6, 2014. doi: 10.1088/2041-8205/785/1/L6.

T. Skyrme. The effective nuclear potential. *Nucl. Phys.*, 9:615–634, 1959. doi: 10.1016/0029-5582(58)90345-6.

S. J. Smartt et al. A kilonova as the electromagnetic counterpart to a gravitational-wave source. *Nature*, 2017. doi: 10.1038/nature24303.

M. Soares-Santos et al. The Electromagnetic Counterpart of the Binary Neutron Star Merger LIGO/Virgo GW170817. I. Dark Energy Camera Discovery of the Optical Counterpart. *Astrophys. J.*, 848(2):L16, 2017. doi: 10.3847/2041-8213/aa9059.

T. M. Sprouse, K. A. Lund, J. M. Miller, G. C. McLaughlin, and M. R. Mumpower. Emergent nucleosynthesis from a 1.2 second long simulation of a black-hole accretion disk. 9 2023.

D. Steeghs, M. Dyer, D. Galloway, V. Dhillon, P. O'Brien, G. Ramsay, D. Pollacco, E. Thrane, S. Poshyachinda, E. Palle, K. Ulaczyk, R. Cutter, E. Stanway, K. Ackley, A. Obradovic, Y. L. Mong, A. Casey, M. Brown, E. Rol, J. Mullaney, S. Littlefair, L. Makrygianni, E. Daw, J. Maund, R. Starling, R. Eyles, U. Sawangwit, D. Mkrtichian, S. Awiphan, S. Aukkaravittayapun, P. Irawati, M. Kennedy, R. Breton, D. Mata-Sanchez, T. Heikkila, and R. Kotak. LIGO/Virgo S190425z: GOTO observations. *GRB Coordinates Network*, 24224:1, January 2019.

Andrew W. Steiner, Matthias Hempel, and Tobias Fischer. Core-collapse supernova equations of state based on neutron star observations. *Astrophys. J.*, 774:17, 2013. doi: 10.1088/0004-637X/774/1/17.

J. R. Stone and P. G. Reinhard. The Skyrme Interaction in finite nuclei and nuclear matter. *Prog. Part. Nucl. Phys.*, 58:587–657, 2007. doi: 10.1016/j.ppnp.2006.07.001.

E. Symbalisty and D. N. Schramm. Neutron star collisions and the r-process. *Astrophys. J. Letters*, 22: 143–145, 1982.

Masaomi Tanaka, Daiji Kato, Gediminas Gaigalas, and Kyohei Kawaguchi. Systematic opacity calculations for kilonovae. *Mon. Not. Roy. Astron. Soc.*, 496(2):1369–1392, August 2020. doi: 10.1093/mnras/staa1576.

N. R. Tanvir et al. The Emergence of a Lanthanide-Rich Kilonova Following the Merger of Two Neutron Stars. *Astrophys. J.*, 848:L27, 2017. doi: 10.3847/2041-8213/aa90b6.

S.A. Teukolsky. Rotating black holes - separable wave equations for gravitational and electromagnetic perturbations. *Phys.Rev.Lett.*, 29:1114–1118, 1972. doi: 10.1103/PhysRevLett.29.1114.

Saul A. Teukolsky. Perturbations of a rotating black hole. 1. Fundamental equations for gravitational electromagnetic and neutrino field perturbations. *Astrophys. J.*, 185:635–647, 1973. doi: 10.1086/152444.

I. Tews, J. Margueron, and S. Reddy. Critical examination of constraints on the equation of state of dense matter obtained from GW170817. *Phys. Rev.*, C98(4):045804, 2018. doi: 10.1103/PhysRevC.98.045804.

Marcus Thierfelder, Sebastiano Bernuzzi, David Hilditch, Bernd Brügmann, and Luciano Rezzolla. The trumpet solution from spherical gravitational collapse with puncture gauges. *Phys.Rev.*, D83:064022, 2011. doi: 10.1103/PhysRevD.83.064022.

Jonathan Thornburg. A Fast apparent horizon finder for three-dimensional Cartesian grids in numerical relativity. *Class. Quant. Grav.*, 21:743–766, 2004. doi: 10.1088/0264-9381/21/2/026.

Samuel D. Tootle, L. Jens Papenfort, Elias R. Most, and Luciano Rezzolla. Quasi-universal Behavior of the Threshold Mass in Unequal-mass, Spinning Binary Neutron Star Mergers. *Astrophys. J. Lett.*, 922(1): L19, 2021. doi: 10.3847/2041-8213/ac350d.

S. Typel, G. Ropke, T. Klahn, D. Blaschke, and H. H. Wolter. Composition and thermodynamics of nuclear matter with light clusters. *Phys. Rev.*, C81:015803, 2010. doi: 10.1103/PhysRevC.81.015803.

Stefano Valenti, David J. Sand, Sheng Yang, Enrico Cappellaro, Leonardo Tartaglia, Alessandra Corsi, Saurabh W. Jha, Daniel E. Reichart, Joshua Haislip, and Vladimir Kouprianov. The discovery of the electromagnetic counterpart of GW170817: kilonova AT 2017gfo/DLT17ck. *Astrophys. J.*, 848(2):L24, 2017. doi: 10.3847/2041-8213/aa8edf.

Shinya Wanajo, Yuichiro Sekiguchi, Nobuya Nishimura, Kenta Kiuchi, Koutarou Kyutoku, and Masaru Shibata. Production of all the r-process nuclides in the dynamical ejecta of neutron star mergers. *Astrophys. J.*, 789:L39, 2014. doi: 10.1088/2041-8205/789/2/L39.

Steven Weinberg. Nuclear forces from chiral lagrangians. *Physics Letters B*, 251(2):288–292, November 1990. doi: 10.1016/0370-2693(90)90938-3.

Simon Weissenborn, Irina Sagert, Giuseppe Pagliara, Matthias Hempel, and Jürgen Schaffner-Bielich. Quark Matter In Massive Neutron Stars. *Astrophys. J. Lett.*, 740:L14, 2011. doi: 10.1088/2041-8205/740/1/L14.

Ryan T. Wollaeger, Oleg Korobkin, Christopher J. Fontes, Stephan K. Rosswog, Wesley P. Even, Christopher L. Fryer, Jesper Sollerman, Aimee L. Hungerford, Daniel R. van Rossum, and Allan B. Wollaber. Impact of ejecta morphology and composition on the electromagnetic signatures of neutron star mergers. *Mon. Not. Roy. Astron. Soc.*, 478(3):3298–3334, 2018. doi: 10.1093/mnras/sty1018.

S. E. Woosley and Thomas A. Weaver. The Evolution and Explosion of Massive Stars. II. Explosive Hydrodynamics and Nucleosynthesis, November 1995.

Meng-Ru Wu, Rodrigo Fernández, Gabriel Martínez-Pinedo, and Brian D. Metzger. Production of the entire range of r-process nuclides by black hole accretion disc outflows from neutron star mergers. *Mon. Not. Roy. Astron. Soc.*, 463(3):2323–2334, 2016. doi: 10.1093/mnras/stw2156.

Zhenyu Wu, Giacomo Ricigliano, Rahul Kashyap, Albino Perego, and David Radice. Radiation hydrodynamics modelling of kilonovae with SNEC. *Mon. Not. Roy. Astron. Soc.*, 512(1):328–347, 2022. doi: 10.1093/mnras/stac399.

Francesco Zappa, Sebastiano Bernuzzi, David Radice, Albino Perego, and Tim Dietrich. Gravitational-wave luminosity of binary neutron stars mergers. *Phys. Rev. Lett.*, 120(11):111101, 2018. doi: 10.1103/PhysRevLett.120.111101.

Yossef Zenati, Julian Krolik, Leonardo Werneck, Zachariah Etienne, Scott Noble, Ariadna Murguia-Berthier, and Jeremy Schnittman. The Dynamics of Debris Disk Creation in Neutron Star Mergers. 4 2024.

W. H. Zurek and W. Benz. Redistribution of Angular Momentum by Nonaxisymmetric Instabilities in a Thick Accretion Disk. ApJ, 308:123, September 1986. doi: 10.1086/164483.

Feryal Özel and Paulo Freire. Masses, Radii, and the Equation of State of Neutron Stars. *Ann. Rev. Astron. Astrophys.*, 54:401–440, 2016. doi: 10.1146/annurev-astro-081915-023322.